Development of Radiation Hard Planar Silicon Tracking Detectors for the ATLAS Experiment at the HL-LHC

Dean Forshaw

The University of Liverpool
Particle Physics Group

June 2014

Thesis submitted in accordance with the requirements of The University of Liverpool for the degree of Doctor of Philosophy

Abstract

To extend the physics reach of the LHC, upgrades to the accelerator are planned which will increase the integrated annual luminosity by a factor of 10 (to 250 - 300 $\mathrm{fb}^{-1}/\,year$). This will increase the occupancy and the radiation damage of the inner trackers. To cope with the elevated occupancy, the ATLAS experiment plans to introduce an all silicon inner tracker for use during High Luminosity LHC (HL-LHC) operation. With silicon, the occupancy can be adjusted by using the appropriate pitch for the pixels/micro-strips. Constraints due to high radiation damage mean that only sensors with electrode configuration designed to read out the electron signal (*n-in-p* and *n-in-n*) are considered.

The work presented within this thesis has been undertaken as part of the CERN-RD50 and ATLAS Upgrade collaborations. The main focus has been, firstly, on the development of radiation hard silicon detectors and the possible exploitation of the charge multiplication effect observed in irradiated silicon detectors that collect charge via electrons. Secondly, the production and optimisation of *n-in-p* planar pixel detectors designed specifically for ATLAS's new Inner Tracker (ITk). The prototype sensors were produced by Micron Semiconductors Ltd, UK.

Declaration

This dissertation is the result of my own work, except where explicit reference is made to the work of others, and has not been submitted for another qualification to this, or any, other university. This dissertation does not exceed the word limit for the respective Degree Committee.

Dean Forshaw

Contents

1 Introduction **3**

2 The Large Hadron Collider (LHC) **5**

2.1 The LHC Accelerator Complex 6
2.2 Current Performance 7
2.3 LHC upgrade 8
2.3.1 LS1 - Consolidation 10
2.3.2 LS2 - LINAC4 12
2.3.3 LS3 - HL - LHC 12

3 Physics Motivation **17**

3.1 The Standard Model of Particle Physics 17
3.2 Issues with the Electroweak Model - Why We Need the Higgs Mechanism 19
3.3 Higgs Mechanism 20
3.4 Physics Beyond the Standard Model 22
3.5 HL-LHC Physics 24
3.5.1 Higgs Boson Couplings 25
3.5.2 Weak Vector Boson Scattering 27
3.5.3 Direct and indirect searches for BSM Higgs bosons 29
3.5.4 Search for BSM Physics Signatures 29

4 The ATLAS Experiment **33**

4.1 Overview 33
4.2 DAQ and Trigger 36
4.2.1 System Overview 36
4.2.2 Upgrades 38
4.3 Muon Spectrometer 40
4.3.1 System Overview 40
4.3.2 Upgrades 42

4.4 Calorimeter System . . . 46
4.4.1 System Overview . . . 46
4.4.2 Upgrades . . . 47
4.5 Inner Detector . . . 51
4.5.1 System Overview . . . 51
4.5.2 Transition Radiation Tracker (TRT) . . . 53
4.5.3 SemiConductor Tracker (SCT) . . . 53
4.5.4 Pixel Detector . . . 54
4.5.5 Upgrades . . . 60

5 Physics and Properties of Silicon as a Semiconductors 69
5.1 Crystal Structure . . . 69
5.2 Energy Bands . . . 70
5.3 Carrier Concentration . . . 72
5.3.1 Intrinsic Silicon . . . 72
5.3.2 Doped Silicon . . . 73
5.4 *p-n* Junction . . . 75
5.5 *p-n* Junction Diode Characteristics . . . 77
5.6 Temperature Effects . . . 80
5.7 Junction Breakdown . . . 80
5.7.1 Thermal Instability . . . 80
5.7.2 Tunnelling Instability (Zener break-down) . . . 81
5.7.3 Avalanche Multiplication . . . 81

6 *p-n* Junction as a Particle Detector 83
6.1 Segmentation . . . 84
6.2 Energy Loss of Particles . . . 86
6.2.1 Heavy Charged Particles . . . 87
6.2.2 Electrons and Photons . . . 89
6.2.3 Neutral and Charged Hadrons . . . 91
6.3 Signal Generation . . . 92

7 Sensor Design Aspects 95
7.1 Sensor Layout Variants . . . 95
7.1.1 *n-in-n* . . . 96
7.1.2 *n-in-p* . . . 97
7.2 Guard Rings . . . 98

7.3 AC vs DC coupled readout . . . 99
7.4 Powering Options . . . 99
7.5 Inter-Pixel Isolation . . . 100

8 The Effects of Radiation Damage on Detector Performance 103
8.1 Surface Effects . . . 103
8.1.1 Implications of Surface Damage . . . 104
8.2 Bulk Defects . . . 104
8.3 Defect Annealing . . . 105
8.4 The NIEL Scaling Hypothesis . . . 106
8.4.1 Hardness Factors . . . 108
8.5 Implications of Bulk Defects . . . 109
8.6 The Leakage Current . . . 112
8.7 Summary . . . 113

9 Methodology 115
9.1 Measurement of IV Characteristics . . . 115
9.2 Thermal imaging . . . 116
9.3 Irradiation Facilities . . . 117
9.4 ALiBaVa Readout System . . . 119
9.4.1 Instrumentation . . . 119
9.5 Operation of ATLAS FEI4 readout chip . . . 122
9.5.1 FE-I4 Chip Overview . . . 122
9.5.2 Pixel Array Performance . . . 125
9.5.3 USBpix System . . . 127
9.5.4 RCE system . . . 128
9.5.5 Tuning . . . 128
9.6 Test Beam . . . 133
9.6.1 Beam Test Facilities . . . 134
9.6.2 The EUDET Telescope . . . 136
9.6.3 Cooling . . . 137
9.6.4 Track Reconstruction . . . 138
9.6.5 Data Analysis . . . 140

10 RD50 Studies 143
10.1 Calibration . . . 143

10.2 Mixed Irradiation 146
10.2.1 Irradiation and Characterisation 147
10.2.2 Results after Irradiation 148
10.2.3 Conclusion 151
10.3 CNM Planar Trenched Detectors 152
10.3.1 Geometry Description 152
10.3.2 Pre-irradiation Characterisation 153
10.3.3 Irradiation and Characterisation 156
10.3.4 Conclusion 160
10.4 Evolution of charge sharing between ATLAS IBL pixels 162
10.4.1 Geometry Description 163
10.4.2 Charge collection as a function of bias voltage 164
10.4.3 Charge sharing as a function of bias voltage 166
10.4.4 Conclusion 169
10.5 Thick vs Thin planar Sensors 171
10.5.1 Irradiation and Characterisation 172
10.5.2 Conclusion 174
10.6 Charge Multiplication Device Characterisation 175
10.6.1 Geometry Description 175
10.6.2 Irradiation and Characterisation 178
10.6.3 Results after Irradiation 178
10.6.4 Conclusion 181

11 Quad FE-I4 Modules 183
11.1 CERN PIXEL IV Design 184
11.2 Wafer Characteristics 185
11.3 Module Characterisation 187
11.3.1 Pre-Irradiation 189
11.3.2 Post-Irradiation 194
11.4 Summary 198

12 Alternative Geometry Single FE-I4 Modules 201
12.1 CERN PIXEL V 202
12.2 Simulation 204
12.3 Poly silicon resistors vs Punch Through Bias structures 206
12.4 Wafer Characteristics 208

12.5 Single Module Characterisation 211
12.5.1 Pre-Irradiation 211
12.5.2 Post-Irradiation 214
12.6 Test Beam Results 216
12.6.1 125x100 μm^2 ($1 \cdot 10^{15}$ n_{eq}/cm^2) 216
12.6.2 250x50 μm^2 ($1 \cdot 10^{15}$ n_{eq}/cm^2) 222
12.6.3 500x25 μm^2- un-irradiated 225

13 Conclusion 229

Bibliography 233

Chapter 1

Introduction

Some of the most fundamental questions in physics relate to the structure of matter and the forces which bind particles together. To this end, particle physics experiments have been utilised to elucidate the nature of the fundamental particles and forces, and to measure their properties. The "Standard Model" of particle physics was conceived to help explain the particle spectrum and their interactions in a single coherent framework [1–5]. This model not only fits observed data with high precision but has also led to many successful predictions [6]. Until recently the Higgs boson [7–9], the particle theorised by the Standard Model to explain the observed masses of fundamental particles, had never been observed. However, in 2012, the LHC (see Chapter 2) announced the discovery of a "Higgs-like" particle [10]. Despite its success, the Standard Model leaves some vital questions unanswered such as: why is there such a range of fundamental mass scales, the nature of the dark matter and dark energy required by cosmology, and the origin of the matter/anti-matter asymmetry in the universe. To answer these questions, different Standard Model extensions, such as supersymmetry, have been developed. The Large Hadron Collider (LHC) was built to search for the Higgs boson and to explore possible extensions to the Standard Model.

To provide stringent tests of the Standard Model, accurately measure the properties of the newly discovered Higgs boson and to search for evidence of physics beyond the Standard Model, Experiments require detectors with high efficiency and high accuracy together with large data sets. The ATLAS experiment is one of two giant, general purpose detectors (GPDs) at the LHC [11–14] designed to [15] study a wide variety of physics channels at the LHC. The ATLAS detector consists of several different sub-detector systems, which are arranged in an onion like structure around the interaction point. At the heart of ATLAS is the Inner Detector tracker (ID) which consists of the pixel

detector, the SemiConductor Tracker (SCT) and the transition radiation tracker (TRT). The pixel detector is primarily used for tracking particles close to the interaction point with the highest spatial precision. However, due to the proximity to the interaction point this detector system suffers the highest levels of radiation damage during operation. For this reason, the pixel detector has a limited operational lifetime since the high levels of radiation will affect the performance of the pixel sensors and associated readout electronics. The existing pixel system (installed June 2007 [16]) was designed to survive for around 10 years, which corresponds to 300 kGy of integrated ionising radiation or a total fluence of over $1 \cdot 10^{15} \mathrm{n_{eq}/cm^2}$ (1 MeV neutron equivalent) for nominal LHC operation [15].

The LHC will be upgraded in phases to extend its physics reach well beyond that originally foreseen (see Section 2.3) by means of increased luminosity. Consequently, the ATLAS detector will need to be upgraded to allow for continued efficient operation and to cope with the radiation damage of detector components exposed to doses well above their original design. The focus of this thesis is on the upgrades needed for the ATLAS detector as the peak luminosity, and hence the event rate, increases with each LHC upgrade, ultimately leading to the High Luminosity LHC (HL-LHC) [17]. During HL-LHC operation, the ATLAS detector system will have to operate in much harsher conditions than originally anticipated. The main topic of this thesis is the ongoing development of radiation-hard pixel detectors for HL-LHC [18]. The innermost pixel barrel layers need to withstand a total received fluence of up to $2 \cdot 10^{16} \mathrm{n_{eq}/cm^2}$, which corresponds to an integrated luminosity of $\sim 3000\, fb^{-1}$ over ten years (up by a factor of ten from the nominal design value of $300\, fb^{-1}$). The work presented in this thesis has been undertaken within the context of the ATLAS upgrade and CERN RD50 [19] programmes, with Micron Semiconductors Ltd, UK [20] providing the prototype detectors developed for use in this extreme environment.

Chapter 2

The Large Hadron Collider (LHC)

The Large Hadron Collider (LHC) [21] is located at the European Organisation for Nuclear Research (CERN) laboratory close to Geneva. It is a proton-proton collider with a design centre-of-mass energy of $14\,TeV$, making it the highest energy particle accelerator to date. The LHC also has the capability to collide beams of heavy ions such as lead nuclei. The LHC machine is situated in the former Large Electron Positron (LEP) collider tunnel which lies around $100\,m$ below ground and has an approximate circumference of 27 km.

The LHC circulates two beams of proton/ion bunches in separate beam pipes in opposite directions, colliding them at a number of interaction points. Superconducting dipole magnets provide the $8.4\,T$ magnetic field required to bend the particle beams around the LHC ring. These superconducting magnets need to be cooled to $\sim 1.9\,K$, which is achieved using liquid Helium, which at this temperature is a superfluid [22].

Within the LHC, protons are accelerated using 16 superconducting radio frequency (RF) cavities, with an acceleration gradient of $16\,MV/m$. A continuous beam is not desirable or possible at the LHC. Instead the particles are grouped into bunches of protons/ions. The LHC beams can accommodate $n_b = 2808$ bunches of $N = 1.15 \cdot 10^{11}$ protons on average. The bunches are separated by $25\,ns$, which corresponds to a collision rate of $f = 40\,MHz$.

The LHC needs very high luminosity to see rare processes such as the creation of the Higgs bosons or signatures of new physics. To detect these events, fast response, finely segmented and radiation-hard detectors are needed. There are four main experiments, each with their own interaction point positioned around the LHC ring. CMS (Compact Muon Solenoid) and ATLAS (A Toroidal LHC ApparatuS) are both general purpose

detectors (GPDs) looking for new physics, precision measurements of the Standard Model and the Higgs boson. LHCb (Large Hadron Collider beauty experiment) is a forward arm spectrometer which concentrates on CP-violation and ALICE (A Large Ion Collider Experiment) concentrates on heavy ion collisions.

2.1 The LHC Accelerator Complex

The LHC accelerator complex consists of many different accelerators chained together, with the final accelerator being the LHC ring [23]. Figure 2.1 shows the full CERN accelerator complex. As mentioned above, the LHC can accelerate proton and ion beams. Each beam type has its own LINear ACcelerator (LINAC) where the beam originates. LINAC 2 accelerates protons and the LINAC 3 accelerates heavy ions, both of which go through separate injector paths to the PS, SPS and LHC accelerator chain.

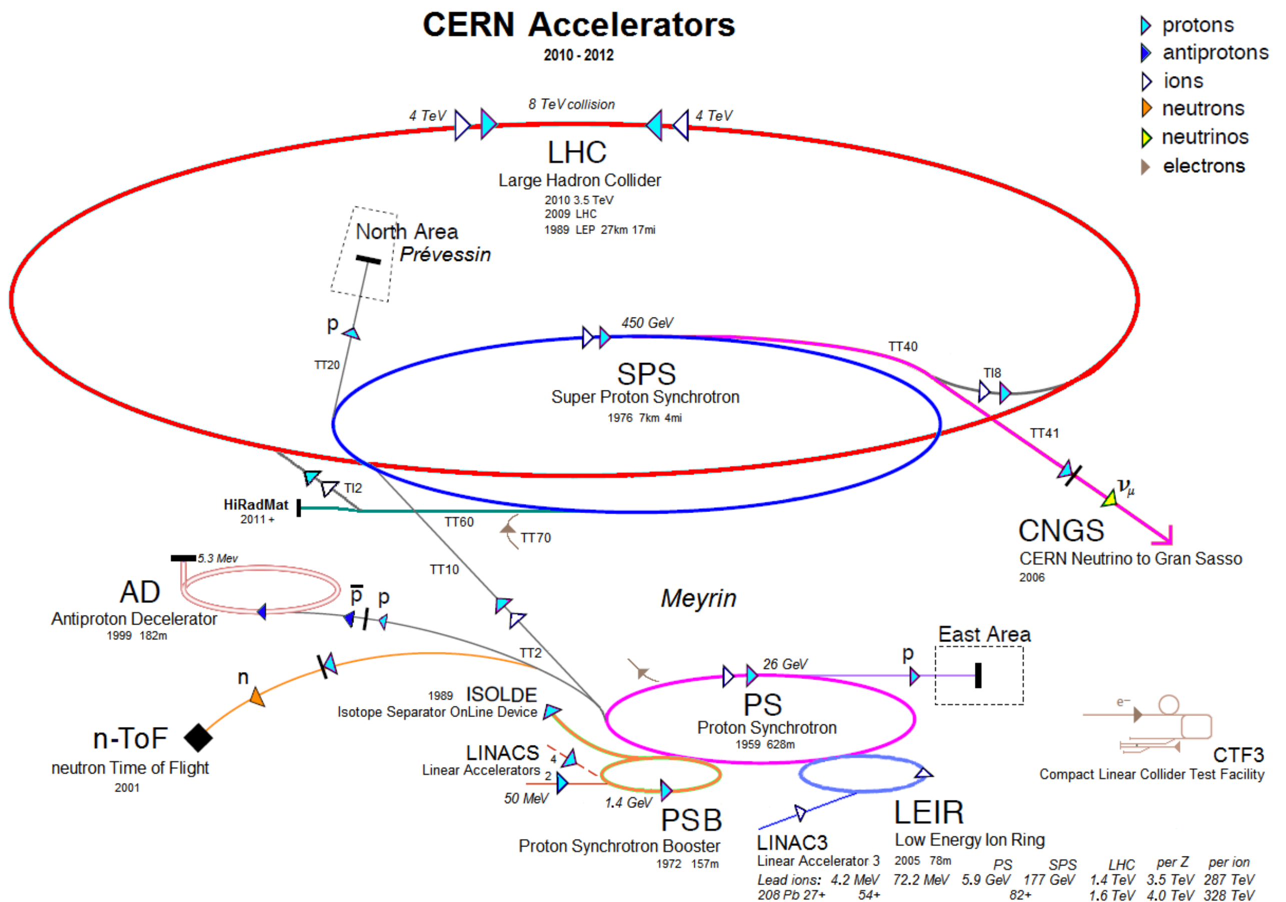

Figure 2.1: An illustration of the complete CERN accelerator complex [24].

In particular, protons are accelerated in bunches in LINAC 2 up to 50 MeV. They are then injected into the Booster and leave for the Proton Synchrotron (PS) with an energy of 1.4 GeV. The proton beam is accelerated up to 26 GeV in the PS and then injected into the Super Proton Synchrotron (SPS) where it is accelerated again up to an energy of 450 GeV. The proton bunches are injected in both directions into the LHC where they are accelerated to their final energy. The particle bunches are then compressed and their orbits adjusted to bring them into collision at the interaction points. In ATLAS, for a luminosity of $\mathcal{L} = 10^{34} cm^{-2} s^{-1}$ and a collision rate of 25 ns, an average of 27 proton collisions are produced per bunch crossing at 14 TeV centre of mass energy [21, 25].

2.2 Current Performance

The total integrated luminosities the LHC delivered to ATLAS in 2011 and 2012, for collision energies of 7 TeV and 8 TeV respectively, are shown in Figure 2.2. The increase in delivered luminosity is due to steady improvements of the LHC's performance through each year with peak instantaneous luminosity of $7 \cdot 10^{33} cm^{-2} s^{-1}$ during 2012 [26, 27]. An overview of beam parameters for the LHC in 2012 at nominal design and for HL-LHC is given in Table 2.1.

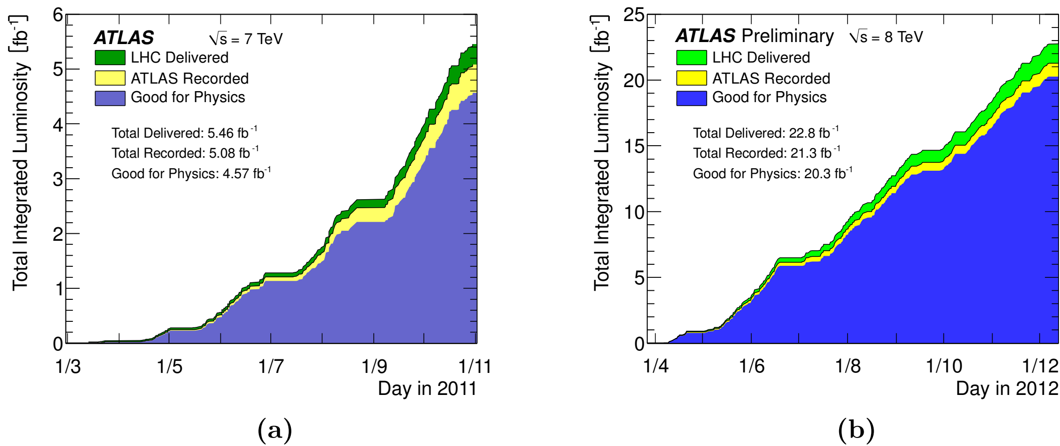

Figure 2.2: The Total integrated luminosity delivered by the LHC (green), good for physics (blue) and recorded by the ATLAS detector (yellow) over time for 2011 (a) and 2012 (b). For beam energies of 7 TeV and 8 TeV respectively [26, 28].

Parameter Name	Symbol [Unit]	Current	Design	HL-LHC
Bunch Spacing	[ns]	50	25	25
Number of bunches	n_b	1374	2808	2808
Number of particles/bunch	N_b [10^{11}]	1.6	1.15	3.2
Revolution frequency	f_{rev} [kHz]	11.245	11.245	11.245
Normalised emittance	ϵ_n [μm]	2.4	3.75	2.5
Beta function at IP	β^* [m]	0.6	0.55	0.15
Crossing angle	θ_c [μrad]	290	300	590
RMS bunch length	σ_z [cm]	≥ 9	7.55	7.50
Peak/levelled Pile-up	$< \mu >$	28	27*	140*
luminosity	$\mathcal{L}$ [$10^{34}\, cm^{-2}\, s^{-1}$]	0.7	1	7.4
Energy	$\sqrt{8}$ [TeV]	8	14	14

Table 2.1: Current average (Oct. 2012) and nominal design beam parameters of the LHC in proton operation mode. The current values are always given at the interaction point (IP) of the ATLAS experiment. Additionally, the current planning for the HL-LHC is given. For pile-up estimation the inelastic p-p cross-section is used [27, 29]. An asterix indicates the values have been updated according to the latest understanding from ATLAS and CMS [25].

2.3 LHC upgrade

To increase the physics reach of the LHC an upgrade is planned in three steps, each coinciding with a long shutdown (LS) of the machine lasting between 18 and 34 months. Each LS has a different focus on LHC performance improvements. Figure 2.3 illustrates the proposed schedule for long shutdowns, physics runs, beam commissioning and technical stops starting after LS1 (Section 2.3.1) and going to 2035. LS4 and LS5 will not be discussed in this thesis as the majority of the work presented is aimed at upgrades necessary at LS3 (Section 2.3.3).

Figure 2.4 shows an earlier projection for the expected peak luminosity increase (with levelling after LS3) and total integrated luminosity [29]. Luminosity levelling refers to limiting the delivered luminosity, to decrease pile-up while maximising the amount of data taken by an experiment. The expected levelled luminosity of $5 \cdot 10^{34} cm^{-2} s^{-1}$ will lead to 250 - 300 fb^{-1} of integrated luminosity per year and $\sim$3000 fb^{-1} over 10 years, which is more than 10 times the integrated luminosity to be taken over the first 10 years of LHC operation. Methods of luminosity levelling are discussed in Section 2.3.3.

Figure 2.3: The current LHC schedule beyond LS1 as of January 2014 for both the LHC and its injectors [17]. Blocks in green refer to planned physics runs, yellow: beam commissioning, red: shutdowns and blue: technical stops.

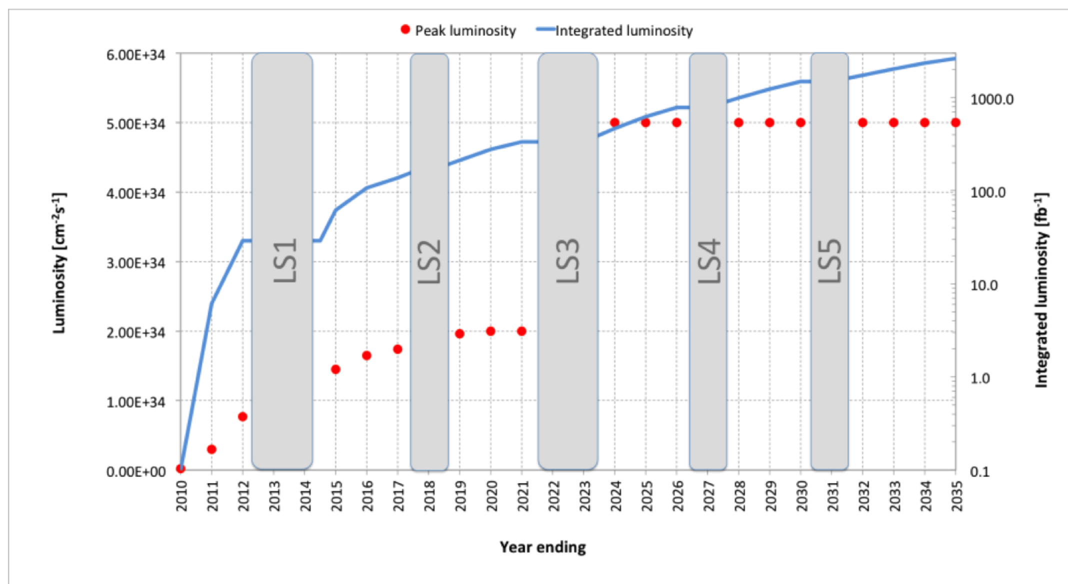

Figure 2.4: Indicative projection of peak luminosity increase and total integrated luminosity after each successive long shutdown. The peak luminosity after LS3 includes luminosity levelling leading to 250 - 300 fb^{-1} of integrated luminosity per year [29]. This plot has yet to be updated in the light of the December 2013 revision to the schedule.

2.3.1 LS1 - Consolidation

LS1 is dedicated to the consolidation of the LHC and its injectors needed primarily to reach the nominal performance in energy originally foreseen for the machine. The connections between the superconducting dipole magnets has been improved enabling higher current flow through them, up to $16\,kA$ to enable safe operation at $13\,kA$ [30]. This allows the magnetic field of the bending dipole magnets to reach their nominal value of $8.4\,T$, required for operation up to $\sqrt{s} = 14\,TeV$. The increase in beam energy enables β^{*} (see Section 2.3.2) to be decreased by a factor of 2, and the peak luminosity can be increased four-fold compared with beam parameters from 2011 [31]. Consolidations of the ATLAS detector systems are also necessary during LS1. An illustration of the main LHC consolidations is shown in Figure 2.5. Further details on any important improvements and/or modifications to the ATLAS detector is detailed in Chapter 4.

Figure 2.5: Illustration of the main LHC consolidations during LS1, in each case basic information is displayed regarding number of components that have to be replaced or tested [32].

2.3.2 LS2 - LINAC4

The second long shutdown (LS2), currently planned to start in the middle of 2018, will focus on upgrades to the LHC injectors in preparation for HL-LHC (LS3 upgrades). A new LINAC (LINAC4) [33] will be connected to the LHC accelerator complex as a replacement for LINAC2. This, in combination with collimator upgrades throughout the accelerator complex, will allow for a greater number of particles per bunch to be injected into the LHC. The injection energy at the Proton Synchrotron Booster (PSB) will be increased from 50 MeV to 160 MeV using LINAC4 and the injection energy in the PS will go from 1.4 GeV to 2 GeV by increasing the field of the PSB magnets, replacing power supplies and changing transfer equipment (to help reduce losses). The peak instantaneous luminosity of the LHC beams is strongly dependant on the injected beam characteristics. As a result of the injector upgrades the the achievable peak instantaneous luminosity This increases the achievable peak instantaneous luminosity in the LHC, because since this is strongly dependent on the characteristics of the injected beam.

Equation (2.1) details parameters which are specific to the collider (blue) and which are specific to its injectors (red). In particular the transverse beam brightness $\left(\frac{N_b}{\varepsilon_b}\right)$ is very important as it governs space charge effects at low energies in the injectors. This all leads to an expected peak luminosity (taking account of inner triplet cooling limitations) of $\mathcal{L} \approx 2.0 \cdot 10^{34}\, cm^{-2}\, s^{-1}$ [17] after LS2 [31, 34].

$$\mathcal{L}_{LHC} = \frac{\gamma}{4\pi} \underbrace{\frac{1}{\beta^*} f_{rev} F}_{\text{Collider Specific}} \cdot \underbrace{(n_b N_b)\left(\frac{N_b}{\varepsilon_b}\right)}_{\text{Injector Dependant}} . \tag{2.1}$$

2.3.3 LS3 - HL - LHC

The third long shutdown, LS3, planned for the end of 2022 is intended to build upon upgrades to the LHC injectors in LS2 and transform the LHC into the High Luminosity - LHC (HL-LHC). This new machine will have the same maximum collision energy (14 TeV) but will be capable of providing an annual integrated luminosity of 250 - 300 fb^{-1}. This increase in luminosity has substantial implications on the experiments. The harsher environment at the HL-LHC will necessitate significant detector upgrades for ATLAS and CMS. Details on upgrades to the ATLAS detector systems are given in Chapter 4.

The implications for the ATLAS physics programme, considering the upgrades to the collider and detector systems, are discussed in Section 3.5.

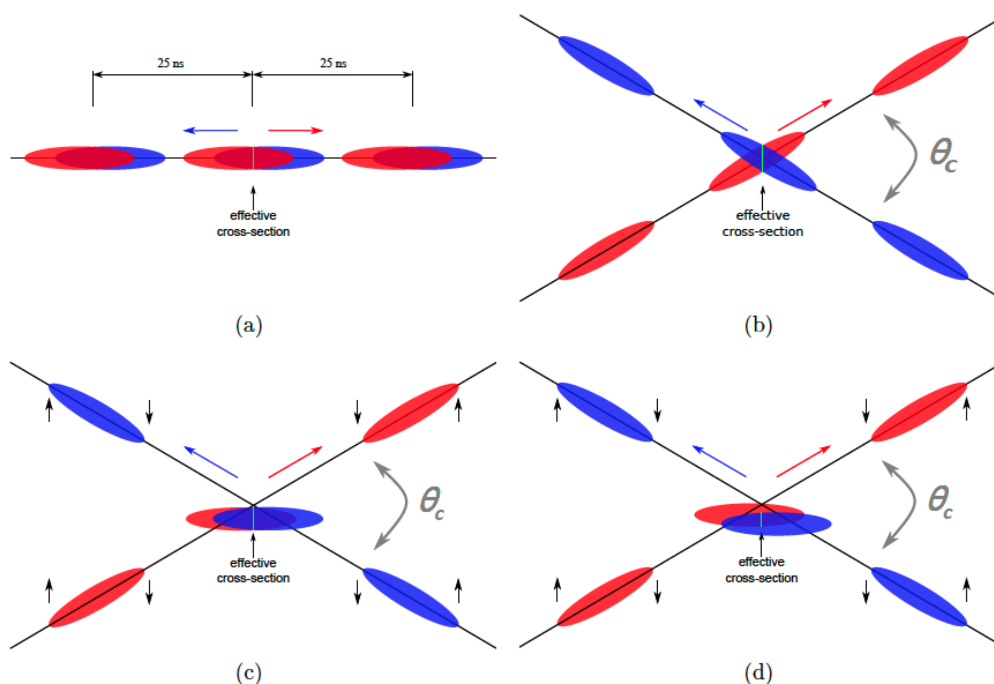

Figure 2.6: Illustrations of bunch collision schemes at the interaction point. (a) Head on collision case, (b) collision with a small crossing angle θ_c. The HL-LHC scenarios using crab cavities are illustrated in (c) without and (d) with luminosity levelling. Image taken from [35].

The luminosity increase for ATLAS (and CMS) will be realised through upgrades to injector systems, final focusing and crab cavities. The crab cavities are placed either side of an interaction point and provide rotation to the charged particle bunch, using a time varying magnetic field. Figure 2.6(a) illustrates a conventional head-on collision. This method of bunch collision makes it harder to retain the lifetime of the fill. The LHC's present bunch colliding method is illustrated in Figure 2.6(b). Here the beams are collided with a small crossing angle Θ_c. The effect of colliding bunches with crab cavities is illustrated in Figure 2.6(c), each bunch is rotated with respect to each other so that more of each bunch is "collided", while allowing greater control over the dimensions of the interaction region. All of these improvements culminate in an expected effective luminosity at HL-LHC of $2 \cdot 10^{35}\, cm^{-2}\, s^{-1}$. Such an increased luminosity would lead to an unacceptable event pile-up in the HL-LHC experiments and to much shorter average fill durations due to higher collision rates.

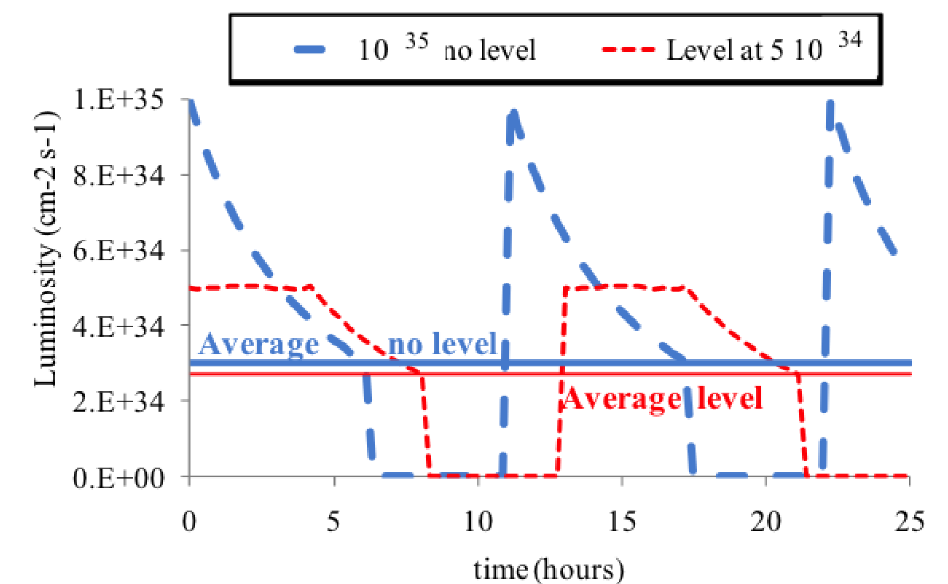

Figure 2.7: Peak (dashed line) and average delivered (solid line) luminosity profiles with time, with (red) and without (blue) luminosity levelling [36].

To limit the effects of high event pile-up and to maximise the total usable luminosity, luminosity levelling will be employed. This method decreases the effective luminosity and therefore the event pile-up and allows large amounts of (usable) integrated luminosity to be recorded. This is because each LHC fill lasts longer, decreasing the fraction of the time spent filling the LHC and therefore the average down-time of the experiments between data taking [37, 39]. Figure 2.7 shows the peak luminosity as a function of time in hours for levelled (red) and unlevelled (blue) beams. Dashed lines represent the instantaneous peak luminosity whereas the solid lines indicate the average peak luminosity. The peak luminosity of an un-levelled beam quickly falls with time during each fill, an effect much less dramatic with luminosity levelling. Furthermore, the use of luminosity levelling has very little effect on the average recorded luminosity.

The method in which beam luminosity is levelled has not yet been decided. However, a nominal value of $5 \cdot 10^{34}\, cm^{-2}\, s^{-1}$ is envisaged at the HL-LHC. This will decrease the number of interactions per bunch crossing, within the ATLAS detector, to about 140 on average with respect to $\sim$ 200 expected at peak luminosity, making detector operations less critical. The two main methods for luminosity levelling are: (1) crab kissing, where the crab cavities actually shift each bunch slightly to decrease the effective luminosity by decreasing the effective bunch cross-section, illustrated in Figure 2.6(d); (2) beam-beam wire compensations, either using conventional current carrying wires or electron lens

[43, 44]. Both methods will not be discussed in any detail, but the aim of either method is to vary β^* in Equation (2.1) [17, 104] to maximise the usable integrated luminosity [45].

Chapter 3

Physics Motivation

This chapter will give a short overview of the Standard Model of particle physics and some of its possible extensions. Accurately testing the Standard Model is one of the goals of the Large Hadron Collider (LHC) and ATLAS experiment. ATLAS and CMS separately discovered the Higgs boson. The discovery was announced at CERN on 4th July 2012 [46]. One aim for the future of the LHC complex is to act as a "Higgs factory" [37], creating large numbers of Higgs bosons in order to precisely measure their characteristics. For this reason a brief introduction into the Higgs mechanism and the physics goals of ATLAS at HL-LHC will be presented.

3.1 The Standard Model of Particle Physics

The Standard Model of particle physics is a theory in which the fundamental constituents of matter and the interactions between them at sub-atomic distance scales are described [47]. It is a theory that includes three of the four fundamental forces observed in nature: electro-magnetism, the weak force and the strong force, all mediated via spin-1 bosons. However it does not describe gravity, which is the weakest of all forces and at LHC energies is $\sim 10^{39}$ times weaker than the next weakest force [48]. As such its effects at the sub-atomic level are irrelevant to current colliders. The Standard Model contains twelve elementary spin-1/2 fermionic matter particles, and their anti-particles. These twelve particles can be divided into two groups of six particles, leptons and quarks, where only the latter experience the strong interactions [2–4, 6].

These fermions can be arranged into three generations. Matter around us is made of elementary particles of the first generation, electrons and up and down quarks, where

Three Generations of Matter (Fermions)

		I	II	III	Bosons (Forces)
Quarks	mass→ charge→ spin→ name→	2.4 MeV, ⅔, ½, u, up	1.27 GeV, ⅔, ½, c, charm	171.2 GeV, ⅔, ½, t, top	0, 0, 1, γ, photon
Quarks		4.8 MeV, -⅓, ½, d, down	104 MeV, -⅓, ½, s, strange	4.2 GeV, -⅓, ½, b, bottom	0, 0, 1, g, gluon
Leptons		<2.2 eV, 0, ½, ν_e, electron neutrino	<0.17 MeV, 0, ½, ν_μ, muon neutrino	<15.5 MeV, 0, ½, ν_τ, tau neutrino	91.2 GeV, 0, 1, Z^0, weak force
Leptons		0.511 MeV, -1, ½, e, electron	105.7 MeV, -1, ½, μ, muon	1.777 GeV, -1, ½, τ, tau	80.4 GeV, ±1, 1, $W^\pm$, weak force

Figure 3.1: Overview of the Standard Model particles [49].

the latter are constituents of protons and neutrons. The charged particles in higher generations are much heavier than particles in the first generation, making them and anything composed of them unstable. Figure 3.1 shows the twelve elementary matter particles along with the four force mediating bosons. For every Standard Model fermion there is also a corresponding anti-particle. These anti-particles have the same mass as their fermion counter-parts but with opposite quantum numbers such as electric charge [1]. Quarks and anti-quarks carry colour charge with three states, red, green and blue [50].

Fermions and their anti-matter equivalents interact via the three elementary forces. The electromagnetic force is mediated via the photon and it couples through electric charge. The photon is massless and charge-less, making the electromagnetic force a long range force. The weak force is mediated via the W and Z gauge bosons. These gauge bosons are massive, resulting in a very short range over which this force can act. All matter particles interact via the weak force [51]. The final elementary force is the strong force, so named because it is the strongest of all the forces discussed here. It only couples to particles that carry a colour charge, quarks and gluons. The strong force is mediated via gluons, which are massless and come in 8 different varieties. However, the range over

which the strong force interacts is very short because although massless, the gluons carry colour charge and interact with themselves, limiting the range of the force. Particles that interact via the strong force are not observed as free particles as the interaction is so strong that only bound colour singlet (colourless) states exist in nature. These colour singlet states can either be: baryons which are fermions since they have half integer spins, composed of 3 quarks with differing colour charge i.e. red, green, blue; and mesons, which are bosons since they have a total integer spin and consist of quark anti-quark pairs [1, 5].

3.2 Issues with the Electroweak Model - Why We Need the Higgs Mechanism

The electroweak model has some serious shortcomings. Local $SU(2)_L \times U(1)_Y$ gauge invariance forbids massive fermions and massive gauge bosons to exist, however the three generations of elementary matter particles (fermions) and the $W^{+/-}$ and Z^0 force carrying particles (bosons) are known to have masses [5]. Additionally, in these models several Standard Model cross-sections such as WW-scattering would violate unitarity at high energies as $\sigma(WW \longrightarrow ZZ) \propto E^2$ [52]. Example Feynman diagrams of this process are shown in Figure 3.2.

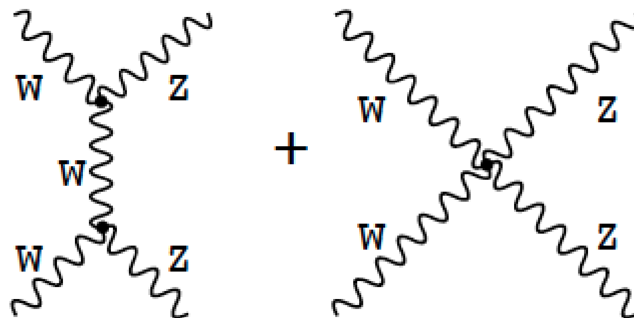

Figure 3.2: Feynman diagrams illustrating WW-scattering $\sigma(WW \longrightarrow ZZ)$ [52]

For the theory to be renormalizable, local gauge symmetry must be respected. To do this while allowing masses to enter the theories a new field is introduced that keeps the full Lagrangian invariant under $SU(2)_L \times U(1)_Y$, but has a ground state where the

vacuum is not invariant under this symmetry. This is referred to as spontaneous symmetry breaking of a local gauge invariant theory or the Higgs mechanism. The inclusion of the Higgs field solves all issues with non-zero gauge boson masses and prevents the violation of unitarity described above [52]. It also introduces a self-interacting massive scalar gauge particle, the Higgs boson discussed in the following section.

3.3 Higgs Mechanism

The Higgs mechanism can be illustrated considering an Abelian Yang-Mills theory [53, 54]. In this case, the Higgs mechanism can be realised by taking a Yang-Mills Lagrangian

$$\mathcal{L}_A = -\frac{1}{4}F^{\mu\nu}F_{\mu\nu} \text{ with } F^{\mu\nu} = (\partial^\mu A^\nu - \partial^\nu A^\mu) \ , \tag{3.1}$$

and adding a term for a complex scalar field.

$$\mathcal{L}_\phi = (D^\mu\phi)^* D_\mu\phi - V(\phi) = (D^\mu\phi)^* D_\mu\phi - \mu^2\phi^*\phi - \lambda(\phi^*\phi)^2 \ , \tag{3.2}$$

where $D^\mu = \partial^\mu + igA^\mu$, and $\lambda > 0$ for the scalar potential to be bounded from below. The full Lagrangian:

$$\mathcal{L} = \mathcal{L}_A + \mathcal{L}_\phi \ , \tag{3.3}$$

is invariant under a $U(1)$ gauge transformation acting on fields as:

$$\phi(x) \to e^{i\alpha(x)}\phi(x) \ , \qquad A^\mu(x) \to A^\mu(x) + \frac{1}{g}\,\partial^\mu\alpha(x) \ . \tag{3.4}$$

A gauge field mass term (i.e. a quadratic term in A^μ) would not be gauge invariant and cannot be added to the Lagrangian $\mathcal{L}$ if the $U(1)$ gauge symmetry has to be preserved.

However, the Lagrangian in Equation (3.3) can still describe a massive gauge boson, provided the potential $V(\phi)$ develops a non-trivial minimum at $\phi^*\phi \neq 0$. This leads to a degeneracy of the minima depending on the sign of the parameter μ^2, in $V(\phi)$. For $\mu^2 > 0$ there is a unique minimum at $\phi^*\phi = 0$, but for $\mu^2 < 0$, the potential develops a degeneracy at the minimum satisfying the equation $\phi^*\phi = -\frac{\mu^2}{2\lambda}$. This is illustrated in Figure 3.3, where the potential $V(\phi)$ is plotted as a function of its real and imaginary parts $\phi = \phi_1 + i\phi_2$. For the case resulting in a unique minimum at $\phi^*\phi = 0$, the Lagrangian in Equation (3.3) describes a massless vector boson, e.g. the photon, in electrodynamics. However, the case with a degenerate minimum ($\mu^2 < 0$) behaves very differently. Choosing the ground state to be a suitable value of ϕ, and expanding the potential in the viscinity of the chosen minimum transforms the Lagrangian in such a way that the original gauge symmetry is spontaneously broken.

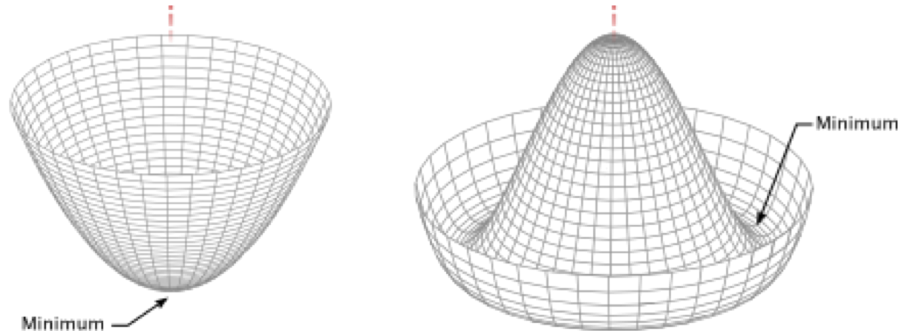

Figure 3.3: The potential $V(\phi)$ plotted with an arbitrary value of λ, and arbitrary positive (left) and negative (right) value of μ^2 [55].

Spontaneously breaking the original gauge symmetry reveals some interesting effects. To show this, an arbitrary minimum has been chosen, ϕ_0 and the ϕ field is shifted accordingly.

$$\phi_0 = \left(\frac{-\mu^2}{2\lambda}\right)^{1/2} \equiv \frac{\nu}{\sqrt{2}} \quad \rightarrow \quad \phi(x) = \phi_0 + \frac{1}{\sqrt{2}}(\phi_1(x) + i\phi_2(x)) \ . \tag{3.5}$$

Then Equation (3.3) can be rearranged such that:

$$\mathcal{L} = \underbrace{-\frac{1}{4}F^{\mu\nu}F_{\mu\nu} + \frac{1}{2}g^2\nu^2 A^\mu A_\mu +}_{\text{massive vector field}} \underbrace{\frac{1}{2}(\partial^\mu \phi_1)^2 + \mu^2\phi^2}_{\text{massive scalar field}} \underbrace{+\frac{1}{2}(\partial^\mu \phi_2)^2 + g\nu A_\mu \partial^\mu \phi_2 +}_{\text{Goldstone boson}} ... \tag{3.6}$$

The modified Lagrangian now contains a massive vector field A_μ with mass of $M_A^2 = g^2\nu^2$, originating from the kinetic term in $\mathcal{L}_\phi$. A massive real scalar field, ϕ_1 with a mass, $M_{\phi_1} = -2\mu^2$ that becomes the Higgs boson and a massless scalar field ϕ_2, a so-called Goldstone boson, which couples to the gauge vector boson A_μ. However, since the Lagrangian considered here is gauge-invariant (enforcing $U(1)$), the phase factor $e^{\frac{i\chi(x)}{\nu}}$ in Equation (3.7) can be removed using an appropriate gauge transformation $\phi \rightarrow \phi' = e^{\frac{-i\chi(x)}{\nu}}\phi$, such that

$$\phi(x) = \frac{e^{\frac{i\chi(x)}{\nu}}}{\sqrt{2}}(\nu + H(x)) \quad \stackrel{U(1)}{\rightarrow} \quad \frac{1}{\sqrt{2}}(\nu + H(x)) \ , \tag{3.7}$$

where the χ degree of freedom is the field excitation giving rise to massless Goldstone bosons. Using this choice of gauge, referred to as unitarity gauge the Lagrangian becomes:

$$\mathcal{L} = \mathcal{L}_A + \frac{g^2\nu^2}{2}A^\mu A_\mu + \frac{1}{2}(\partial^\mu H \partial_\mu + 2\mu^2 H^2) + ... \ , \tag{3.8}$$

which unambiguously describes the dynamics of a massive vector boson A_μ of mass $M_A^2 = g^2\nu^2$, and a massive scalar field $M_H^2 = -2\mu^2 = 2\lambda\nu^2$, the Higgs field. The number of degrees of freedom before and after the $U(1)$ symmetry is spontaneously broken is the same. The theory goes from having one massless vector field with 2 degrees of freedom and one complex scalar field with 2 degrees of freedom, to a theory with one massive vector field with 3 degrees of freedom and one real scalar field with 1 degree of freedom. This can be generalised to the case with $SU(2)_L$ to 3 massive vector bosons, and a real scalar field, the Higgs field. Finally, the Higgs field can be chosen such that in terms of the vacuum expectation value ν, $M_W = \frac{1}{2}\nu g$, $M_Z = \frac{1}{2}\nu\sqrt{g^2 + g'^2}$ and $M_\gamma = 0$ where g and $g^{'}$ are the $SU(2)_L$ and $U(1)_Y$ coupling strengths respectively. This allows ν to be numerically calculated using the measured masses of the W and Z bosons [54–56].

3.4 Physics Beyond the Standard Model

Despite the success of the SM, there are questions that it fails to answer. There are experimental observations in cosmology that are not explained by the SM and theoretical problems that imply a lack of completeness [57, 58]. Some of these problems are illustrated through the following theories of physics beyond the SM (BSM), which attempt to answer some of the open questions by introducing new concepts [59].

One of the biggest issues in the SM is the inability to include gravity, since General Relativity and Quantum Mechanics are difficult to include in a common framework. In todays particle physics experiments, the energy range is such that gravitational effects are far too weak to be relevant. However there is an energy scale at which both Quantum Mechanics and Relativity have to be reconciled, the Planck scale, $\approx 10^{19}\,GeV$. At least at this energy scale a new theory is needed. Quantum Gravity attempts to develop models that unite Quantum Mechanics with General Relativity to describe quantum phenomena at ultra-high energies. Furthermore, the coupling constants of the electromagnetic, the weak and the strong force are dependent on the energy scale. At very high energy scales they all approach each other. Grand Unified Theories (GUTs) aim to combine the three fundamental forces such that these merge at high energies into a single interaction characterised by a single larger gauge symmetry, with unifying coupling constants. A theory that could further link gravity with GUTs would then be the famed “Theory of Everything”.

Astrophysical measurements such as the speed of rotation of galaxies as a function of radius, the motion of galaxies in clusters and the cosmic microwave background temperature fluctuations [60] show that SM matter contributes only about 5% of the mass of the universe. The rest is unknown dark matter and dark energy. Besides the dark matter and dark energy problem, the universe does not contain any visible primordial anti-matter. Since matter and anti-matter would be formed in equal amounts during the Big Bang, the obvious lack of anti-matter in our universe requires explanation. It can be concluded that the laws of nature favour matter over anti-matter. A possible mechanism for this might be CP-violation but predicted and observed rates in the Standard Model are far too small. Therefore, additional sources of CP-violation are needed from Beyond Standard Model physics.

Another fundamental problem is the size of weak force compared to gravity, the weak force is 10^{32} stronger than gravity. In particular, why the Higgs has such a low mass.

The Higgs mass gets some very large quantum corrections (10^{16}) due to the presence of virtual particles contributing through loop diagrams. These corrections are much larger than the mass of the Higgs. This means a very large cancellation is required to explain the smallness of the Higgs mass which is deemed unnatural, implying the need for new physics near the electroweak scale. New symmetries and new particles, such as in supersymmetry: whose supermassive particles would couple very strongly to the Higgs could help explain the Higgs large quantum corrections. Alternatively, theories with extra dimensions could allow the Planck scale to be close to the electroweak scale, with the weakness of gravity only being apparent on distance scales larger than those of the extra compactified dimensions.

There are many more problems like the large number of free parameters or the large mass range in the Standard Model. The Standard Model depends on 28 free parameters [61], which have to be measured experimentally, with no explanation of their origin. Consequently the Standard Model is thought to depend on some deeper principles which have yet to be discovered. The LHC was built partly to seek answers to such questions. It was designed in such a way that it has a large discovery potential and can confirm or set limits on many different theories. The unprecedented energy it achieves may even reveal something completely unexpected.

3.5 HL-LHC Physics

This section will give a brief introduction to the physics programme expected at the HL-LHC, based on the corresponding ECFA report [37]. The upgrade from the LHC to the HL-LHC is described in Chapter 2, and necessary upgrades to ATLAS to enable efficient operation at HL-LHC are described in Chapter 4. Although many aspects of the Standard Model and Beyond the Standard Model physics will be probed, such as precision tests and studies of rare processes, the central focus to define the upgrades will be to perform accurate measurements of the properties of the 125 GeV Higgs boson discovered in 2012 [10] (and any other discovery found before the HL-LHC upgrade). The HL-LHC will be used as a “Higgs factory” [38] enabling the comparison of much higher precision measurements to Standard Model predictions [37]. The HL-LHC will also directly probe the Higgs potential through the possible measurement of the triple Higgs coupling, which could be observable as an interference effect in Higgs boson pair production. The studies in the following subsections assume a SM Higgs boson, and

HL-LHC luminosities outlined in the ATLAS Phase-II LoI and discussed in Section 2.3.3 [18].

3.5.1 Higgs Boson Couplings

While Higgs boson coupling measurements are already underway at the LHC, the luminosity increase of the HL-LHC will enable much greater statistical precision of these coupling measurements, compared to what is possible with the LHC. Higgs production rates will increase at the HL-LHC allowing some rare Higgs production and decay modes to be studied for the first time. For an estimate on the precision with which the SM Higgs boson couplings can be measured, decays already being investigated with 7 and $8\,TeV$ analysis are considered:

- $H \rightarrow \gamma\gamma$ in the 0-jet and 2-jet final state, the latter with vector-boson fusion (VBF) selection. The analysis is carried out analogously to [10].
- Inclusive $H \rightarrow ZZ^* \rightarrow 4l$ following a selection close to [10].
- $H \rightarrow WW^* \rightarrow l\nu l\nu$ in the 0-jet and 2-jet final state, the latter with VBF-selection. The analysis is carried out analogously to [10].
- $H \rightarrow \tau^+\tau^-$ in the 2-jet final state with VBF selection as in [62].

In addition to these channels, a number of other channels are considered which are only accessible with very high luminosities [18]:

- $WH/ZH \text{with} H \rightarrow \gamma\gamma$ and $t\bar{t}H \text{with} H \rightarrow \gamma\gamma$: these channels have low signal rates at the LHC, significantly more signal events are expected the with HL-LHC. The selection of the diphoton system is done in the same way as for the inclusive $H \rightarrow \gamma\gamma$. The $t\bar{t}H$ initial state yields the cleanest signal with a signal to background ratio of 20%, compared with 10% for ZH and 2% for WH.

  The $t\bar{t}H$ initial state is of special interest, as it yields a precise measurement of the square of the top-Yukawa coupling, which is otherwise not directly accessible. Figure 3.4 (left) shows the expected signal in the $t\bar{t}H$ 1-lepton final state and Figure 3.5 shows the expected measurement precision.

- $H \rightarrow \mu\mu$ also has a low signal rate at the LHC, with a signal to background ratio of only 0.2%. However, the expected narrow peak allows a signal extraction at very

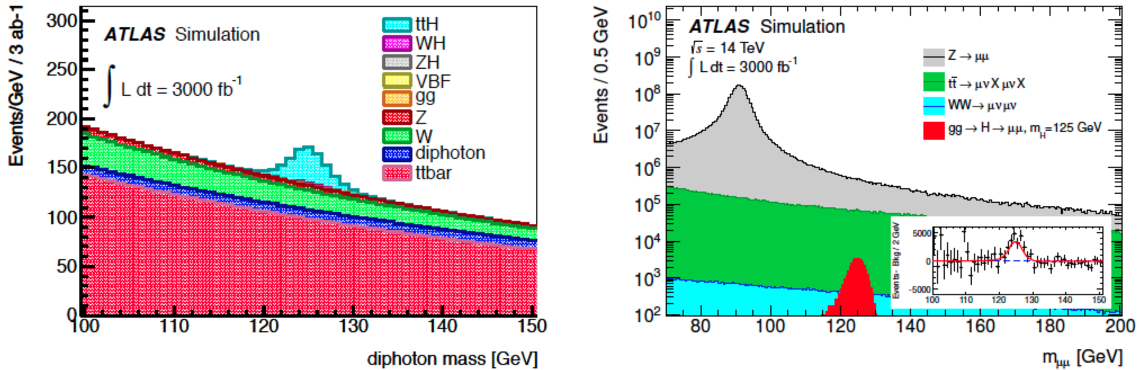

Figure 3.4: (left) Expected $\gamma\gamma$ invariant mass distributions for the $t\bar{t}H$,$H \to \gamma\gamma$ channel in the 1-lepton selection for an assumed integrated luminosity of 3000 fb^{-1} at $\sqrt{s} = 14\,TeV$. (right) Expected invariant mass distribution for the inclusive $H \to \mu\mu$, for an assumed integrated luminosity of 3000 fb^{-1} at $\sqrt{s} = 14\,TeV$. The inset show the expectation for the $H \to \mu\mu$ signal after the subtraction of the fitted background [18].

high luminosities, resulting in an expected signal with significance above 6σ with 3000 fb^{-1} at $\sqrt{s} = 14\,TeV$ in the inclusive channel. Figure 3.4 (right) shows the expected signal compared to the large continuous background, Figure 3.5 shows the expected precision.

Also the exclusive $t\bar{t}H$with$H \to \mu\mu$ channel was studied. While the expected signal rate is only about 30 events at 3000 fb^{-1}, a signal to background ratio of better than unity can be achieved and hence this channel gives information on both the top- and μ-Yukawa coupling with a precision on the total signal strength of about 25 %.

An overview of the expected measurement precision in each channel for the signal strength μ with respect to the SM Higgs boson expectation for a mass of 125 GeV is given in Figure 3.5 for assumed integrated luminosities of 300 fb^{-1} (LHC) and 3000 fb^{-1} (HL-LHC).

The $\gamma\gamma$ and ZZ^* final states profit most from the increase in luminosity, as both statistical and systematic uncertainties are significantly reduced, providing the best precision on signal strength [18]. The $\gamma\gamma$ is especially important, as this final state can be used as a clean probe of different production modes and their associated couplings [37].

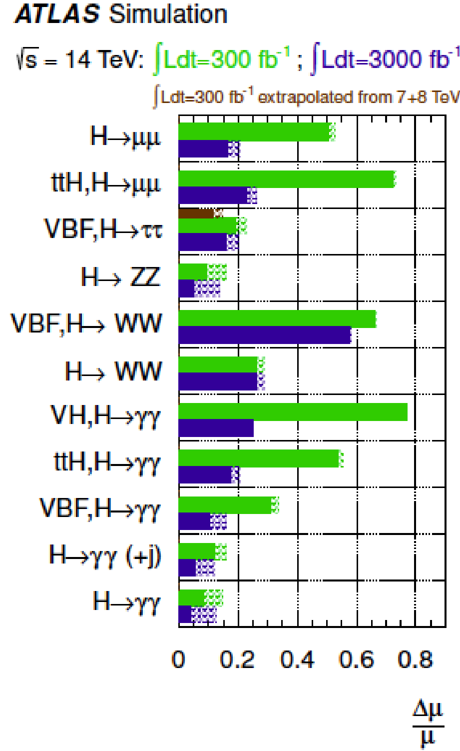

Figure 3.5: Illustration of the expected measurement precision on the signal strength, $\mu = (\sigma \times BR)/(\sigma \times BR)_{SM}$ in all considered channels. The bars give the expected relative uncertainty for a Standard Model Higgs boson with a mass of 125 GeV (the dashed areas include current theory uncertainties from QCD scale and PDF variations [63]) for luminosities of 300 fb^{-1} and 3000 fb^{-1}. For the $\tau\tau$ final state the thin brown bars show the expected precision reached from extrapolating all $\tau\tau$ channels studied in the current 7 and 8 TeV analysis to 300 fb^{-1}, instead of using the dedicated studies at 300 fb^{-1} and 3000 fb^{-1} that are based only on the VBF $H \rightarrow \tau\tau$ channels [18].

3.5.2 Weak Vector Boson Scattering

A major reason to expect new physics at the TeV energy scale is due to the prediction of an untamed rise of the longitudinal weak boson scattering cross-section which would violate unitarity at this scale. In the SM, the Higgs boson is responsible for providing additional diagrams which cancel this divergence. However, other mechanisms that enhance high energy WBS are possible, even after the SM Higgs mechanism is established. Therefore the measurement of the energy dependence of the vector boson scattering cross-section remains a very important measurement [18, 37].

WBS can be parameterised by an effective Electroweak Chiral Lagrangian (EWChL), which includes two new operators that conserve the custodial SU(2) symmetry [40]. These new operators, which induce anomalous quartic couplings that are not strongly constrained by precision electroweak measurements, are scaled by numerical coefficients a4 and a5. The experimental sensitivity to weak boson scattering has been calculated using two separate approaches to unitarising the scattering amplitudes from the EWChL.

The sensitivity to new high mass resonances was was calculated based on a scheme that merges high-mass resonances with the low energy behaviour of the EWChL using a minimal K-matrix unitarisation method [41]. The WHIZARD [42] generator was used to generate weak boson scattering mediated by a new high mass resonance in addition to a 126 GeV Higgs boson [18].

To give an example, the fully leptonic channel, $ZZjj \rightarrow llll jj$ has a small cross-section but can provide a clean, fully-reconstructable ZZ resonance peak. A leading jet-jet mass requirement of 1 TeV reduces the contribution from jets accompanying non-WBS diboson production. Figure 3.6 shows the jet-jet invariant mass distribution and the reconstructed 4-lepton invariant mass distribution. The high-mass (1 TeV) resonance is easily visible in this simulated dataset normalised to 3000 fb^{-1} [45].

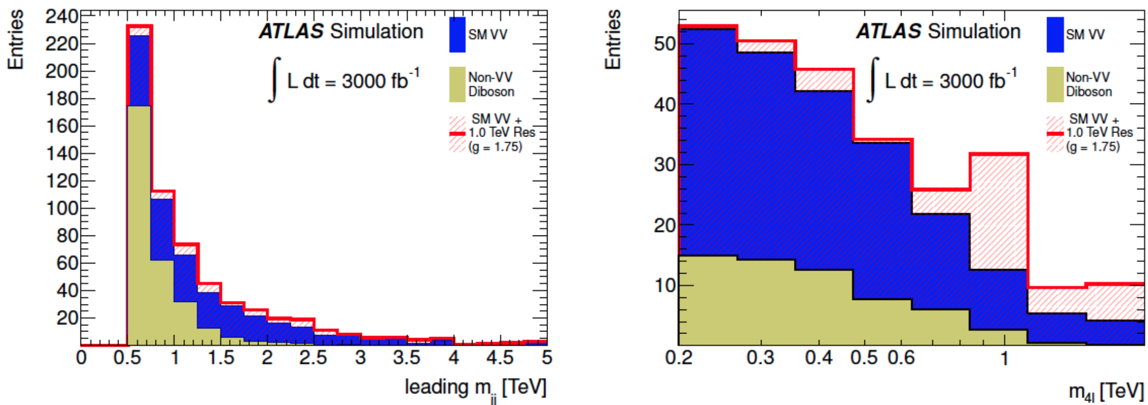

Figure 3.6: The leading jet-jet invariant mass (m_{jj}) distribution for selected simulated events in the $pp \rightarrow ZZ + 2j \rightarrow llll + 2j$ channel (left), and the reconstructed 4-lepton mass (m_{4l}) spectrum for this channel after requiring $m_{jj} > 1\,TeV$ (right). The WBS events are generated using WHIZARD [42] without and with a ZZ resonance mass of 1 TeV, in addition to a Standard Model 126 GeV Higgs boson. The non-WBS diboson background is generated using MADGRAPH [45, 64]

3.5.3 Direct and indirect searches for BSM Higgs bosons

Extended Higgs sectors are predicted by many Beyond the Standard Model theories, including supersymmetric extensions of the Standard Model and various composite models. These theories can be tested through the coupling measurements of the observed Higgs boson and direct searches for new particles. The two Higgs doublet model (2HDM) provides an effective description of some such extensions. They provide relations between the coupling of the observed Higgs boson and the event yields and properties of additional new scalars. 2HDMs contain five physical Higgs bosons, two CP-even scalars h and H, a CP-odd pseudo-scalar, and a pair of charged Higgs bosons $H^{\pm}$. The parameter space regions are shown in Figure 3.7(left) for 500 GeV H and Figure 3.7(right) for 500 GeV A, where A refers to a new particle.

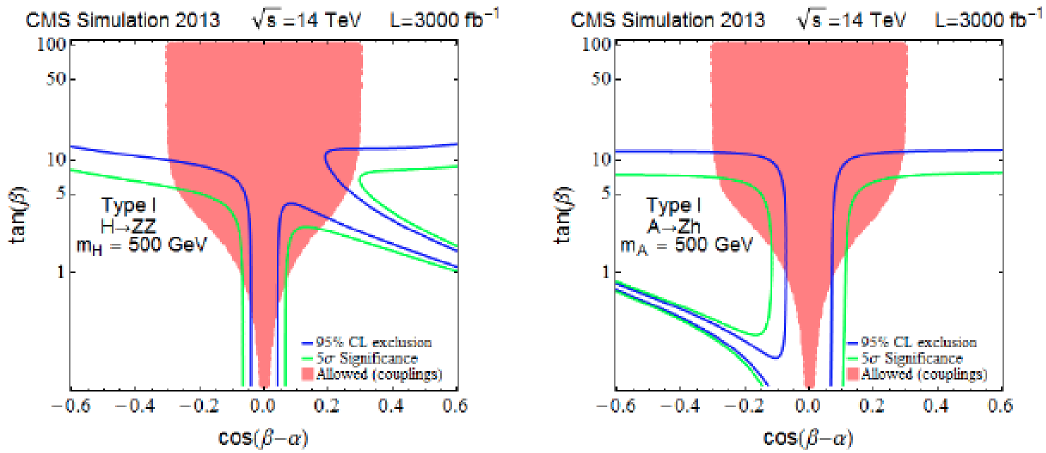

Figure 3.7: The enclosed region of parameter space for which 500 GeV H (left) and A (right) bosons could be excluded at 95 % CL (blue), and the region of parameter space which could yield a 5 σ observation (green), in the context of Type I 2HDMs. The red coloured regions correspond to the expected 95 % CL allowed region from Higgs precision measurements with 3000 fb^{-1}.

3.5.4 Search for BSM Physics Signatures

Supersymmetry

Supersymmetry (SUSY) is a hypothetical symmetry of nature which relates fermions and bosons. SUSY particles with masses at the electroweak scale could represent new degrees of freedom that cancel quadratic divergences in the Higgs sector. Figure 3.8 shows the

cross-sections for the pair production of SUSY particles depending on their masses under a set of model parameters choices defined in [65, 66]. While production cross-sections for strongly produced supersymmetric particles are relatively large; cross-sections for electroweak supersymmetric particles, such as the neutralinos and charginos are several orders of magnitude smaller and will benefit from the large integrated luminosity possible at the HL-LHC [37].

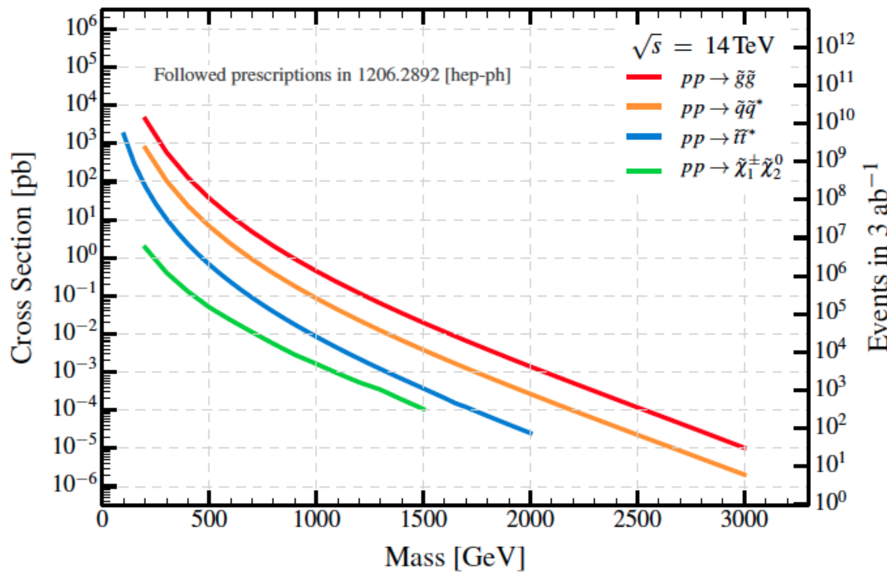

Figure 3.8: Next-to-leading order cross-sections for the production of supersymmetric particles at the LHC as a function of the average mass of the pair-produced supersymmetric particles. The $\widetilde{\chi}_1^{\pm}$ and $\widetilde{\chi}_2^0$ are assumed to be wino-like [37].

Non-Supersymmetric Extensions of the Standard Model

There are also non-supersymmetric solutions that could cancel the quadratic divergences. The search for evidence of these will continue with the HL-LHC. The sensitivity for discovering a heavy vector-like quark is used as a benchmark (see below). In addition to the question of naturalness (where by model parameters should not vary by many orders of magnitude), the HL-LHC will also provide an opportunity to further study the electroweak symmetry breaking mechanism of the Standard Model, e.g. verifying that vector boson scattering cross-sections are damped by the Higgs boson as expected. However, if discrepancies are found in runs 2 or 3 of the LHC, then this could point to other theoretical models such as Technicolor or Compositeness, for example. This

would make the HL-LHC essential to explore any new physics with greater precision than possible with the LHC [18].

Search for Heavy vector-like quarks

Vector-like quarks differ from Standard Model Quarks in their electroweak couplings. While Standard Model quarks have V-A (Vector - Axial) coupling to the W leading to different couplings of the left- and right-handed chiral states to the W, vector quarks would have only a vector-coupling to the W. The vector like mass term avoids violating gauge invariance without the need for a Yukawa coupling to the Higgs boson and is predicted in various theories such as little Higgs and Technicolour/Compositeness models. The existence of vector-like quarks could also provide a natural solution to cancel the diverging contributions of top quark loops to the Higgs boson mass. Studies for the future Search for vector-like quarks with 2/3 charge have been performed in single- and multi-lepton channels, which have been statistically combined for a common result [67]. With 3000 fb^{-1}, vector-quark masses up to 1.5 TeV can be probed [37]. Further information can be found in Ref [67]. Figure 3.9 (left) shows the Feynman diagram for vector boson scattering. The reconstructed mass spectrum for the charged leptons and photons in selected $Z\gamma\gamma$ events is shown in Figure 3.9 (right).

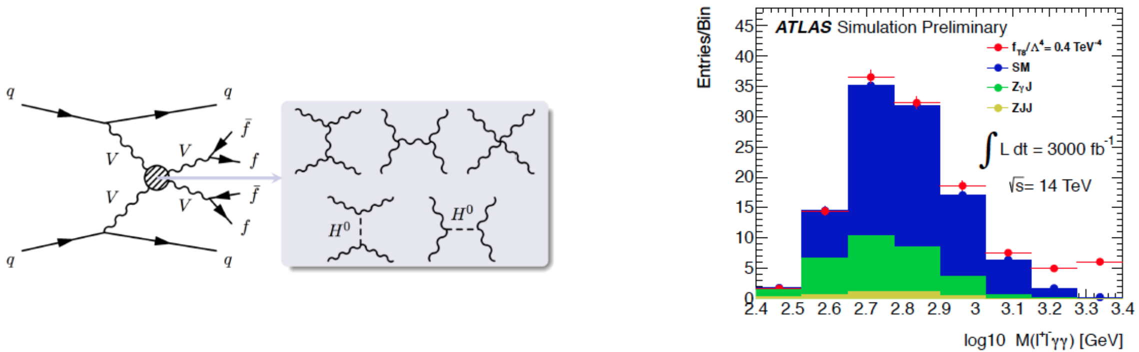

Figure 3.9: Left: The Feynman diagram for vector boson scattering. Right: The reconstructed mass spectrum for the charged leptons and photons in selected $Z\gamma\gamma$ events [37].

Chapter 4

The ATLAS Experiment

4.1 Overview

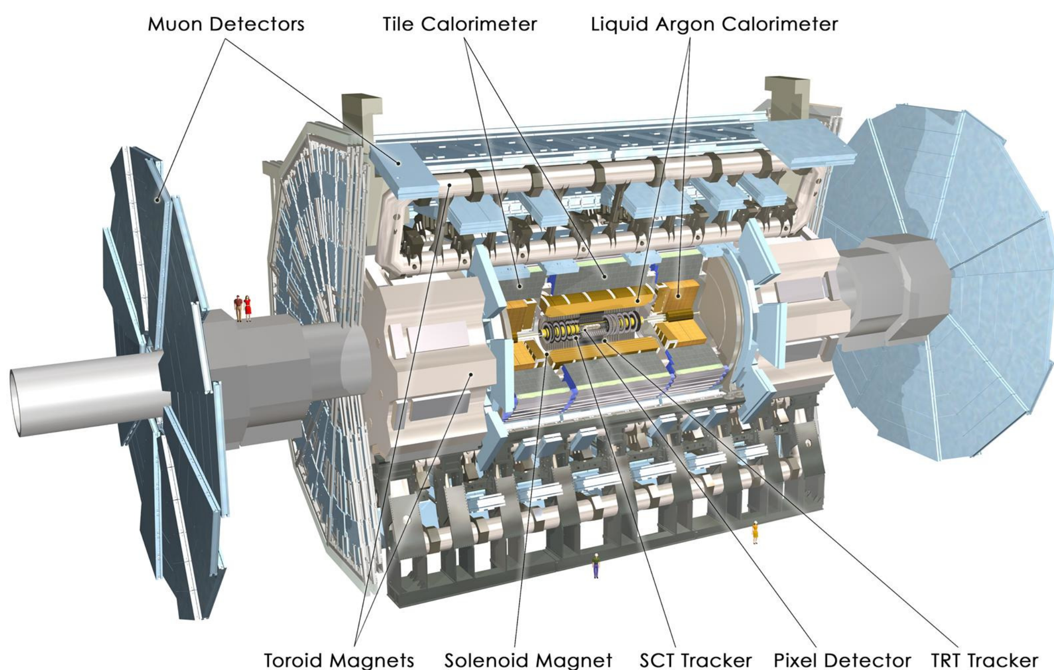

Figure 4.1: The ATLAS detector with sub-detectors

The ATLAS detector has a diameter of $25\,m$, a length of $46\,m$ and a weight of 7000 tons. The detector is a classical 4π detector. This means that nearly the whole solid angle is covered by the detector, with only a small angular range (close to where the beam pipe goes in and out of the apparatus) not instrumented. The detector is typical for a collider experiment, with each sub-detector specialised for a separate task.

ATLAS has a forward-backward symmetric cylindrical geometry and consists of a barrel part and end-caps on each side. For an explicit geometrical description of the detector, polar coordinates are used. The ATLAS coordinate system is right-handed and has its origin in the centre of the detector [13, 15]. The z-axis points in the direction of the beam pipe, the azimuthal angle ϕ is measured around the z-axis and the pseudo-rapidity η is defined as:

$$\eta = -ln\left[tan\left(\frac{\theta}{2}\right)\right] , \tag{4.1}$$

where θ is the polar angle between the particle direction and the z-axis.

Considering the collision rate of the proton bunches, about a billion collisions are produced per second. However, not all of the 40 million per second bunch crossings will contain "interesting" physics and it is not possible to store all of these events because of the data bandwidth and disk space required. ATLAS, and the other LHC experiments, uses a trigger system [71] to reduce the data rate by determining if the event has any interesting characteristics. Any event that does not meet the trigger requirements is discarded. More information of the Trigger system is given in Section 4.2.

The detector can be divided into several sub-systems (see Figure 4.1), in which different particles types leave different unique signatures. The innermost part of the detector is the tracking system. Here the paths of charged particles are measured with very high accuracy in a $2\,T$ solenoidal magnetic field. The tracking system consists of three sub-detectors. The innermost sub-detector is the pixel detector, the middle sub-detector is the silicon micro-strip detector array(SCT) and finally the outer sub-detector in the tracking system is the transition radiation tracker (TRT). These three sub-detectors together are known as the Inner Detector (ID). The measurement of the curvature in the magnetic field allows the transverse momentum of all charged particles to be determined.

This is followed by the calorimetry system, which is composed of the electromagnetic (ECAL) and the hadronic (HCAL) calorimeters. These systems are designed to absorb and measure the energy of electro-magnetically interacting and strongly interacting particles respectively. The ECAL works through photon pair production and bremsstrahlung working together to create particle showers, while nuclear interactions lead to hadronic showers in the HCAL. Both systems are designed to fully contain the particles and

their resulting showers. It is convenient to describe the calorimeter and the material it is comprised of in terms of radiation lengths X_0 (electromagnetic calorimeter) and interaction lengths λ (hadronic calorimeter). X_0 is the mean distance over which high energy electrons or photon beams lose their energy, leaving $1/e$ of their original energy and λ is the mean distance over which $1/e$ of incident hadrons have not interacted. In ATLAS, both systems are sampling calorimeters with absorber layers integrated with detection media. The ECAL uses lead as an absorber since it has both high density and a high atomic number while the HCAL uses a thick high mass absorber made of steel and copper. While hadronic showers can commence in the electromagnetic calorimeter, the energy loss mechanism is primary due to nuclear interactions which mainly take place in the much more massive hadronic calorimeter. More information on both systems design and composition are given in Section 4.4.

The outermost part of the ATLAS detector is the muon spectrometer. This consists of a large toroidal magnetic system and muon trackers. Muons are the only charged particles that can pass without interaction through the calorimeters. Since muons only weakly interact with matter this system is the largest detector system within ATLAS. The strong magnetic field from the toroidal magnet is used along with muon tracking information to measure their momentum. More information on this detector system is given in Section 4.3.

4.2 DAQ and Trigger

4.2.1 System Overview

The ATLAS trigger and data-acquisition (DAQ) system consists of three levels of online event selection [72], the level-1 (L1) and level-2 (L2) triggers followed by the Event Filter (EF). This three tier system is required to reduce the total data stored by the experiment without losing events that contain interesting physics [73]. Figure 4.2 illustrates the ATLAS trigger mechanism [74]. Each step refines the previous decision using larger fractions of the data and more advanced algorithms. The L1 system is a hardware based trigger that uses dedicated electronics on the detector systems. The L2 and EF systems are software based triggers.

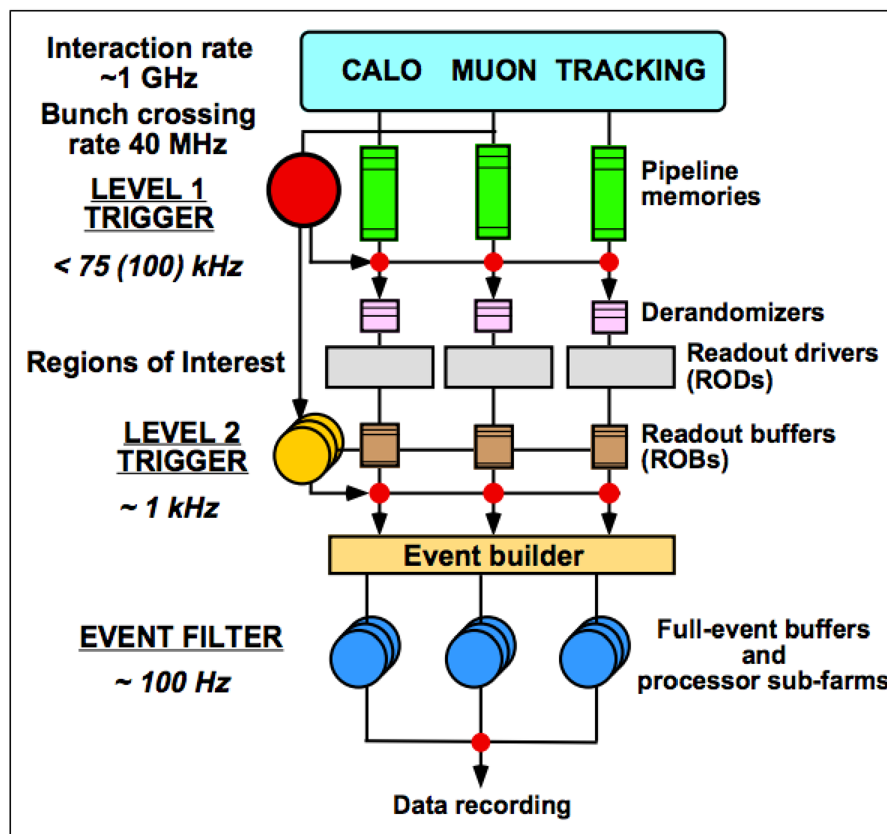

Figure 4.2: The three levels of the ATLAS trigger system, starting from the top, level-1 (L1), to the bottom, event filter (EF) [74].

Level-1 Trigger (L1)

The L1 trigger accepts data at the full LHC bunch crossing rate of 40 MHz and provides a decision for each bunch crossing. The latency (the time taken to collect, make a decision and distribute the data) of the L1 trigger is $\sim 2\,\mu$s. During this period, all the detector data is held within pipeline memories. The maximum output rate of the L1 trigger is typically set to $75\,kHz$, but it can be operated at $100\,kHz$ with an increased dead time [75]. Important signal characteristics the L1 trigger system looks for include high p_t muons, electrons, photons, jets and τ-leptons decaying into hadrons, as well as large missing transverse energies [73, 76].

Level-2 Trigger (L2)

The L2 trigger is a software based trigger which uses the output from L1 with the full event information available [73]. The L2 system looks at regions of interest (RoI's) defined by the L1 trigger to reduce the amount of data it has to process. The maximum data output rate for L2 is ~ 1 kHz. The latency of the trigger system is event dependent and can range from 1 - $10\,ms$, depending on track multiplicity.

Event Filter (EF)

The final selection is performed by the event filter (EF) via the event builder, which reduces the event rate down to about $200\,Hz$. At this stage the event is fully reconstructed, with a typical processing time per event of ~ 1 s. The decision to accept or reject an event is defined by a set of one or more signatures (for example E_T^{miss} and a lepton) with pre-set thresholds [76]. The data is then stored to be used in offline analysis at a typical rate of around a few hundred events per second [73, 75].

4.2.2 Upgrades

The DAQ and trigger systems will require consolidation and upgrades over time. However, the higher luminosity and pile-up will necessitate upgrades to the detector systems and therefore to the DAQ and trigger systems. The following sections will briefly outline the planned interventions (for more details refer to the references in each section).

Phase-0

There are several significant changes to the DAQ and trigger systems during LS1 but the main detector upgrade is the integration of the IBL (described in Section 4.5.5 into the existing pixel system. Some consolidation of degraded hardware across all detector systems is also necessary.

Phase-I

The Phase-I upgrade of the Trigger and Data Acquisition (TDAQ) system will allow ATLAS to efficiently trigger and record data at instantaneous luminosities up to $3 \cdot 10^{34}\text{cm}^{-2}\text{s}^{-1}$, which is about three times greater than the original LHC design luminosity. The increase in luminosity results in higher pile-up, which during 2012 peaked at around 40 and is expected to increase to 80 after LS1 (see Section 2.3.1). The bunch space reduction from $50\,ns$ to $25\,ns$ will help reduce the in-time pile-up but will increase out-of-time pile-up events [77] which the trigger systems (as well as the detectors systems) will have to resolve.

The TDAQ system will have to adapt to changes made to the detector sub-systems and their dedicated front-end electronics. One significant change is the improvement to the Liquid Argon (LAr) calorimeter electronics [78]. Here the most important change is the new L1 electromagnetic calorimeter feature extractor (eFEX) which will allow finer granulated data from the LAr to be used to improve selection of electrons, photons and tau's. There will also be the new jet extractor (jFEX) for improved triggering on hadronic processes. The muon inner stations in the forward direction will be replaced with the New Small Wheel (NSW, Section 4.3.2) [79] and the data from the NSW will need to be included in the L1 muon trigger. The inclusion of the NSW necessitates new L1 muon electronics. The upgraded L1 trigger electronics from the muon system will then be used by the new Muon-to-Central-Trigger-Processor Interface (MUCTPI). This

is used to create object quantities (e.g. η, ϕ and momentum) to better select interesting events from background. A new hardware based Fast TracKer (FTK) system [80] will be added to process the inner detector data. The FTK will be used to reconstruct tracks in the silicon tracking detectors quickly enough to enable their use at the start of the High-Level Trigger, HLT (L2 and EF) processing (see Section 4.5.5. The hardware changes outlined will require changes to the data flow software and improvements to HLT selection algorithms. Further details on the upgrade of the TDAQ system can be found in Ref [77–81].

Phase-II

A new trigger architecture is being developed to deal with the constraints imposed by the detector and to provide a more flexible trigger system. The main features are summarised [18] below:

- A split L0/L1 hardware trigger with a total L1 acceptance rate of 200 kHz and total latency of 20 μs.
- The L0 trigger would distribute the L0 accept at a rate of at least 500 kHz within a latency of 6 μs. The Phase-II L0 trigger is functionally the same as the Phase-I L1 system and consists of a feature extractor (FEX) based on electromagnetic calorimeter and jet triggers and the Phase-I L1 muon trigger. The L0 accept is generated by the central trigger system which incorporates a topological triggering capability.
- The L1 system will reduce the rate to 200 kHz within an additional latency of 14 μs. This reduction will be accomplished by the introduction of track information within a Region-of-Interest (RoI), full calorimeter granularity within the same RoI and the introduction of a refined muon selection based on the use of the MDT information.
- An increased use of offline-like algorithms in the High-Level Trigger (HLT) software trigger, with an anticipated output rate of up to 5 - 10 kHz.

4.3 Muon Spectrometer

4.3.1 System Overview

The muon system consists of components for triggering and tracking. Detectors for triggering need to be very fast and to have a good timing resolution and adequate momentum resolution. High precision tracking detectors are used to measure the bending of the muon track in the magnetic field. In addition, there are special requirements at positions close to the beam pipe. Due to the higher particle rate in high η regions, different detectors technologies are needed there. Thus, there are four different detector types in the muon spectrometer. For triggering in the central region ($|\eta| < 1.05$) Resistive Plate Chambers (RPC) are used, which are finely segmented gaseous parallel electrode-plates operating in avalanche mode. The Thin Gap Chambers (TGC) in the forward regions ($1.05 < |\eta| < 2.7$) are multi-wire proportional chambers. Both identify charged particles originating in the interaction region. Monitored Drift Tubes (MTD), are used in the barrel region and for most of the forward wheels ($|\eta| < 2.0$) for high resolution tracking. In the region $2.0 < |\eta| < 2.7$ there are also Cathode Strip Chambers (CSC), which are multi-wire proportional chambers with strip cathodes [82], The entire muon system is illustrated and labelled in Figure 4.3.

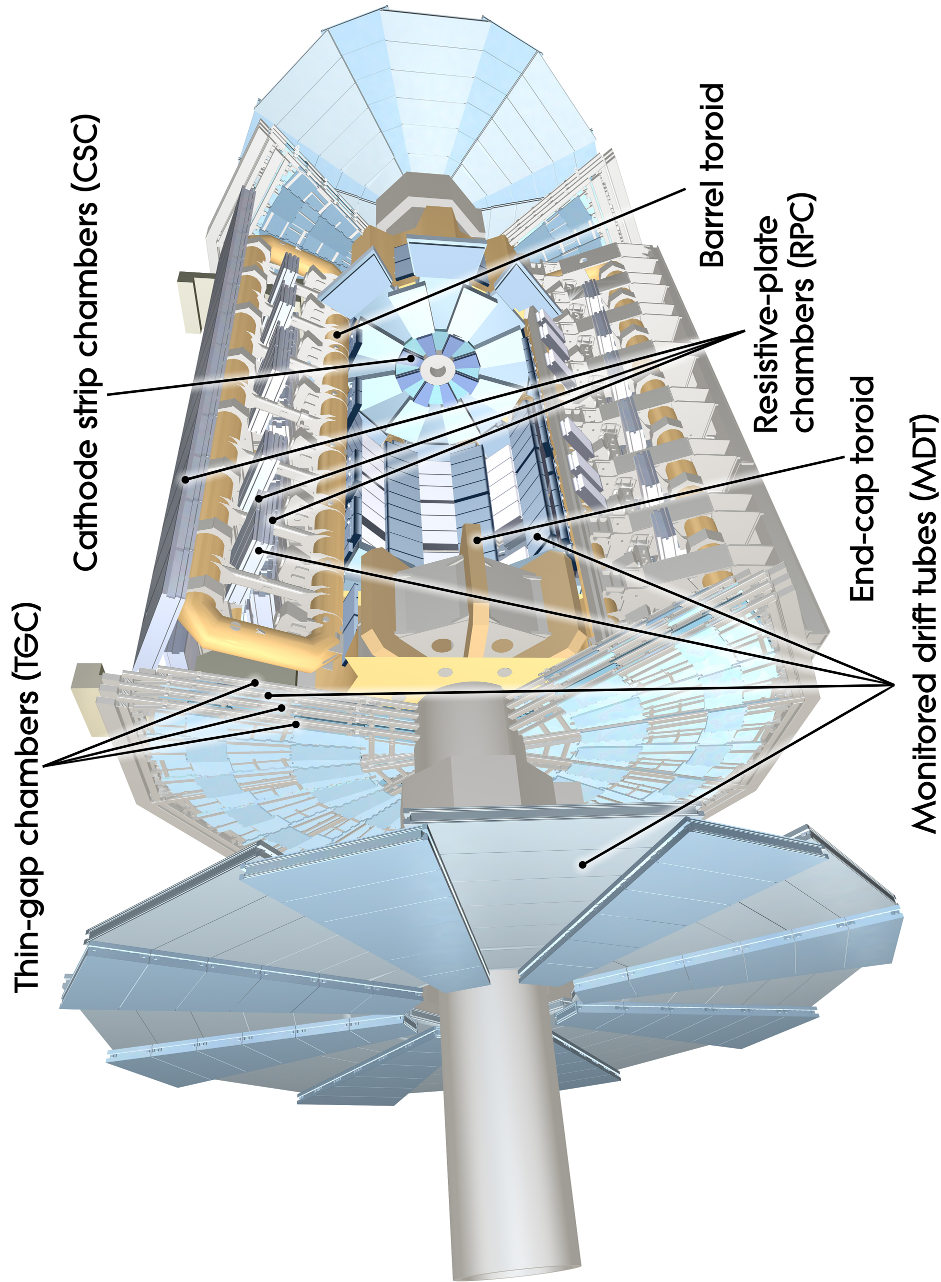

Figure 4.3: The ATLAS muon system in its entirety, with the various types of sub-detector system labelled [83].

4.3.2 Upgrades

Phase-I - New Small Wheel (NSW)

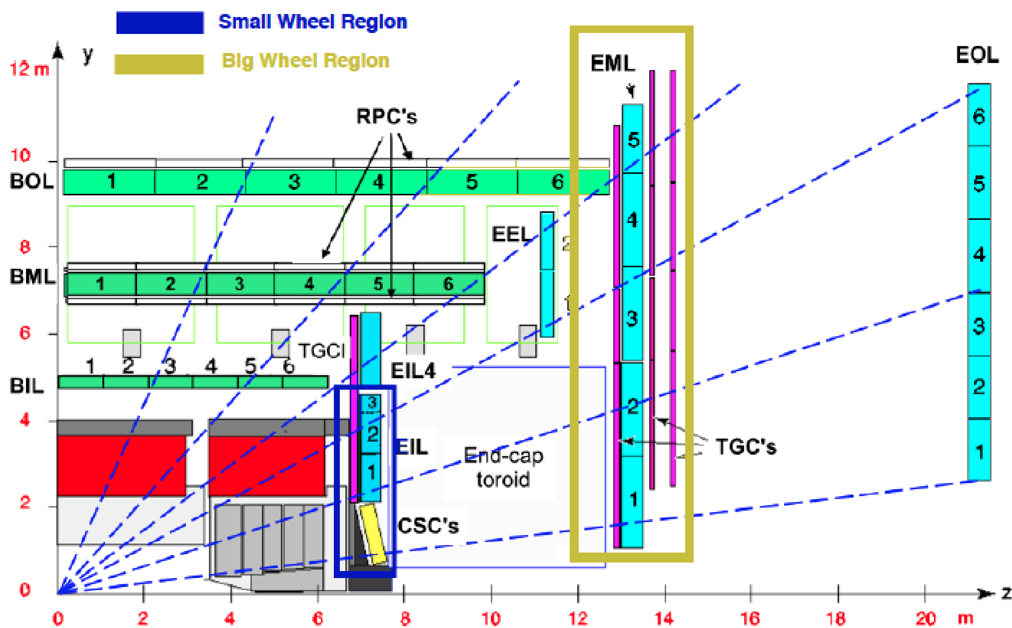

Figure 4.4: A $z-y$ view of 1/4 of the ATLAS detector. The blue boxes indicate the end-cap Monitored Drift Tube chambers (MDT) and the yellow in the small wheel area indicates the Cathode Strip Chambers (CSC). The green boxes are barrel MDT chambers. The trigger chambers, Resistive Plate chambers (RPC) and Thin Gap Chambers (TGC), are indicated white and magenta boxes. This is a cut-out on the muon spectrometer at the large sectors, hence the names End-cap Inner Large (EIL), End-cap Middle Large (EML) and End-cap Outer Large (EOL). The detector regions of the Small Wheel and Big Wheel are also outlined [82].

The Phase-I upgrade of the muon spectrometer will focus on the inner station of the end-caps [82]. The small wheel is located between the end-cap calorimeter and the end-cap toroid (see Figure 4.4). This region of the muon system has the highest cavern background flux of low energy photons and neutrons which cause random hits leading to high hit occupancies in the detectors. To enable ATLAS to fully benefit from the instantaneous luminosities above nominal value and therefore improve the physics performance of the experiment, new small wheels will be installed. The NSW will have to meet the following conditions:

- Precision tracking with performance at high luminosity equal or better than present tracking at current luminosity.
- Real time segment reconstruction at every bunch crossing, while providing track positions and angular resolution better than 1 mrad for use by the L1 trigger. The trigger data of the new small wheels should arrive at the building electronics no later than the main trigger data from the EM station.

The NSW is designed to be radiation tolerant to HL-LHC fluences ($5 \cdot 10^{34} cm^{-2} s^{-1}$). The detector has to maintain sufficient performance even with background hit rates of 14 kHz/cm^2 expected at the smallest radius of acceptance (R=100 cm).

The η coverage of the proposed NSW and the existing Small Wheel is $1.3 < |\eta| < 2.7$. The remaining region, $1.0 < |\eta| < 1.3$ is covered by the muon end-cap systems EIL4 detectors (see Figure 4.4). The end-cap fake rate will be heavily reduced by using the Thin Gap Chambers (TGC) in the EIL4 along with the NSW to provide a rough hit confirmation for comparison, although only 50 % of the full azimuthal angle is covered by the TGCs due to the barrel toroid coils. A minor upgrade is under investigation to extend the reach to regions with no current coverage.

Reducing the fake and low energy single-lepton trigger rates is particularly important in the muon system as luminosity is increased, because the single-lepton L1 trigger rates will increase proportionally to the instantaneous luminosity, while the single-lepton trigger efficiency stays roughly the same. In particular this will effect many Higgs analysies. Table 4.1 shows a comparison of the expected muon L1 trigger rate for the present system and the upgrade with the NSW at a luminosity of $3 \cdot 10^{34} \mathrm{cm}^{-2}\mathrm{s}^{-1}$, with $\sqrt{s} = 14\,TeV$ and 25 ns bunch spacing. A clear reduction in the L1 trigger rate in the forward region is seen with the upgrade, which is further decreased with the addition of EIL4. For more details on the NSW upgrade with drawings and the various physics studies please see Ref [79, 82, 84].

Phase-II - Monitored Drift Tubes (MDT) and Trigger Systems

The HL-LHC will necessitate significant detector upgrades to the muon spectrometer. The muon tracking system and the triggering system are both affected. The monitored Drift Tube (MDT) precision tracking chambers will have to maintain excellent spatial resolution and tracking efficiency in a high hit rate environment caused by γ conversions and neutron

L1MU threshold (GeV)	L1 rate (kHz)
$p_T > 20$	60 ± 11
$p_T > 40$	29 ± 15
$p_T > 20$ barrel only	7 ± 1
$p_T > 20$ with NSW	22 ± 3
$p_T > 20$ with NSW and EIL4	17 ± 2

Table 4.1: The expected L1 single muon trigger rate (based on 2011 data at $7\,TeV$) for a luminosity of $3 \cdot 10^{34}\mathrm{cm}^{-2}\mathrm{s}^{-1}$, $\sqrt{s} = 14\,\mathrm{TeV}$ and 25 ns bunch spacing for different p_t thresholds with and without the NSW upgrade. The extrapolated uncertainty to 14 TeV is also shown.

interactions. The MDT readout system must cope with the higher occupancies and increased L1 trigger rate, which will need to go well beyond the current limit of $100\,kHz$.

The trigger system will have to maintain a high level of efficiency when finding high-p_T tracks and improve rejection of fake triggers which currently already account for about 90 % of all L1 muon triggers in the end-caps. Figure 4.5 shows the composition of the overall L1 muon triggers in 2011 and 2012 runs as a function of η. Magenta shows the distribution of valid L1 triggers with $p_T > 20\,MeV$. Tracks which do not pass the Small Wheel are in white, red are tracks that do not come from the interaction point and green are tracks with radial co-ordinates in the EI and EM stations that do not match. The β (v/c) cut, finally selects tracks with a small deflection caused by the magnetic field consistent with a track with $\beta > 20\,GeV$. The installation of the NSW in Phase-I should eliminate the first three sources of fake triggers in the end-caps [18]. Currently the MDT trigger information is only used at L2, while in the new trigger scheme it could be made available at L0 or L1 to help reduce the overall trigger rate.

The RPC L1 barrel trigger system currently has a maximum $100\,kHz$ readout rate which is incompatible with the proposed $500\,kHz$ L0 trigger rate, but its maximum acceptance latency of $6.4\,\mu$s is compatible with the future L0 latency requirement. Increasing the L1 trigger rate will mandate significant changes to the existing infrastructure, including a redesign of large parts of the trigger system. This redesign will take advantage of significant technological advances made since the 90's when the current trigger system was conceived. Smaller higher bandwidth optical connections allow trigger processing to be performed off-detector, where FPGAs will be used to execute trigger algorithms instead of dedicated ASICs. The trigger electronic improvements will enable improved RPC tracking accuracy (see Ref. [18]).

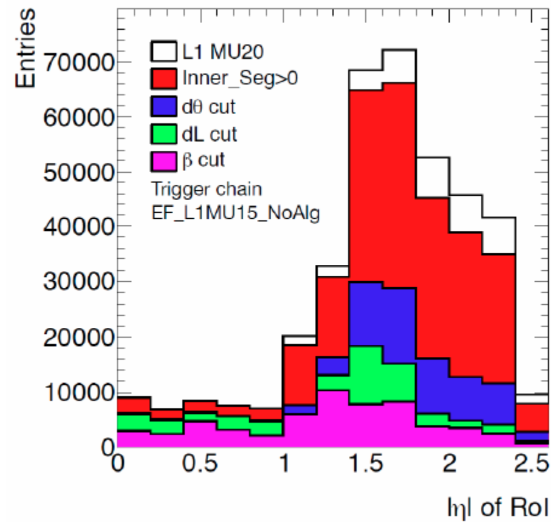

Figure 4.5: Composition of the L1 muon triggers. Magenta shows the distribution of valid high-p_T triggers, coming from the IP [18].

The L1 trigger in the end-caps is generated by Thin Gap Chambers (TGCs) inside the big wheel [13]. The new L0/L1 trigger scheme will require a complete replacement of the TGC readout electronics, similar to the RPC. There is also a need to reduce the fake trigger rate. The majority of fake triggers has been shown to primarily come from tracks not originating from the interaction point (see Figure 4.5). To veto these triggers a precision measurement before the magnet is needed. New TGCs will be installed in EI station where the New Small Wheel will be installed during Phase-I. For more information on the new hardware being installed and the changes to the muon trigger system see Ref. [18].

4.4 Calorimeter System

4.4.1 System Overview

The calorimeter system, which is divided into an electromagnetic and a hadronic part, measures the deposited energy of particles showering in the detector material. In the ATLAS detector, both parts are sampling calorimeters with active and passive material [87]. The passive material needs to have a high density to induce a shower and absorb the particle energy [13, 87], whereas the active material detects the shower. Both sub-systems are designed so that they measure the total energy of particles. The calorimeter system is illustrated and labelled in Figure 4.6.

The ECAL consists of two barrels (end to end) with a small 4 mm gap at $z = 0$ m. The ECAL covers a range of $|\eta| < 1.475$. The end-caps of the ECALs is instrumented by two wheels (one at each end). The coverage for these wheels is $1.375 < |\eta| < 2.5$. The ECAL uses accordion shaped lead absorbers filled with Liquid Argon (LAr) as the sampling element all housed in three separate cryostats, one for each end-cap and one for the barrel. The barrel section is named electromagnetic barrel (EMB) and the end-caps are named electromagnetic end-cap (EMEC). Both structures are split into three layers, a thin finely segmented initial layer designed to give a high precision hit position, a second layer to contain the majority of the shower and a third layer to estimate the shower leakage from the ECAL to the HCAL, to distinguish very large energy electromagnetic showers from hadronic showers. Additionally, in the region $|\eta| < 1.8$ an extra layer named the pre-sampler is used to estimate the energy losses from photons and electrons before reaching the calorimeters.

The hadronic calorimeters are designed to measure the energy of all remaining particles (except for muons), reconstruct hadronic jets and hadronic τ decays in order to perform a total energy measurement for the event. The hadronic calorimeter in the barrel region is composed of three cylinders, one long barrel (LB) which is split into two readout partitions and two extended barrels (EB), placed either side of the LB. The sections cover $|\eta| < 1.0$ for the LB and $0.8 < |\eta| < 1.7$ for the extended barrels. These three sections are referred to as the HCAL but are also known as the TileCal because they use scintillating tiles as a sensing element. The absorber used is steel, which allows it to act as a return yoke for the magnetic field of the inner detectors solenoid. The hadronic calorimeter also features end-caps (HEC) positioned at each end directly behind the EMEC. Copper is used as the absorber in the HEC's. Due to the positioning of the

HEC's the same sensing elements as the electromagnetic calorimeter (LAr) is used which requires them to be enclosed in the two EMEC cryostats. The region covered by the HEC's is $1.5 < |\eta| < 3.2$.

Finally, contained in the same cryostats as the end-caps are the forward calorimeters (FCAL). The FCAL's are located nestled inside the ECAL end-caps and the HEC close to he beam pipe, providing coverage from $3.1 < |\eta| < 4.9$. Due to their relative small sizes a dense tungsten matrix is used as the absorber. Liquid Argon is used as the sensing element because of the intrinsically high radiation tolerance of the material.

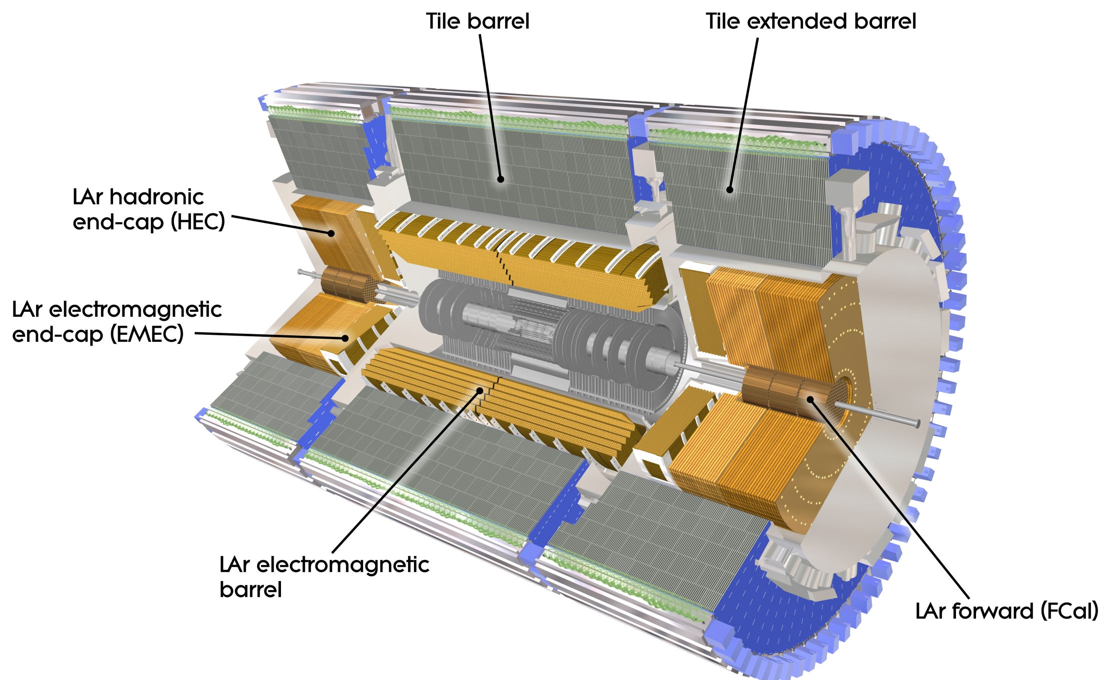

Figure 4.6: The ATLAS calorimeter system showing the electromagnetic and hadronic subsystems [85].

4.4.2 Upgrades

Phase-I - Liquid Argon (LAr) Calorimeter

An upgrade to the LAr is planned during LS1 to provide higher-granularity and higher resolution information to the L1 calorimeter trigger processors. A 10-fold increase in granularity can be seen in Figure 4.7, which compares the energy deposition of an

electron in the existing trigger readout system to that in the proposed upgraded system. The upgrade also improves the trigger energy resolution and efficiency for selected electrons, photons, leptons, jets and missing transverse energy (E_T^{miss}), thus enhancing discrimination against backgrounds and fakes from an environment with a large number of interactions per LHC bunch crossing (pile-up). As the LHC's luminosity increases above its initial design value, the improved calorimeter trigger electronics will allow ATLAS to deploy more sophisticated algorithms, utilising the higher granularity super-cells which has the advantage of providing longitudinal shower information for the L1 trigger, and higher energy precision. Furthermore, at the start of HL-LHC operation, the current electronics is expected to be 15 - 20 years old. It is foreseen that the front-end electronic will have to be replaced due to radiation damage and the need for ATLAS to upgrade its trigger system to provide the real-time performance capabilities that the current system cannot satisfy. Replacing the front-end electronics implies that the back-end electronics will also need to be replaced [86].

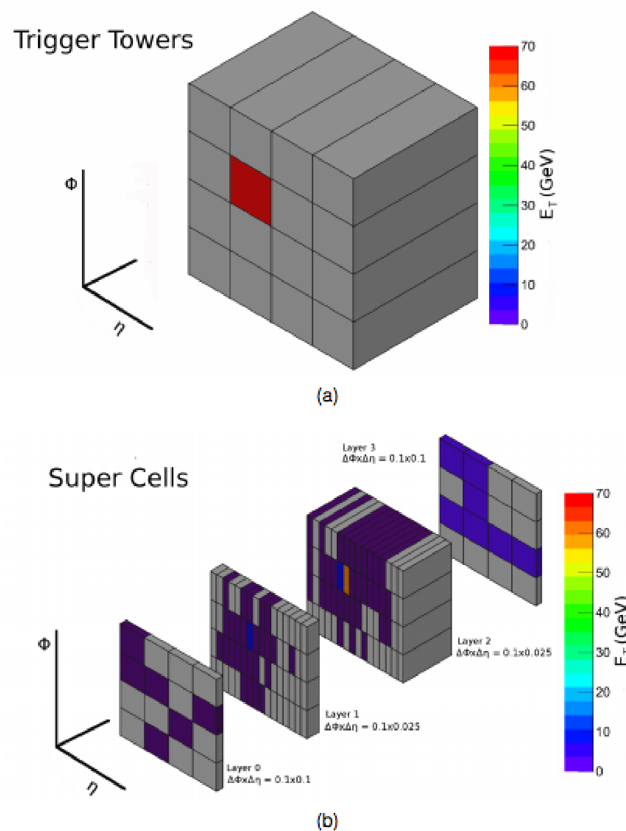

Figure 4.7: An electron (with 70 GeV of transverse energy) as seen by the existing L1 Calorimeter trigger electronics (a) and by the proposed upgraded trigger electronics (b) [86].

Phase-I - Tile Calorimeter (TileCal)

ATLAS hadronic (Tile) calorimeter system will undergo minor upgrades during LS2; the majority of the upgrade is foreseen to occur in LS3. At Phase-I even the elements with high radiation exposure (the gap and cryostat scintillator systems) are not expected to suffer any significant damage. The gap and cryostat scintillators are designed to correct for energy losses in dead material between the TileCal barrel, extended barrel and the central and forward electromagnetic calorimeter cryostats. These systems will suffer from radiation damage but have been designed to be easily replaceable. The cryostat scintillators in the $1.2 < |\eta| < 1.6$ region will suffer from significant (for scintillators) radiation exposure of up to 10 kGy/year and are expected to suffer significant light loss (up to a factor of 2) after 10 years of nominal LHC operation. The luminosity increase corresponding to HL-LHC operation will cause even greater radiation damage, so new radiation-hard scintillators and wavelength shifting fibres are being investigated [84].

Phase-II - Liquid Argon (LAr) Calorimeter

The LAr barrel electromagnetic calorimeter is expected to continue to perform well at HL-LHC luminosities up to $3000\,\text{fb}^{-1}$. However, depending on running conditions and radiation damage the FCAL, performance may degrade and it is unclear how the end-cap calorimeters (EMEC and HEC) will be affected. The present HEC cold electronics may suffer from degradation due to the increased neutron damage. As a precaution, new more radiation hard ASIC's are under development.

For the forward region, a new FCAL detector with a reduced gap size, modified HV distribution and cooling is being investigated to replace the existing one. Another option is to install a new small calorimeter in front of the existing FCAL. This new calorimeter, called the Mini-FCAL (Figure 4.8), would reduce the particle flux in the current FCAL allowing it to operate at HL-LHC luminosities. Both options necessitate the development of new front-end and back-end electronics which is not discussed here as both options are still under development. For more details on the systems and the different variants proposed see Ref. [18].

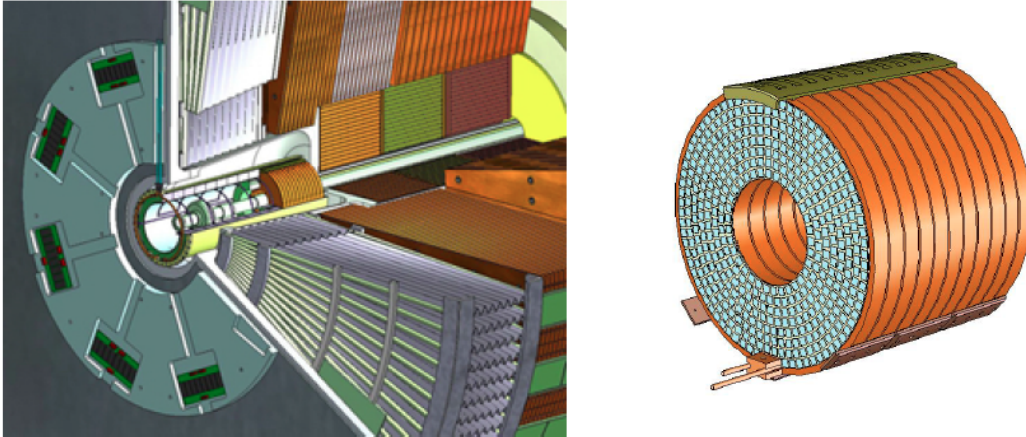

Figure 4.8: The left hand illustration is an overview of the Mini-FCAL showing the surrounding detectors and cryostat with part of the beam pipe still in place. The right hand diagram shows the diamond detector option for the Mini-FCAL with the first absorber removed so that the diamond detector layer can be seen. The cooling pipes are visible at the bottom [18].

Phase-II Tile Calorimeter (TileCal)

The existing scintillators used in the TileCal detectors are believed to be radiation tolerant enough to cope with the HL-LHC operation. This is due to significant shielding from the calorimeter elements located within the cryostats. However a full replacement of the readout electronics is foreseen to ensure compatibility with the new L0/L1 trigger architecture, to meet the increased radiation tolerance requirements of the front-end readout electronics and to provide higher granularity information to the trigger processors. The upgraded on-detector electronics will be organised in independent modules with separate power, cooling and monitoring services. The readout architecture is based on continuous digitisation and data transfer off-detector at each bunch crossing of all the readout channels. This design uses a optical data transfer system with built-in redundancy. More information on the planned readout architecture, replacement electronics and the demonstrator system can be found in Ref [18].

4.5 Inner Detector

4.5.1 System Overview

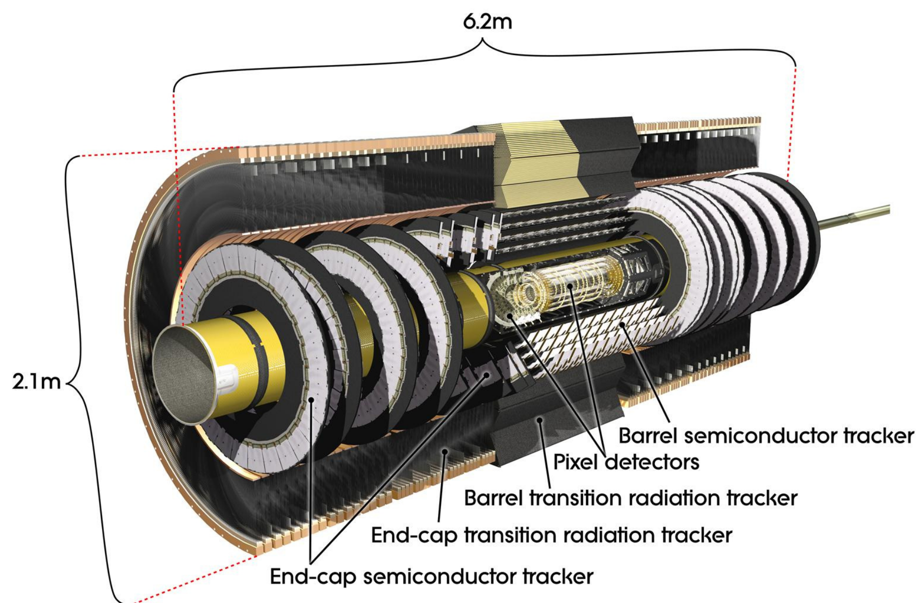

Figure 4.9: Scheme of the ATLAS inner detector barrel being crossed by one high-energy particle, labeled and with dimensions [88].

Figure 4.9 shows the structure of the ID [72] for the initial LHC running programme 2010 - 2013. The multi-layered structure comprises, from the inside to the outside, the following three successive sub-detectors: the pixel detector, the SCT and the TRT. Table 4.2 quantitatively describes key parameters of all the sub-systems within the ID [89, 90].

The pixel detector consists of pixelated silicon detectors positioned as close to the interaction point as possible. It has the highest density of readout channels in ATLAS, with a pixel cell size of $400 \times 50\,\mu\text{m}^2$ and has the best spatial hit resolution within the whole Inner Detector system. This allows for precision determination of primary and secondary vertex locations. The detector consists of three barrel layers around a central beam pipe with end-caps at either end providing coverage in the forward region, consisting of three disks each. The pixel detector provides, at least three space point measurements per track. A more detailed description of the pixel system is given in Section 4.5.4.

System	Position	Area (m^2)	Resolution σ (μm)	Channels (10^6)	η coverage
Pixels	1 Inner barrel layer	0.2	$R\phi$=12, z=66	16	2.5
	2 barrel layers	1.4	$R\phi$=12, z=66	81	1.7
	3 end-cap disks, on each side	0.7	$R\phi$=12, z=77	43	1.7-2.5
Silicon strips	4 barrel layers	34.4	$R\phi$=16, z=580	3.2	1.4
	9 end-cap wheels, on each side	26.7	$R\phi$, z=580	3.0	1.4-2.5
TRT	Axial barrel straws		170 (per straw)	0.1	0.7
	Radial end-cap straws		170 (per straw)	0.32	0.7-2.5
	36 straws per track				

Table 4.2: Parameters of the Inner Detector. The resolutions quoted are typical values (the actual resolution in each detector depends on $|\eta|$) [13, 89]

The SCT is designed to provide eight precision measurements per track in the intermediate radial range, contributing to the measurement of momentum, impact parameter and vertex position. In the barrel, eight layers of silicon micro-strip detectors provide precision point in the Rϕ and z coordinates, using a small stereo angle to obtain the z-measurement. Each silicon detector is 636 x 640 mm^2 with 780 readout strips with 80 μm pitch. The end-cap modules, mounted on disks, are very similar in construction but use tapered strips with one set aligned radially. A more detailed description of the SCT is given in Section 4.5.3.

The TRT, the outermost component of the Inner Detector, is a straw tracker interleaved with polypropylene transition radiation foils. The straws (drift tubes) have a 4 mm diameter and vary in length, with the longest straws being 144 cm long. The smallest straws have a position resolution of $\sim$ 200μm per single hit. The TRT has a very large volume compared to the pixel and SCT detectors, which was driven by the cost of extending the silicon pixel and strip systems. A detailed description of the TRT will be given in Section 4.5.2.

4.5.2 Transition Radiation Tracker (TRT)

The TRT [15] is a gaseous detector operated within a 2 T magnetic field. It is composed of straw drift tubes with interleaved polypropylene. These foils generate the transition radiation for electrons/positrons, which is detected within the straws in addition to the ionisation signal of all charged particles. Each straw has a diameter of 4 mm and is composed of kapton reinforced with carbon-fibre for mechanic strength and thermal conductivity. A gold plated tungsten anode wire (31 μm diameter) is strung inside each straw and the straw is filled with a gas mixture for absorbing the transition radiation. A typical gas mixture used in the TRT is composed of 70% Xe, 27% CO_2, and 3% O_2. However, the gas mixture can be changed. A detailed description of the evolution of the gas mixtures used can be found in [91]. The detector is operated by grounding the anode wire and applying a high bias voltages to the cathodes. Typically the cathodes are biased with - 1.5 kV which leads to a gas gain of $2.5 \cdot 10^4$, for the gas mixture stated above. To cope with the expected high hit rates, each of the $\sim$ 53 k straws are segmented (including anode wires) using a glass bead in the centre of the straw. They are read out at both ends creating $\sim$ 106 k readout channels in total. The hit occupancy in the innermost layers is so large that the straws in the first nine layers are segmented into three sections, where the inner sections are desensitised to reduce the overall hit rate [92–94].

The TRT is formed from a central barrel detector with end-caps at either end in the forward region [89]. Continuous tracking is possible within the barrel using axial drift tubes (straws) because of the high hit rates. As a result, the straw layout enables the measurement of about 36 measurements (typically) per charged particle track with a transverse momentum $p_t > 0.5\,GeV$ and pseudo-rapidity $|\eta| > 2.0$ (except for the barrel/end-cap transition region) [90]. The TRT barrel covers a radius range of 56 - 108 cm.

4.5.3 SemiConductor Tracker (SCT)

The system is an order of magnitude larger in surface area than previous generations of silicon micro-strip detectors [90]. The SCT will be subjected to significant radiation throughout its operational lifetime, from charged and neutral particles from the collision point and from backscattering neutrons originating in the calorimeters. The innermost barrel layer of the SCT will see the most radiation. This is estimated to be of the order of $10^{14}\mathrm{n_{eq}}/\mathrm{cm}^2$ after 10 years of operation [95].

The barrel of the SCT features eight layers of silicon micro-strip sensors to provide precision measurements in the $R\phi$ and z directions within ATLAS. Each silicon sensor is approximately 636 x 640 μm^2 with 768 readout strips and a pitch of 80 μm, with half the sensors mounted at a small stereo angle along z ($\sim$ 40 mrad). The readout electrode choice is p-in-n. Modules consist of two silicon sensors glued back-to-back to a heat transport plate. In barrel modules, the hybrids are mounted on bridges which sit above the surface of the silicon sensors. The readout chain consists of a front-end (FE) amplifier and discriminator, followed by a binary pipeline which stores the hits above threshold until the L1 trigger decision [96].

The end-cap modules are similar to the barrel modules but with tapered strip detectors, with one set aligned radially and with hybrids mounted at the ends. Disks are constructed using three types of modules named inner, middle and outer modules. The outer and middle modules each use two pairs of back-to-back sensors while the inner module uses a single pair. In total, five different types of tapered sensors are used. To obtain optimal η coverage across all end-cap wheels, the strips length varies with radius within the disk. The outermost radii end-cap modules have sensor strip lengths of 55 to 72 mm. The rest of the end-cap modules have sensor strip lengths that vary from 54 to 61 mm. The strip pitch for the module varies with radius between 57 μm in the innermost modules to 90 μm in the outermost modules [97, 98]. Table 4.2 lists the important characteristics of the SCT, including number of channels and spatial resolutions. Tracks within the SCT can be distinguished if they are separated by more than $\sim$ 200 μm [15, 89].

4.5.4 Pixel Detector

The pixel system [100] has to be as close to the interactions as possible in order to detect short-lived (10^{-12}s) [28] particles such as b hadrons and τ leptons. The system consists of three barrel layers and a total of six end-cap disks, 3 at either end of the barrel. The barrel layers, from inside out, are Layer-0 (also known as the b-Layer), Layer-1 and Layer-2, mounted at radii of 50.5 mmm 88.5 mm and 122.5 mm from the interaction point respectively. Figure 4.10 shows a barrel cut away view of the ID with each layers mounting radii. More details on the barrel and disks sections are given in Table 4.3 and Table 4.4 respectively.

Layer	Radius (mm)	No. of Staves	No. of Modules	No. of Channels	Active Area [m^2]
b-layer	50.5	22	48	13,178,880	0.28
Layer 1	88.5	38	48	22,763,520	0.49
Layer 2	122.5	52	48	31,150,080	0.67
Total		112	1456	67,092,480	1.45

Table 4.3: Barrel layer arrangement and dimensions for the ATLAS pixel detector [13, 101].

	Radius (mm)	No. of Sectors	No. of Modules	No. of Channels	Active Area [m^2]
Disk 1	495	8	48	2,211,840	0.0475
Disk 2	580	8	48	2,211,840	0.0475
Disk 3	650	8	48	2,211,840	0.0475
Total, one end-cap		24	144	6,635,520	0.14
Total, both end-caps		48	288	13,271,040	0.28

Table 4.4: End-cap arrangement and dimensions for the ATLAS pixel detector [13, 101].

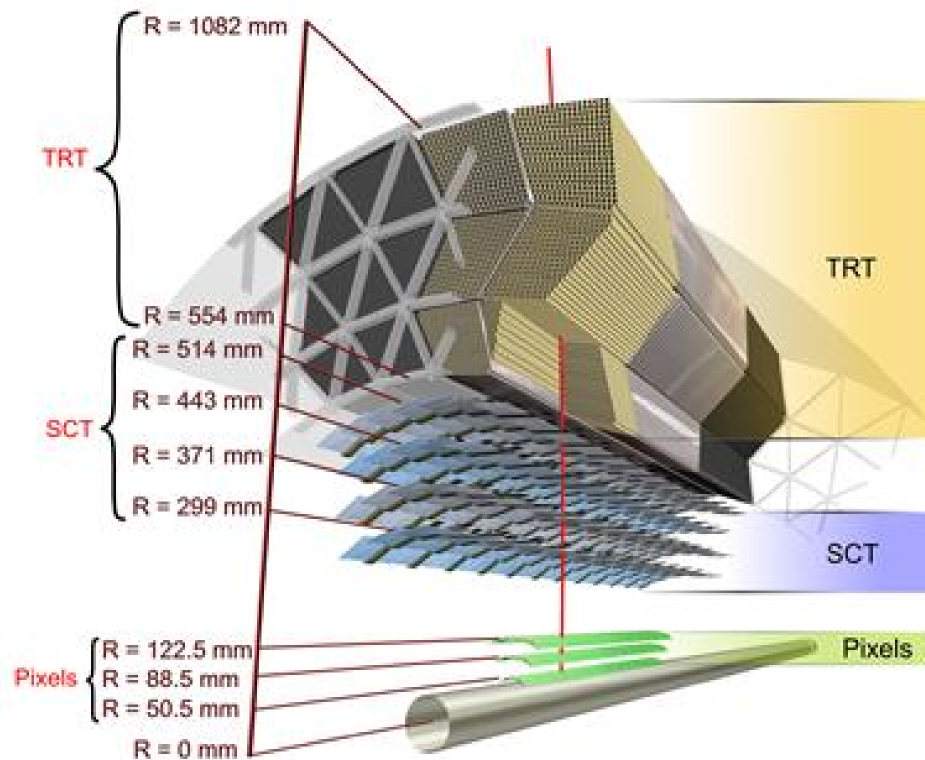

Figure 4.10: Cut away view of the inner detector. The inner detector is composed of the following sub-detectors in order of radius: the pixel detector which is closest to the beam pipe, the silicon micro-strop detector (SCT) and the transition radiation detector (TRT) the inner detector is enclosed by a solenoid (not shown in this picture) [99].

The two-dimensional segmentation of the pixel sensors allows for the measurement of space points without the ambiguities associated with crossed strip geometries used in the SCT (see Section 4.5.3). However [89], pixel sensors require more advanced readout electronics and interconnections. The readout chip's segmentation matches that of the sensor, with each segment featuring individual readout circuitry, including buffers to store data while waiting for a L1 trigger decision. Each readout chip is bump-bonded to a sensor with high density connection methods [102]. Readout chips and sensors have to be radiation-hard to over 300 kGy and $\sim\ 1 \cdot 10^{15}\,\mathrm{n_{eq}/cm^2}$ of ionising radiation over an operational life time of 10 years. The maximum leakage current for Layer-1 after 10 years (or 5 years for the B-Layer) is expected to remain below 550 μA per module for a 600 V maximum operating voltage and a nominal operating temperature of about - 13 °C

[118]. The corresponding leakage current heating will contribute about 300 mW to the total module power dissipation. As a result the cooling system will have to be capable of removing a total power of around 13 kW from 240 pixel detector staves and disk sectors [100].

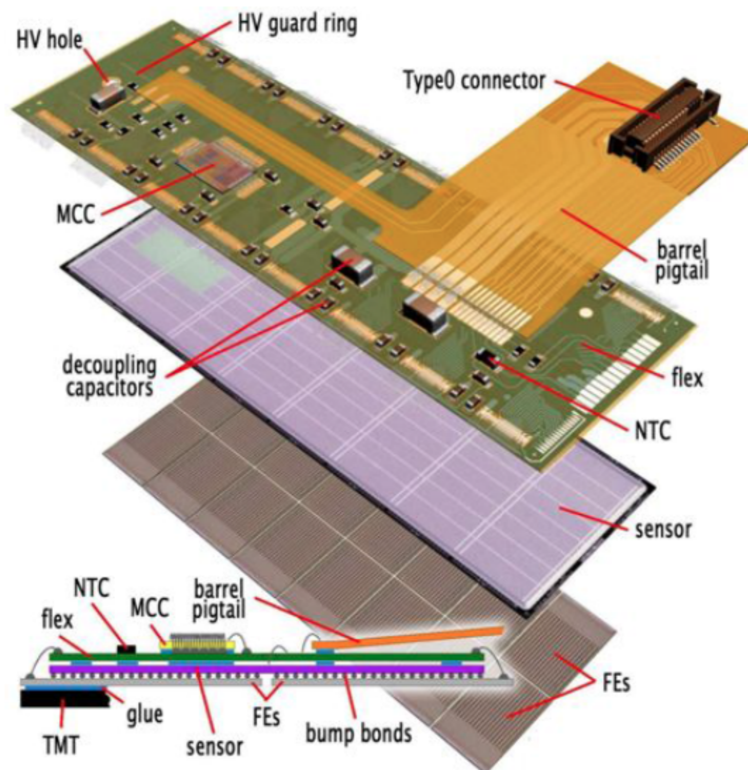

Figure 4.11: The ATLAS FE-I3 hybrid pixel module. The module readout electronics are mounted on a polyamide printed circuit board (flex-hybrid). The flex-hybrid is attached with an adhesive to the sensor. The sensor is bump-bonded to 16 FE-I3 readout chips. The flex-hybrid also provides the high voltage and low voltage to the attached components. The sensor is wire-bonded through a hole in the flex-hybrid, exposing the sensor backplane (p-implant). Wire-bonds are also used to electrically interconnect the FE-I3 readout chip to the flex-hybrid [103].

Barrel layers and disks consist of staves and sectors respectively (see Table 4.3 and Table 4.4 for more details). It is on these staves/sectors that hybrid pixel modules are mounted. A hybrid pixel module is the smallest unit in the pixel detector, illustrated in Figure 4.11. It consists of a flex-hybrid containing the readout electronics and a sensor [103]. The sensors used are 250 μm thick *n-in-n* technology, with an active area of 164 x 608 mm^2 [104]. This sensor is then interconnected via solder-bump technology to 16 FE-I3 [105] readout chips (2 columns of 8 readout chips), each featuring 2880

readout channels. To enable the whole sensor to remain active between the boundaries of the FE-I3 readout chips, some of the readout channels are connected to multiple pixels (referred to as ganged pixels) and/or to pixels with a slightly larger cell dimension (see, Figure 4.12). In total, this leads to 47,232 pixels per module arranged as 144 columns by 328 rows [28].

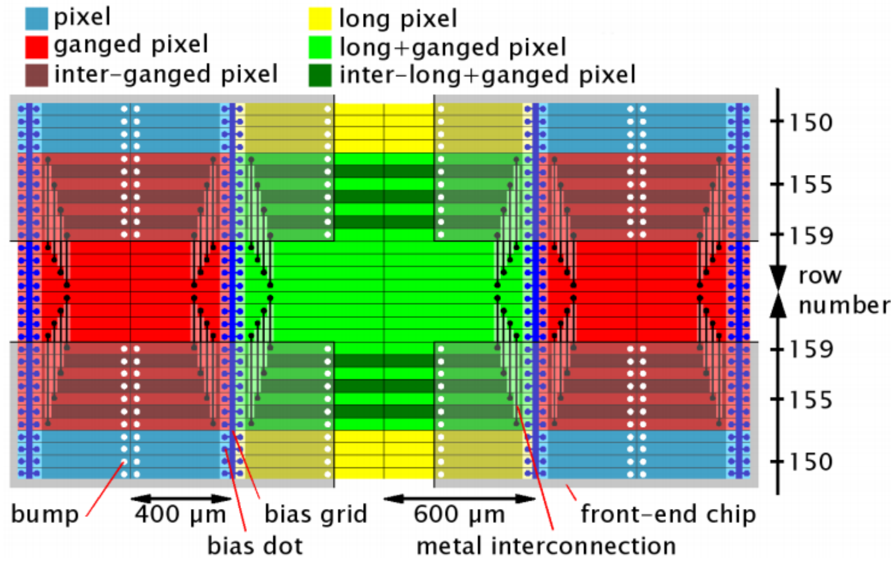

Figure 4.12: Layout and interconnection of FE-I3 pixel types in the inter chip region. The FE-I3 pixel readout chip is indicated by light grey shading, whereas all four sensors meet in the middle. Normal pixels (red and blue): 50 x 400 μm^2. Long pixels (green and yellow): 50 x 600 μm^2 [106].

The standard pixel cell dimension (pitch) is 400 x 50 μm^2, along the z- and ϕ-directions, respectively, as installed in the barrels. However, as mentioned above, some pixels have larger cell dimensions (11% of pixels per module have a cell dimension of 600 x 50 μm^2 [106]). The resulting hit resolutions per barrel layer (and combined) in both z- and $r\phi$-directions is dependent on the inclination (η) of the particle tracks being measured. The charge sharing between pixels and therefore the cluster size increases with pseudo-rapidity, η. This effect is exploited by using charge weighted clustering algorithms to increase the spatial hit precision of the particle track. However, this effect is influenced by several parameters [103]:

- The position and incident angle the particle track has with respect to the sensor surface.
- The intrinsic sensor properties - such as the inter-pixel capacitance and the capacitance to the backplane.

- The operational conditions - The applied reverse bias and the radiation damage
- The operational conditions of the readout chip - Time-over-Threshold (ToT), crosstalk, charge resolution etc...
- The presence of magnetic field - The charge carriers inside the sensor will be deflected by the Lorentz angle

For a detector close to the interaction point, the material budget is an important factor to consider. Added material will cause increased multiple scattering and showering of traversing particles, adding uncertainties to the spatial position measurement [35]. This is particularly important for lower energy particles of order a few GeV. Equation (4.2) describes multiple scattering through small angles, where βc and z are the velocity and charge number of the incident particle respectively, and x/X_0 is the thickness of the scattering medium in radiation lengths [107],

$$\theta_0 = \frac{13.6and}{\beta cp} z\sqrt{x/X_0}\,[1 + 0.038\,ln(x/X_0)]\,. \tag{4.2}$$

To minimise material, the mechanics that support the pixel modules are composed of thermally conductive carbon composites surrounding low density carbon foam cores to provide both mechanical stability and cooling distribution. Cooling is supplied to the mechanics using small aluminium pipes embedded inside the foam cores. Here C_3F_8 is used to provide a bi-phase evaporative cooling system. A large contribution to the material budget for a pixel detector comes from the services, which include but are not limited to power/data cables and cooling tubes. Figure 4.13 shows the distribution of material described by the radiation length (X_0) and the interaction length (λ) as a function of $|\eta|$. The pixel layers (coloured in purple) represent a substantial contribution at $|\eta| > 1.5$ [13].

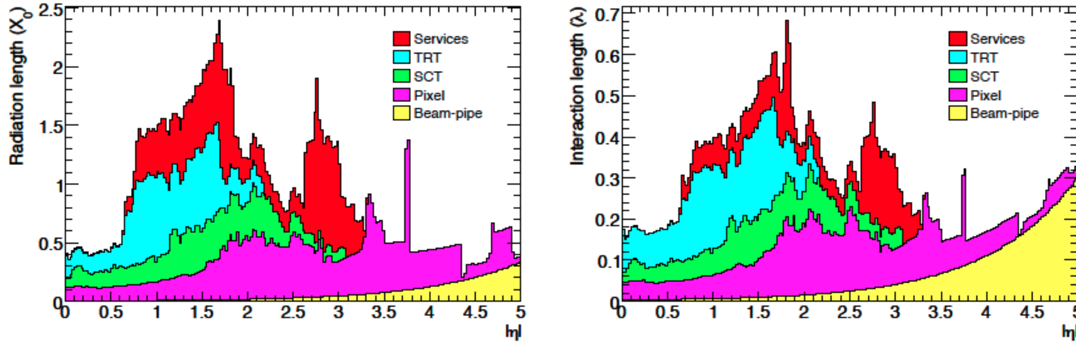

Figure 4.13: Distribution of material by radiation length (left) and interaction length (right) within the ATLAS Inner Detector as a function of $|\eta|$ [13].

4.5.5 Upgrades

Phase-0 - Insertable B-Layer (IBL)

The inner detector had a new fourth pixel barrel layer added during LS1, the Insertable B-Layer (IBL). This layer sits inside the existing layers at a radius of 34 mm. The motivations for adding this extra pixel barrel layer are:

- Tracking Robustness: Failures of modules in the b-layer, and in the other pixel barrel layers can appear with time. Although these failures can be compensated for during reconstruction, they can result in inefficiencies and increased track fake rates. Loss of data from the b-layer has a major effect on the impact parameter resolution, which directly affects b tagging. The IBL enables the recovery of b tagging efficiency even in the case of significant levels of failure in the b-layer.

- Luminosity: The pixel detector was designed to cope with peak instantaneous luminosities of $\sim 1 \cdot 10^{34}\text{cm}^2\text{s}^{-1}$, The Phase-I upgrades will increase the peak luminosity by at least a factor of 2 [17] after LS2 (see Section 2.3.2). The existing system can have difficulties coping with the increased pile-up, the hit occupancy will also reach a level where inefficiencies in the readout can occur. Ultimately this will impair ATLAS b-tagging efficiency. To combat this the IBL will have a finer granularity compared to the b-layer, reducing the pixel cell size from 400x50 μm^2 to 250x50 μm^2.

- Tracking Precision: The IBL will be mounted closer to the interaction point improving the quality of impact parameter reconstruction for tracks, and thereby improving b-tagging performance.

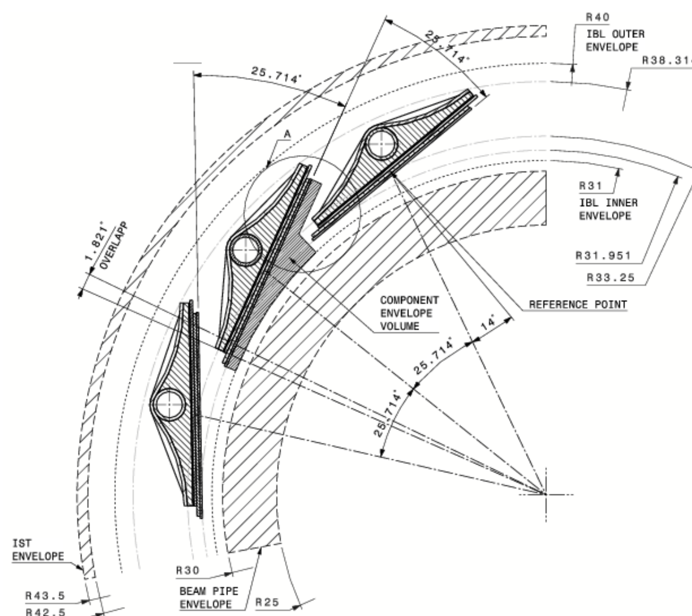

Figure 4.14: Layout of the Insertable B-Layer in R/ϕ [81]. Dimensions are given in mm.

To cope with the limited space available, the IBL is mounted on a new beam pipe with a smaller radius. The IBL is constructed of 14 staves; each stave consisting of 12 double chip modules of planar *n-in-n* sensors and 8 single chip modules of 3D silicon sensors. The latter will be located at the high η regions at the ends of the staves. The staves will be mounted, tilted by 14° with respect to $r\phi$ direction, at a mean radius of 3.3 cm with respect to the nominal beam spot, the layout in the r/ϕ direction is shown in Figure 4.14.

The small radius coupled with increased event pile up, hit occupancy and increased radiation damage compared to layer-0, causes a significant issue for the existing readout electronics (FE-I3). The main effect would be an increase in hit inefficiencies [108]. In response, a new readout chip with a different readout architecture was designed for the IBL, as well as for future pixel detector upgrades, called the FE-I4 readout chip [109–111]. The FE-I4 is built using 130 nm CMOS feature size, and is made radiation hard using thin gate oxide transistors. The FE-I4 comes in two flavours, FE-I4B, which is the finalised chip used in the IBL and FE-I4A, which was the prototype readout chip. Both readout chips are basically the same, although the FE-I4A is missing some circuitry, such as the internal Time-over-Threshold (ToT) charge calibration circuitry, needed for operation in ATLAS.

The FE-I4 is currently the largest readout chip produced for high energy physics experiments. Its physical size is 20.2 x 18.8 mm^2 with an active area of 20.2 x 16.8 mm^2. This results in an active to inactive surface ratio of about 90 %, which is significantly higher than that for the FE-I3, $\sim$ 75 %. The increase in size and active fraction of the FE-I4 is important to minimise the amount of necessary overlaps between interconnected readout chips on modules and across staves. This is particularly important for the IBL as space is limited, but also helps reduce the material budget and stave cost [112]. The active area holds a pixel matrix organised in 80 columns and 336 rows. Two columns form an architectural unit called a Double Column. All pixels have a cell size of 250 x 50 μm^2 with a two stage amplifier circuit. Four analogue pixels share one common digital logic cell. A detailed description of this can be found in [113]. The hit information is stored in the 4-pixel digital regions of the pixel matrix until the L1 trigger arrives. This new architecture avoids moving the information associated with un-triggered hits to the periphery, which was shown to be the main source of inefficiency in FE-I3 at the expected hit occupancies [108, 114]. Figure 4.15 illustrates the relative sizes of the FE-I3 and FE-I4 readout chips.

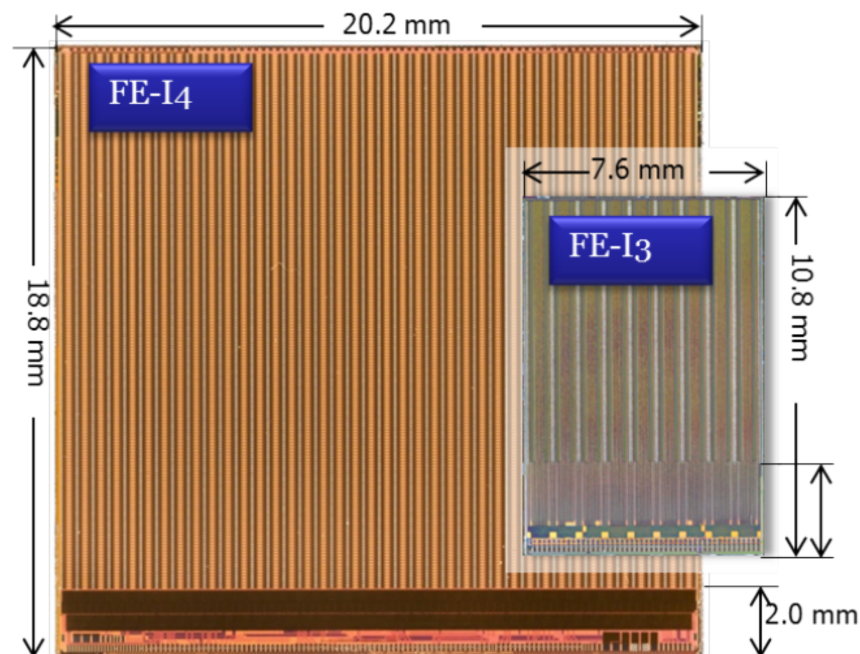

Figure 4.15: To scale picture of FE-I4 in comparison to FE-I3 readout chip [114].

The IBL staves have a similar construction to the existing pixel layer staves and are assembled from carbon fibre face-sheets surrounding a foam core into which a titanium

cooling tube is embedded. A schematic of the cross-section of the IBL [81], indicating the tilt of the staves with respect to the interaction point, and the overlap between neighbouring staves is shown in Figure 4.14. Each stave will be tilted in the radial direction by 14°, which is primarily due to space constraints between the new slimmer beam pipe and Layer-0 while retaining the required overlap between staves. It also has the added benefit of compensating for the Lorentz angle and reduced hit efficiency observed in normal (perpendicular) incident tracks passing through the biasing implants in the planar devices and the electrode implants in the 3D devices. The main IBL parameters are given in Table 4.5, and some important sensor parameters given in Table 4.6.

	Value	Unit
number of staves	14	
Number of modules per staves (single/double FE-I4)	32 / 16	
Pixel size (ϕ, z)	50, 250	μm
Module active size W x L (single/double FE-I4)	16.8x40.8 / 20.4	mm^2
Coverage in η, no vertex spread	$\|\eta\| < 3.0$	
Coverage in η, 2σ (=112mm) vertex spread	$\|\eta\| < 2.58$	
Active z extent	330.15	mm
Geometrical acceptance in z (min, max)	97.4, 98.8	%
Stave tilt angle in ϕ (centre of sensor, min, max)	14.00, -0.23, 27.77	degree
Overlap in ϕ	1.82	degree
Centre of the sensor radius	33.25	mm
Sensor thickness:		
Planar silicon	200	μm
3D silicon	230 $\pm$ 15	μm
Radiation Length	1.54	% of X_0

Table 4.5: Main IBL layout parameters.

IBL modules come in two styles, single and double chip modules. Single chip modules consist of 3D (technology) silicon sensors approximately the same size and with the same segmentation foot-print as the IBL FE-I4 readout chip. The double chip modules, utilise standard planar (technology) silicon sensors. Double chip sensors use a single guard ring structure to surround all readout pixels, just as with the existing FE-I3 pixel modules. The small area between FE-I4 chips on the sensor is kept active by extending the pixel

Requirement	Value	Conditions
NIEL (Section 8.4) dose tolerance	$5 \cdot 10^{15}$ n_{eq}/cm^2	-
Ionising dose tolerance	250 Mrad	-
Hit efficiency in active area	> 97 %	Single Minimum Ionising Particle (MIP)
MIP $r\phi$ resolution	< 10 μm	2T B-field, 15° incidence
MIP z resolution	72 μm	Digital resolution for 250 μm pixel
Maximum bias voltage	1000 V	-

Table 4.6: Sensor requirements for IBL devices.

cell size in the middle two readout columns (centre of the double chip) to 500x50 μm^2 instead of the standard 250x50 μm^2 [81].

The service quarter panels which carry electrical power, cooling and optical data both into and out of the pixel detector have been replaced as part of the IBL integration. However, the main reason for full replacements of these panels is because of failures in the opto-board transmitters which are used to transfer data to and from the pixel detector. The opto-board electronics were found to be in-sufficiently radiation tolerant and will be replaced with an electrical readout. The new service quarter panels (nSQP's) have been designed to allow the critical optical components to be placed in a more accessible location so they can be serviced without removing the pixel detector. The electrical readout uses a radiation tolerant repeater chip, used to boost electrical signals [115, 116]. The replacement has also allowed limitations in the readout bandwidth from the pixel system to be corrected so that for Phase-I luminosities there should now be no risk of readout link saturation.

Phase-I - FTK

The only significant change to the ID, will be the inclusion of the Fast TracKer (FTK). The FTK is an electronics system designed to do global track reconstruction after each L1 trigger giving the L2 trigger access to the track information, allowing for improved event selection at HLT. The FTK will use data from the pixel and SCT systems as well as the new Insertable B-Layer (IBL) pixel detector. An identical copy of the data sent between the pixel and strip Read-Out Drivers (RODs) to the DAQ Read-Out System (ROS) is sent to the FTK following a L1 trigger. After processing, the FTK fills the ROS

with all its track information. The L2 trigger can then request the track information for a region of interest or for the full detector (pixel and SCT).

The FTK has to provide very fast processing of track information, as a result it has been designed to be a highly parallel, the system is segmented in 64 $\eta - \phi$ towers, each withs its own pattern recognition hardware and track filters. The FTK will operate in two stages. in the first stage, 8 of the 12 silicon layers are used to perform pattern recognition and do initial tracking fitting. The track fitting is carried by a dedicated system called the Associative Memory (AM), the specific details regarding the track fitting procedure will not be discussed, instead refer to the FTK TDR [80]. The second stage takes tracks calculated in stage 1, which are then extrapolated onto the 4 remaining logical silicon layers not used in stage 1. Hits from all 12 logical layers are then used to refine the track candidates using tighter cuts (compared to stage 1). Figure 4.16 shows a functional sketch of the FTK, which is FPGA based with the exception of one specially designed custom chip for the AM. Further details on the FTK can be found in [80].

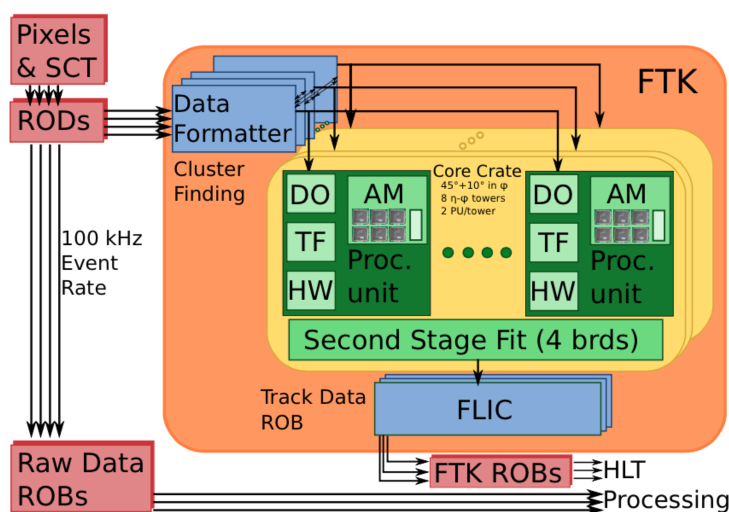

Figure 4.16: Functional sketch of FTK. AM is the Associative Memory, DO is the Data Organizer, FLIC is the FTK-to-L2 Interface Crate, HW is the Hit Warrior, ROB is the ATLAS Read-Out input Buffer, ROS is a silicon detector Read-Out Driver, and TF is the Track Fitter [80].

Phase-II - The Inner Tracker (ITk)

To withstand the much harsher radiation and occupancy conditions of the HL-LHC a complete replacement of the present ID [117] is necessary. This replacement has been named the new Inner Tracker (ITk) and will be an all-silicon tracking system. The

ID was designed to operate for 10 years at a peak luminosity of $10^{34}\mathrm{cm}^{-2}\mathrm{s}^{-1}$, with an assumed pile-up of 23 events per 25 ns bunch crossing, and a L1 trigger rate of 100 kHz. The ID's performance parameters do not meet for the extreme requirements needed for high luminosity (HL-LHC) operation [18]. The three main reasons for a replacement are:

Radiation Damage: The current pixel detector was designed for a maximum integrated fluence of $\sim 10^{15}$ $\mathrm{n_{eq}/cm^2}$, corresponding to an integrated luminosity of 400 fb^{-1} [118–121]. The IBL was designed to operate for luminosities up to 850 fb^{-1} which is still much lower than the HL-LHC expected luminosity of 3000 fb^{-1}, giving an expected fluence $2 \cdot 10^{16}$ $\mathrm{n_{eq}/cm^2}$ at this radius. The SCT is also not sufficiently radiation-hard. $2 \cdot 10^{14}\mathrm{n_{eq}/cm^2}$ is the design limit compared with an expected dose of $10^{15}\mathrm{n_{eq}/cm^2}$ predicted at HL-LHC.

Bandwidth Saturation: The front-end electronics for both pixel and SCT sub-systems use zero suppression and have been designed to accommodate occupancies corresponding to up to 50 pile-up events, about twice the LHC design value. Limitations in the buffering and the links between the on-module electronics and the read-out driver card (ROD) will lead to inefficiencies in the pixel detector when 0.2 % to 0.4 % pixel hits per 25 ns bunch crossing are exceeded per pixel, which is expected for luminosities of $\sim 3 \cdot 10^{34} cm^{-2} s^{-1}$ [115, 116]. A similar saturation effect is expected for the SCT, where limitations will come from the s-link between the ABCD front-end chip and the RODs.

Occupancy: with the expected pile-up at the HL-LHC, the SCT would be unable to resolve close neighbouring particles, and the TRT straws would approach 100% occupancy. Some degradation in the TRT's ability to resolve high density neighbouring hits has already been observed in the most central heavy-ion collisions.

The extreme conditions at the HL-LHC dictate a more modular inner detector design, because the pixel barrel layers (the first two in particular) will suffer enormous amounts of radiation. The pixel barrel layers and disks should be designed so that they can be accessed and even replaced without interfering with the strip barrel layers. During HL-LHC operation more than 1000 tracks per event per unit of rapidity are expected [122], given the current ID track acceptance range and granularity (including IBL). It would be a major challenge to associate tracks with their correct primary or secondary vertices at high efficiency. With this in mind, the main requirements for the new inner tracker should be:

- Measure the transverse momentum and direction of isolated particles, in particular electrons and muons. The combination of tracker and muon spectrometer information gives the optimum evaluation of muon transverse momentum at all but the highest momentum.
- Reconstruct the vertices in high pile-up events and identify the vertex associated with the hard interaction. This information can then be used to improve the evaluation of particle isolation, and the measurement of jet energy and total missing energy.
- Identify secondary vertices in b-jets with high efficiency and purity, even in highly boosted jets.
- Measure tracks in the core of high energy jets, with good double-track resolution to allow high efficiency and sufficient redundancy to reduce fakes.
- Identity the decays of tau leptons, including impact parameter information and in combination with calorimeter measurements
- Reconstruct the tracks associated with converted photons

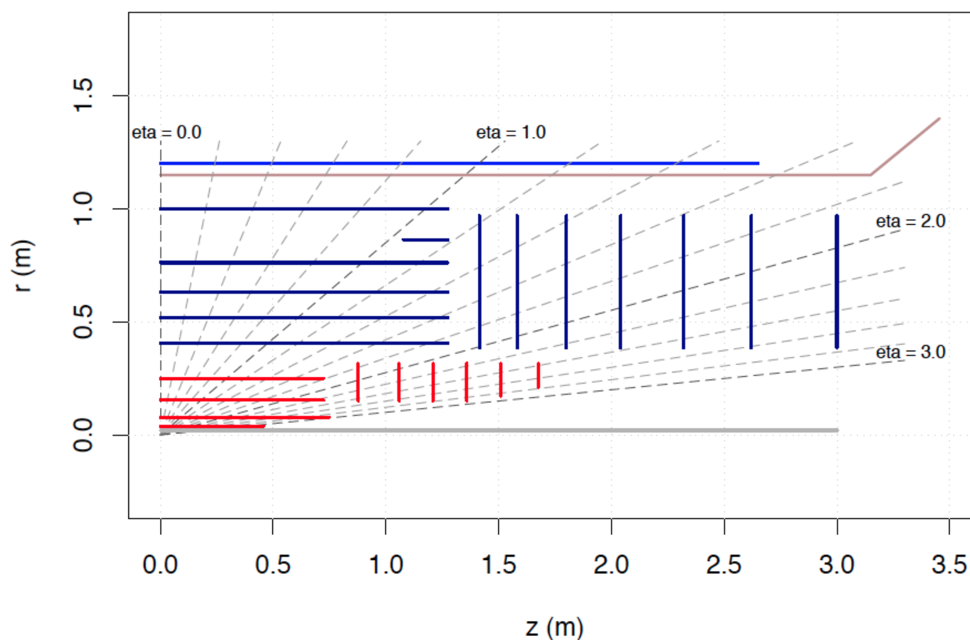

Figure 4.17: The proposed baseline layout design for the ATLAS inner TracKer (ITk) in the Phase-II upgrade. The ITk will be an entirely silicon detector. It consists of two main sections: pixels in red and strips in blue [18, 126].

Figure 4.17 shows the baseline layout for the ITk, which will be an all-silicon tracker featuring pixel sensors at inner radii surrounded by micro-strip sensors [123]. The central layers (barrel) are arranged in cylinders, with four pixel layers followed by three short strip layers and two long strip layers. Given that the outer radius of the beam pipe will be 33 mm and to enable the ITk to be modular, an inner support tube (IST) at 110 mm and a pixel support tube (PST) at 345 mm are proposed. The forward region will be covered by six pixel disks and seven strip disks. Each strip layer is double-sided with axial strip orientation on one side and sensors rotated by 40 mrad on the reverse, giving the z co-ordinate measurement. The tracker will be surrounded by a polyethylene moderator to reduce the energy of neutrons being backscattered towards the tracker from the calorimeters [124].

The ITk will have to cope with unprecedented levels of radiation over its lifetime at the HL-LHC. The very innermost layers will receive high levels of neutron and charged particle radiation damage, currently estimated (using FLUKA and PYTHIA8) to be $1.4 \cdot 10^{16}\,\mathrm{n_{eq}/cm^2}$ and 7.7 MGy at the centre of the innermost barrel layer, decreasing with increasing radius, for $3000\,\mathrm{fb}^{-1}$ [18].

Initial assessments of cost versus radiation tolerance lead to a design with only the inner pixel layers (layer-0 and Layer-1) using *n-in-n* geometry sensors; with a pixel cell size of $150\,\mathrm{x}\,25\,\mu\mathrm{m}^2$ read out with a new pixel ASIC chip (FE-I5) still in early development. The outer pixel layers and disks will use *n-in-p* geometry sensors, with a pixel cell size of $250\ \mathrm{x}\ 50\,\mu\mathrm{m}^2$ and will be read out with a new version of the IBL FE-I4 chip (FE-I4c) [125]. However, investigations are underway with results discussed in this thesis on using alternative geometry pixel cell sizes while maintaining the FE-I4 bump bonding foot-print or using the FE-I5 at all pixel radii (Chapter 12).

Chapter 5

Physics and Properties of Silicon as a Semiconductors

The purpose of this chapter is to briefly discuss the semiconductor physics relevant to silicon crystals and their use as diodes.

5.1 Crystal Structure

Silicon is an element of the IV-th group of the periodic table, characterised by four electrons in its outermost orbital (valence electrons). Through the formation of covalent bonds it assumes a diamond lattice structure. Pure silicon is too reactive to be found in nature. Instead various crystal growth methods are used to produce mono-crystalline ingots, which are the basic material used to produce silicon sensors. The production techniques utilised will not be discussed here, but a good summary can be found in [127].

Electronic devices and detectors are processed on thin slices (wafers) cut from ingots of crystalline silicon. The lattice orientation of a silicon wafer is determined by the orientation of the seed used to grow the ingot. The crystal orientation is defined by the Miller indices of the cutting plane (wafer surface), denoted by (h,k,l). The notation $< h, k, l >$ refers to the vector perpendicular to the (h,k,l) plane. There are three possible orientations for wafers used to produce silicon detectors, $< 100 >$, $< 110 >$, and $< 111 >$ illustrated in Figure 5.1. The difference between the three orientations lies in the density of unpaired electrons (broken covalent bonds) at the wafer surface. This will influence the electrical properties of the detectors. Typically, $< 111 >$ and $< 100 >$ silicon is used in high energy physics as they are more radiation tolerant compared to $< 110 >$ silicon.

The resistivity (the initial concentration of defects/impurities of a wafer) depends on the crystal growth technique used. For ionising radiation sensors, the resistivity of the crystal should be large in order to reach full depletion in a thick substrate at low bias voltages [128]. Results in this thesis will focus on $< 100 >$ silicon with bulk resistivities of $\sim 10\,k\Omega/cm$.

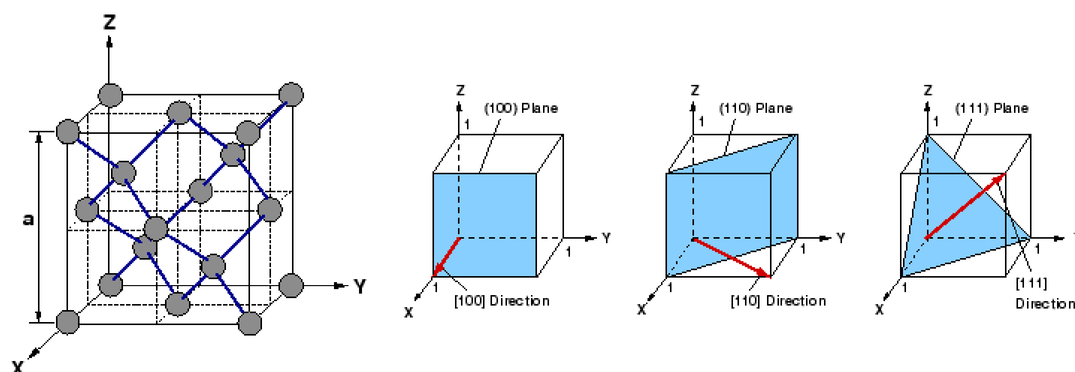

Figure 5.1: From left to right, diamond structure of the silicon crystalline lattice. (100), (110), and (111) lattice orientation planes (blue). The orientations $< 100 >$,$< 110 >$, and $< 111 >$ refer to the perpendicular vector to the corresponding plane [129].

5.2 Energy Bands

Energy bands are formed of a large number of closely spaced discrete energy levels in crystalline materials (such as silicon). The wave functions of electrons in neighbouring energy levels overlap. The Pauli exclusion principal forbids multiple electron energy levels with the quantum properties (such as energy) and therefore a series of closely spaced energy levels is formed. As a result, two energy bands are formed. The valence band and the conduction band. Charge carriers in the valence band are bound to atoms, and are free in the conduction band. The size of the energy gap between these bands is what dictates if a material is an insulator (large energy gap), conductor (no energy gap) or semiconductor (small energy gap). A typical illustration of these energy bands is shown in Figure 5.2.

At room temperature the band gap for high purity silicon is 1.12 eV. Experimental results have shown that the band gaps of silicon (and most semiconductors) decreases with increasing temperature, yielding the following expression for E_g as a function of temperature, T:

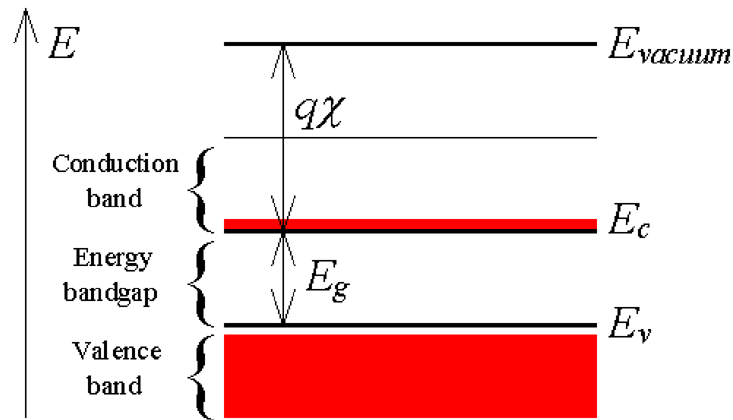

Figure 5.2: Illustration of the energy bands used to describe semiconductors. The valence and conduction bands are indicated by E_v and E_c respectively.

$$E_g(T) = E_g(0) - \frac{\alpha T^2}{T + \beta} \tag{5.1}$$

Where $E_g(0)$, α and β are $1.16\,eV$, $7.02 \cdot 10^{-4}\,k^{-1}$ and $1108\,k$ respectively.

5.3 Carrier Concentration

Semiconductor properties can be altered by introducing controlled amounts of impurities. This process is referred to as “doping”. If the impurities give electrons to the conduction band they are referred to as donors, and if they give holes to the valence band they are referred to as acceptors. The following sections will describe intrinsic (pure) silicon and doped silicon (Section 5.3.1 and Section 5.3.2 respectively).

5.3.1 Intrinsic Silicon

A semiconductor is referred to as intrinsic if the concentration of impurities is lower than the concentration of thermally generated carriers. This last quantity can be calculated by integrating over all valence and conduction band states, taking the density of states and the probability of occupation into account using the Fermi-Dirac distribution. The resulting electron (n) and hole (p) concentrations are, respectively:

$$n = N_c e^{-\frac{E_c - E_F}{kT}} \quad \text{and} \quad p = N_\nu e^{-\frac{E_F - E_\nu}{kT}} \ , \tag{5.2}$$

where N_c and N_ν are the density of the states in the conduction and valence bands respectively, k is the Boltzmann constant, T is the temperature and E_F is the Fermi level. Intrinsic silicon has the Fermi level in the middle of the band gap ($E_c - E_F = E_F - E_\nu$), and equal electron and hole carrier concentrations $n = p = n_i$ because they are produced in equal amounts by thermal excitations.

5.3.2 Doped Silicon

Doping is the addition of controlled amounts of specific impurity atoms to alter the conductivity of the silicon sample by increasing either the electron or hole free carrier concentration. The position of the Fermi level can be written as, if $N_\nu = N_c$:

$$E_F = \frac{E_c + E_\nu}{2} + \frac{kT}{2} ln\left(\frac{N_\nu}{N_c}\right) \quad . \tag{5.3}$$

By introducing small amounts of impurity atoms into a crystal lattice structure, the number of free electrons and holes can be altered. For example, when a group III element like boron is introduced into the crystal structure so that it sits substitutionally on a lattice site. This atom can accept an electron from a neighbouring silicon atom so that it may have a complete set of four valence electrons bonded covalently with its four nearest neighbour silicon atoms. This creates a hole in the valence band without a corresponding electron in the conduction band, called an acceptor state, N_A. The effect of adding boron to the lattice is to shift the Fermi level down towards the valence band. Thus doped silicon is referred to as a p-type semiconductor. Similarly, when a group V element such as phosphorus is added to the silicon crystal structure, it can donate its fifth valence electron to the conduction band so that it has four remaining valence electrons to form four covalent bonds. The donated electron in the conduction band is not balanced by a hole in the valence band, called a donor state, N_D and has the effect of pushing the Fermi level up towards the conduction band is referred to as an n-type semiconductor.

The Fermi level is affected by the doping concentration. It can be calculated from the acceptor and donor concentrations as:

$$E_F = E_\nu + kT\, ln\left(\frac{N_\nu}{N_A}\right) \quad \text{and} \quad E_F = E_c + kT\, ln\left(\frac{N_c}{N_D}\right) \quad . \tag{5.4}$$

By adding such impurities, it is possible to create an excess of one carrier type. For example, doping with a significantly high number of donors $N_D \gg n_i$ makes the material n-type, where the majority of carriers are electrons. Similarly adding acceptors so that $N_A \gg n_i$ gives a p-type material, where the majority of carriers are holes.

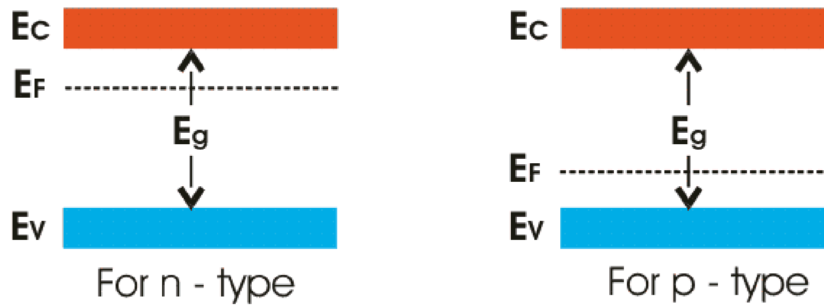

Figure 5.3: Band gap diagram showing the position of the Fermi level E_F with respect to the valence and conduction bands for n-type (left) and p-type (right) semiconductors [130].

Doping atoms introduce energy states in the forbidden band gap. The energy states introduced by group III and V elements are known as shallow levels as they are situated very close to the conduction band in an n-type and to the valence band in a p-type material. This is illustrated in Figure 5.3 for both n- and p-type semiconductors [131]. At room temperature all the impurity (donor or acceptor) atoms can be regarded as being ionised.

5.4 *p-n* Junction

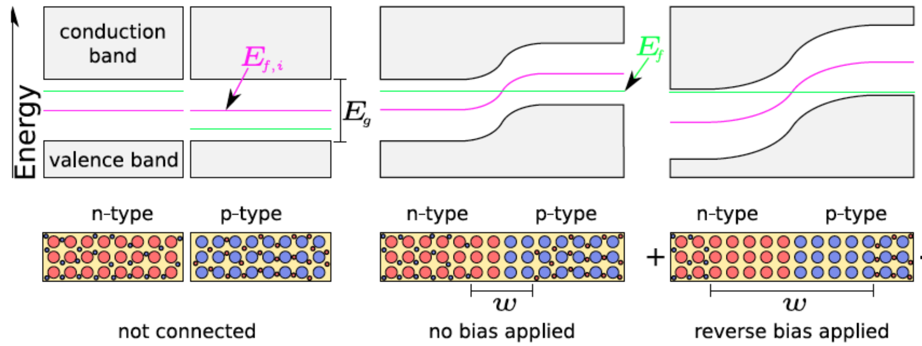

Figure 5.4: Illustration of the working principal of the pn-junction. The upper images show the band structure in both n-type and p-type silicon. The lower images show the acceptor, donors, electrons and holes (large blue, large red, small blue and small red circles respectively) in the doped silicon materials. The width of the depletion region is denoted by w and E_F denotes the Fermi energy level.

The *p-n* junction is formed when *n*-type and *p*-type silicon are in contact with each other. The large carrier concentration gradients at the junction cause carrier diffusion. Holes form the p-side diffuse into the n-side, and electrons from the n-side diffuse into the p-side. As holes continue to leave the p-side, some of the negative acceptors (N_A) near the junction are left uncompensated because acceptors are fixed in the semiconductor lattice, whereas the holes are mobile. Similarly, some of the positive donors (N_D) near the junction are left uncompensated as the electrons leave the n-side. Consequently, a negative space charge forms near the p-side of the junction and a positive space charge forms near the n-side. this space charge region creates an electric field that is directed from the positive charge to the negative charge.

Equilibrium is reached when the junctions potential difference prevents further charge transfer across the junction. This value of the potential is called built in voltage (V_{bi}) . The space charge region around the *p-n* junction now has no free carriers and as such is called the depletion region. Figure 5.4 shows the band diagram for the *p-n* junction. At thermal equilibrium a depletion region with width $W = x_n + x_p$ exists, where x_n and x_p are the widths of the depletion regions in the *n*-type and *p*-type silicon implants respectively. The charge density ρ in the depleted region is given by $\rho = q\,N_A$ in *p*-type silicon and $\rho = q\,N_D$ in *n*-type silicon, where q is the electronic charge with units, e. The electric field in the depleted region can be calculated by solving the one dimensional Poisson equation:

$$\frac{d^2V}{dx^2} = +\frac{qN_A}{\epsilon_{Si}} \tag{5.5}$$

In the p-type $(-x_p \leq x < 0)$ and:

$$\frac{d^2V}{dx^2} = +\frac{qN_D}{\epsilon_{Si}} \tag{5.6}$$

For n-type silicon $(0 \leq x < n_n)$, where ϵ_{Si} is the permittivity of silicon. Given the electric field $E = -\frac{dV}{dx}$ and using the boundary conditions that $E = 0$ at the limits of the depletion region, the electric field value $E(x)$ can be calculated, where the maximum field occurs at $x = 0$, with value:

$$E_{max} = \frac{qN_A x_p}{\epsilon_{Si}} = \frac{qN_D x_p}{\epsilon_{Si}} \tag{5.7}$$

Since the built in voltage V_{bi} is the integral of the electric field distribution across the junction [131], the width of the depletion region can be calculated as:

$$W = \sqrt{\frac{2\epsilon_{Si}}{q}\left(\frac{N_A + N_D}{N_A N_D} V_{bi}\right)} \ , \tag{5.8}$$

for a two-sided abrupt junction. This reduces to:

$$W = \sqrt{\frac{2\epsilon_{si} V_{bi}}{qN_B}} \ , \tag{5.9}$$

for a one-sided abrupt junction.

5.5 *p-n* Junction Diode Characteristics

If an external voltage with the same sign as the built in voltage V_{bi} (reverse bias) is applied to a *p-n* junction diode, the width of the depletion region increases. If the external voltage has the reverse polarity of the built in voltage V_{bi} (forward bias), then the width of the depletion region shrinks [133]. Typical current-voltage (IV) characteristics for an ideal *p-n* junction diode operating under reverse bias are shown in Figure 5.5

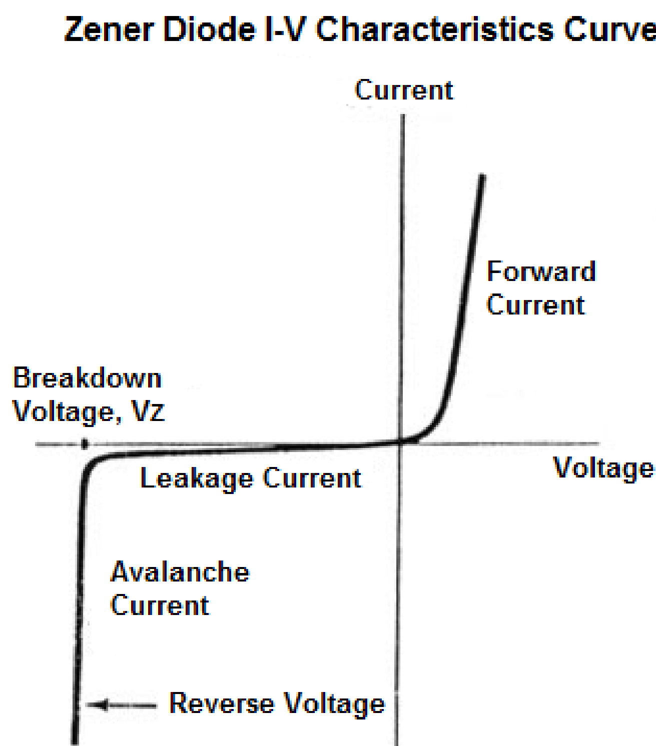

Figure 5.5: Typical current voltage (IV) characteristics for an ideal *p-n* junction diode under reverse bias.

In forward bias, when the applied external voltage compensates for the built in voltage of the *p-n* junction, the current rapidly increases. This is caused by the diffusion current being larger than the drift current. When the diode is operated with reverse bias, the current remain very low until breakdown. At this point the current increases drastically due to avalanche breakdown. This occurs when the electric field reaches values of $\sim 300\,\mathrm{kV/cm}$ [131].

When a voltage V is applied to the junction, the total electrostatic potential variation across the junction is given by $(V_{bi} + V)$ for reverse bias and $(V_{bi} - V)$ for forward bias.

Substituting these voltages values in Equation (5.9) yields the depletion layer width as a function of the applied voltage for a one-sided abrupt junction ($N_A \gg N_D$ or $N_D \gg N_A$):

$$W = \sqrt{\frac{2\epsilon_{Si}}{qN_B}\,(V_{Bi} + V)}\ , \tag{5.10}$$

because the depletion layer width of one side is significantly smaller than the other (i.e. $x_p \gg x_n$). N_B is the bulk doping concentration (concentration of the bulk material) and V is the applied bias voltage. This equation can be rearranged to define an equation to calculate the depletion voltage V_D required to deplete a thickness $W = d$ of silicon,

$$V_D = \frac{qN_B}{2\epsilon_{Si}}\,d^2 - V_{bi}\ . \tag{5.11}$$

High energy physics silicon particle detectors are always operated in reverse bias mode. Devices fabricated by Micron Semiconductors Ltd typically have depletion voltages of $\sim 80\,\mathrm{V}$ for $300\,\mu\mathrm{m}$ thick, $10\,\mathrm{k}\Omega$ bulk resistivity devices.

The depleted layer within the detector may be treated as a dielectric, so in practice a *p*-*n* junction diode is a voltage dependant capacitor when operated in reverse bias. The capacitance C per unit area may be written as:

$$C = \frac{\mathrm{d}Q}{\mathrm{d}V}\ , \tag{5.12}$$

where dQ is the incremental increase in charge per unit area upon an incremental change of the applied voltage dV. For a one-sided abrupt junction the capacitance is given by:

$$C = \frac{\mathrm{d}Q}{\mathrm{d}V} = \frac{\mathrm{d}(qN_BW)}{\mathrm{d}[(qN_B/2\epsilon_{si})W^2]}\ , \tag{5.13}$$

$$C = \sqrt{\frac{q\epsilon_{Si}N_B}{2(V_{bi} + V)}} \ . \tag{5.14}$$

Plotting $1/C^2$ as a function of applied bias voltage for a device allows for the determination of the its depletion voltage (V_D). The resulting plot is characterised by a linear increase with bias voltage until a saturation point is reached. Indicating that the device is fully depleted and the point of saturation is the full depletion voltage. In the remainder of this thesis this technique has been used to determine a device's depletion point even if this is not explicitly shown or said.

5.6 Temperature Effects

The ideal reverse saturation current density is a function of the thermal equilibrium minor carrier concentrations (n_{p0} and p_{p0}). These carrier concentrations are proportional to n_i^2. Therefore the current density has a strong temperature dependance. For a silicon *p-n* junction, the ideal reverse current density will increase by approximately a factor of four for every 10 °C increase in temperature. Similarly, the forward bias current is temperature dependant. However, the change in forward bias current with temperature is less sensitive than that of the reverse current [134].

5.7 Junction Breakdown

When a sufficiently high electric field is applied to a *p-n* junction, the junction “breaks down” and conducts a very large current. Three breakdown mechanisms will be briefly discussed: thermal instability, tunnelling instability and avalanche multiplication.

5.7.1 Thermal Instability

Breakdown due to thermal instability in semiconductors is a major cause of device failure and it is the main reason for cooling in high energy physics tracking detectors to remain below room temperature during operation. A device’s reverse bias generates a reverse current, which can increase with voltage (and temperature). The reverse current generates heat and the whole crystals temperature increases. This in turn increases the reverse current. This process can be stabilised by providing sufficient cooling to reduce the reverse current or to lower the bias voltage. However, when very high currents are unavoidable thermal instability can cause thermal runaway. Thermal runaway is a process in which the cycle of reverse current $\rightarrow$ temperature increase $\rightarrow$ reverse current increase becomes unstoppable, using the available cooling power. At this point the reverse current of a device increases exponentially [133].

5.7.2 Tunnelling Instability (Zener break-down)

Zener breakdown is characterised by a significant current flow between energy bands via the tunnelling process. In a highly doped junction, the conduction and valence bands on opposite sides of the junction are sufficiently close during reverse bias that electrons may tunnel directly from the valence band on the p-side into the conduction band on the n-side. This effect only occurs as a devices internal electric field gradient approaches 10^6 V/cm in silicon. The tunnelling current density is given by:

$$J_t = \frac{\sqrt{2m^*}q^3\varepsilon V}{4\pi^2\hbar^2 E_g^{1/2}} \exp\left(-\frac{4\sqrt{2m^*}E_g^{3/2}}{3q\varepsilon\hbar}\right) , \tag{5.15}$$

where ε is the electric field at the junction, E_g the band gap, V the applied voltage, and m^* the effective electron mass.

This mechanism is easily distinguishable from avalanche multiplication because of its negative temperature coefficient, i.e. the breakdown voltage decreases with increasing temperature [133].

5.7.3 Avalanche Multiplication

The avalanche multiplication effect (or impact ionisation) is the most important mechanism in junction breakdown. This is because the avalanche breakdown voltage imposes an upper limit on the reverse voltage for most semiconductor devices (diodes). A thermally generated electron in the depletion region gains kinetic energy from the electric field. If the field is sufficiently high, the electron can gain enough kinetic energy that on collision with an atom, it can break the lattice bonds, creating an electron-hole pair. The newly created electron and hole both acquire kinetic energy from the field generating further electron-hole pairs.

Assuming all conditions for avalanche multiplication have been met (high electric field), the electron current I_n will increase with distance through the depletion region to reach a value of $M_n I_{n0}$ at W, where M_n is the multiplication factor defined as

$$M_n \equiv \frac{I_n(W)}{I_{no}} \; . \tag{5.16}$$

Similarly the hole current will increase from $x = W$ to $x = 0$.

Given that the avalanche breakdown voltage is defined as the voltage at which M_n approaches infinity and knowing the field dependence of the ionisation rates, the critical field (maximum electric field at breakdown) can be calculated [133]. This combined with Poisson's equation allows for the calculation of the breakdown voltage, V_B for one-sided abrupt junctions:

$$V_B = \frac{\varepsilon_c W}{2} = \frac{\epsilon_s \varepsilon_c^2}{2q} \left(N_B\right)^{-1} \tag{5.17}$$

This effect is of particular interest for detectors that have to be very radiation tolerant. Radiation tolerant devices are often designed to be operated at very high bias voltages to reach full or partial depletion. In fact, soft charge multiplication in electron collecting detectors has been seen after irradiation at very high bias voltages, increasing the signal and improving the performance of the devices. Significant work has been dedicated to explore the effects of charge multiplication and to enhance and control the process (Section 10.3 and Section 10.6).

Chapter 6

p-n Junction as a Particle Detector

High resolution silicon detectors are used in high energy physics to track particle trajectories. These detectors are all based on the p-n junction (see Section 5.4). The p-n junction can function as a particle detector whilst operated in reverse bias mode, either fully or partially depleted. Particles which traverse and interact within the depleted region generate charge carriers. The potential difference across the device drifts these carriers to either side of the junction, electrons $\rightarrow n^+$ and holes $\rightarrow p^+$ where n^+ and p^+ refer to very high concentrations of dopants in each type of silicon. The charge collected at either end of the junction can be read out (using amplifying electronics). The readout side of the junction can then be segmented to provide the required spatial hit resolution. A schematic diagram of a silicon particle detector is given in Figure 6.1.

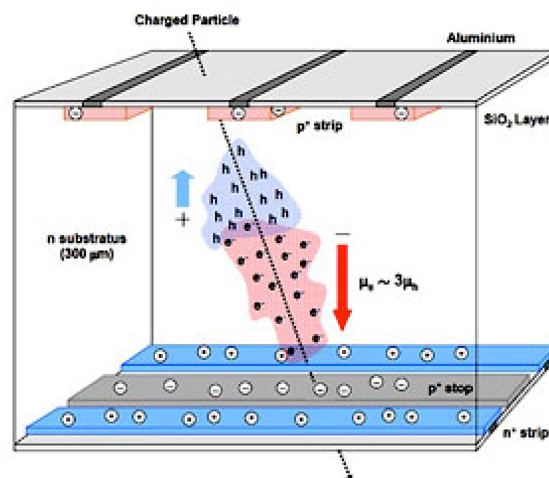

Figure 6.1: Illustration of charge deposition from a particle within a double-sided silicon micro-strip detector.

Details on traditional types of segmentation for particle detectors are given in Section 6.1, followed by a description of charged and neutral particle energy loss (Section 6.2) and signal generation (Section 6.3) in silicon detectors.

6.1 Segmentation

In order to realise high resolution trajectory measurements, fine segmentation of the readout electrodes is needed. There are two main types of segmentation widely used is particle physics experiments, pixels and micro-strips.

Devices with a strip or micro-strip structure use long rectangular readout electrodes. To give an idea of its typical size, a typical micro-strip detector could feature electrodes $10\,\mu$m wide with a pitch of around $100\,\mu$m with lengths varying depending on the device longitudinal size. This segmentation doesn't allow for two dimensional hits to be measured with a single device. Instead, multiple layers of devices are needed, with some of the devices rotated with respect to each other.

Pixelated devices use smaller electrode structures than strip or micro-strip detectors, but they can vary in size and shape depending on their use. Pixels are arranged in a regular two dimensional array, creating a grid like structure. This allows for the determination of two dimensional hit information from a single device. The readout electrode density is much higher compared to strip or micro-strip structures, which adds readout complications.

The major drawback from using pixel segmentation in devices is the added readout complication. Since strip and micro-strip electrodes are typically as long as the detector, the readout electronics can be positioned at one or either ends of the sensor. Pixelated detectors need a different arrangement for the readout electronics. The readout chip has the same or similar readout channel grid structure as the detectors electrode grid structure. This has a number of consequences:

- The readout chip needs to be directly attached to the sensor, as each detector electrode has to be connected to the relevant readout channel.
- The readout chip has to be more advanced due to the high channel density and the need for a larger readout bandwidth. This necessitates the use of smaller transistor technology which increases production costs

Nonetheless, particle physics central trackers require very high channel granularity to separate high multiplicity events very close to the interaction points. This is not possible using strip or micro-strip trackers. The ability of pixel detectors to measure two spatial coordinates of hits with a single device also reduces the number of detector layers needed, which is especially important close to the interaction point where space is limited and material has to be reduced to mitigate the effect of multiple coulomb scattering on the charged particles tracks.

6.2 Energy Loss of Particles

In order to be detected a particle must interact with the material and transfer energy to the detector. Different types of particles interact in different ways with matter. Charged particles primarily lose energy due to ionisation and radiative effects such as Bremsstrahlung and Cherenkov radiation. Hadrons additionally can undergo nuclear interactions while photons interact via the photo-electric effect, Compton scattering and pair production. Figure 6.2 illustrates some examples of the most important energy loss mechanisms exploited by silicon tracking detectors. They are described in the following sections for charged particles, photons and Hadrons respectively.

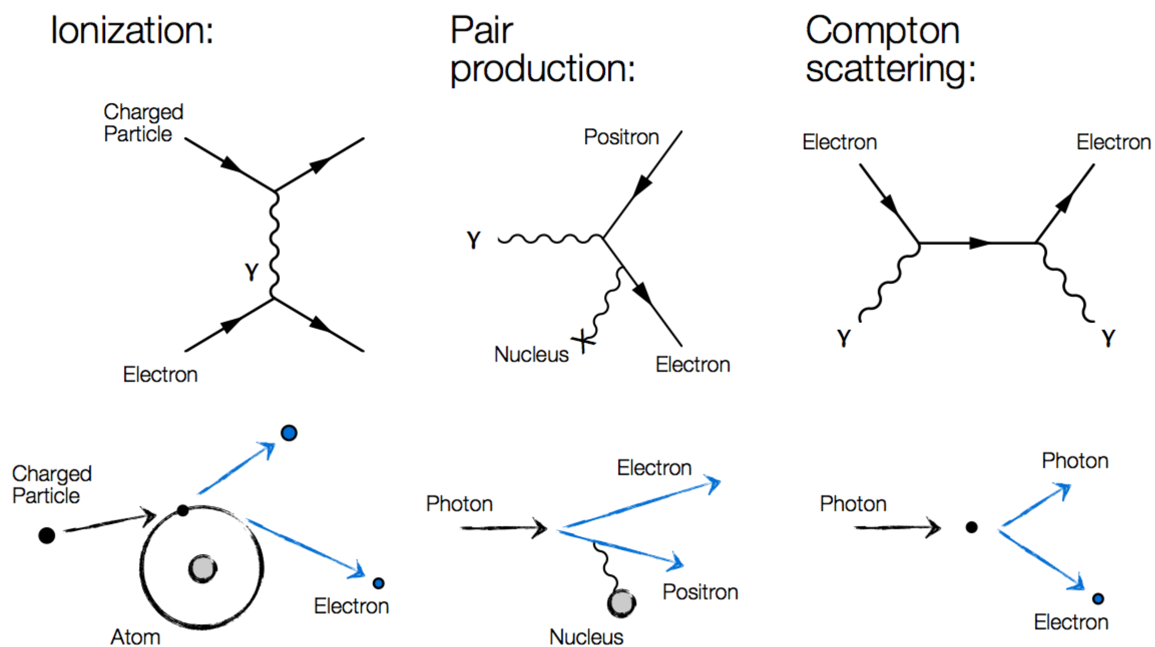

Figure 6.2: Illustration of the three main energy loss modes in a silicon tracking detector. Left, Ionisation, middle, pair production and right, Compton scattering.

6.2.1 Heavy Charged Particles

If a charged particle with a mass well above the electron mass ($M \gg m_e$) penetrates matter, the main energy loss process is ionisation, creating electron-hole pairs. The amount of energy lost per unit distance at high energies through ionisation is dominated by elastic collisions with electrons in the material and is described by the Bethe-Bloch formula [135]:

$$-\left(\frac{dE}{dx}\right) = 2\pi N_A r_e^2 m_e c^2 \rho \frac{Z}{A}\frac{z^2}{\beta^2}\left\{ln\left(\frac{2m_e c^2\beta^2\gamma^2 W_{max}}{I^2}\right) - 2\beta^2 - \delta - 2\frac{C}{Z}\right\} \tag{6.1}$$

With:

r_e: The classical electron radius
m_e: The electron mass
N_A: Avagadro's number
I: mean excitation potential
Z: The atomic number of the absorbing material
A: The atomic weight of the absorbing material
ρ: The density of the absorbing material
z: The charge of the incident particle in units of e
δ: Density correction
C: Shell correction
W_{max}: The maximum energy transfer in a single collision

The Bethe-Bloch formula has a minimum at $\beta\gamma \approx 3.5$ which corresponds to an energy loss of $\left(\frac{dE}{dx}\right) \approx 1.5$ MeV $cm^2\, g^{-1}$. Particles with a momentum corresponding to energy losses close to this value are called Minimum Ionising Particles (MIPs).

At higher energies radiative energy loss becomes more important, such as muons. Electromagnetic radiation (Bremsstrahlung) is emitted if charged particles are accelerated in the Coulomb field of a nucleus, as illustrated in Figure 6.3.

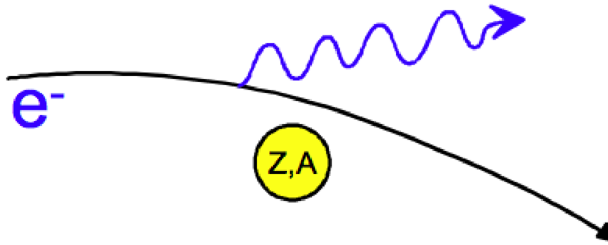

Figure 6.3: Illustration of Bremsstrahlung generation.

A summary of the total energy loss for muons in copper as a function of momentum is shown in Figure 6.4. Energy losses described at small energies (MeV/c), below the minimum ionisation point are not relevant to this thesis and will not be discussed.

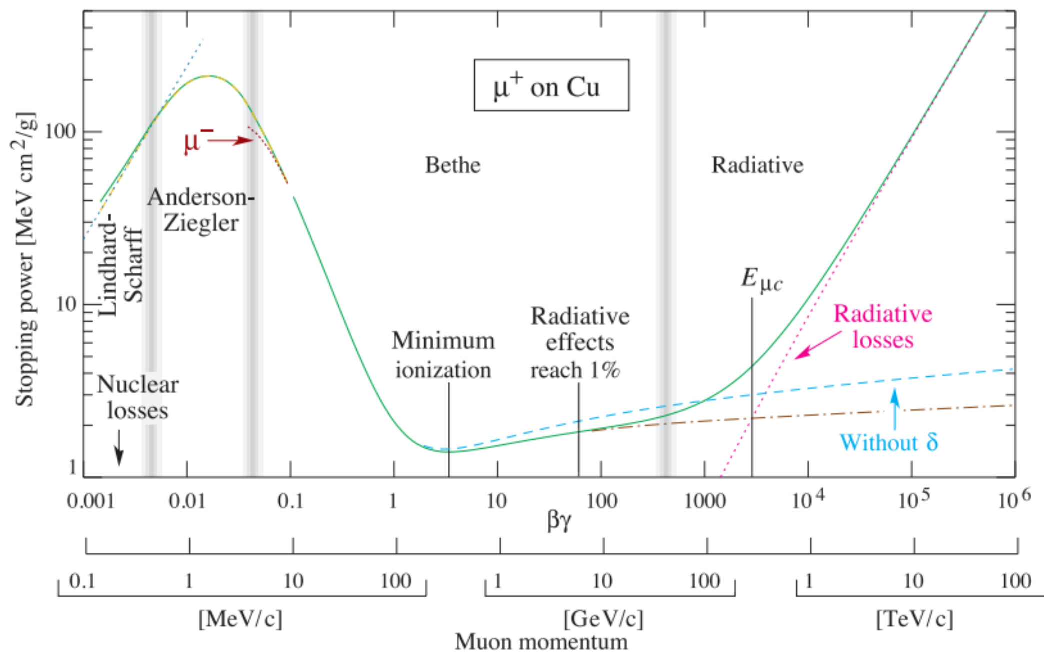

Figure 6.4: Stopping power $-\left(\frac{dE}{dx}\right)$ for positive muons (anti-muon) in copper as a function of $\beta\gamma = p/Mc$ over nine orders of magnitude in the muon momentum. The solid curve indicates the total stopping power [136].

6.2.2 Electrons and Photons

High-energy electrons (and positrons) predominantly lose energy in matter by bremsstrahlung, and high-energy photons by pair production. The characteristic amount of matter traversed for these related interactions is called the radiation length X_0. It is characterised as both (a) the mean distance over which a high-energy electron loses all but $1/e$ of its energy by bremsstrahlung, and (b) 7/9 of the mean free path for pair production by a high-energy photon [137].

Electrons

At low energies electrons and positrons primarily lose energy by ionisation, although other processes (Moller scattering, Bhabha scattering, e^+ annihilation) contribute, as shown in Figure 6.5 where lead is the stopping material. While ionisation loss rates rise logarithmically with energy, bremsstrahlung losses rise nearly linearly (fractional loss is nearly independent of energy), and dominates above a few tens of MeV in most materials [137].

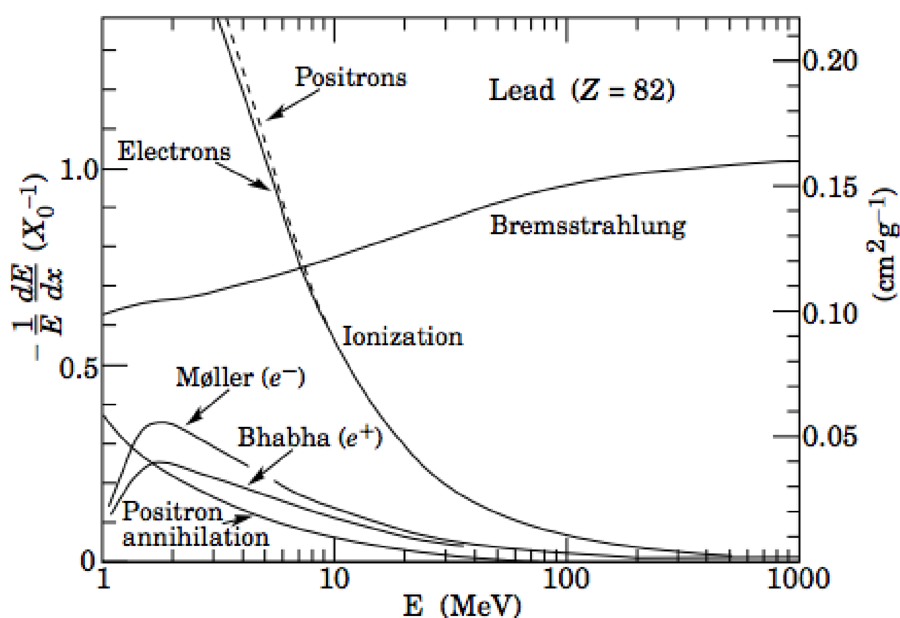

Figure 6.5: Fractional energy loss per radiation length in lead as a function of electron or positron energy. Electron (positron) scattering is considered as ionisation when the energy loss per collision is below 0.255 MeV, and as Moller (Bhabha) scattering when it is above [137].

Photons

Photons behave differently compared to charge particles when they interact with matter. The photon is massless and chargeless and interacts primarily via the following processes:

- **Photo-electric effect:** An electron is emitted by absorbing a photon with energy greater than or equal to the binding energy of the electron. Any extra energy contributes to the kinetic energy of the electron. If the photon energy is between $O(eV)$ and $O(100\,\text{keV})$, the photoelectric effect is the dominant process.
- **Compton scattering:** The photons scatter off quasi-free electrons, transferring some of their energy to the electrons they scatter from.
- **Pair production:** This is the creation of an electron-positron pair after the interaction of a photon with sufficient energy with a nucleus. For photons with energy greater than twice the electron mass $O(\text{MeV})$, pair production is the most important process.

The cross-section of these processes depend on the material and the energy of the photons. A beam of photons will be attenuated as they pass through matter, the intensity of the photon beam decreases exponentially as:

$$I(x) = I_0 e^{-\mu x} \tag{6.2}$$

Where x is the material thickness, I_0 the initial intensity and μ the material specific and energy dependant mass attenuation coefficient.

6.2.3 Neutral and Charged Hadrons

Neutral hadrons can interact through nuclear interactions. The total hadron-nucleon interaction cross-section is composed of three components:

$$\sigma_{total} = \sigma_{elastic} + \sigma_{quasi-elastic} + \sigma_{inelastic} \tag{6.3}$$

Where only inelastic interactions (absorption interactions) are responsible for hadron attenuation in matter. Elastic scattering occurs when energy (kinetic) is transferred from one object to another, leaving the incident and target particles intact. If the amount of energy transferred between incident and target particle is small relative to the incident energy and all constituents remain unchanged the interaction is characterised as being quasi-elastic.

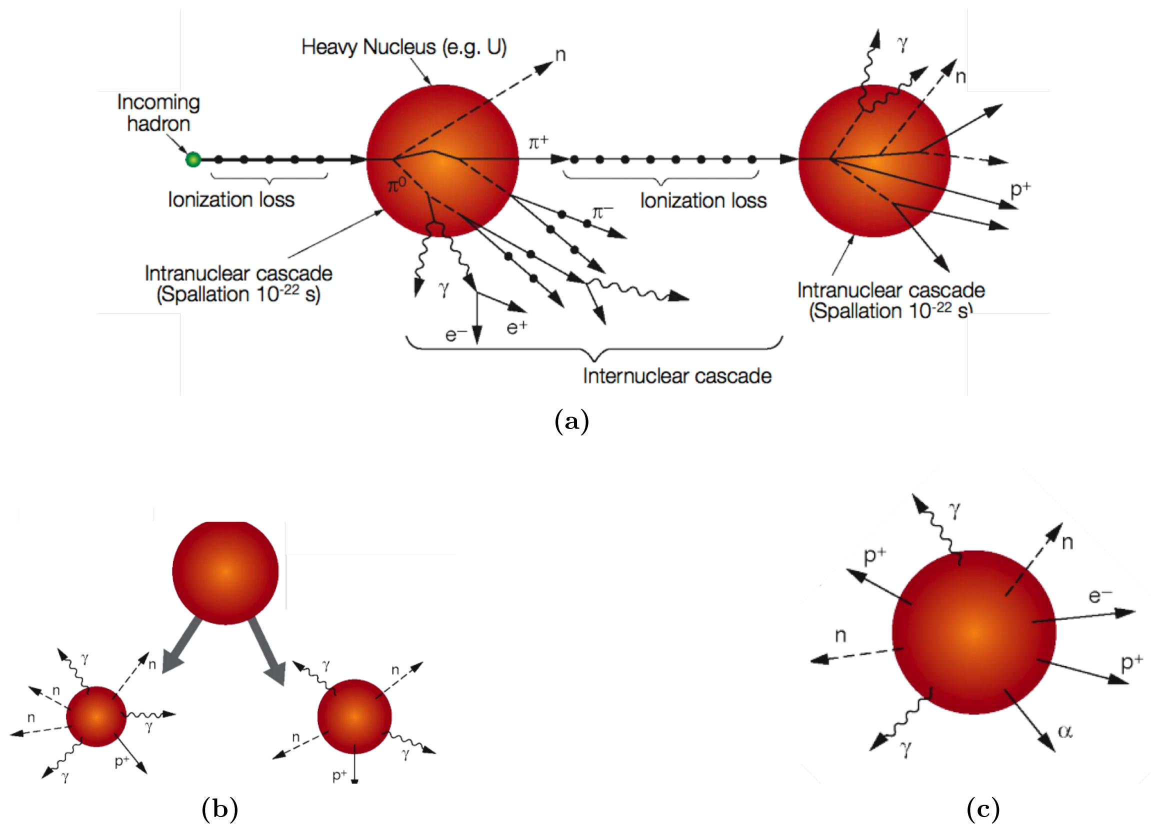

Figure 6.6: Illustrations of three elastic methods by which hadrons lose energy with matter. (a) Intra- and Inter-nuclear cascades, (b) nuclear fission and (c) nuclear evaporation.

The three main inelastic processes are inter- and intra-nuclear cascades, nuclear fission and nuclear evaporation which are illustrated in Figure 6.6a, Figure 6.6b and Figure 6.6c respectively. Intra-nuclear interactions occur when energy is transferred to the nucleons of a nucleus (via strong/electro-weak processes), which is then redistributed to other nucleons via a cascade process. Particles that escape the nucleus and therefore reduce the overall energy of the nucleus are referred to as inter-nuclear cascades. Nuclear fission and evaporation can occur when the incident energy transfer from the target nucleons is fully distributed leaving the nucleus in an excited state. The nucleus can then split into two or more smaller nuclei or can radiate the extra energy in the form of neutral and charged particles until it is energetically stable.

6.3 Signal Generation

The most important effects for the operation of silicon detectors in high energy physics experiments are thermal excitations and electron-hole pair generation by charged particles. However electron-hole pair generation can also happen through via photon interactions.

The signal generation by charged particles originates from ionisation of the particles with the silicon crystal lattice, creating electron-hole pair for every 3.6 eV of energy loss. However, the number of collisions and energy transferred for a given charged particle is not constant due to statistical fluctuations. The resulting energy spectrum is described by a Landau distribution, shown in Figure 6.7 for particles that have enough energy to easily pass through the detector. The peak of the distribution defines the Most Probable Value (MPV) of the energy loss. The mean energy deposited in the device is always greater than the MPV, because large energy deposits associated with δ rays (also known as δ electrons) create long tails on the distribution.

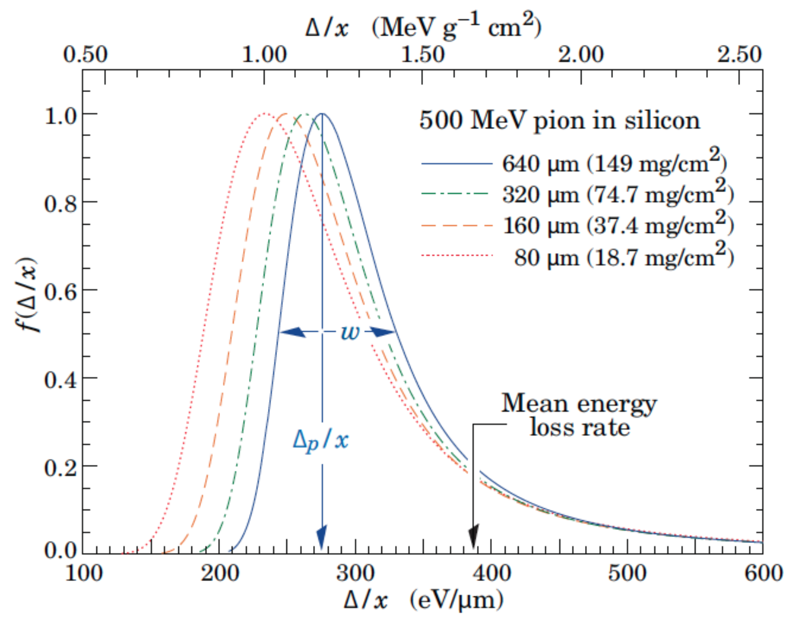

Figure 6.7: Probability distribution for charge deposition for 500 MeV pions in varying thickness materials, normalised to unity at the MPV Δ_p/x [137, 138].

Chapter 7

Sensor Design Aspects

7.1 Sensor Layout Variants

The following will describe variations in silicon sensor layouts, commonly used for high energy physics particle detectors. Only silicon technologies that readout electrons of the n doped side are discussed, *n-in-n* and *n-in-p* technologies are discussed in Section 7.1.1 and Section 7.1.2 respectively. Another popular technology variant widely used in high energy physics, is the *p-in-n* type. However, this variant reads out the hole current signal. The work in this thesis is focused on radiation tolerant devices intended for use within ATLAS at the HL-LHC. The latter technology is not be discussed, because of its rapid deterioration in performance after irradiation. Further details on the enhanced radiation tolerance of n-side readout detectors are given in Chapter 8.

All the work within this thesis focusses on planar silicon detectors. Planar refers to the electrode implantation depth compared to the thickness of the silicon substrate. Typically, electrodes are implanted with a depth of a few microns. When electrode depths are comparable to the substrate thickness, devices are referred to as 3D.

7.1.1 *n-in-n*

A planar *n-in-n* sensor consists of a lightly n-doped ($10^{13}\,cm^{-3}$) substrate, with segmented n^+ implantation on the frontside and one large p^+ implant on the backside. In this context n^+ and p^+ implants have high doping concentrations ($10^{15}\,cm^{-3}$). A negative bias voltage is connected to the p-doped electrode on the backplane, which is surrounded by multiple guard rings (Section 7.2).

Under reverse bias the depletion region extends from the backside p^+ implant propagating to the front of the device where the readout electrodes are located. The n^+ electrodes are only isolated from each other at full depletion. This is shown in Figure 7.1(a). *n-in-n* geometry devices undergo type inversion of the bulk from n- to p-type after sufficient radiation damage (see Section 8.5). After this the depletion region extends from the frontside n^+ readout electrodes to the p^+ implant on reverse side of the detector. Now the pixels n^+ electrodes are isolated from each other even if the device is not fully depleted. This is shown in Figure 7.1(b).

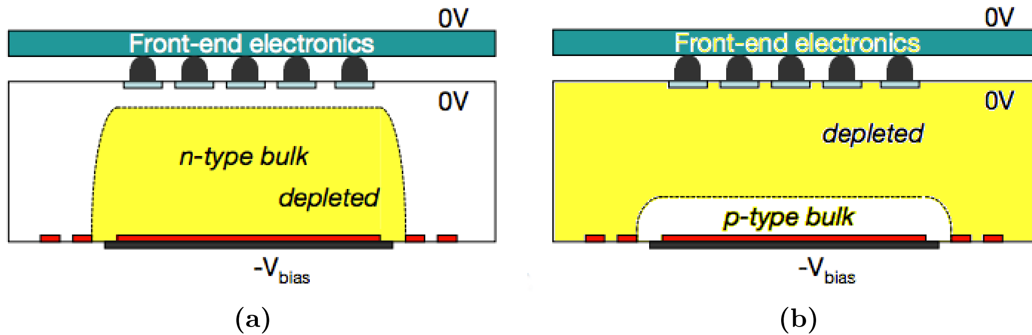

Figure 7.1: Development of the depletion zone (yellow) in an *n-in-n* sensor before (a) and after (b) type inversion. The depletion zone grows from different sides of the sensor. Before type inversion, the depletion region extends from the backside p^+ implant, after type inversion it extends from the frontside n^+ pixel side. This allows efficient operation of *n-in-n* devices even if they are only partly depleted [81].

n-in-n detectors collect the charge from electrons at the readout electrodes. This makes this design more radiation tolerant compared to devices that collect charge using holes, because electrons have a higher carrier mobility than holes. The effect of type inversion also helps to make *n-in-n* geometry more very radiation tolerant, since even when the maximum applied bias voltage is insufficient to reach full depletion the area

surrounding the readout electrodes is still depleted enabling the generated charge to be collected faster.

7.1.2 *n-in-p*

Planar pixel sensors which feature a p-type bulk and n^+ implants on the frontside and a large p^+ implant on the back side, are named *n-in-p* sensors [139]. There are no guard rings on the reverse side of the device, instead guard rings are implemented on the frontside of the device. The reverse side is totally covered by a homogeneous p^+ implant. A schematic view of an *n-in-p* detector is illustrated in Figure 7.2.

Since the bulk material is p-type, there is no type inversion after irradiation. The junction is between the frontside n^+ electrodes and the p-type bulk, with the depletion region extending from the front side. This design is simpler to produce, test and operate. The main draw back with this technology are the large surface currents that form on the frontside edges because of the conductive cut edges. This effect is negligible unless the device is irradiated and can be a major issue for pixel modules, because there is often a large potential between the surfaces of the readout chip (GND) and sensor (HV) which is illustrated in Figure 7.2.

Making radiation hard sensors that are cost effective is very important. The size of future pixel detectors will depend on the cost per unit area. For large area pixel detectors these costs need to be contained and as such *n-in-p* devices are extensively studied in this thesis.

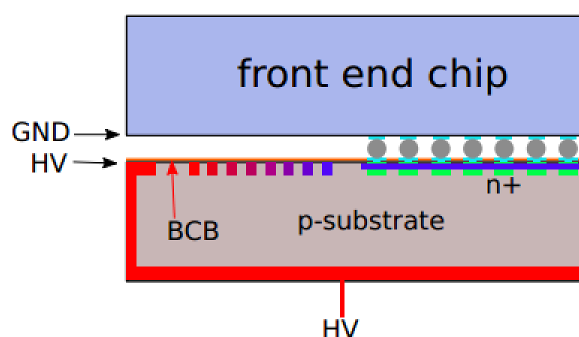

Figure 7.2: Schematic view of a *n-in-p* sensor, illustrating the different potentials between the sensor (HV) and the front-end chip (GND) [104].

7.2 Guard Rings

The purpose of a multi-guard ring structure is to establish a gradual voltage drop between the sensitive region (readout implants) which is at ground potential and the cut edge which has the same potential as the backside implant (where HV is applied). The cut sides are considered to be highly conductive because of damage that is caused while separating (cutting) individual sensors on wafers. The presence of guard rings limits the electric field at the sensor edge, avoiding subsequent breakdown and preventing the depletion region from extending into the edge region.

All but the innermost guard ring which is also referred to as the bias ring are left floating. These floating guard rings are self-biasing via the tunnelling mechanism utilised in punch through bias structures. The spacing of the guard rings and their metal (field plate) overlap influences the voltage drop between guard rings. Field plates that extend outwards from the implant reduce the electric fields at the edge region. This is a common technique used in electronics since the 1960's [140]. The number of guard rings needed depends on a devices' operating voltage before and after radiation damage. The RD50 standard guard ring structure will be used as the baseline. Any variation from this guard ring geometry is explicitly stated. Guard rings are typically placed on the same side of the *p*-*n*-junction i.e. front side on a *n-in-p* sensor and on the backside of a *n-in-n* sensor, see Figure 7.3. To implement guard rings on *n-in-n* sensors a double sided process is required, which is more difficult and therefore more costly than the single sided processed required for *n-in-p* sensors.

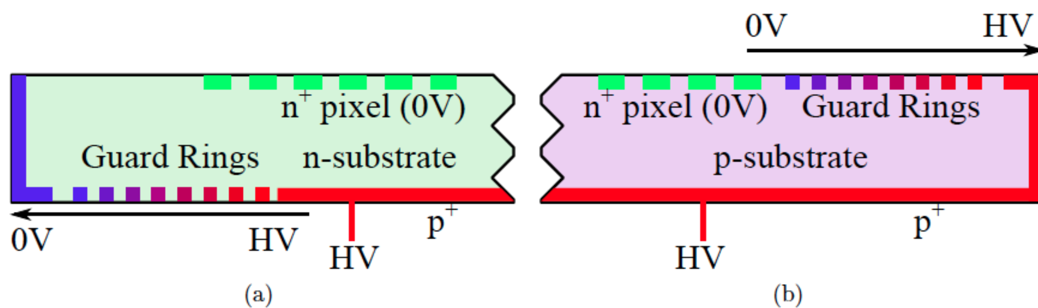

Figure 7.3: Schematic of the electric potential distribution for (a) *n-in-n* sensors and for (b) *n-in-p* sensors. The $^+$ sign indicates a higher doping concentration.

7.3 AC vs DC coupled readout

Each strip or pixel of a silicon sensor must be connected to its own readout channel. This can be done in two different ways, using DC or AC coupling. In DC coupled devices there is a direct connection from the implanted strip or pixel to the amplifier. This implies that the amplifier must sink a fraction of the detector leakage current that corresponds to that strip or pixel, increasing its noise. The leakage current depends on the applied bias voltage, radiation damage and substrate thickness. It is difficult to build an amplifier that can handle such a wide range of input currents. The solution is to adopt AC coupling where the leakage current passes through a resistor and the signal component is collected through a coupling capacitor, reducing noise increases due to high sensor leakage currents. AC coupling is the preferred technique for high energy physics detector readout. Schematic layouts of AC and DC coupled devices are illustrated in Figure 7.4b and Figure 7.4a respectively.

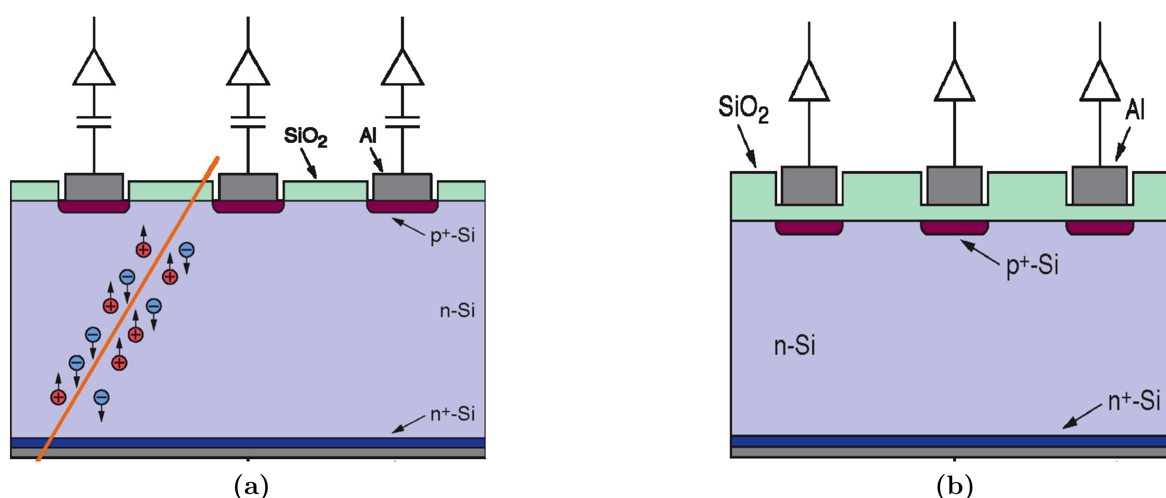

Figure 7.4: Schematics for (a) DC coupled and (b) AC coupled detectors.

7.4 Powering Options

In order to measure the current-voltage (IV) characteristics, high voltage with relevant polarity for reverse biasing, is applied to a detector backside implant. The readout implants then have to be grounded to complete the electrical circuit. The easiest way to achieve this would be to connect all implants to the first guard ring, which is also referred to as the bias ring. Creating a direct connection between every readout implant and

the bias ring however, would short them all together removing the design segmentation. There are two common methods to prevent this effect: biasing through poly silicon resistors (PSR) or punch through bias structures (PTB). PSRs are defined by planar photolithography and are made with high resistivity poly-silicon. Each readout electrode is connected to the bias ring by one PSR. This is the main solution adopted with micro-strip sensors. The high density of channels in pixelated detectors require a metal ground distribution grid (bias rails) to connect the PSRs to individual pixels. It is very important that all PSRs used have similar resistance values (narrow spread around the nominal value) to guarantee a homogeneous power distribution across the device. Typical poly silicon resistor values are around $1\,M\Omega$ [141]. Punch through bias structures (PTBs) consists of small implants of the same type as the readout implants separated by a small distance. Each PTB implant is connected to a metal bias rail connected to the bias ring. These structures utilise the tunnelling effect to achieve a current from the bias structure to the readout implants.

Both powering methods have drawbacks. The PSRs, while being a surface process that doesn't interfere with the implant structure, require extra processing time. PTBs require alterations to the strip/pixel implant structures, and have been found to increase device reverse currents, because they are usually made as small as possible they often feature jagged edges after processing which generate high field regions. Furthermore, since each biasing implant generates its own electric field similar to the readout implants, they will parasitically collect charge during operation and because they are not readout this charge is lost. Typically strip / micro-strip sensors have there biasing structures at one edge next to the bias ring. For pixelated devices, each readout implant either requires its own biasing structure or shares on between its nearest neighbours. The characterisation of devices with the same readout implant structure which uses either of these methods is discussed in Chapter 12, where more details are given. CAD drawings of the structures are also shown.

7.5 Inter-Pixel Isolation

Inter-pixel isolation is required for devices with n^+ readout electrodes within a p-type bulk because of the formation of a permanent electron accumulation layer at the silicon to silicon dioxide interface regions. This electron accumulation layer is a by-product of the processing techniques used and is caused by the dielectric layer on top of the

silicon trapping positive ions during the detector processing steps. This effect is also be caused by ionising radiation and made worse because more static positive charge builds up in the dielectric, until saturation is reached at approximately $2 \cdot 10^{12}$ ions cm^{-3}. The positively charged oxide attracts electrons at the interface with the silicon, forming the accumulation layer. This electron accumulation layer connects all the readout implants together, essentially creating a diode. In contrast, if the readout electrodes are p^+ implants then this accumulation layer would act to isolate the readout electrodes [140].

To isolate the n^+ readout electrodes from each other, p-type doping is implanted between the n^+ readout electrodes to create a static negative charge that removes the electrons at the interface. Choosing the isolation geometry and the implant parameters involves a compromise between strong isolation and lower breakdown voltage. The higher the isolation implant doping concentration, the stronger the isolation is. However, high concentrations of p-type implants can cause high field regions at their edge. This can cause early device breakdown if the electric fields at the reaches $\sim 300\,\mathrm{kV/cm}$ [142]. There are three commonly used methods for isolating n^+ implants in *n-in-n* and *n-in-p* devices, they are: homogeneous p-spray, p-stop and moderated p-spray. These three methods are illustrated in Figure 7.5.

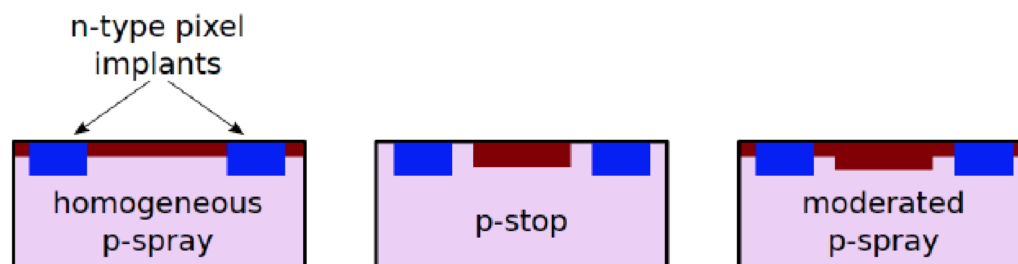

Figure 7.5: Three common forms of inter-pixel isolations: p-spray, p-stop and moderated p-spray. The n-type pixels are marked in blue and the p-type isolation is coloured in red [143].

The homogeneous p-spray option uses an unstructured implant with a relatively low concentration over the whole sensor area. This is the easiest to implement during processing, but it leads to a direct contact between the n-type pixel implant and the p-spray implant. This can cause sensor break down during normal sensor operation if the concentration of the p-spray is too high. P-stop isolation is achieved by implanting distinct p-type implants between the n^+ readout implants. These implants can either be separate or linked together. This method requires an extra processing step during production as the p^+ implants require their own mask stage. The p-stop isolation implant

uses a higher doping concentration compared to the p-spray method. Since the doping concentration is high the placement of the p^+ implants must be very accurate. If the p^+ isolation implant and the n^+ readout implant touch or overlap a p-n-junction would be formed, creating a high electric field.

The moderated p-spray method is a hybrid method that features the advantages of the homogeneous p-spray and p-stop methods and requires the same amount of processing steps as the p-stop method. A central p-stop is implanted into a p-spray region. This has the advantage of having good isolation, but since it is surrounded by p-spray the electric fields produced at the interfaces are severely reduced [142].

Chapter 8

The Effects of Radiation Damage on Detector Performance

This section discusses the effects of irradiation on silicon detectors. Particles passing through the detectors can interact with the electrons in the material via ionising energy loss, as discussed in Section 6.2, and by non-ionising energy loss by scattering off lattice atoms. Both effects take place in the silicon bulk but also in the dielectric (often SiO_2) used to electrically passivate the sensor surface. Both bulk and surface effects must be considered when investigating the effects of radiation on device performance [143]. This section will focus on the electrical effects of irradiation damage specific to *n-in-n* and *n-in-p* sensor geometries.

8.1 Surface Effects

Surface effects occurs in the dielectric (oxide and/or nitride layers) used on the surface of the silicon crystal, and in the silicon-dielectric interface. For silicon detectors the most commonly used dielectrics are silicon oxide (SiO_2, about 100 nm thick) or silicon nitride ($SiN_3, > 100\,nm thick$) layers. There are two types of surface effects:

Effects within the volume of the SiO_2 or SiN_3 layer: Radiation passing through the oxide creates electron-hole pairs. These electron-hole pairs typically recombine, but some of the more mobile electrons can escape the dielectric under the influence of electric fields leaving behind the less mobile ions. These trapped ions create a fixed positive charge in the dielectric [145].

Defects at the interface between silicon and the dielectric layer: Radiation can cause the introduction of new energy states at the interface between silicon and insulator. These states can be occupied by electrons or holes affecting the surface charge [131, 146].

8.1.1 Implications of Surface Damage

The positive charge in the insulating layers attracts negative charge carriers forming a conductive accumulation layer of electrons. In n^+ readout detectors this increased accumulation layer impacts on the inter-electrode isolation. this can partially compensate the negative space charge introduced via the p-stop, p-spray or moderated p-spray implants discussed in Section 7.5. It has been experimentally observed that the oxide charge saturates at relatively low irradiation doses, $(2-3)\cdot 10^{12}\, e^{-}\, cm^{2}$ [131, 145] and does not exceed a value of about $2\cdot 10^{12}\, cm^{-3}$.

8.2 Bulk Defects

Displacement damage occurs when the energy transferred to a silicon atom by the incident radiation is sufficient to remove it from its crystal lattice site. Such atoms are known as primary knock-on atoms (PKAs). The minimum energy required for displacement is $\sim 15\,\mathrm{eV}$ [131]. These PKAs may possess enough energy to knock other silicon atoms from their lattice sites, giving rise to a cascade. The damage to the crystal lattice causes changes in the electric properties of silicon. The main long term effects are:

- alteration of the effective doping concentration,
- an increase in the leakage current,
- an increase in the trapping of produced charges (with reduction of the recorded signal).

The two main point defects created by radiation damage are: vacancies, which are lattice sites with missing atoms, and interstitials, which are atoms displaced from their lattice sites. Interstitials are not limited to silicon atoms but can also be composed of impurity atoms present in the crystal. Vacancies can be occupied by impurities present

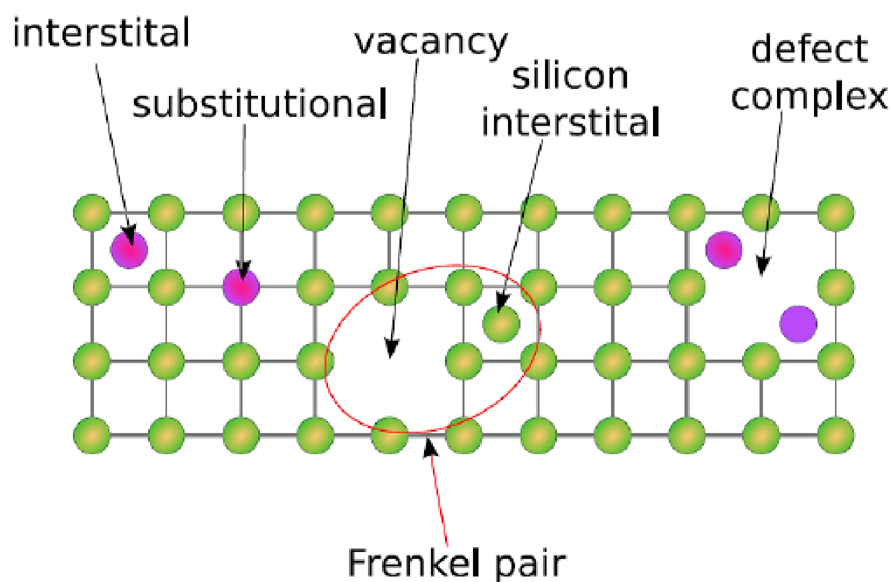

Figure 8.1: Possible defects that can occur in a silicon crystal lattice, silicon atoms are shown in green, other atoms in purple [143]. A Frenkel pair is a type of point defect which forms when an atom creates a vacancy and becomes an interstitial.

in the silicon bulk, creating substitutionals. Point defects can also combine creating defect complexes. Various defect types are illustrated in Figure 8.1 [150].

8.3 Defect Annealing

Not all defects generated by radiation are stationary or permanent. The mobility of defects strongly depends on the temperature and on how loosely they are bound to a lattice position. Above certain activation energies, which can be supplied by thermal excitations, defects can become quasi free and start to migrate until they are trapped by deep potential sinks from other crystal defects or until the temperature is decreased. Moving defects can form new complex defects or they can recombine and recover the damage [127, 149]. Such interactions are generally referred to as annealing and are often described in two parts, beneficial and reverse annealing (Figure 8.2) as they lead to a decrease or increase of the effective doping concentration.

Beneficial and reverse annealing have very different time dependences and a strong dependence on temperature. Beneficial reduces the radiation induced concentration of negative space charge and typically takes place in the first ten days after irradiation (at

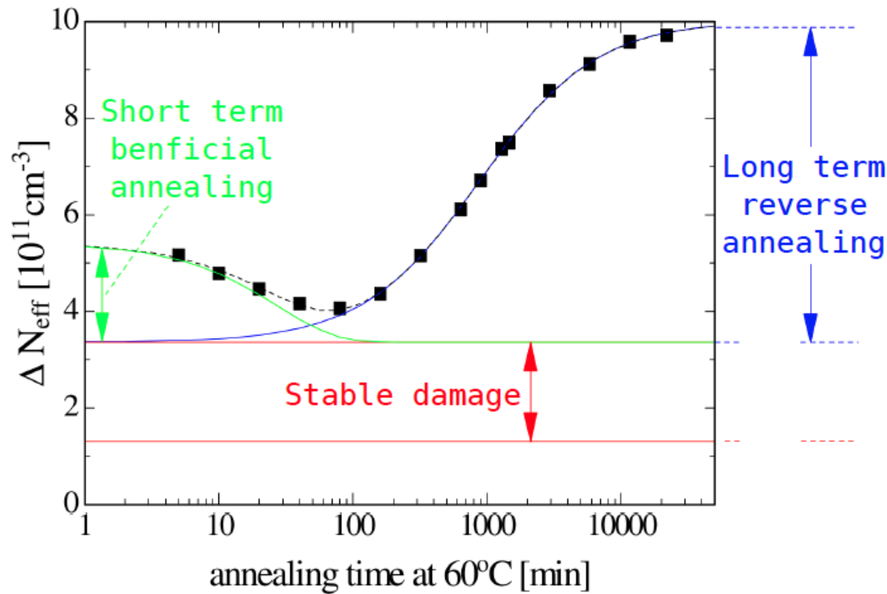

Figure 8.2: Change of the effective doping concentration as a function of annealing time at a temperature of $60°C$ showing short term, long term annealing and stable damage [143].

room temperature). In contrast, reverse annealing increases the negative space charge concentration and occurs over a larger time scale. Stable damage does not depend on annealing of the device, but only on the total received fluence.

With carefully chosen annealing parameters, the operational lifetime of a device can be extended, using beneficial annealing to partially recover the crystal lattice structure. This can be done by keeping devices at low temperatures and limiting the time they are kept warm after irradiation.

8.4 The NIEL Scaling Hypothesis

The damage to the silicon lattice created by different types of particles with different energies differs substantially. For example, the ratio of the concentration of point defects (a single atom displaced from the lattice) to that of damage clusters (a crystal disordered region with a typical radial dimension of tens of nanometers) is different for different particles, and for the same particles with different energies. In order to model the radiation induced damage of a material for these different particles and energies, the Non-Ionising Energy Loss (NIEL) hypothesis was introduced [127, 148]. The basic assumption

of the hypothesis is that the damage $D(E)$ to the material scales linearly with the amount for energy imparted in displacing collisions.

Each interaction that leads to displacement damage, a PKA with a specific recoil energy E_R is produced. The amount of recoil energy associated with displacement damage depends on the amount of recoil energy and can be analytically calculated using the Lindhard partition function $P(E_R)$ [144]. Using this, NIEL can be calculated and is expressed by the displacement damage cross section:

$$D(E) := \sum \sigma_\nu(E) \ \cdot \ \int_0^{E_R^{max}} f_\nu(E, E_R) P(E_R) dE_R \ . \tag{8.1}$$

Equation (8.1) is also referred to as the damage function and is related to the NIEL by:

$$D(E) = \frac{A}{N_A} \frac{dE}{dx}(E)\bigg|_{non-ionising} \quad , \tag{8.2}$$

where E is the energy of the incident particle, $\frac{dE}{dx}$ the energy loss, A is the atomic weight of the target material and N_A is Avagadro's constant. The NIEL value can also be referred to as the displacement-KERMA (Kinetic Energy Released to MAtter). For silicon: $100\,MeV\ mb = 2.144\,keV cm^2/g$. Figure 8.3 shows the summary for the displacement damage for protons, neutrons, electrons and pions.

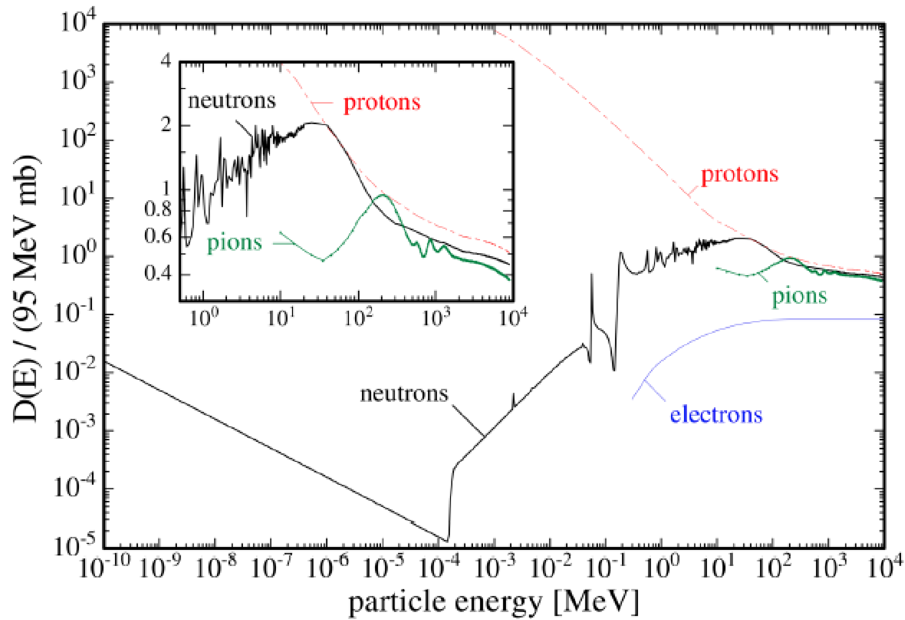

Figure 8.3: Summary of the displacement damage functions $D(E)$ for protons, neutrons, electrons, and pions [127]. The normalisation of the ordinate to 95 $MeV\ mb$ represents the damage equivalent to 1 MeV neutrons [147].

8.4.1 Hardness Factors

In order to compare the damage generated by different particles with individual energy loss spectra $\phi(E)$ a hardness factor κ is defined to refer the different radiation fields to that of a monochromatic energetic particle. The chosen normalisation is to 1 MeV neutrons:

$$\kappa = \frac{\int D(E)\phi(E)dE}{D(E_n = 1MeV) \cdot \int \phi(E)dE} \quad . \tag{8.3}$$

The displacement damage function value caused by 1 MeV neutrons is calculated to be

$$D(E_n = 1MeV) = 95MeVmb \tag{8.4}$$

The equivalent 1 MeV neutron fluency Φ_{eq} can be calculated by:

$$\Phi_{eq} = \kappa\Phi = \kappa \int \phi(E)dE \quad . \tag{8.5}$$

8.5 Implications of Bulk Defects

The main effects on detector performance due to bulk defects are an increase in leakage current, a reduction of the signal pulse height (signal strength) and a change of the depletion voltage, which changes with the effective doping concentration. In the following, the origins of these effects is discussed [151]. Figure 8.4 illustrates five ways in which energy levels associated with radiation damage can affect the electrical performance of sensors namely generation, recombination, trapping, compensation and tunnelling. Additional defect effects will also be explained, although they are not easily illustrated.

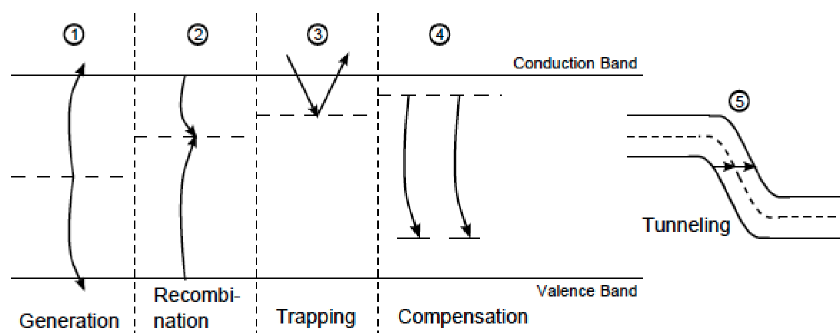

Figure 8.4: Schematic illustration of five implications of defects in silicon [170].

- **Generation** Refers to the thermal creation of electron-hole pairs when an electron is exited from the valence band to the conduction band via an energy state in the band gap (as in the Shockley-Hall-Read process [127]). The closer a state is to the centre of the band gap the higher the generation rate is, leading to higher leakage currents at a given temperature.

- **Recombination** Occurs when an electron-hole pair cancel via a single energy state in the band gap. This mainly affects the forward current of the device, but the free carrier life time and drift length are also reduced, thus reducing the signal size. This effect depends on the density of recombination sites, their energy levels and the capture cross-sections for both carriers.

- **Trapping** Occurs when a localised energy state exists very close to either the conduction band or the valence band. These energy states can capture ("trap") electrons or holes for some time before they are released again. This affects the mobility of charge and hence the time needed to readout the charge generated by the ionising radiation [131].

The effective trapping time ($\tau_{eff_{e,h}}$) decreases with fluence according to:

$$\frac{1}{\tau_{eff_{e,h}}} = \beta_{e,h}\Phi_{eq} \quad , \tag{8.6}$$

where the trapping damage constants, $\beta_{e,h}$, for electrons and holes have been experimentally measured to be [152]:

$$\beta_e = 5.7 \cdot 10^{-16} cm^2/ns \tag{8.7}$$

$$\beta_h = 7.7 \cdot 10^{-16} cm^2/ns \quad . \tag{8.8}$$

If charge carriers are trapped they cannot be collected by the readout implants and readout, reducing signal size. The reduction of the amount of charge collected contributing to the signal can be expressed as:

$$N_{e,h}(t) = N_{e,h}(0) \cdot exp\left(-\frac{t}{\tau_{eff_{e,h}}}\right) \quad . \tag{8.9}$$

Charge trapping is the dominant effect in the reduction of charge collection efficiencies (CCEs) for pixel detectors at LHC fluences.

- **Tunnelling:** Defect centres facilitate the tunnelling of charge carriers though a potential step, from the valence band to the conduction band. This effect causes an increase in the leakage current.

- **Scattering:** Radiation induced defects can act as scattering centres which reduce the mobility of carriers. As a consequence the drift velocity and current decreases and a smaller signal is seen.

- **Poole-Frenkel effect:** After high irradiation doses the generation of thermally excited charge carriers is enhanced in high electric field regions [153]. This is known as the Poole-Frenkel effect and it is the source of additional leakage current.
- **Change of effective doping concentration:** Most bulk defects in irradiated silicon exhibit acceptor like behaviour and compensate (see Figure 8.4) for the donors present in the device. Hence, the effective doping concentration, $N_{eff} = N_D - N_A$, becomes more negative with irradiation. The change in the doping concentration as a function of the equivalent fluence Φ_{eq} can be parameterised as an exponential reduction of donors and a linear increase of acceptors [143]:

$$N_{eff}(\Phi_{eff}) = N_D \cdot e^{-a\Phi_{eq}} - N_A - b\Phi_{eq} \quad , \tag{8.10}$$

with

$$a = (3.54 \pm 0.16) \cdot 10^{-13} cm^2$$
$$b = (7.94 \pm 0.64) \cdot 10^{-2} cm^{-1}$$

Figure 8.5 shows the effective bulk doping concentration and the depletion voltage for an *n-in-n* silicon detector as a function of fluence. For n-type silicon the radiation induced decrease of the effective doping concentration can lead to full compensation of donors and a space charge sign inversion (SCSI) into a p-type bulk, this is also referred to as type inversion. This is expected to happen at around $(1-3) \cdot 10^{13} \mathrm{n_{eq}/cm^2}$ [154]. After the SCSI the depletion zone develops from the front side n-implant in an *n-in-p* sensor. The continuous increase of the acceptor concentration leads to an increase of the full depletion voltage V_{dep} which depends on the effective concentration N_{eff} as:

$$V_{dep} = \frac{|N_{eff}|\, q}{2\epsilon\epsilon_0} d^2 \tag{8.11}$$

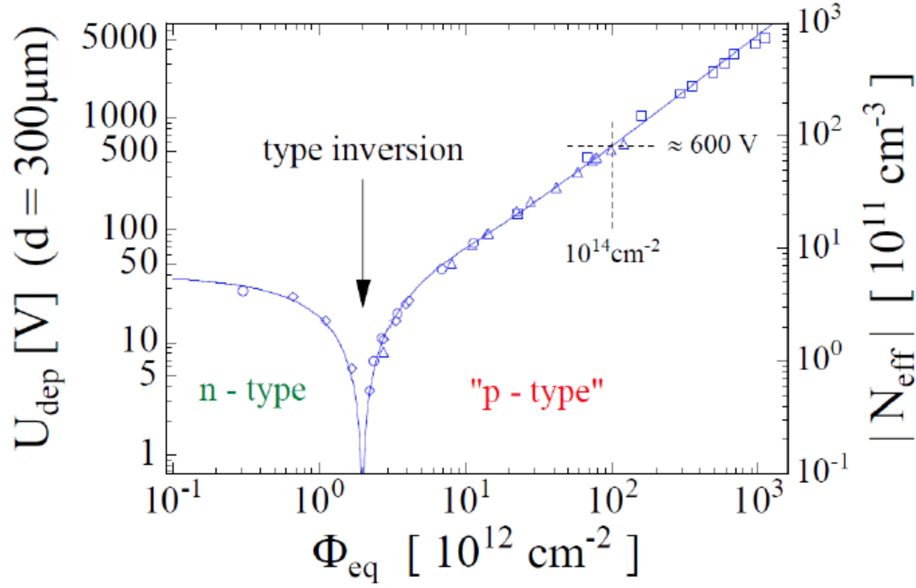

Figure 8.5: Relationship between the depletion voltage, U_{dep}, (left) and effective doping, N_{eff}, (right) as a function of the fluence for a 300 μm *n-in-n* silicon detector [127].

8.6 The Leakage Current

The current of a reversed biased silicon device (e.g. diode) is called the leakage current or the reverse current (refer back to Chapter 5). For the ideal diode, this current is solely due to carrier diffusion across the junction. In reality impurities, edge and interface effects also contribute to the leakage current. Moreover, radiation damage (see Section 8.2) increases this leakage current. The total leakage current after irradiation has two components, the bulk generated current and the surface generated current. Typically the bulk generated current dominates, as in the case of devices described in this thesis. Thus, only the mechanisms that cause bulk currents are described in this thesis (see Section 8.5).

The change in total leakage current per unit volume ΔI_{vol} of a silicon device is proportional to the fluence Φ and can be parameterised as:

$$\Delta I_{vol} = I_{vol}(\Phi) - I_{vol}(\Phi = 0) = \alpha\Phi \tag{8.12}$$

Where the constant α is the reverse current damage factor. The reverse current is proportional to the depleted volume and therefore it follows a square root dependence with the reverse bias, until it saturates for voltages above the full depletion voltage.

A device leakage current is also strongly influenced by its temperature. The temperature dependence of the leakage current has been observed experimentally to fit the form:

$$I \propto T^2 \, exp\left(-\frac{E_A}{k_B T}\right) \tag{8.13}$$

Where E_A is the activation energy and T is the temperature in kelvins.

In order to compare current measurements taken at different temperatures, the following relationship is used to normalise the current to what would be measured at a reference temperature (typically $20°C$):

$$I_{20} = \left(\frac{293.2}{T}\right)^2 e^{\left[\frac{E_A}{k_B}\left(\frac{1}{T}-\frac{1}{293.2}\right)\right]} I_T \quad , \tag{8.14}$$

where I_T is the current at a temperature T, I_{20} is the current normalised to $20°C$. The activation energy, E_A, has been measured to be 0.62 eV [155].

In order to compare damage and its effect on leakage current due to different particles with different energies, fluence values have to take into account the NIEL radiation damage factor. The linearity of α can also be exploited for the determination of the NIEL damage factor experimentally by irradiating identical detectors with different particle types with different energy spectra.

8.7 Summary

In summary, Radiation from both ionising and non-ionising sources affects the performance of silicon sensors. Radiation induced effects from surface damage has been found to be small in comparison to bulk damage. The main consequences of bulk radiation damage are increased leakage currents, increased full depletion voltages, reduced signals and increased noise. In order to maintain stable operation after irradiation devices need to be cooled to allow devices to be biased at increasingly high bias voltages while keeping the leakage current and therefore noise to a minimum.

Chapter 9

Methodology

The experimental methods and set-ups used to obtain the results discussed in the following chapters, are introduced together with a discussion of the respective advantages, disadvantages and uncertainties.

9.1 Measurement of IV Characteristics

The measurement of the current voltage (IV) characteristic of a device is a powerful tool that can be used to assess its quality. The value of the reverse current and the devices breakdown voltage allows one to assess the ability to operate a detector at high bias voltages. Reverse current measurements can be used to detect flaws in sensor designs and damage, such as scratches that can occur during handling. Any damage or defects due to defective processing will result in an increase in reverse current.

Probe stations have been used to measure the IV characteristics of sensors without the use of their intended readout electronics. The probe station holds the sensor wafer/single sensor down to a chuck by applying vacuum. The device is tested by connecting a high voltage power supply (e.g. Keithley) to the chuck and probe needles. The probe needles are used to contact relevant implants (e.g. bias ring) completing an electrical circuit. The set-up used for lab tests for this thesis also includes a component analyser used for device (CV) and inter-implant (CVI) capacitance measurements (Wayne-Kerr). The IV/CV characteristics are recorded automatically using a computer, which takes repeated measurements at every point for the determination of the statistical uncertainties, after an initial settling time after being ramped up to, or down to the required voltage.

In the case of irradiated sensors, measurements are performed inside a freezer, where temperatures can be set as low as - 50 °C. The sensors are glued/strapped to an aluminium heat-sink which is mounted on a small reusable PCB with a plugable connection routed out of the freezer via cables. The connection between sensor and PCB is made using wire bonds. The testing lab is an ISO 4 clean room where humidity is controlled. ISO 4 is a classification where the maximum concentration of particles/m^3 of air does not exceed 10,000, for particles equal to and larger than 0.1 μm. The humidity within the freezers is controlled using a constant flux of nitrogen flushed into the freezer volume and passed over the device under test, preventing the formation of frost or moisture.

9.2 Thermal imaging

To identify defects in sensor designs, the infra-red black body emission spectrum of sensors is recorded and analysed whilst sensors are being operated close to their voltage limit (breakdown voltage). The measurements were performed with a Flir SC660 thermal camera [156], mounted in a vacuum chamber, the vacuum chamber was only used as a convient dark box to perform tests. Wafers/single devices where mounted to custom holders and high voltage was applied via probe needles or wire bonds. The thermal camera records thermal pictures for a set time, during this time the bias voltage and therefore the leakage current is increased. Close to device breakdown, high current regions start to heat up, revealing the location of processing or design flaws. Figure 9.1 shows the thermal behaviour of a large area (40 x 40 mm^2) pixel sensor. Two hot spots can be seen at the dicing street of the sensor. A dicing street is the point at which the sensor is cut from the wafer. The cause of the hot spots in Figure 9.1 was understood to be due to the implant type used at the cut edge.

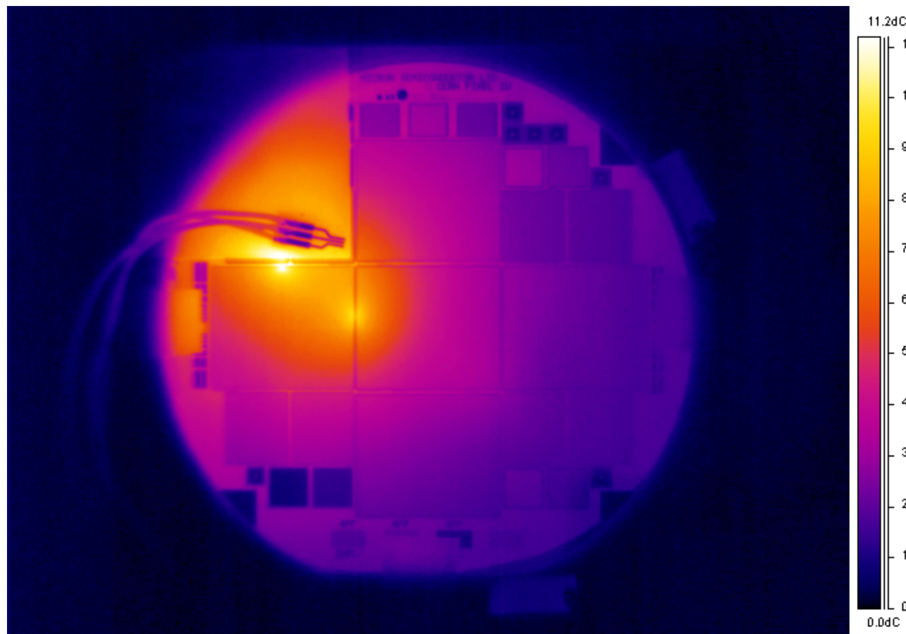

Figure 9.1: Thermal image showing hot spots generating large leakage currents causing breakdown on a micron ATLAS quad pixel sensor, while on wafer.

9.3 Irradiation Facilities

A number of facilities are used to irradiate sensors to various fluences using different particles types and energies. The different irradiation facilities along with the energy and hardness factor needed to scale received fluence to n_{eq}/cm^2 are discussed in the following sections.

Ljubljana - TRIGA Mark II research reactor

The reactor centre of the Jožef Stefan Institute (JSI) in Ljubljana [157] offers the possibility for irradiations with reactor neutrons with a continuous energy spectrum. Neutrons with an average energy above $100\,keV$ and ranging up to $10\,MeV$ are available with a steerable flux up to $5 \cdot 10^{12} n/cm^2 s^{-1}$ and a hardness factor of 0.9. Due to limitations in space and shielding, only samples with a diameter of up to $4cm$ can be irradiated. For this reason, only sensors or bare modules (sensor and electronics assemblies) can be installed. The subsequent handling required to mount the devices on to a readout board, also referred to as the daughter-board for testing means that some unavoidable annealing occurs: this is around 1 day at room temperature [104]. The dose is determined using the known flux of the reactor, which is periodically calibrated by measuring the leakage currents of reference silicon diodes. The typical uncertainty on received dose is around $10\,\%$.

The irradiation of sensors with neutrons mounted to FE-I4 readout chips is problematic, because these assemblies contain tantalum, which activates due to neutron radiation. FE-I4 modules irradiated to HL-LHC fluences ($2 \cdot 10^{16}\,\mathrm{n_{eq}/cm^2}$) would take years to cool down to a level where they could be handled safely and it is not possible to mount fresh (non-irradiated) FE-I4 readout chips on irradiated detectors, if one wants to assess the properties of the sensor alone. The latter is because the connection between them is made using a high temperature (~ 230 °C) interconnect method (bump bonding). This is proven to damage the irradiated sensor provoking their failure. As a result, no FE-I4 modules were irradiated as part of the work contained in this thesis.

CERN - PS

The CERN PS irradiation facility [158] is used to irradiate sensors with high energy protons in the East hall. The momentum of the protons is $24\,GeV/c$ and the flux reaches $(2-9)\cdot 10^9 p/cm^2 s^{-1}$. This in combination with the hardness factor 0.62 [159] leads to rather long irradiation times to reach HL-LHC fluences. The diameter of the beam is 2 cm which doesn't allow large area sensors to be irradiated without the need to scan the beam over the sample, further increasing the irradiation time. The dosimetry is performed by measuring the activation of Al foils with an NaI or Ge spectrometer. This yields an uncertainty on the sustained dose of $\pm$ 6 %.

Karlsruhe - Compact Cyclotron

Low energy protons are delivered for irradiation by Zyklotron AG which operates a cyclotron at the Karlsruhe Institute for Technology (KIT) [160]. The protons have an energy of $23\,MeV$ and are delivered with a typical beam current of approximately $9 \cdot 10^{12} p/cm^2 s^{-1}$. The beam spot size is 7 mm in diameter. A scanning table is used to irradiate samples with larger sizes than the beam spot. The hardness factor is 2.0. To prevent annealing, samples are cooled during irradiation. The dosimetry is measured using Ni foil and a Germanium spectrometer. The resulting dosimetry uncertainty is $\pm$ 13.75 %.

Birmingham - MC40 Cyclotron

Irradiations can be performed at the Medical Physics MC40 cyclotron in the School of Physics and Astronomy at the University of Birmingham, UK. The cyclotron has the capability to produce various ion beams up to energies of $40\,MeV$. However, irradiations to date (January 2014), have only used $27\,MeV$ protons, which have a hardness factor of ~ 2. The delivered beam current can be altered depending on the target fluence and

irradiation time. A typical beam current of 0.5 μA can be expected when irradiated up to $1 \cdot 10^{15}\,\mathrm{n_{eq}/cm^2}$. However, to deliver larger fluences to samples, higher beam currents can also be used. To prevent annealing of samples, they are mounted in a cooling box. The beam is collimated to an area of $1\,cm^2$ and its uniformity is checked using Grafchromic film [161]. The beam fluence is determined using a Faraday cup which measures the charge of the beam incident on the samples and cross-checked using Ni foils, the uncertainty on the dose is $\sim 10\,\%$ [161].

9.4 ALiBaVa Readout System

The ALiBaVa (Analogue Liverpool Barcelona Valencia) readout system, is an analogue electronics based readout system conceived within the framework of the CERN RD50 collaboration and designed to easily characterise multichannel silicon detectors, providing high sensitivity to low signals and high speed. The front-end electronics are based on the LHCb Beetle ASIC [162] developed for the LHCb VELO [163]. It features 128 input channels with low noise analogue front-end amplifiers, a 10 bit ADC and a clock speed of $40\,MHz$. The system is typically used to test micro-strip sensors with variable inter-strip distances using lasers, radioactive sources or particle beams.

The test setup in Liverpool University is detailed in Section 9.4.1 with a discussion of the data acquisition and analysis chain as well as the uncertainties on the measurements.

9.4.1 Instrumentation

The system consists of two main components, a mother-board and a daughter-board, see Figure 9.2a. Test structures are wire bonded via a $80\,\mu$m glass pitch adapter which connects to the Beetle chip. There are normally two Beetle chips per daughter-board (see Figure 9.2b) but alternative flavours of daughter-board exist with the Beetle chips in different locations. Both Beetle chips can be operated simultaneously, thus a total of 256 channels can be read out. The daughter-board along with the sensor are placed in a cooled environment, as required for the measurement of irradiated sensors, while the mother-board is operated at room temperature. The mother-board receives signals from the daughter-board and the trigger system. The mother-board is connected to a PC via a USB cable for control and transfer of data.

The 128 input channels of the Beetle chip have independent amplifiers and pulse shapers (see Figure 9.3). The output signal of the shaper rises in around $10ns$ from 10% to 90% of the peak signal and falls below 30% of the peak signal over the following $30ns$. The time elapsed between the first induced trigger and the second clock induced time stamp is distributed between 0 and $100ns$. After 128 clock cycles of $25ns$ length i.e. $3.2\,\mu$s after the second time stamp the trigger signal is passed from the mother-board to the daughter-boards, which then returns the serialised data from the 256 channels from the two Beetle chips for the appropriate time slice. The analogue data is digitised with a 10 bit Analogue to Digital Converter (ADC) and passed on to the computer together with the timing information. To ensure uniform signal gain only data from a narrow time window is accepted. Figure 9.4a shows the recorded cluster charge as a function of time for a Beetle chip connected to a detector illuminated with minimum ionising particles (MIP). A $10ns$ window is selected around the peak where the Beetle signal has minimum variation of gain. A sufficiently large data sample to allow for small statistical uncertainty on the fitted most probable value is collected and processed. Figure 9.4b shows the resulting energy spectrum (in ADC units) for all hit clusters above threshold [104].

The equivalent noise charge (ENC) in units of electron charge of the Beetle chip is given [162] as:

$$ENC = 539.1\,e + 51.89/pF \cdot C_{in} \approx 670\,e \quad , \tag{9.1}$$

where C_{in} is the input capacitance of the sensor (typical values for miniature $1\,\mathrm{x}\,1\,cm^2$ sensor is around 2.5 pF). Additional effects such as shot noise caused by the leakage current lead to typical total noise levels of $ENC_{total} = (800-900)\,e$ for the more irradiated detectors used in this thesis. The Liverpool set-up features a daughter-board holder in a freezer capable of cooling down to -50 °C which is flushed with nitrogen or dry air. The sensor is cooled by blowing the cold gas over its surface. The trigger system consists of plastic scintillator bars attached to Hamamatsu photomultipliers [164]. The trigger system can be used in coincidence mode allowing the use of two sets of scintillator/PMT's or singularly.

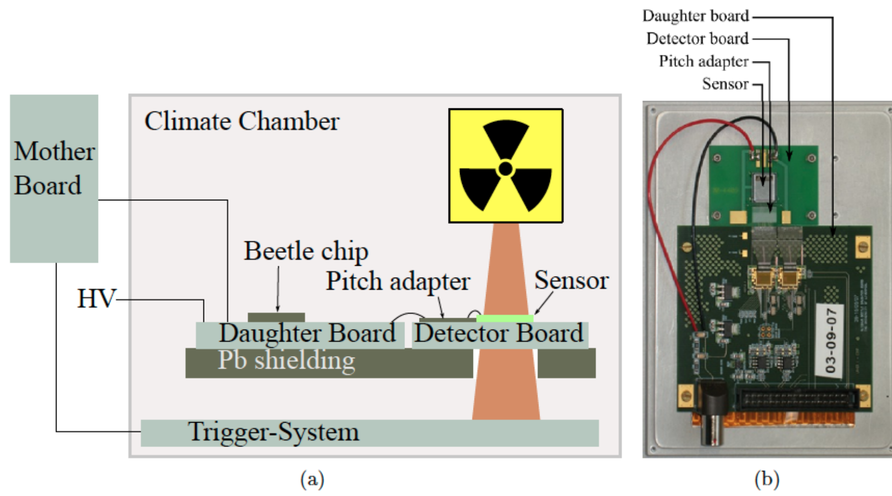

Figure 9.2: (a) Schematic drawing of the alibava set-up. (b) Photograph of the daughter and detector board with a sensor and the decoupling pitch adapter [104].

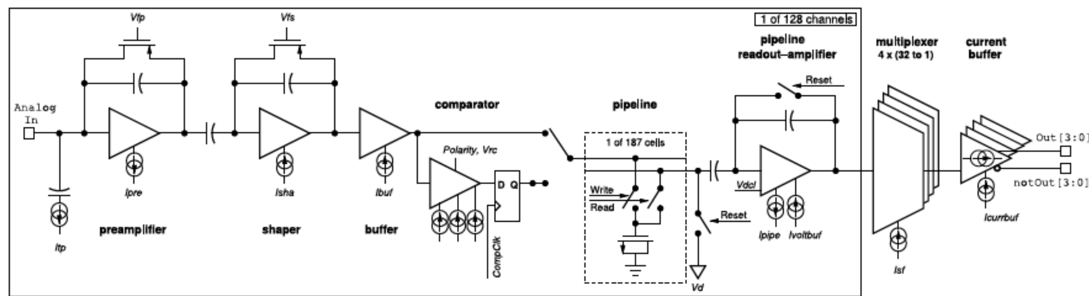

Figure 9.3: Schematic block diagram of a Beetle input channel. Adapted from [162].

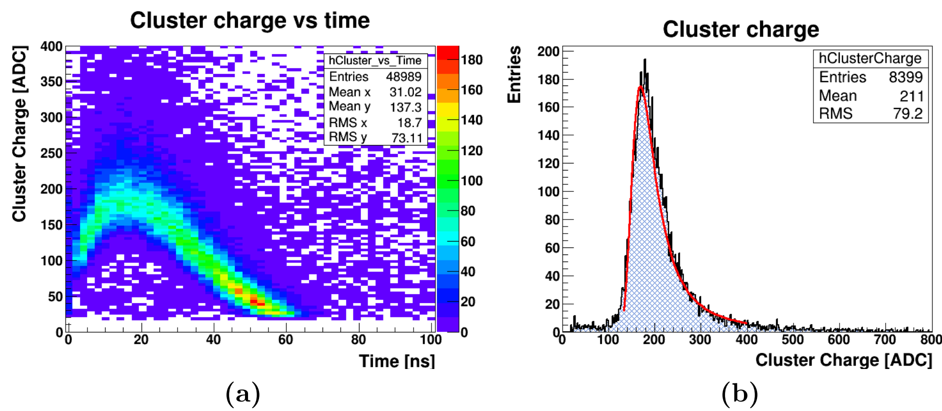

Figure 9.4: (a) cluster charge as a function of readout time in ns. (b) cluster charge spectrum of in time events (8-18 ns) using the AliBaVa readout system.

9.5 Operation of ATLAS FEI4 readout chip

The ATLAS FE-I4 readout chip was designed for the IBL pixel detector system Section 4.5.5. All results regarding HL-LHC ATLAS pixels modules are obtained with modules made with the FE-I4 chip. The following sections outline the different methods in which FE-I4 modules are readout and tested. Two DAQ systems have been used to readout FE-I4 modules, USBpix and RCE. These systems are outlined in Section 9.5.3 and Section 9.5.4 respectively.

9.5.1 FE-I4 Chip Overview

The FE-I4 readout chip contains 26,880 pixels arranged in 80 columns with a 250 μm pitch by 336 rows with a 50 μm pitch. It is designed in a 130 nm feature size bulk CMOS process. The FE-I4 pixel cell size (250 x 50 μm^2) is smaller than its predecessor, the FE-I3, which has a pixel size of 400 x 50 μm^2. The reduction in pixel size improves hit resolution along z-axis within ATLAS (beam direction) and at the same time lowers pixel hit occupancy. The FE-I4 features significantly more digital functionality with respect to the FE-I3. Despite this, the active area of the chip has been increases to almost 90 %. The FE-I4's additional digital functionally means that an additional module controller chip is no longer needed. The FE-I4 is substantially larger than the FE-I3 which allows for a simpler module design which reduces material used in the detector as well as the cost of module production. Some key features of the FE-I4 chip relative to the FE-3 chip are given in Table 9.1.

	FE-I3	FE-I4
Year	2003	2010
Feature size	250 nm	130 nm
Chip size	7.6 x 10.8 mm^2	20.2 x 18.8 mm^2
Active area	74 %	89 %
Size of pixel array	18 x 160 (2880)	80 x 336 (26880)
Pixel size	400 x 50 μm^2	250 x 50 μm^2
Number of transistors	3.5 M	87 M

Table 9.1: Summary of key features of the FE-I4 chip compared to its predecessor, the FE-I3 chip [165].

The FE-I4's analogue [113] pixel circuitry is based on a two stage architecture. The first front end stage is attached with a DC contact to the sensor pixel and features a pre-amplifier with leakage current compensation circuitry, AC coupled to a second amplification stage. This is followed by a comparator with global and local threshold adjustment. Each pixel has 13 configuration bits used for masking, threshold setting, feedback current adjustment and local test charge injection. A simplified diagram of the 2 stage amplifier circuit is shown in Figure **??**

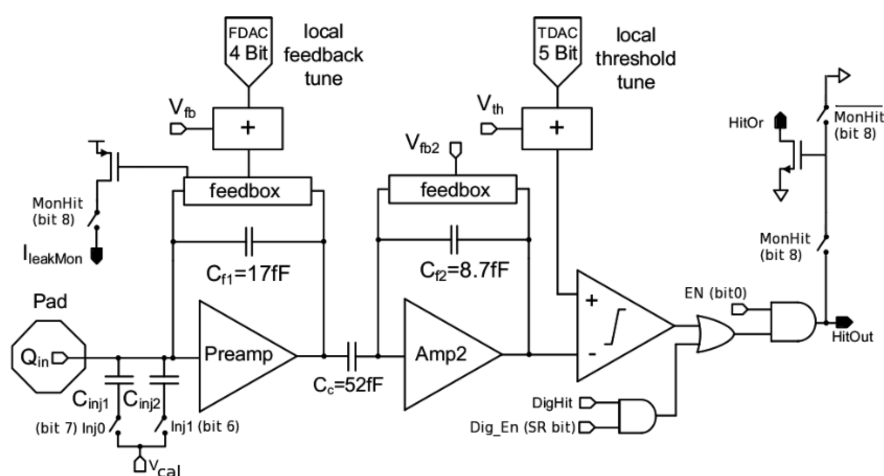

Figure 9.5: Analog pixel schematic diagram. Output pins are solid, input pins are open [113].

A time-over-threshold (ToT) triggering scheme is used. Whereby, if a signal is above threshold the time (25 ns blocks) is counted as the signal charge falls linearly to the baseline. The peak of the resulting ToT distribution is proportional to the signal height. The ToT method is illustrated in Figure 9.6. From left to right, the relationship between the preamplifier signal and the discriminator output signal for changes in the injected charge, threshold and feedback current.

The analogue pixels are arranged via double columns (same as FE-I3) with the readout of four pixels organised by a common digital region (see Figure 9.7). Hit processing and the ToT measurement occur independently for each pixel locally with its digital region. Each digital region features five memory blocks to store hits during the trigger latency. Due to space constraints and to reduce pile-up from out of time hits, the ToT resolution is 4 bits [112].

The advantages of using a regional architecture is the reduction of data being transferred to the periphery, because trigger verification occurs within pixel digital blocks. With this logic, hits that are not associated with the trigger are discarded before being

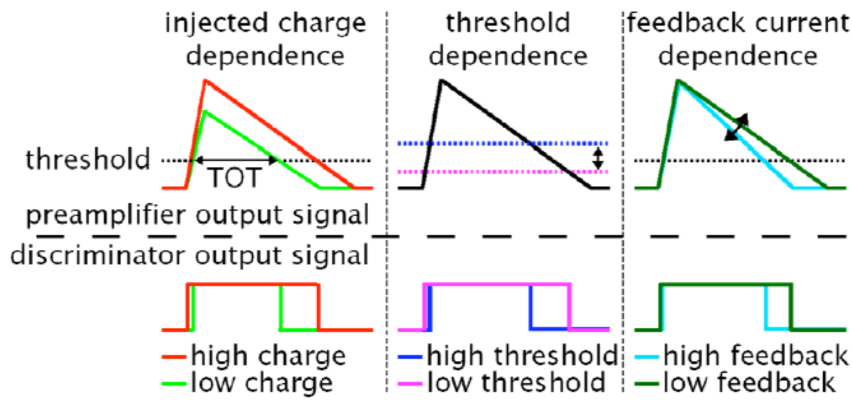

Figure 9.6: Comparison of the relationship between the preamplifier signal and the discriminator output signal for changes in the injected charge, threshold and feedback current [112].

sent to the periphery. This reduces dead time during readout while also achieving a lower power consumption. In contrast to the column drain architecture used in the FE-I3, the regional readout architecture of the FE-I4 scales to larger pixel arrays. Therefore, the FE-I4 design serves as a baseline for future chip designs, such as the 65 nm CMOS size foreseen for use in the ATLAS inner pixel barrel layers (FE-I5).

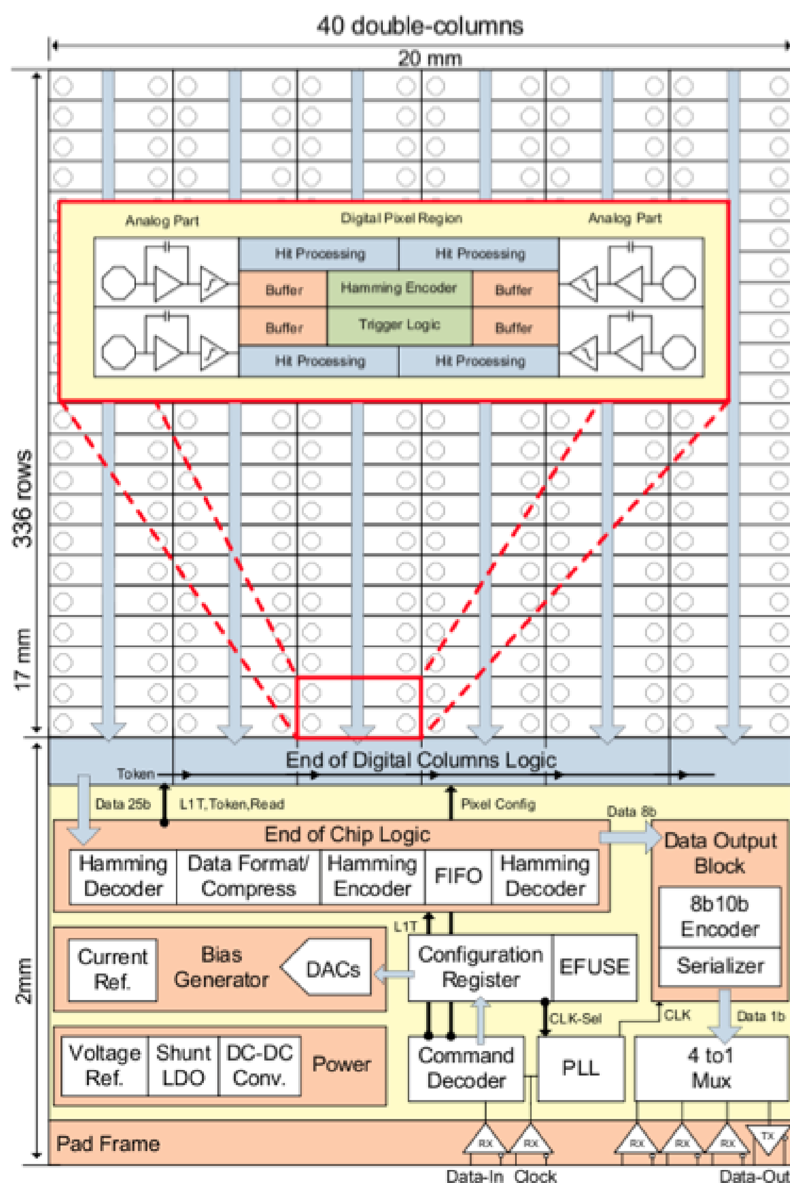

Figure 9.7: Schematic view of the FE-I4 readout architecture. The pixels are arranged in double columns and four analogue pixels share a common digital region [113].

9.5.2 Pixel Array Performance

Two versions of the FE-I4 have been produced, FE-I4A and FE-I4B. FE-I4A are the prototype chips produced to test chip performance. As a consequence of extensive testing of the FE-I4A, modifications were made for the final version for the IBL. For detailed information on the changes implemented see [165]. FE-I4 modules based on either version

of the readout chip are discussed in Chapter 11 and Chapter 12. This section will outline important differences in pixel response between FE-I4A and FE-I4B.

In FE-I4A chips, selected pixel columns have alternative feedback capacitors or discriminator designs. This was done to test their performance before final IBL production. In sixteen pixel columns the baseline metal-metal feedback capacitor was replaced with a Vertical Natural Capacitor (VNCAP) [113]. The value of the capacitor determines the pixel amplifier gain and therefore affects the threshold of that channel. This is clearly visible in the FE-I4A threshold distribution in the end columns (Figure 9.8a), pixel columns featuring VNCAPs have a slightly darker colour. The lack end columns are turned off due to noise. A low standby current discriminator is used in two FE-I4A columns to study possible power reductions. In all cases the baseline design performs equally well as the proposed alternatives. The baseline design was adopted for the FE-I4B ensuring a uniform response across the pixel array (Figure 9.8b).

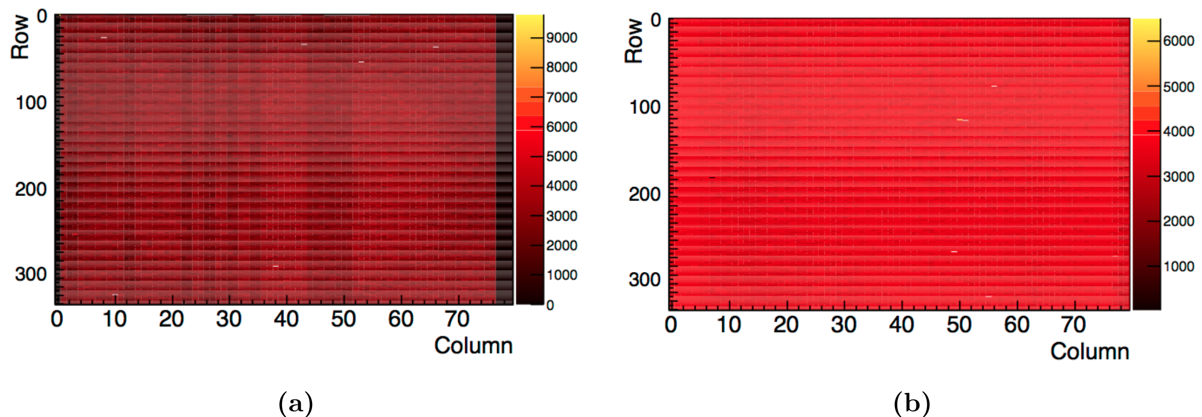

(a) (b)

Figure 9.8: Un-tuned threshold distributions in (a) FE-I4A and (b) FE-I4B. Black pixels are turned off due to noise. Columns whose pixels feature VNCAPs can clearly be seen in a darker shade of red.

FE-I4A chips also have some missing circuitry, mostly in the periphery but also in the end pixel columns. Three pixel columns are affected, columns 0, 78 and 79, as well as three small groups of pixels on row 0, which, because their circuitry is not complete, cannot be configured as the other pixel columns. As a result, these pixels are masked out on all FE-I4A modules tested within this thesis. This is shown in Figure 9.9; the total number of pixels masked out is 2040 out of 26880.

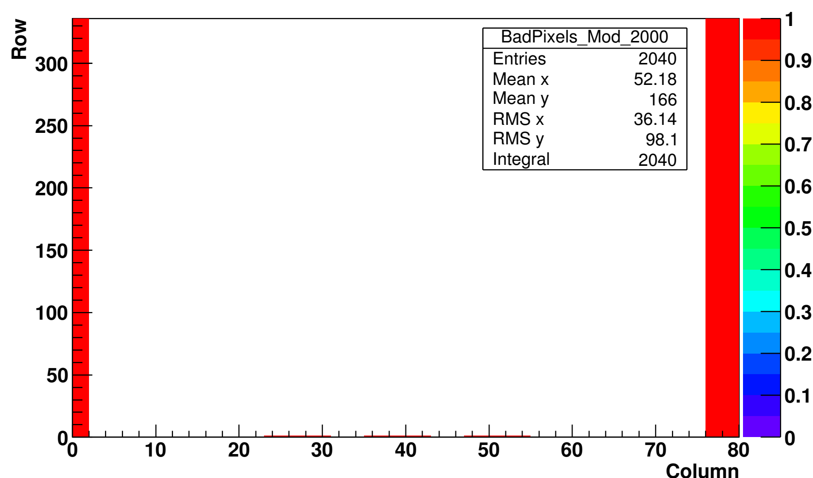

Figure 9.9: 2D mask plot showing pixels that are masked (red) and are not tuned or readout by the DAQ system.

9.5.3 USBpix System

The USBpix [166, 167] system is a modular device used as an interface between the ATLAS pixel front-end readout card and the data acquisition software on a local computer. Developed as an alternative to TurboDAQ [168], the previous ATLAS pixel detector test system, USBpix was designed to be small and portable using the minimum amount of components. The only further components required for operation are two power supplies, one to supply low voltage to the readout chip and another to supply high voltage to the sensor. The USBpix is composed of a Multi-IO board, which was developed at the University of Bonn, Germany, and a front end adapter card. Two adapter cards are available one for the FE-I3 and FE-I4 readout chips respectively. Figure 9.10 shows a photograph of the USBpix system connected to an FE-I4 single chip readout card.

The Multi-IO board features a compact FPGA, which handles all of the communications between the FE-I4 and the computer. The USBpix system only has the resources to read out a single FE-I4 chip. Multi-chip FE-I4 modules would require USBpix systems to be daisy chained together to a single computer. For this reason a more powerful DAQ system (RCE system) was acquired to be used with multi-chip FE-I4 modules.

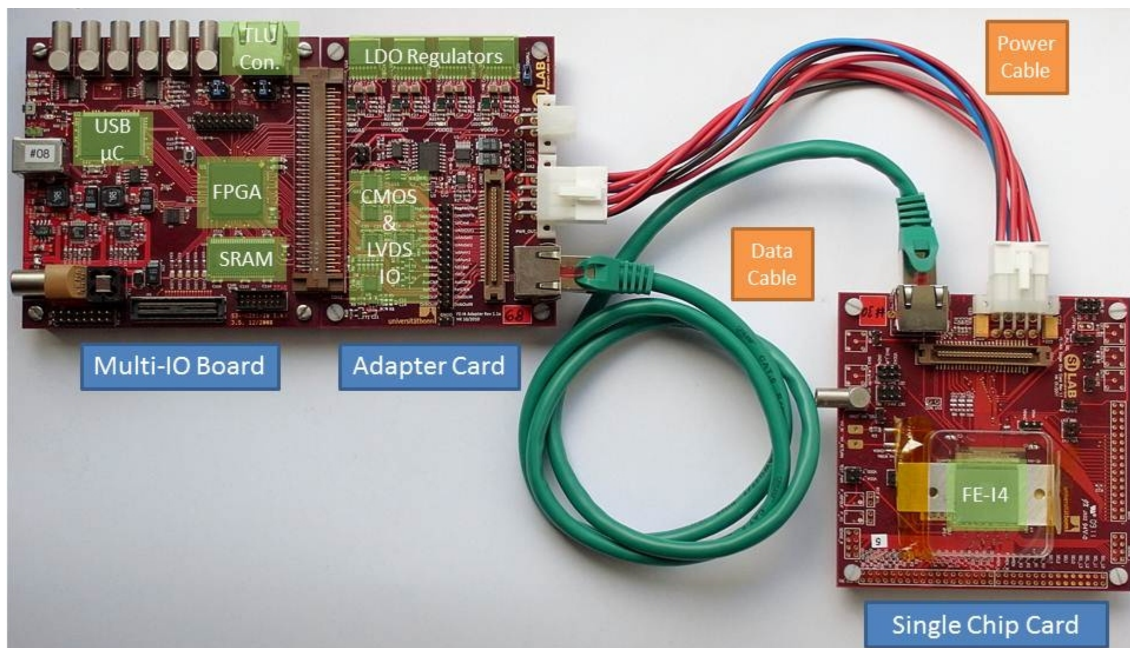

Figure 9.10: Photograph of the USBpix system [167]. The Multi-IO board and an FE-I4 adapter card are shown on the left and a single chip FE-I4 readout card, connected via a data cable and power cables, is to the right.

9.5.4 RCE system

The ATLAS RCE system is a generic DAQ system based on modular building blocks. It consists of an RCE (Reconfigurable Cluster Element) board which handles data processing, a rear transmission board for sending and receiving data, a network switch to connect multiple RCE boards together if necessary and a telecommunications standard ATCA crate, which provides power and cooling to the RCE and rear transmission boards. A HSIO (High Speed IO) board and an adapter card are used to connect and send data from pixel modules to the RCE system. A schematic overview of the system is shown in Figure 9.11. The Liverpool RCE system is configured to readout up to a maximum of eight FE-I4 readout chips simultaneously.

9.5.5 Tuning

Tuning refers the setup steps required to accurately calibrate an FE-I4 module. The tuning of FE-I4 modules is done in the same way in both USBpix and RCE systems, with the exception that the RCE can process multiple numbers of FE-I4 chips simultaneously, depending on system configuration.

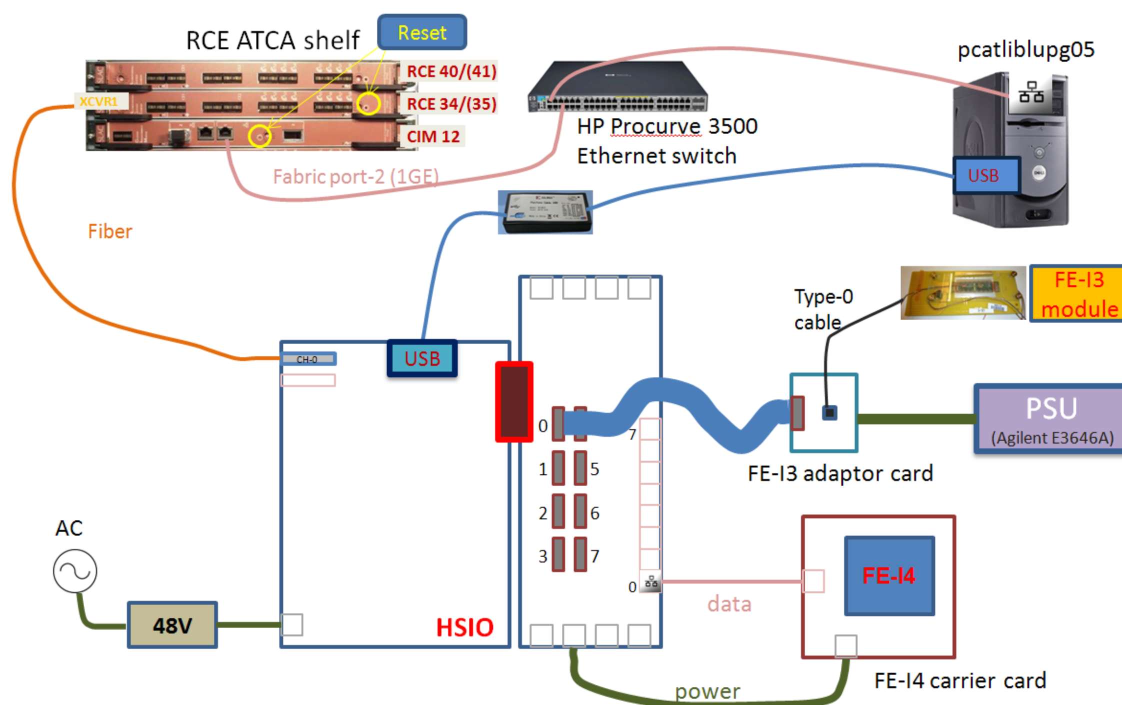

Figure 9.11: Illustration of the RCE system configured to readout ATLAS FE-I4 pixel modules.

To compare the response of different sensors, the behaviour of the attached FE-I4 readout chip has to be accounted for. The calibration of the front-end has to be well understood in order to define the threshold of the discriminator as well as the relationship between injected signals charge to ToT. In the following, some of the standard scans [169, 170], which are included in both the USBpix and RCE systems, are described.

Analogue and Digital Test: Via the external charge injection circuit, a defined charge can be injected several times directly into the discriminator (Digital Test) or the amplifier (Analogue Test) of each pixel. These tests show whether the analogue and the digital parts of a pixel cell work as expected, comparing the injected charge with the output. If the readout pixel is fully functional, it should read back the same number of hits as were injected. Figure 9.12a and Figure 9.12b shows results from analogue and digital tests respectively, performed with the ATLAS RCE system. In each case 50 charges were injected. Any variation in the number of hits read out indicates a none uniform pixel response.

GDAC Tune: The purpose of this tuning is to set the global discriminator threshold and feedback current values for the whole FE-I4 chip, to the value specified by the user. An algorithm uses an iterative process to automatically vary many parameters, while

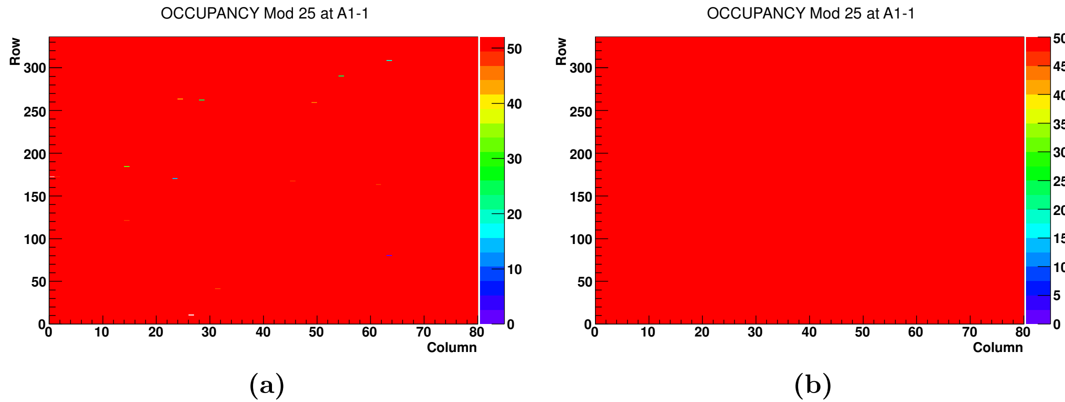

(a) (b)

Figure 9.12: Results for (a) analogue test and (b) digital test for every pixel on an FE-I4b readout chip. In both cases 50 charges are injected and read back using the RCE system

injecting and reading back all the pixel thresholds and comparing them to the user defined target. The parameters that provided the best outcome are then stored.

TDAC Tune: The purpose of this tuning is to fine tune the threshold for each pixel. This is done in the same way as the GDAC tune, but uses smaller steps and individually tims each pixels operating voltage.

FDAC Tune: The purpose of this tuning is to adjust the in-pixel ToT response to a certain charge for every pixel i.e. ToT = 10 at a charge of 20 ke. It is done is a similar way to the GDAC and TDAC tunes but instead focuses on calibrating the ToT to charge for each pixel.

TDAC and FDAC tunes are performed several times (>2 each), in an iterative way. This allows the system to find a compromise between the best parameters from each type of tuning.

Threshold Scan: This scan is a precision test that determines the precise discriminator threshold in each pixel without altering any parameters in the configuration of the FE chip. A given charge is injected into the analogue part of the FE multiple times. This procedure is repeated with different charges. The ideal outcome would be a step function with no hits if the injected charge is below threshold and if above threshold the number of charge injections is equal to the number of hits. However, due to noise effects, charge values close to the threshold will sometimes cause a hit and sometimes not. Figure 9.13 shows results from a threshold scan with the RCE system. These histograms allow for the determination of module tune quality. The quality of a tune is specified by the user.

However, important features include a threshold with a narrow distribution around the target value with low noise (also with a narrow spread). Figure 9.13b and Figure 9.13d show some good quality tune results. Some noisy pixels/channels can be seen and would be masked out before operation. Any noise channels are then masked out

ToT Scan: This scan injects a known amount of charge, and reads back the ToT response for each pixel. Typical output histograms are given in Figure 9.14.

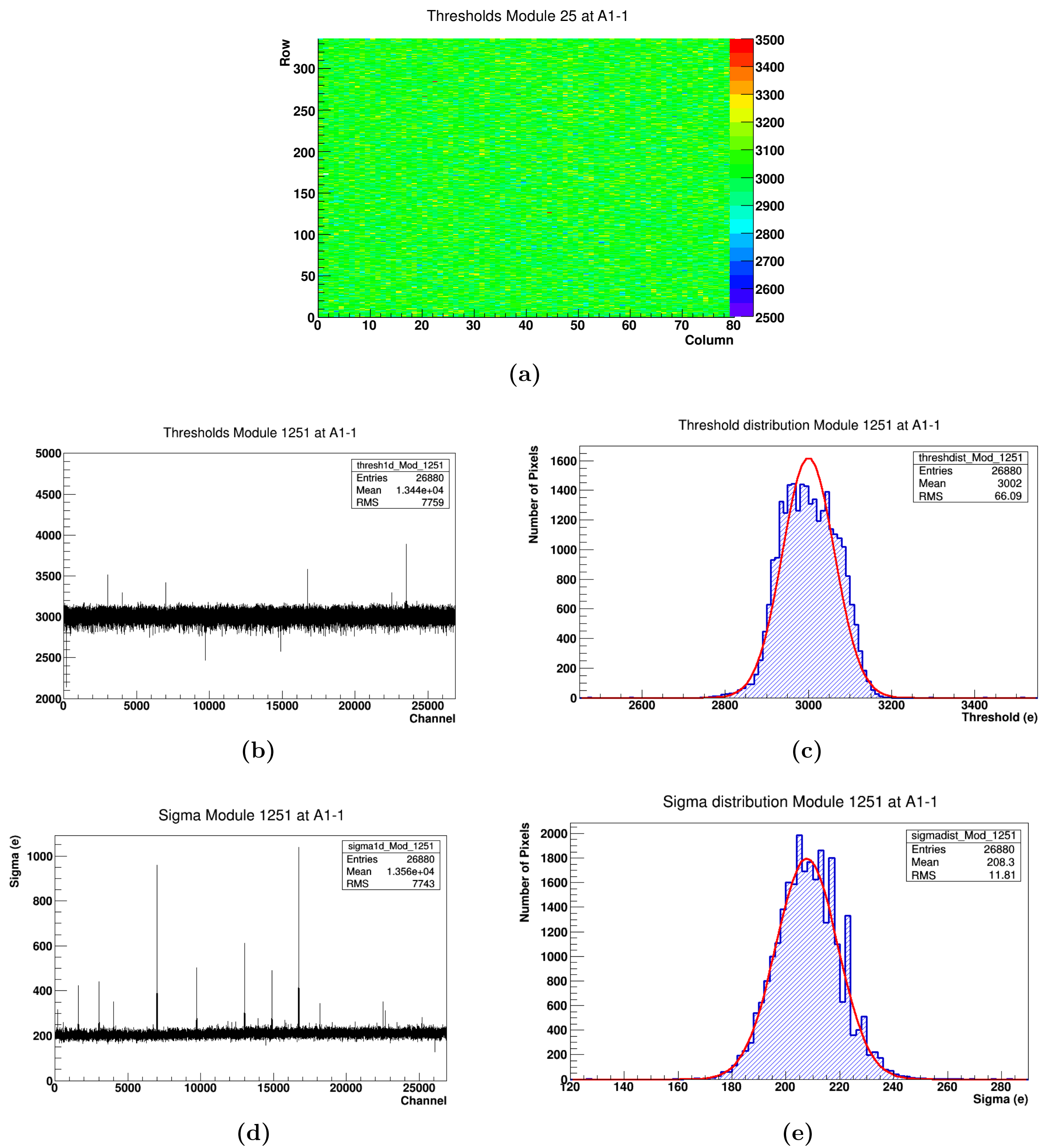

(a)

(b) (c)

(d) (e)

Figure 9.13: Results from a threshold scan of a tuned FE-I4b module. (a) 2D threshold histogram showing each pixels tuned threshold. (b) shows every channels threshold, indicating noisy pixels. (c) shows the spread of the threshold of every pixel with a Gaussian fit performed to determine the average module threshold. (d) the noise of every channel and (e) the spread of noise for every pixel with a Gaussian fit performed to determine the average noise.

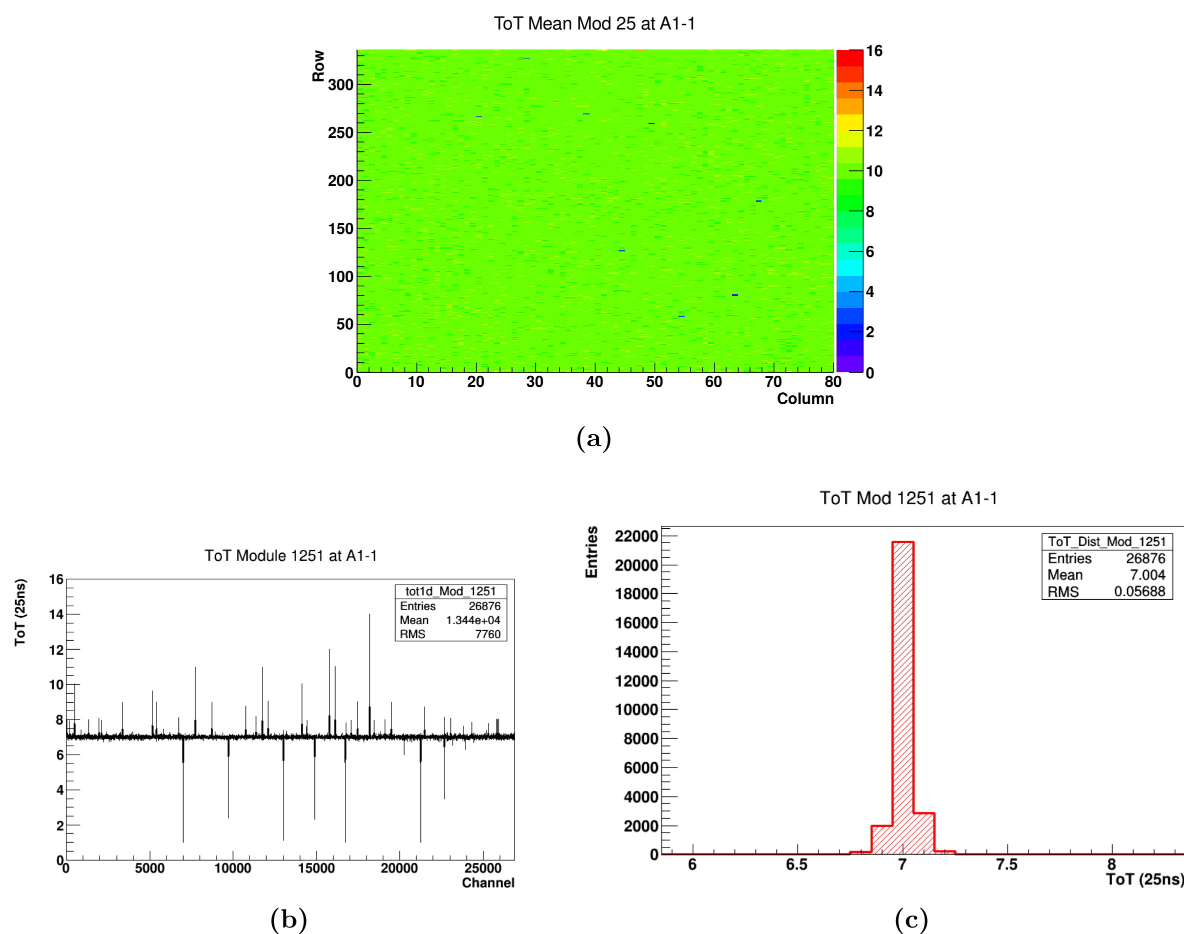

Figure 9.14: (a) 2D colour map indicating each pixel's Tuned ToT (Time over Threshold). (b) shows every channel's tuned ToT indicating channels with drastically different values and (c) shows the spread of tuned ToT values with a Gaussian fit performed to determine the average module ToT value.

9.6 Test Beam

New detectors must to be tested in an environment similar to that which they will be exposed to within ATLAS. This is of particular importance for devices that are intended for use in ATLAS after the high luminosity upgrade. Beam tests are preferable to test with compared to radioactive sources because the momentum of particles is significantly higher and meaningful studies of efficiency and spatial resolutions are possible. The particle type and energy of a particle beam at a test facility is usually well known. The use of a particle telescope enables the measurement of the detector efficiency as a function of a range of parameters, such as trigger threshold, sensor bias voltage, and hit angle. Efficiency measurements for a given detector design are very important since ATLAS relies heavily on highly efficient silicon tracking detectors for its physics programme.

These measurements are not possible with traditional source measurements because of momentum and collimation constraints.

Beam tests on a range of planar pixel silicon devices produced at Micron Semiconductors Ltd, UK, have been performed with positrons ($4\,GeV/c$) at DESY in Hamburg, Germany and with pions ($180\,GeV/c$) at CERN in Geneva, Switzerland. This section describes the DESY and CERN beam-lines used in Section 9.6.1. The General set-up of a beam test is given in Section 9.6.2.

9.6.1 Beam Test Facilities

DESY

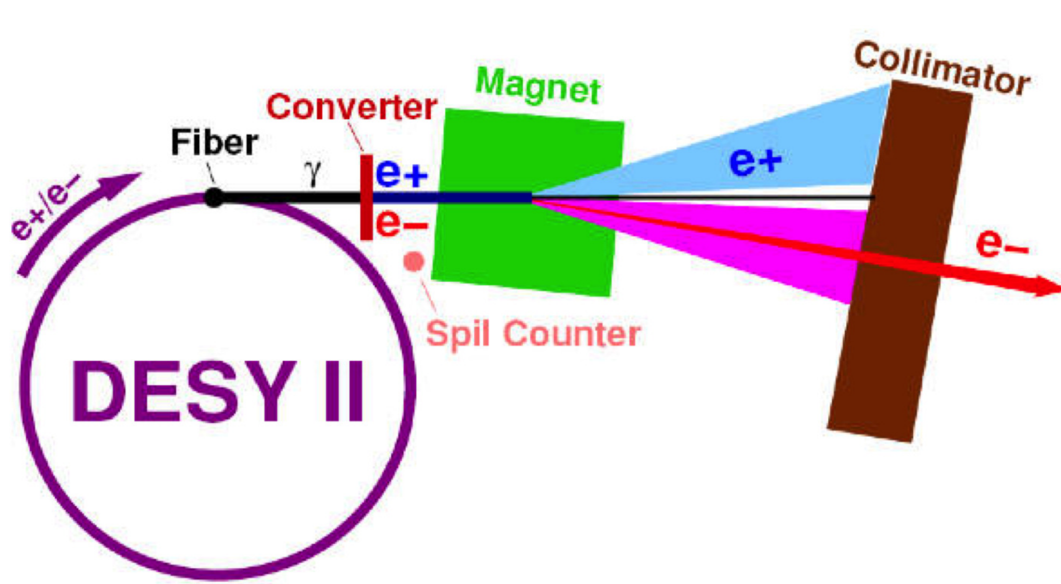

Figure 9.15: A diagram illustrating the process of producing an electron or positron beam for tests at DESY [171].

The Deutsches Elektronen-Synchrotron (DESY) is a German accelerator research centre located in Hamburg. The DESYII injector is an electron/positron synchrotron, used to provide test beams. A bremsstrahlung beam is generated using a carbon fibre, that is moved into the circulating DESYII beam. The photons are converted to electron positron pairs with a metal plate converter. A dipole magnet is then used to separate particles with different momenta. The strength of the magnetic field is controlled so that particles with a given momentum can be extracted using a collimator. Figure 9.15 shows an illustration of the whole process [28, 171].

The maximum energy achievable for electrons/positrons is around $7\,GeV/c$. However, the particle rates vary strongly with energy. This is shown in Figure 9.16 for test beam hall 21/22 (left) and hall 24 (right). Higher energy particle beams suffer less from the effects of multiple scattering and provide a better pointing resolution to the particle telescope. The compromise between particle rate and high energy lead to the choice of a $4\,GeV$ positron beam for our tests.

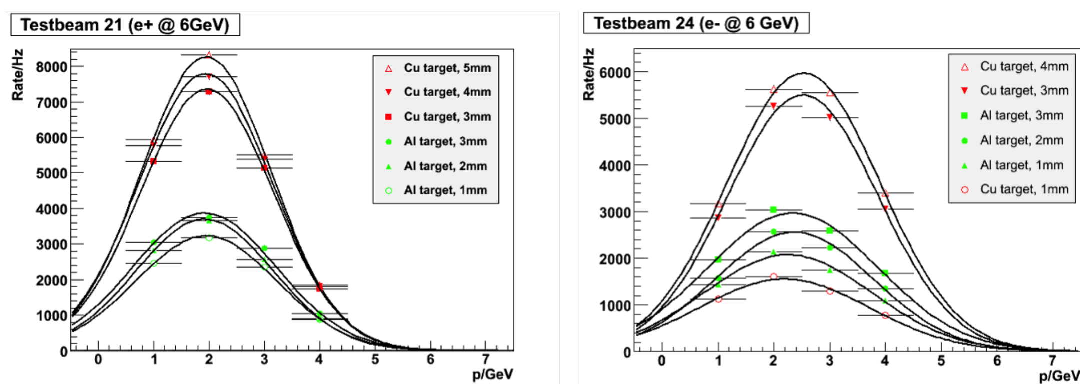

Figure 9.16: Rate vs momentum for test beam hall 21/22 (left) and test beam hall 24 (right), with $6\,GeV$ electron/positrons in DESYII [171].

CERN

Fractions of the SPS beam at CERN are extracted before injection into the LHC and directed towards a set of targets (T2, T4 and T6), producing beams of muons or pions. Only pion beams have been used to characterise modules in this thesis. The pion beam is available for 5-10 seconds in a 50 second super cycle at a typical momentum of $180\,GeV/c$. For more information on the SPS see Section 2.1.

Test beams at CERN are preferred to DESY because the higher momentum particle beam is less affected by multiple scattering, allowing for easier and, more importantly, more accurate reconstructed pointing resolution.

9.6.2 The EUDET Telescope

The EUDET telescope consists of six identical mimosa-26 [172] pixel detectors, divided in two groups (arms) of three planes. The Devices Under Test (DUTs) are mounted in between the two telescope arms. To reduce the track extrapolation error, the DUTs are mounted as close to the telescope arms as possible. The first telescope arm (relative to the beam direction) is referred to as the upstream arm and the arm mounted after the DUTs is referred to as the downstream arm. A coincidence trigger of four scintillators (two up stream and two downstream of the telescope) are used for triggering. The resulting trigger area is $\sim$ 20x10 mm^2 [173].

Further telescopes copied from the EUDET telescopes design have been built by the DESY group. The ACONITE telescope built for ATLAS was used to acquire most of the data presented in the subsequent sections of this thesis. Figure 9.17 shows a picture of the ACONITE telescope at DESY, with two DUTs mounted in-between its telescope arms.

Figure 9.17: Picture of the ACONITE telescope, featuring two telescope arms with two DUT's mounted in-between. The beam direction here (DESY) travels right to left. The upstream scintillators can be seen on the far right.

9.6.3 Cooling

To cool devices during a test beam, DUTs are mounted in a thermal enclosure with copper tape thermally connecting the backs of the DUTs to the metal base plate within the enclosure. If the DUTS are irradiated or have very high reverse currents (due to radiation damage), blocks of dry ice (CO_2) are placed on the metal base plate providing cooling down to - 40 °C. This is illustrated in Figure 9.18.

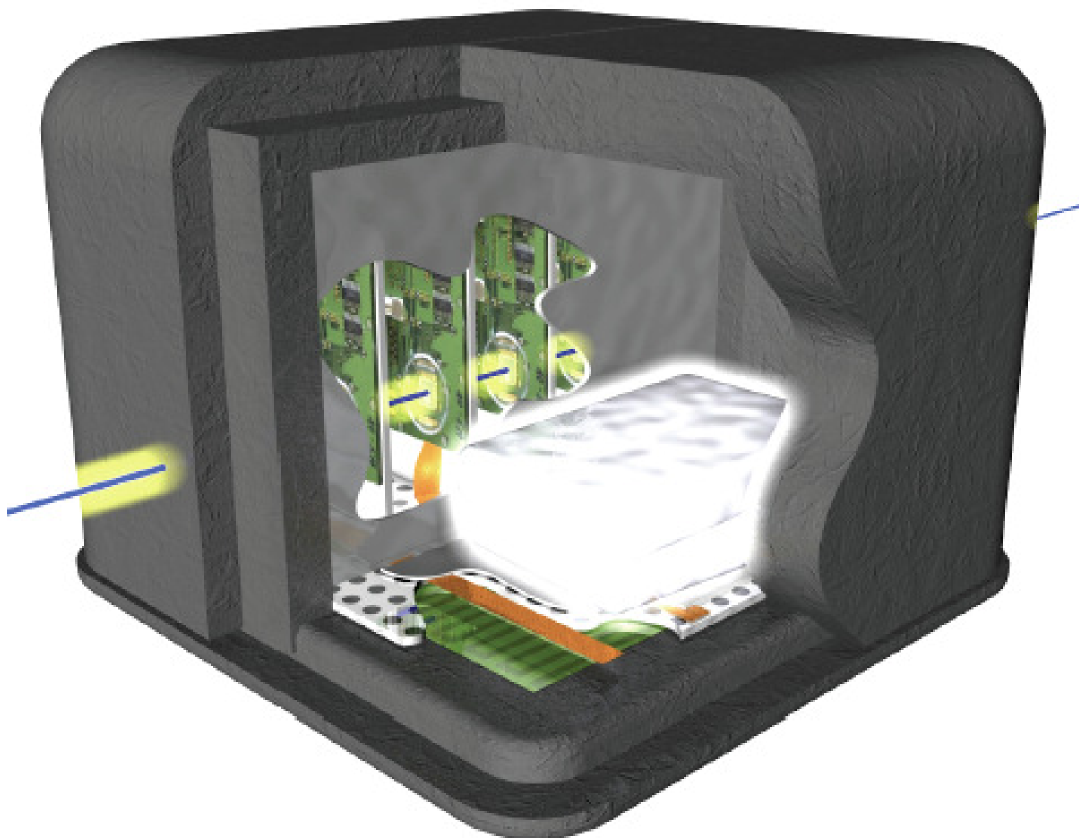

Figure 9.18: CAD image of the thermal enclosure used during test beams. Two separations in the enclosure can be seen where DUTs are mounted (left side) and where the dry ice is mounted (right side) [28].

9.6.4 Track Reconstruction

The tracks from particles traversing the EUDET/ACONITE telescope are reconstructed from raw hit positions by a sequential algorithm. This is performed using MARLIN processors within a software framework called EUTelescope [174]. The flow diagram for this process is given in Figure 9.19.

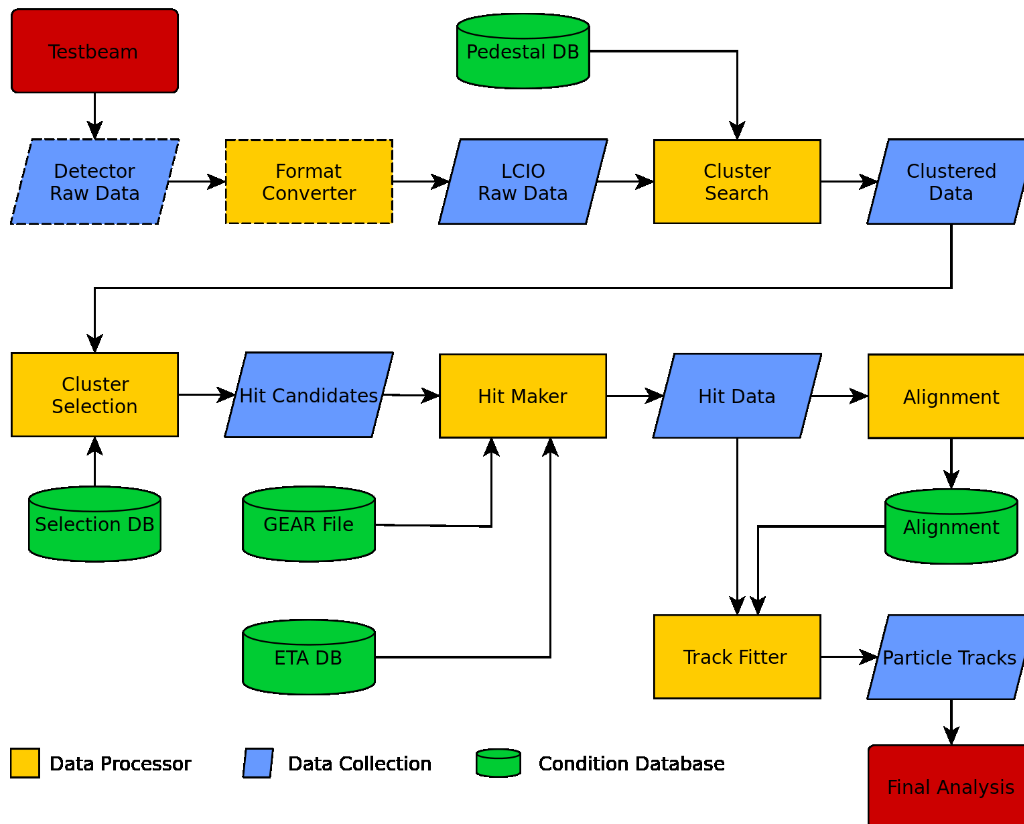

Figure 9.19: Full test beam track reconstruction flow map using the EUTelescope framework. Yellow boxes indicate MARLIN processes. Blue boxes indicate input output data files used at each step and green boxes indicate geometry or database files providing telescope set-up information [174]

Converter:

Data recorded by the telescope for all planes including THE DUTs is decoded and converted to the EUTelescope native data format (.slcio). Every hit in a trigger event has a corresponding time stamp, issued by the telescopes trigger logic unit (TLU) [175]. This enables recovery of data from losses in synchronisation between the telescope and DUTs, providing the de-synchronisation isn't too severe. The mimosa26 telescope sensors use a rolling shutter read-out technique, where the telescope integrates hits during 112 ms

from the arrival of a trigger signal. This is much longer than the 400 ns hit-buffer of the DUTs (FE-I4), so the telescope will record additional tracks that are not present in the DUTs. To correct for this effect, only hits that were recorded within the sensitive time of the DUTs are retained for further use.

Clustering:

A clustering algorithm is run to group hits into clusters for each sensor plane (telescope and DUT). The two main clustering algorithms used are *Cluster Weighted Centre* and *Cluster Charge Weighted Centre*. In both cases the centre of a cluster is calculated based on the cluster size and distribution around its seed however, the charge weighted algorithm also uses the amount of charge in each pixel as a weight to improve its accuracy in low η runs.Here, the cluster hits are still in the sensors local frame of reference.

Hitmaker:

Hits are determined from clusters by transforming from the sensors local coordinate system to a global coordinate system (telescope reference frame), where the z-direction gives the beam direction. During this transformation the pixel sizes in x- and y-directions, the specified z-position of all sensors, and their rotations about all axis are taken into account. A coarse pre-alignment of all telescope and DUT planes is performed using correlations between hit positions in different planes in the global reference frame (telescope reference plane).

Alignment:

Alignment of all sensor planes is performed taking into account their different spatial resolutions and individual track selection criteria based on the pre-alignment calculated in the Hitmaker processing step. The alignment processor utilises the MILLIPEDE II software tool [176, 177], such that the alignment constants and the χ^2 of the track residuals are minimised. All the reconstructions performed for this thesis had the first telescope plane fixed, relative to the nominal beam position.

Fitter:

This is the final reconstruction step, where tracks are fitted to fully aligned planes. A Kalman like fitting algorithm [15, 178] called Deterministic Annealing Fitter (DAF) is used to fit tracks to hits along all sensor planes. This fitter allows for a variety of criteria to be applied. The track fits are unbiased [180], the standard criteria set requires a hit in

at least four out of six telescope planes and in one DUT. Finally, all reconstructed track parameters are stored in a ROOT file for further analysis [173].

9.6.5 Data Analysis

The analysis of reconstructed test beam data is done in several steps using a dedicated data analysis framework (TBmon) [181].

The first analysis step removes noisy and un-responsive pixels by masking them out. A pixel is unresponsive if it registers no hit during the full data taking period and noisy if more than $5 \cdot 10^{-4}$ of all hits registered to a single pixel are not correlated with the particle beam. For un-irradiated devices the amount of pixels masked out, within the scintillator area is usually below 1 %. However, the amount of masked pixels increases after irradiation depending on fluence and can differ from device to device. On average, about 10 % of pixels are expected to be masked out due to issues caused by faults in the readout chip or increased noise (shot noise) due to the increased leakage current in the sensor. Figure 9.20a and Figure 9.20b show the raw hit data (scintillator shape can easily be seen) and resulting pixel mask for a DUT.

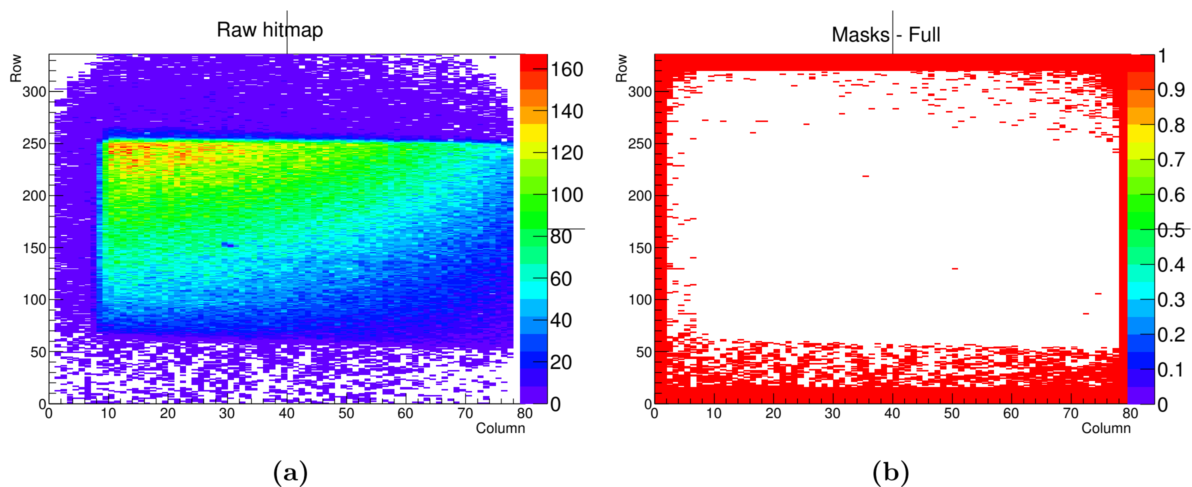

Figure 9.20: (a) 2D raw track hitmap for an FE-I4 sensor, the 2 cmdiameter beam spot and 2x1 cm scintillator outline can be seen. (b) 2D mask histogram showing pixels masked out (red).

Next the LVL1 (level-1) hit distributions of the DUTs are checked. This is to ensure that the hits registered by the DUTs are associated to tracks; this can be seen in Figure 9.21. The LVL1 distribution shows the arrival time of recorded hits with respect

to the external trigger signal (TLU). The pronounced peak shows that hits have a strong correlation with the timing of the external trigger signal. If there is any background noise or entries far away from the main LVL1 peak, cuts can be applied to suppress the hits not associated with tracks.

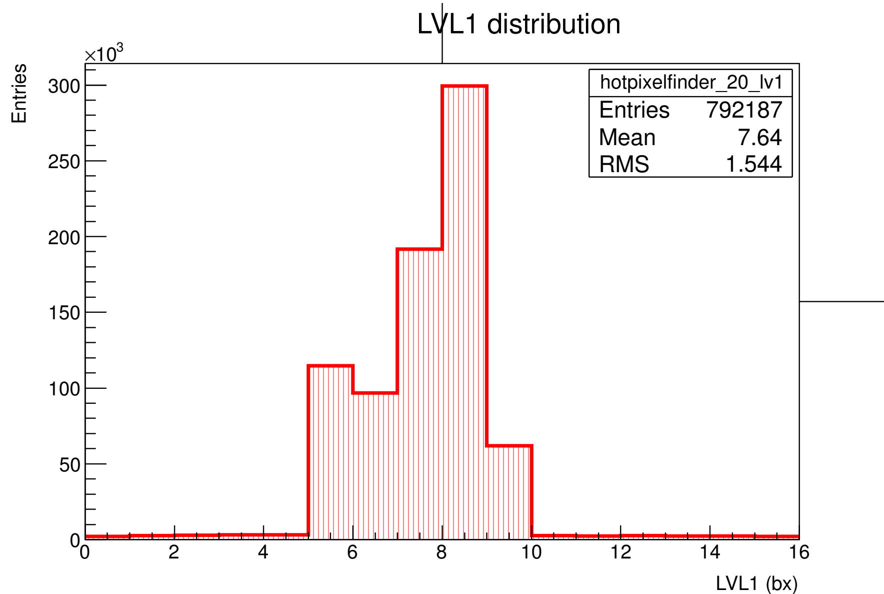

Figure 9.21: LVL1 distribution, showing the arrival time of all hits with respect to the external trigger signal. LVL1 is measured in numbers of $25ns$ long bunch crossings (bx).

In the following analyses, tracks extrapolated from the telescope are "matched" to a hit if the hit and extrapolated tracks impact point on the DUT containing the hit are closer than 400 μm in the long direction and 150 μm in the short direction. The hit position is defined as the η corrected ToT weighted position [182] of all pixels in a cluster.

To estimate the intrinsic spatial resolution of the DUTs the distribution of hit residuals is studied. The hit residual is defined as the distance between the reconstructed hit position on the DUT and the extrapolation of the fitted track to the DUT plane. The intrinsic spatial resolution is estimated by the RMS of the residual distribution for clusters of all sizes. However, the residual distribution of 2-pixel clusters is used to estimate the width of the area between pixels, where charge sharing occurs. The distribution should be gaussian and there are various algorithms for calculating the centre of a cluster and can be found in [182].

The charge sharing probability for each hit within a cluster can be calculated, if hits are found in adjacent pixels next to pixels from a matched track. The probability increases towards the edge of the pixels, since charge carriers are more likely to drift to

neighbouring pixels. Irradiation dose, bias voltage and track inclination also affect this. Figure 9.22 shows the 2D charge sharing distribution for a un-irradiated FE-I4 module at 100V (fully depleted) for perpendicular tracks centred on one pixel and extending by half a pixel pitch in all directions. The overall charge sharing is defined as the number of tracks with at least one hit in neighbouring pixel divided by the number of all tracks.

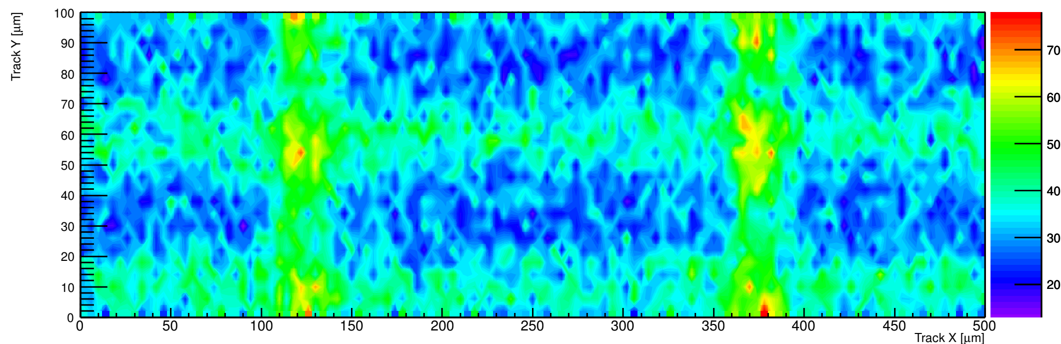

Figure 9.22: 2D charge sharing distribution around a pixel. Charge sharing is defined as the number of tracks with at least one hit in neighbouring pixel divided by the number of all tracks. The colour map is a measure of the ratio of tracks that share charge (cluster size > 1 between pixels with respect to all tracks). The contour range set is arbitrary.

Finally, the determination of a device's hit efficiency is crucial. The hit efficiency for a pixel is defined as the ratio of the number of measured hits close to a track, against the total hit predicted. The expected hits are determined using reconstructed matched tracks.

Chapter 10

RD50 Studies

This section details work performed for the CERN RD50 collaboration [19] to ascertain the radiation hardness of planar silicon sensors intended for use at facilities requiring radiation hardness beyond that for the LHC, such as for ATLAS at HL-LHC, see Section 2.3.3. Unless otherwise stated, all sensors have been produced by Micron Semiconductors Ltd [20]. The majority of the tests involves measuring the leakage currents and CC(V) response (collected charge) using the ALiBaVa system (Section 9.4) as a function of irradiation. Important information regarding the irradiation facilities used to irradiated sensors is detailed in Section 9.3.

10.1 Calibration

The readout system needs to be calibrated to accurately measure the responses of irradiated detectors in term of the value of the collected charge expressed in the number of electrons. Minimum ionising particles are used to induce charge in the detectors. Un-irradiated sensors are assumed to have zero charge trapping, resulting in the whole induced charge being read out. The total induced charge read out for a MIP depends on the device thickness. The readout system has to be calibrated separately for thin ($\sim 100\,\mu$m) and thick ($\sim 300\,\mu$m) sensors because the most probable energy deposited by a MIP is not linear with the material thickness.

To perform the calibration, 1x1 cm^2 *n-in-p* silicon micro-strip sensors of different thicknesses (100, 150, and 300 μm) were produced. Actual wafer thickness can vary slightly from wafer to wafer and across the wafer itself. The wire bonding machine used to connect the sensor to the daughter board was used to measure the average thickness

of each sensor by measuring the touchdown height of the bonding tool in three places across the sensor. The average thicknesses of the sensors were found to be 106, 144, and 296 $\pm$ 3 μm. Knowing the exact sensor thickness allows for an estimation of the most probable value (MPV) of the resulting energy spectrum generated by a MIP for an unirradiated device. An empirical formula for the MPV of the charge ionisation of MIPs in silicon detectors of different thickness is:

$$Q = \frac{d}{3.68}(190 + 16.3\,ln(d)) \quad , \tag{10.1}$$

where Q is the total charge deposited and d is the sensor thickness [183]. Figure 10.1 shows the expected total charge as a function of sensor thickness using Equation (10.1). The average number of electron-hole pairs created per μm is then calculated by dividing by the known device thickness.

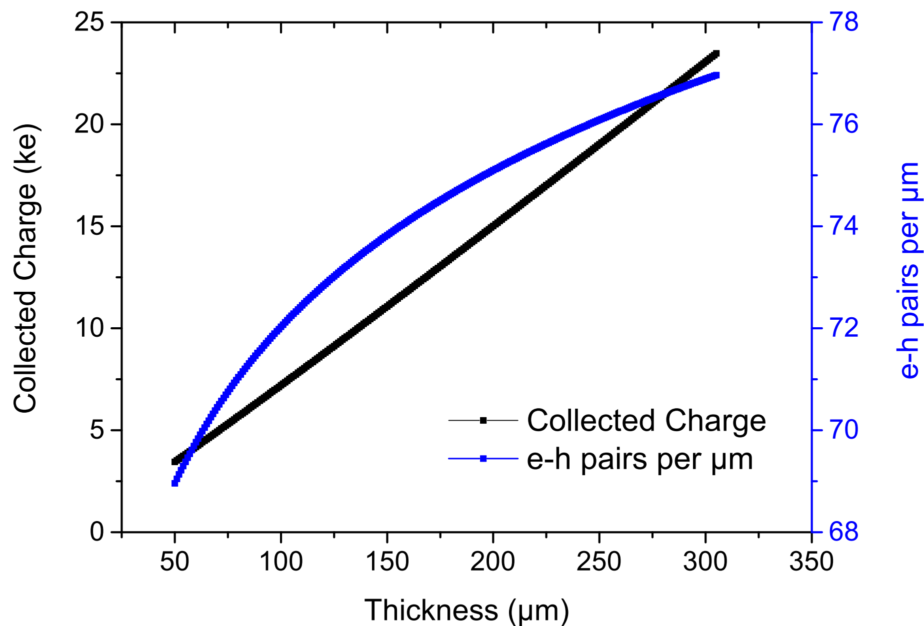

Figure 10.1: The most probable value (MPV) expected as a function of sensor thickness (left y-axis), and the average number of expected electron-hole pairs generated per μm of depleted silicon.

The difference between the number of e-h pairs generated per μm of silicon in thin ($\sim$ 100 - 150 μm) and thick ($\sim$ 300 μm) sensors is noticeable and should be taken into account. However, the change in MPV for deviations in the thickness of order $\pm$ 10 μm is

small. Therefore, it is unnecessary to re-calibrate for small variations in sensor thickness. This is useful as the process of measuring the sensor thickness can damage the surface of the sensor, which can have implications for the leakage current of the device.

As described in Section 9.4 the ALiBaVa system reads out the signal in ADC counts. These are converted to electrons using a calibration constant named ADC_to_e. The ALiBaVa system also allows for the gain to be changed. A pair of jumpers on the ALiBaVa mother board controls whether the system is operated in full or half gain mode. This changes the input voltage to the ADC circuitry. At full gain 2.048V is supplied giving a resolution of 2 mV/bit (10 bit ADC) and at half gain 1.024V is supplied giving a resolution of 1 mV/bit [184]. This feature allows the dynamic range of the system to be tailored to the thickness of devices. The 106 and 144 μm thick sensors calibration was performed in full gain mode and whilst 296 μm sensor was calibrated in half gain mode.

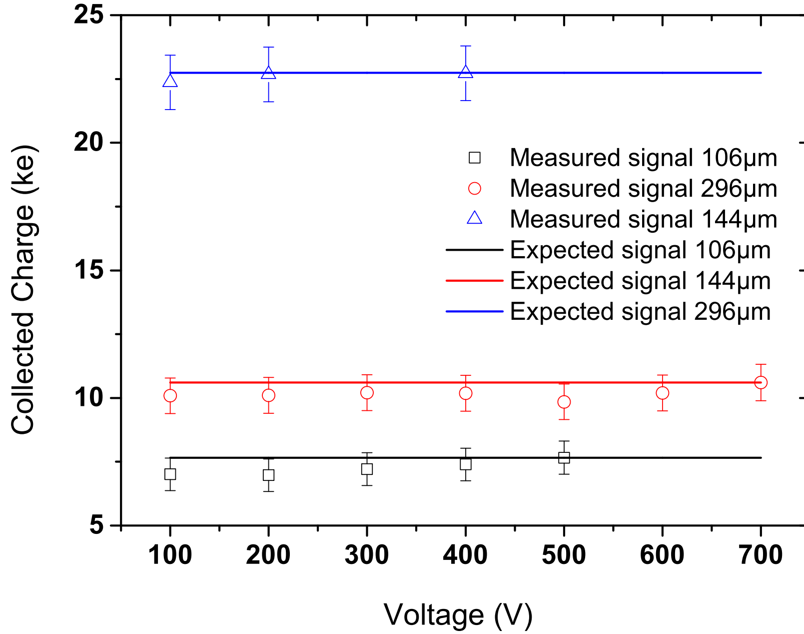

Figure 10.2: Measured and expected total signal charge for 106, 144, and 296 μm thick sensors after calibration has been applied.

Devices are tested at various bias voltages above V_{dep} using the ALiBaVa system. The calibration constant ADC_to_e is then calculated using:

$$ADC_to_e = \frac{Q_{Expected}}{ADC_{Measured}} \tag{10.2}$$

Figure 10.2 shows the expected MPV (ke) for each device thickness (solid lines) used to calculate the ADC_to_e value for each sensor. The actual charge measured (ke) by each sensor at each bias voltage was then overlaid including the uncertainty measurement as a cross check to indicate good agreement. Table 10.1 summarises the results for each sensor thickness.

	106 μm	144 μm	296 μm
Gain Mode	Full	Full	Half
Total Charge (ke)	7.66	10.60	22.73
Number of e-h pairs per μm	72.3	73.6	76.8
ADC_to_e	57.08	59.78	123.47

Table 10.1: Summary of important parameters for the calibration of silicon micro-strip sensors with varying thickness.

10.2 Mixed Irradiation

To understand the performance of sensors after irradiation with different particle types is important to predict their performance in the radiation environment at the HL-LHC. Six 1x1cm^2 sensors produced by Hamamatsu Photonics were irradiated in consecutive irradiation steps with 280 MeV/c pions, 25 MeV/c protons and reactor neutrons, resulting in a combined fluence of up to $3 \cdot 10^{15}\,\mathrm{n_{eq}/cm^2}$. This particle composition and fluence corresponds to the qualification limit specified by the ATLAS experiment for the outer pixels layers at HL-LHC (assuming an integrated luminosity of 3000 fb^{-1}). The limits are based on calculations using FLUKA simulations for the proposed ATLAS upgrade [185]. Figure 10.3 shows the fluence limits for each hadron type as a function of mounting radius.

Sensor qualification was done using 320 μm thick devices (with 300 μm sensitive thickness) by measuring the total signal charge generated by beta particles from a ^{90}Sr source as a function of bias voltage using the ALiBaVa system. Measurements of the collected charge have been made for all sensors as a function of fluence and particle type [186].

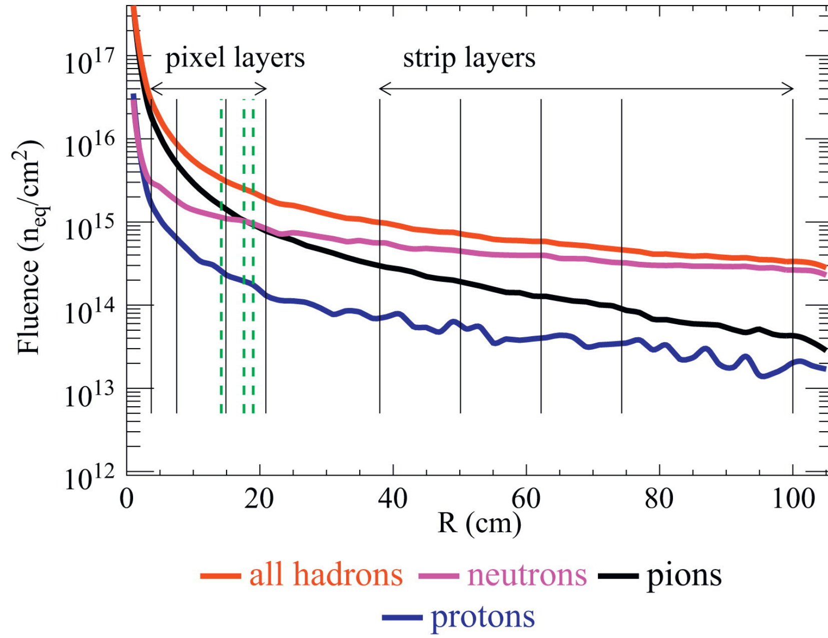

Figure 10.3: Equivalent fluence for different hadron types as a function of the distance from the interaction point for an integrated luminosity of 3000 fb^{-1}. The data is shown for z=0, a safety factor of two was applied, data from Ref [186]. The dashed lines indicate the radii corresponding to the irradiated fluences.

10.2.1 Irradiation and Characterisation

The devices produced by Hamamatsu are *n-in-p* micro-strip detectors (ATLAS07 series), produced on float-zone silicon wafers with a thickness of about 320 μm. Each device has a 20 μm deep p^+ implant on the backside (ohmic contact) meaning that only 300 μm of the sensor thickness is sensitive for particle detection. The bulk resistivity of the wafers is 6.7 $k\Omega$cm and features a single p-stop structure for implant isolation. Each sensor is 1x1 cm^2 and has 104 strips which are 0.8 cm long with a pitch of 74.5 μm. More information on the irradiation facilities used can be found in Section 9.3. The different fluences and their corresponding radii for the ATLAS inner tracker upgrade are listed in Table 10.2. The values are a close approximation to what is expected at each given radii, assuming a final integrated luminosity of 3000 fb^{-1} and a safety factor of two on the fluence calculation.

Two sensors were irradiated at each fluence with their CC(V) being measured after each irradiation step. Additionally, one unirradiated sensor was characterised as a benchmark to cross check the calibration of the system. One device at the lowest fluence suffered destructive breakdown after proton irradiation and therefore was not sent for

Radius (cm)	Pions (280 MeV/c) 10^{15} n_{eq}/cm^2	Protons (25 MeV/c) 10^{15} n_{eq}/cm^2	Neutrons (reactor) 10^{15} n_{eq}/cm^2	Sum 10^{15} n_{eq}/cm^2
19	0.93	0.19	0.95	2.1
17.6	1.2	0.26	1.0	2.5
14.2	1.4	0.26	1.1	2.8

Table 10.2: Table of different fluences applied for mixed irradiation. The first column indicates the distance from the interaction point where the corresponding particle composition is in close approximation expected in the ATLAS tracker upgrade.

subsequent irradiations. The total accumulated annealing time for the devices has been estimated to be about 3 days at 20 °C.

The characterisation of these devices was done in a collaboration between the Universities of Liverpool and Freiburg (Germany). Both sites used the ALiBaVa readout system with a ^{90}Sr source and tested the devices under the same conditions after irradiation, cooling them to - 22 ± 2 °C and taking measurements in 100 V bias steps from 200 V to 1100 V.

10.2.2 Results after Irradiation

Measurement results for the signal as a function of bias voltage for pion and pion plus proton fluences are shown in Figure 10.4a and Figure 10.4b respectively. The different fluence are colour coded and grouped accordingly. For comparison the results from a unirradiated sample are also shown on Figure 10.4a. The signal saturates at around 200 V indicating full depletion of the device. After pion irradiation no saturation in the signal is seen. However, around 900 V the signal increase slows down hinting at the device approaching full depletion. At a fluence of $1.4 \cdot 10^{15}$ n_{eq}/cm^2 full depletion is expected to occur around 1000 V [191].

Charge collection results after pion and proton irradiation are shown in Figure 10.4b. Since the proton dose is low compared to the pion dose the degradation in signal after proton irradiation is not expected to be very large, as can be seen in Figure 10.4b. At 1000 V, sensors at the maximum pion dose ($1.4 \cdot 10^{15}$ n_{eq}/cm^2) have a signal of about $19 \pm 1\,ke$ compared to $18 \pm 1\,ke$ after the subsequent proton irradiation. This trend is seen across all sensors.

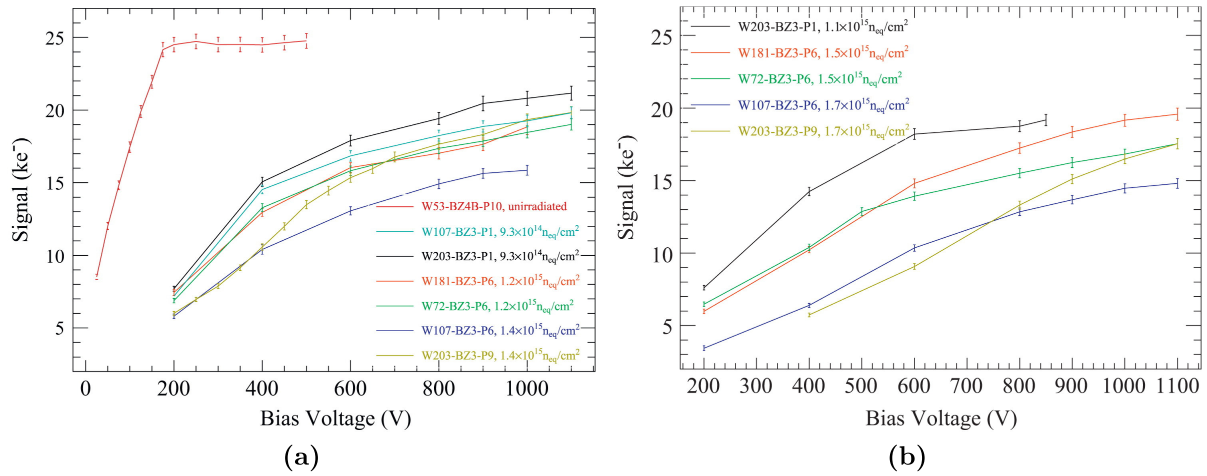

Figure 10.4: (a) Signal (MPV) after pion irradiation as a function of bias voltage, including (red) a unirradiated device for comparison. (b) Signal (MPV) after pion and proton irradiation as a function of bias voltage.

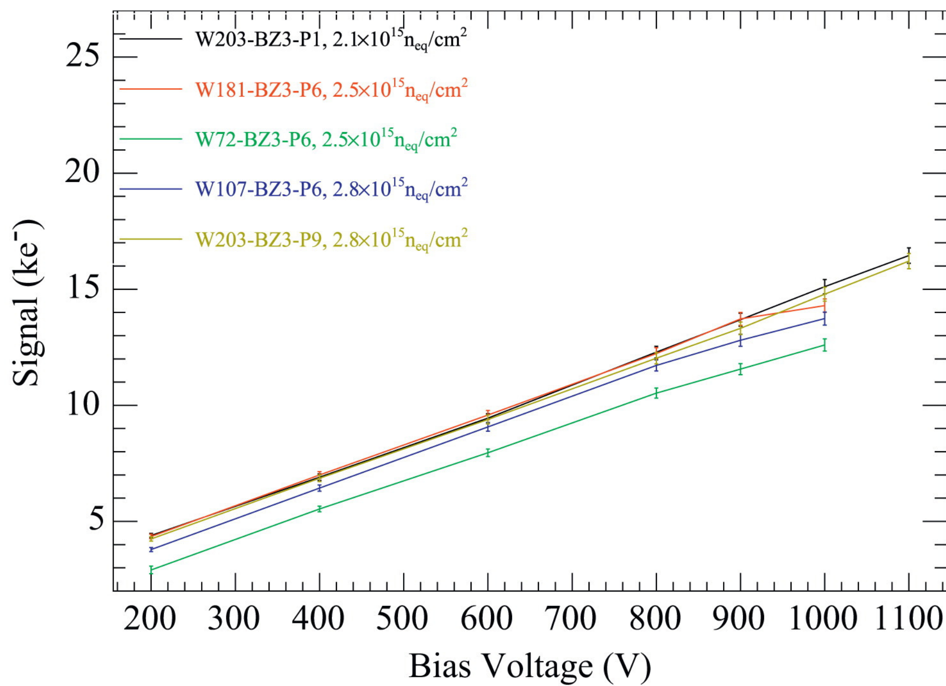

Figure 10.5: Signal (MPV) after mixed irradiation with three types of hadrons (pions,protons and neutrons).

Results from the charge collection measurement after the final irradiation with reactor neutrons are shown in Figure 10.5. Here there is no indication of saturation up to 1100 V. The signal rises almost linearly with bias voltage. The total spread in signal for the most heavily irradiated sensors (mixed irradiation, $2.8 \cdot 10^{15}\, \mathrm{n_{eq}/cm^2}$) at 1000 V

is $(11 - 16) \pm 1\,ke$, which is not far from the signal spread before neutron irradiation $(13 - 19) \pm 1\,ke$, at 1000 V.

The sensor noise measured as a function of the bias voltage is given in Figure 10.6. The noise varies with fluence, from 700 to 850 electrons, this is a small effect because the readout electronics are unirradiated. No significant noise increase is seen as each sensors bias voltage is increased up to 1100 V. Any small change in noise is within the uncertainty. The shot noise contribution in this case is negligible.

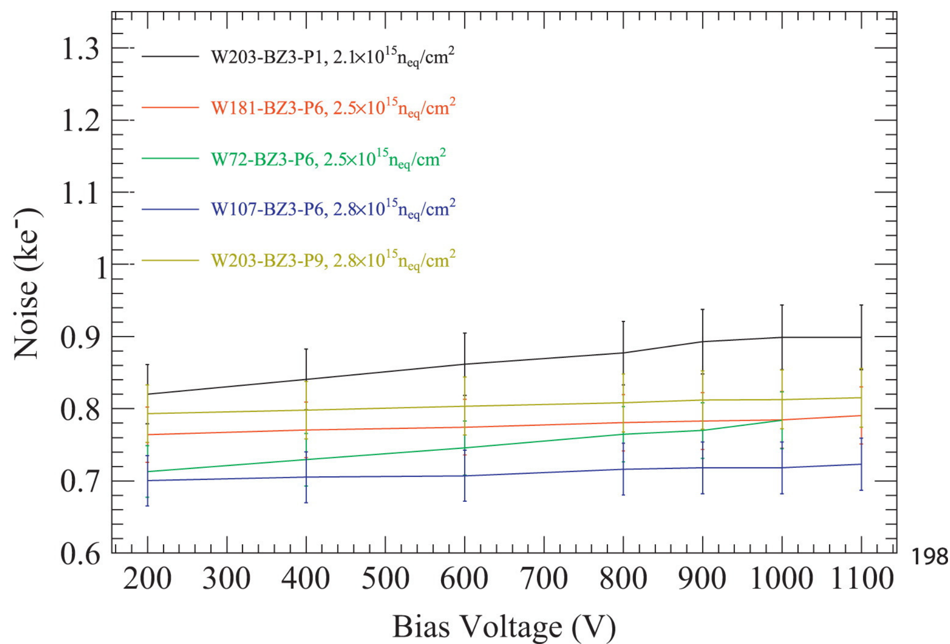

Figure 10.6: Noise of sensors after mixed irradiation (pion, proton and neutron) as a function of bias voltage.

It is foreseen that during the inner tracker upgrade, the existing power cables will be re-used for the outermost pixel layers (14.2, 17.6 and 19.0 cm) where possible as their performance is not expected to degrade. these cables have only been qualified for safe operation up to 500 V. For this reason, to understand the expected signal yield after irradiation when taking into account the limitation on the power cables, Figure 10.7a and Figure 10.7b show the evolution of the signal at 400 and 600 V respectively as a function of the total received fluence.

A quantitative comparison of the signal after irradiation for a given radius and fluence is given in Table 10.3 at 400 and 600 V.

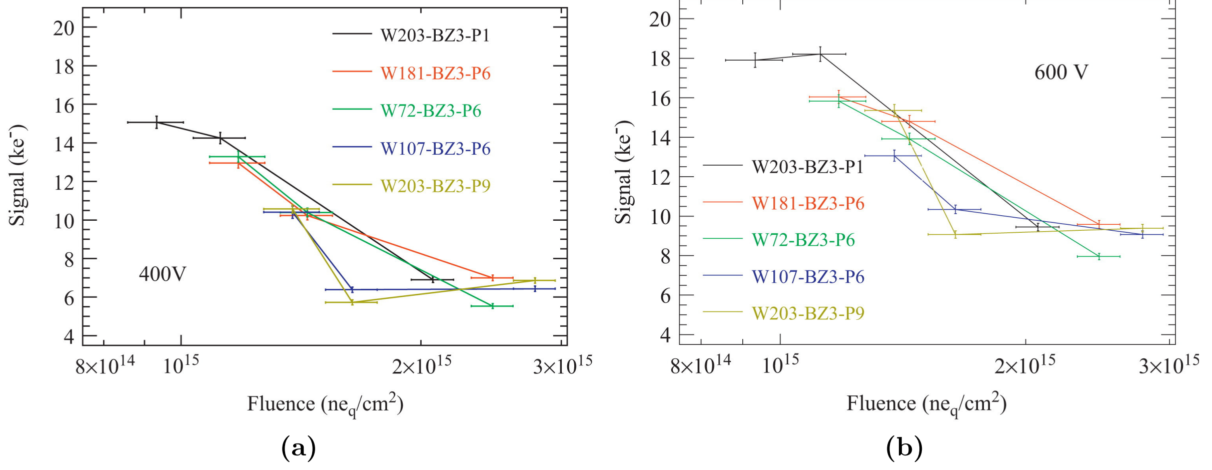

Figure 10.7: Evolution of signal (MPV) as a function of total fluence at (a) 400 V bias voltage and (b) 600 V.

V_{bias} (V)	Signal (ke^-)	Noise (ke^-)
$2.1 \cdot 10^{15}\,\mathrm{n_{eq}/cm^2}$, radius 19.0 cm		
400	7.9 ± 0.4	0.83 ± 0.04
600	10.8 ± 0.6	0.85 ± 0.04
$2.5 \cdot 10^{15}\,\mathrm{n_{eq}/cm^2}$, radius 17.6 cm		
400	6.2 ± 0.1	0.75 ± 0.04
600	8.8 ± 0.2	0.76 ± 0.04
$2.8 \cdot 10^{15}\,\mathrm{n_{eq}/cm^2}$, radius 14.2 cm		
400	6.5 ± 0.5	0.72 ± 0.04
600	9.0 ± 0.7	0.73 ± 0.04

Table 10.3: Measurement results after mixed irradiation (pions, protons and neutrons).

10.2.3 Conclusion

The measurements show degradation (lower charge collection for a given bias voltage) in sensor performance after irradiation with pions, protons and reactor neutrons up to $2.8 \cdot 10^{15}\,\mathrm{n_{eq}/cm^2}$. After the maximum fluence the signal ranges from 11 to 16 ke compared to 24 ke unirradiated. The signal after mixed irradiation is comparable to the signal seen by sensors irradiated with a single particle type. To ensure efficient operation in an experiment a signal to noise ratio of at least 10 should be achieved [187]. Based on the signal measured at 400 and 600 V it is plausible to suggest that the power cables for the outer pixel barrel layers could be used (refer to Table 10.3). Although further tests

would need to be done with a greater number of sensors and with the actual irradiated readout electronics in order to calculate the expected signal to noise at each fluence [188].

10.3 CNM Planar Trenched Detectors

The effect of charge multiplication is well documented within the RD50 collaboration [19]. The presence of very large electric fields in a small region near the readout implant junction accelerates electrons beyond the limit of impact ionisation which releases more charge carriers. This effect can possibly be exploited by manipulating the implant junction to create regions with larger electric field gradients. To this end, deep n^+ structures could enhance or surpress the multiplication, The same effect could also be obtained by varying the doping gradient near the junctions.

To investigate this possibility, a dedicated fabrication run of 1x1 cm^2 300 μm thick, high resistivity p-type bulk devices designed by Liverpool in collaboration with IBN-CNM, Barcelona, were processed. Two technologies have been implemented. A deep p-doping diffusion under the n^+ implant and trenches etched in the middle of each strip into the bulk silicon, filled with n^+ doped poly-silicon to create deep junctions. These devices have been characterised before and after neutron irradiation up to HL-LHC fluences.

10.3.1 Geometry Description

The conventional p-type strip detector structure, shown in Figure 10.8(a) features 128 readout strips with a 75 μm pitch and an implant width of 30 μm. Figure 10.8(b) shows the modification to include trenches, which are etched through the centres of the strip implants and then coated with n-doped poly-silicon, creating a deep structure. This type of detector has been processed in three flavours, with trenches of 5, 10 and 50 μm deep with a 5 μm width. Figure 10.8(c) shows the version with a dedicated p^+ implant ,5 μm wide, under the n^+ strip creating a structure similar to an avalanche photo-diode. Finally, the version shown in Figure 10.8(d) is similar to Figure 10.8(b) but instead of an n-doped poly-silicon coating in the trenches, it features an oxide filled trench with p-type implantation. This structure was only fabricated with 5 μm deep trenches for the purpose of this study.

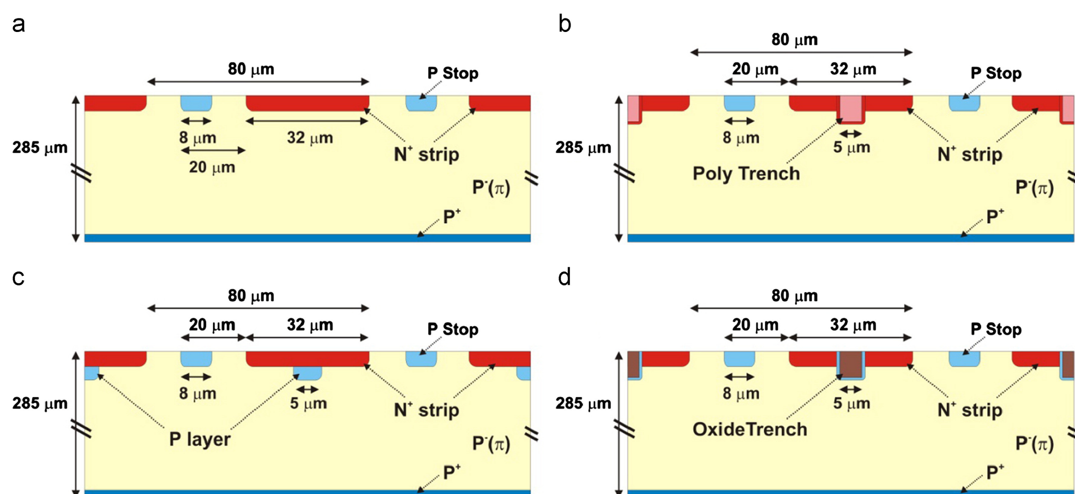

Figure 10.8: Schematic view of the structures studied in the work. (a) Conventional p-type micro-strip detectors; (b) "Poly trench" variation, including a poly-silicon trench doped with phosphorus, along the centre of the strip pitch; (c) "P-Layer" variation, including a p-type diffusion below the n^+ electrode; (d) "Oxide trench" variation, including an oxide filled trench along the centre of the strip and a p-type implantation through the trench. [189]

All structures in Figure 10.8 were previously simulated with the TCAD device simulation package (Sentaurus). The modules have been simplified for 2D simulations based on the schematic views in Figure 10.8. Detailed information about the simulation and processing of these devices at CNM is given in Ref [189].

Figure 10.9 shows the simulated electric field distributions in 2D at a bias voltage of 400 V. Figure 10.9a shows the electric field distribution for the standard sensor. The "Poly trench" structure (b) exhibits a slight increase in electric field strength in the central regions under the strip implants where the trenched are compared to the standard device. The "P-Layer" design (c) also shows an increase in electric field strength in the central region, under the strip implant. The final design variation (d), "Oxide trench", shows similar electric field distributions to the "Poly trench" structure. In all cases the electric field distribution is only influenced under the strip implant near the center, and not affected at the edges of the strip implants.

10.3.2 Pre-irradiation Characterisation

The processing required to make the trenched style detectors is expected to yield devices with degraded current-voltage characteristics compared to standard planar devices, at least while unirradiated. In particular, the AC coupling silicon oxide separating the

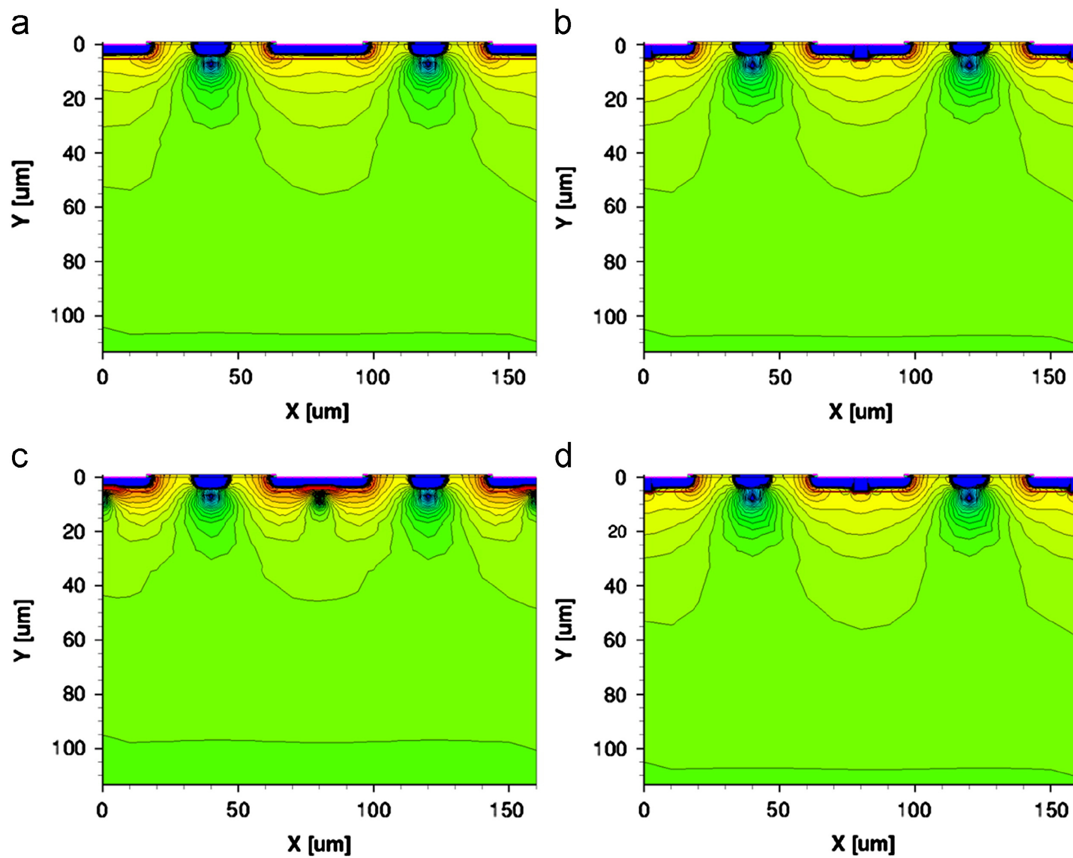

Figure 10.9: Simulated electric field distribution at an applied voltage of 400 V. The 2D sections correspond to: (a) a conventional p-type detector; (b) the “Poly trench” option; (c) the “P-Layer” option and (d) the “Oxide trench” option [189].

implants and the readout metal was anticipated to exhibit some faults, due to sharp edges at and in the trenches caused by the processing technique (Deep Reactive Ion Etching - DRIE). Figure 10.10a shows the leakage (reverse) current for the standard design sensors; Figure 10.10b the deep diffused P-Layer devices; Figure 10.10c the 5 μm deep trenched and Figure 10.10d the 10 μm deep trenched devices. It is apparent that the leakage current of the trenched devices significantly exceeds the leakage current of the standard geometry sensors. The deep diffused P-Layer devices however, have current-voltage characteristics more similar to the standard devices. However, when tested up to voltages of 500 V they do show higher currents.

Despite the high leakage currents exhibited by the junction engineered devices, it has been possible to measure their response to MIPs. The ALiBaVa system and ^{90}Sr radioactive source were used to perform the characterisation as a function of the bias voltage. The devices were all tested under a controlled temperature at - 25 °C to reduce the leakage currents and achieve high bias voltages, this was particularly important for

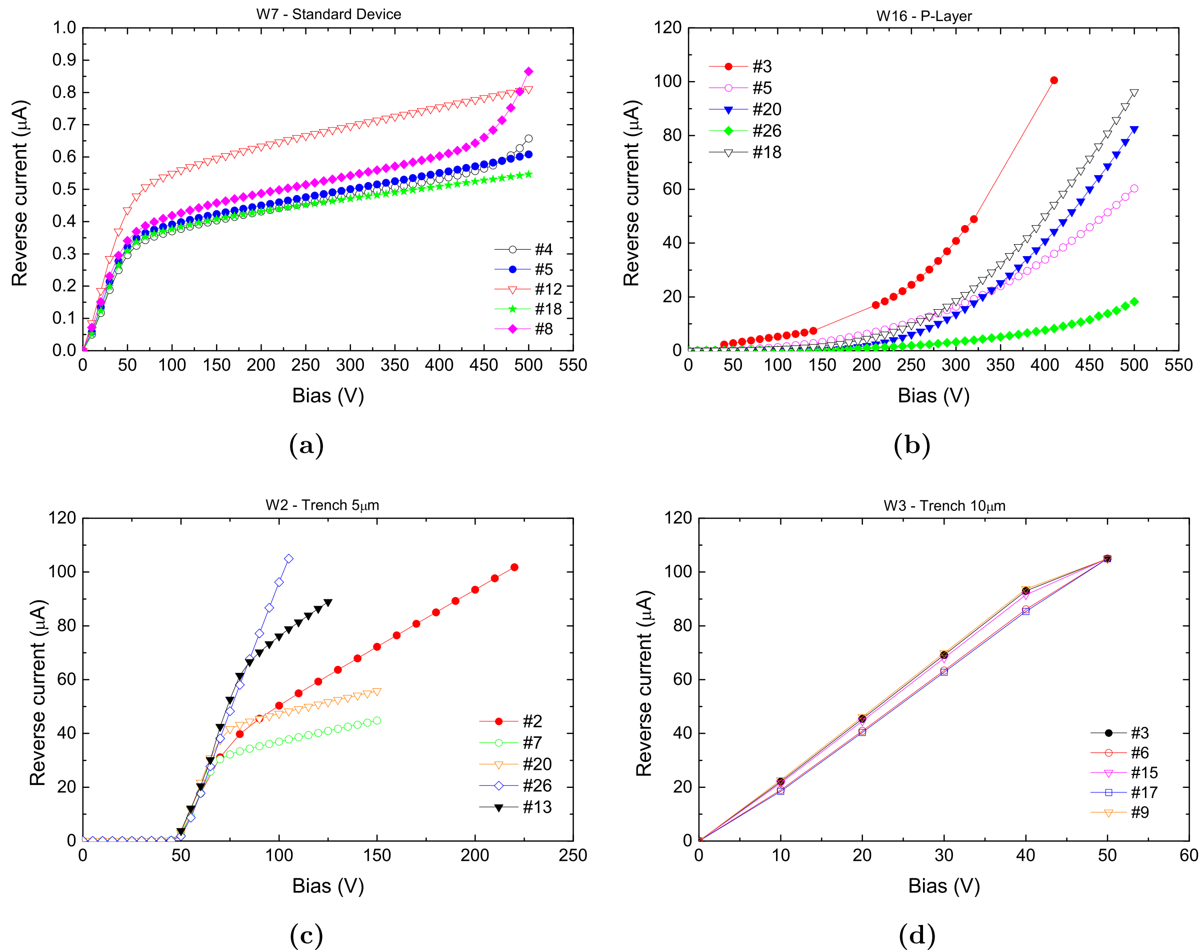

Figure 10.10: IV characteristics measured at 20 °C for standard (a), deep diffused 5 μm diffusion width, (b) detectors. 5 μm (c) and 10 μm (d) deep trench detectors.

the deep trench devices as they had very large leakage currents at room temperature. Figure 10.11 shows the signals for all the devices tested. All devices were expected to plateau before irradiation at a similar point to the standard process device, simulations only indicated slightly higher field regions near the readout implants (increasing the base leakage current). The plateau value of the collected charge for the trenched sensors (W2 and W3, with a 5 and 10 μm deep trench, respectively) appears to be slightly smaller than the standard one (W7). This variation is not explained by differences in the detector thickness (all sensors thicknesses were within 2 μm of each other).

One consequence of the modified junction is the increase of the inter-strip capacitance. This effect has negative consequences on the noise performances of the detector because the parallel noise of readout electronics for segmented silicon sensors depends linearly on the input capacitance [162]. It has in fact been verified that the trenches increase

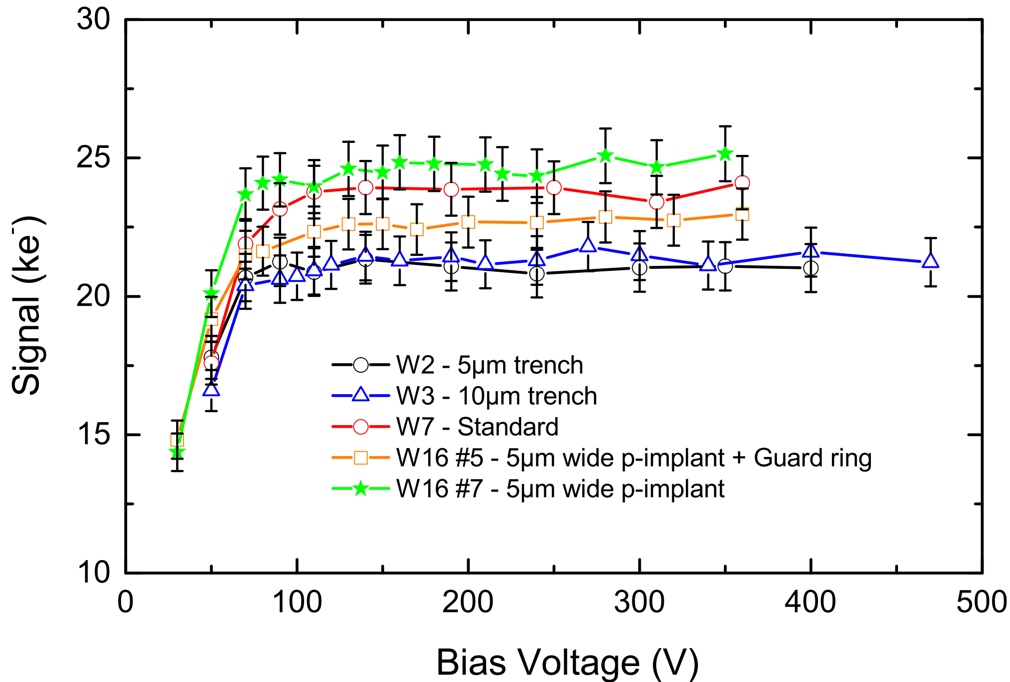

Figure 10.11: Charge collected (signal) as a function of bias voltage with non-irradiated standard (W7), 5 and 10 μm deep trenched (W2 and W3 respectively) and deep diffused (W16) detectors.

the inter-strip capacitance by a substantial fraction. Figure 10.12 shows the inter-strip capacitance (central strip to the two nearest neighbours) measured for reference and trenched sensors. The strip length is 0.8 cm with a pitch of 75 μm. The increase induced by the trench increases with the trench depth. At the higher voltages the inter-strip capacitance of the 5 μm (W2) and 10 μm (W3) trenched detectors is about 30 % and 50 % higher than standard (W7) sensor, respectively. The deep diffused detector (W16) shows the same high saturation value of the inter-strip capacitance as the reference one.

10.3.3 Irradiation and Characterisation

Several devices (standard and junction engineered) were irradiated to 1, 5, 10 and $20 \cdot 10^{15}$ $\mathrm{n_{eq}/cm^2}$ (with a 10 % uncertainty on fluence) with reactor neutrons at the Ljubljana facility (see Section 9.3). IV characteristics were measured at low temperatures (- 25 °C) to prevent annealing and to limit the leakage current and thermal run-away. Low operating temperatures do not affect the electrical behaviour displayed by the junction engineered devices before irradiation. However, after irradiation the junction engineered

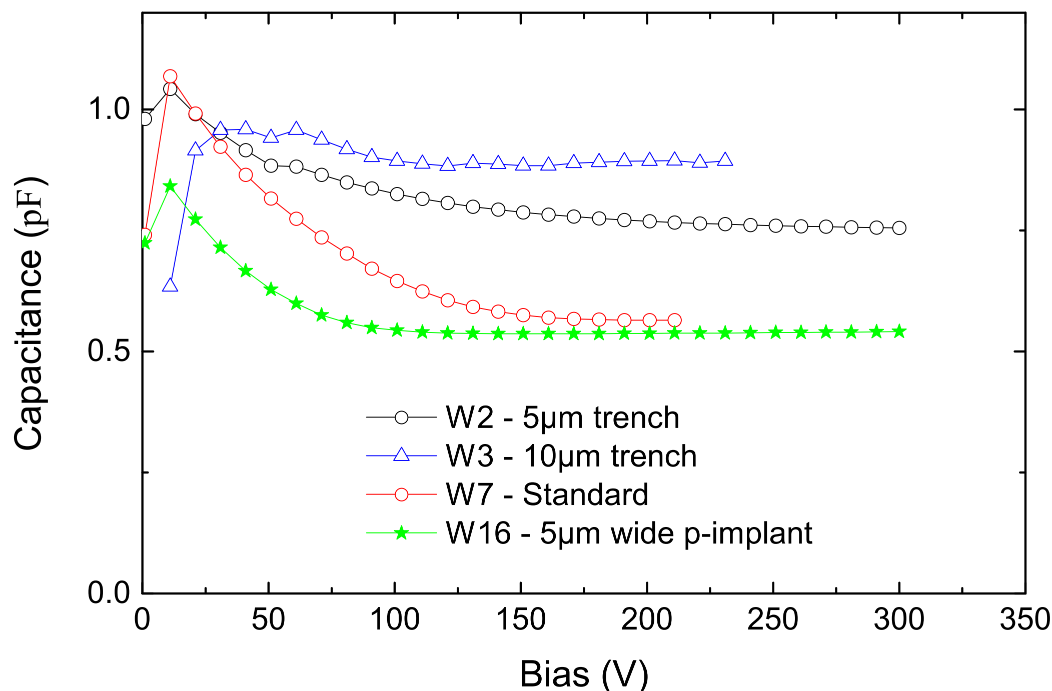

Figure 10.12: inter-strip capacitance (to first neighbours on both sides of the central strips) of reference (W7), 5 and 10 μm deep trenched (W2 and W3, respectively) and deep diffused (W16) detectors. The increase of the capacitance due to the trench is significant.

devices that performed poorly before irradiation have IV characteristics more similar to the reference devices. The measured leakage currents for the standard (W7), the 5 μm deep trench (W2) and the deep diffused p-junction (W16) after the various fluences of 1, 5, 10 and $20 \cdot 10^{15}\,\mathrm{n_{eq}/cm^2}$ are shown in Figure 10.13a, Figure 10.13b, Figure 10.13c and Figure 10.13d respectively. Further tests with the W16 + guard ring implant have not been performed of its poor pre-irradiation performance and limited availability.

After $1 \cdot 10^{15}\,\mathrm{n_{eq}/cm^2}$ (Figure 10.13a) the standard (W7) and 5 μm trench (W2) show almost identical leakage currents. The deeper trenched devices (W3 and W5) show similar behaviour except with larger leakage currents. In contrast, the p-layer device (W16) shows the lowest current of all devices up to 900 V before breaking down.

After $5 \cdot 10^{15}\,\mathrm{n_{eq}/cm^2}$ (Figure 10.13b) the standard (W7) and the deep diffused p (W16) show similar currents up to 1100 V. The 50 μm deep trenched (W5) sensor shows about double the current compared to the standard geometry whilst the W18 sensor, with a wider p-implant diffusion $\sim 26\,\mu$m, has a reverse current about three times higher than the reference. The IV characteristic of the 5 μm deep trench detector (W2) has a

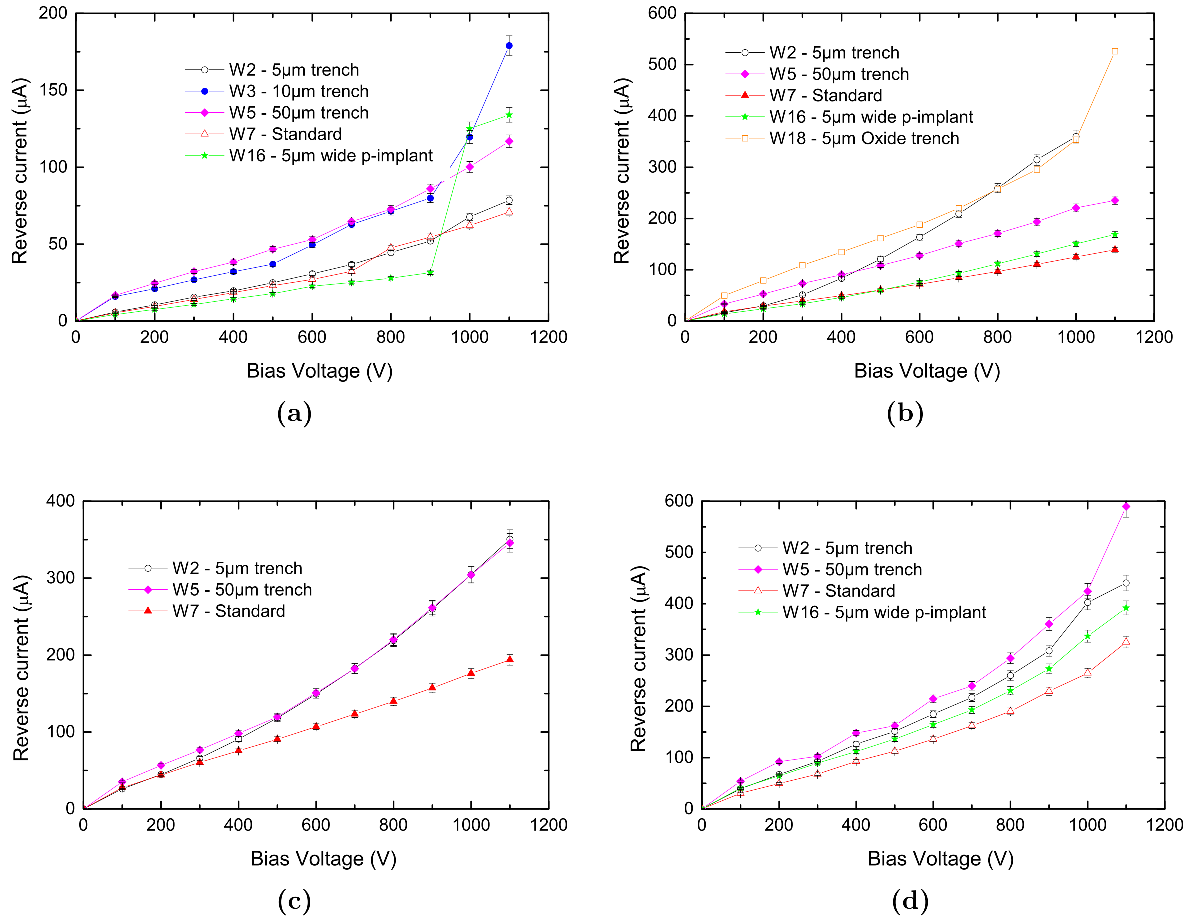

Figure 10.13: IV characteristics measured at -25 °C for standard (W7), 5 μm (W2) and 50 μm (W5) trenched and deep diffused (W16, W18) detectors, after $1 \cdot 10^{15}\,\mathrm{n_{eq}/cm^2}$ (a), $5 \cdot 10^{15}\,\mathrm{n_{eq}/cm^2}$ (b), $10 \cdot 10^{15}\,\mathrm{n_{eq}/cm^2}$ (c) and $20 \cdot 10^{15}\,\mathrm{n_{eq}/cm^2}$ (d).

different behaviour with respect to the other devices with values in line with reference up to 300 V and a steeper increasing rate with bias above this voltage.

After $10 \cdot 10^{15}\,\mathrm{n_{eq}/cm^2}$ it was possible to measure only three types of devices, because of very large leakage currents causing device breakdown and sparking (electrical discharges from the surface of the sensor) which is damaging. Figure 10.13c shows the IV for the reference (W7), 5 μm (W2) and the 50 μm (W5) deep trenched sensors. The current of both trenched devices starts to deviate significantly from that of the reference above 400 V, to be about a factor of two higher at 1100 V. After the higher dose ($20 \cdot 10^{15}\,\mathrm{n_{eq}/cm^2}$) the reference, the deep diffused, the 5 μm and the 50 μm deep trench detectors have similar trends of the IV curves, with respectively higher values at any bias voltage. An increased

reverse current is expected in these devices as the multiplication effect which increases the impact ionisation also increases the reverse current by affecting charge carriers that contribute to it.

All devices in Figure 10.13 have had their MIP response measured. The results are given in Figure 10.14 for each device, after each fluence. Up to and including a fluence of $10 \cdot 10^{15}\,\mathrm{n_{eq}/cm^2}$ the trenched devices show gains in signal amplification when compared to the standard ones. After a fluence of $1 \cdot 10^{15}\,\mathrm{n_{eq}/cm^2}$ the trenched devices start to collect significantly more charge than the standard device.The enhancement in collected charge increases with trench depth. At 700 V, the W2 (5 μm trench) device collects 12.5 $\pm$ 1.0 ke, W3 (10 μm trench) device collects 14.2 $\pm$ 1.2 ke and W5 (50 μm trench) device collects 16.6 $\pm$ 1.3 ke compared to the standard device which collects 11.2 $\pm$ 1.0 ke. In each case, the increased depth of the trench causes an increase in noise. At higher bias voltages (1000 V) the response of all three trenched devices is more similar with respect to each other. At 1000 V the standard device collects 15.3 $\pm$ 1.6 ke, whereas the trenched devices collect 20 $-$ 21 $\pm$ 1.5 ke. However, the trenched devices do experience some issues at very high bias voltages. The isolation between some readout channels appears to be lost and at 1000 V up to 50 % of the sensors readout channels have had to be disabled. The P-Layer flavour shows some increase in signal at very high bias voltages, ¿ 800 V with respect to the standard device (Figure 10.14), with no channel isolation issues.

After $5 \cdot 10^{15}\,\mathrm{n_{eq}/cm^2}$, a trend similar to the results after $1 \cdot 10^{15}\,\mathrm{n_{eq}/cm^2}$ is seen. However, the W2 (5 μm deep) design now shows the best signal amplification, followed by W5 (50 μm deep trench). The improvement in signal amounts to over 80% and almost 50% with the 5 and 50 μm trenched detectors respectively. The deep diffused device labelled W18 (with the p-diffusion as wide as the implanted strips) exhibits much poorer charge collection with respect to reference. At 1000 V 5.4 $\pm$ 1.5 ke charge is collected compared to the 8.1 $\pm$ 0.6 ke of the irradiated standard device. In this case a possible suppression of charge multiplication takes place. The deep diffused device labelled W16 (with a 5 μm narrow diffusion) offers performances in line with the standard device. The 10 μm deep trenched sensor has a lower or equal CC(V) to the reference (W7) detector.

Improved charge collection is exhibited by trenched sensors irradiated to higher neutron doses. After $10 \cdot 10^{15}\,\mathrm{n_{eq}/cm^2}$ trenched sensors can collect up to 40% more charge than reference at same bias voltages. No data is available for P-Layer devices at this fluence, as they stopped functioning, indicating the design is not well suited for HL-LHC fluences.

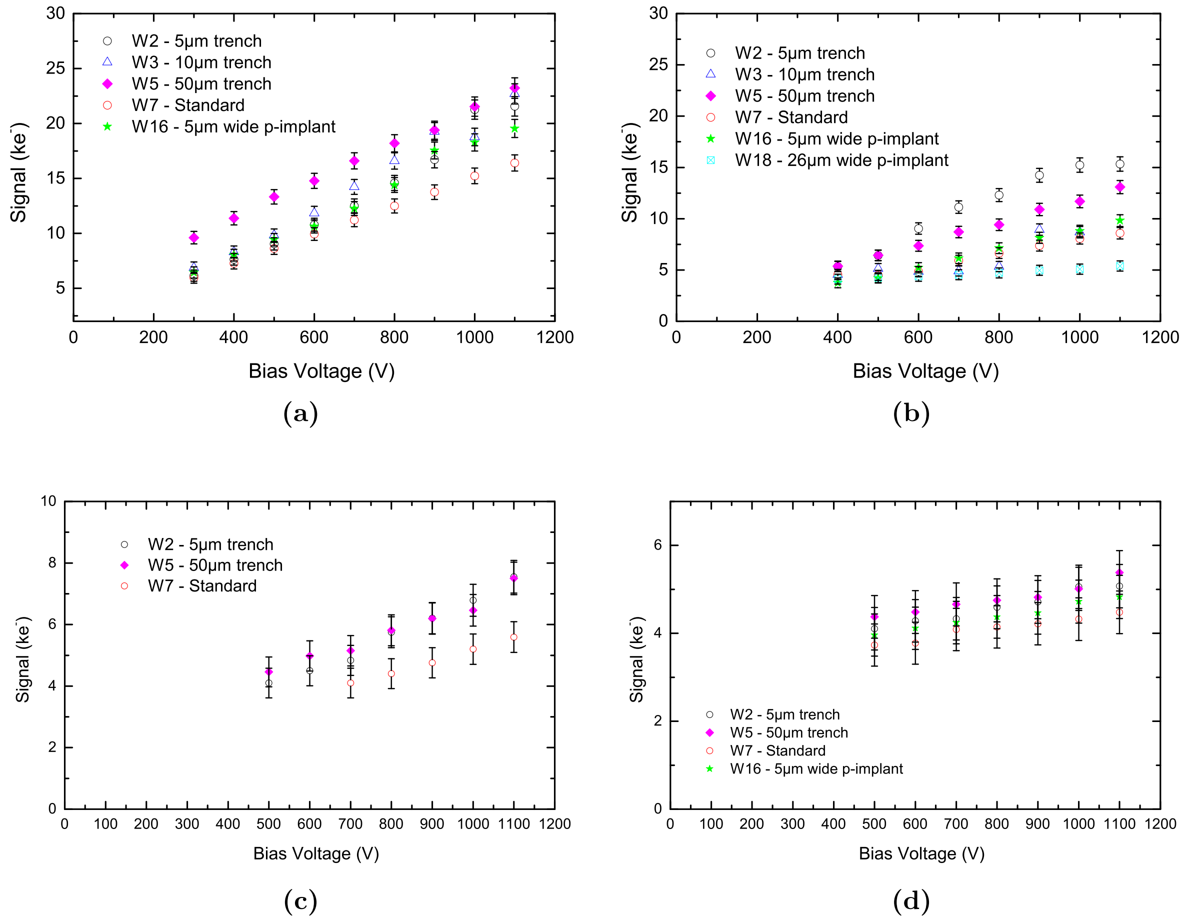

Figure 10.14: CC(V) characteristics measured at - 25 °C for standard (W7), 5 μm (W2) and 50 μm (W5) trenched and deep diffused (W16, W18) detectors, after 1 (a), 5 (b), 10 (c) and $20 \cdot 10^{15}$ n_{eq}/cm^2 (d).

After $20 \cdot 10^{15}$ n_{eq}/cm^2 a greater signal is measured with sensors with trenched strips. A small increase in the signal is also found with the deep diffused (5 μm wide) device. A summary of CC(V) results at 700 V and 1000 V for $10 \cdot 10^{15}$ n_{eq}/cm^2 and $20 \cdot 10^{15}$ n_{eq}/cm^2 doses is shown in Table 10.4.

10.3.4 Conclusion

This study has shown the viability of using junction engineering to manipulate charge multiplication. The data shows significant improvements in signal achieved with 5 and 50 μm trenches etched through the centre of the readout strips. A lesser influence in

Design	$10 \cdot 10^{15}$ n$_{eq}$/cm^2 700 V	1000 V	$20 \cdot 10^{15}$ n$_{eq}$/cm^2 700 V	1000 V
W2 (5 μm trench)	4.8 ± 0.8 ke	6.8 ± 1.0 ke	4.3 ± 0.8 ke	5.0 ± 0.9 ke
W5 (50 μm trench)	5.1 ± 0.9 ke	6.5 ± 1.0 ke	4.6 ± 0.9 ke	5.0 ± 0.9 ke
W7 (std)	4.2 ± 0.7 ke	5.2 ± 0.8 ke	4.1 ± 0.8 ke	4.3 ± 0.8 ke

Table 10.4: Summary of CC(V) results for W2 (5 μm), W5 (50 μm) and W7 (std) devices at 700 and 1000 V for fluences of $10 - 20 \cdot 10^{15}$ n$_{eq}$/cm^2

signal is seen with the P-Layer devices, and the 10 μm deep trenched devices show no improvement after $5 \cdot 10^{15}$ n$_{eq}$/cm^2 .

The impact ionisation responsible for the increased signal should also have a similar effect on the charge carriers contributing to the leakage current. In fact the comparison of the signal and IV characteristics after the various irradiation doses shows that high charge collection is correlated with high leakage currents. One notable exception is found in detectors with wide p-diffusion (W18), after $5 \cdot 10^{15}$ n$_{eq}$/cm^2 . The poor CC(V) results in this case point to issues with the processing required by this design.

These devices were all made with similar high resistivity p-type silicon wafers, with an initial depletion voltage of about 80 V, therefore the different performances cannot be due to differences in the bulk material. The variations in leakage current and charge collection can be linked to the effect of junction engineering on the strength of the peak electric field near the implants after irradiation. This is the first evidence for an important impact of electric field manipulation of micro-strip detectors for high radiation environments. Further studies of the evolution of the electric field as a function of radiation are needed in order to calculate the electric field profile for the various junction geometries with the required precision. Initial results for another charge multiplication study are presented in Section 10.6.

The measurements presented here have also shown increased inter-strip capacitance due to the trench processing which impact on the detector noise. The final aim for junction engineered sensors is the definition of the optimal geometry for achieving at reduced bias voltage, the signal to noise ratio required for fully efficient tracking after severe doses. The more complicated processing, with respect to standard planar sensors has produced sensors with poor pre-irradiation IV characteristics. However, during real operation high bias voltages only need to be applied after irradiation and sensors are foreseen to be cooled. The use of the central trench to modify the electric field shape

can lead to a different response from the detector depending on the MIP hit position. For example a hit in the centre of the strip could have higher multiplication factor than a hit in-between strips. Further studies to investigate the reliability of devices after none standard processing are needed to both optimise and improve the performance of future devices but also to improve the way the none standard processing is done. Significant R&D work still needs to be done to optimise many device parameters, such as amount of charge multiplication and its impact to noise, leakage currents and input capacitance. As well as, further studies focusing on the topological differences in devices with standard processing (see Section 10.6. Nonetheless junction engineering is a promising route to radiation harder segmented silicon sensors and a tool for better understanding the mechanism of charge multiplication in severely irradiated silicon detectors.

10.4 Evolution of charge sharing between ATLAS IBL pixels

The charge sharing between adjacent segmented electrodes is an important parameter for the spatial resolution of silicon tracking detectors. In particular, pixel sensors positioned very close to the irradiation region of hadron colliders (e.g. HL-LHC) are required to provide secondary vertices identification with high precision. Single hit resolutions for a minimum ionising particle (MIP), in the order of 10 μm or less are required. Charge sharing between adjacent electrodes allows for better spatial hit measurements to be made. Charge weighting methods are applied to all hits in clusters above triggering threshold and noise. This yields better hit resolutions than single hit events where the spatial resolution is determined by the implant electrode size.

Hadron irradiation is known to decrease charge sharing in silicon tracking detectors [190] primarily attributed to charge trapping within the bulk, reducing the resolution of the detector. A study of the degradation of charge collection and charge sharing of pixel detectors as a function of hadron irradiation is performed. The pixel sensors used were specially designed for use with the ALiBaVa system, which was designed to test micro-strip detectors. The ALiBaVa system's 10 bit ADC allows for the measurement of detector properties with greater precision compared to conventional pixel readout electronics, which typically have 4 bit ADCs. The reduction of charge sharing due to irradiation is studied with these devices up to the HL-LHC maximum expected fluence of $2 \cdot 10^{16}\ \mathrm{n_{eq}/cm^2}$ for the ATLAS inner pixel barrel layers.

It would be challenging to study the properties of severely irradiated pixel sensors independently of the changes that take place in the readout electronics if both sensor and electronics have been irradiated. ATLAS pixel sensors are bump bonded to their respective readout chip. As already mentioned, because this is a high temperature process. Irradiated pixel sensors cannot be assembled without damaging them. For this reason for the purpose of this study we used the ALiBaVa readout system instead. However, because only 256 channels can be readout with this system (two Beetle chips), an alternative design of pixel sensors was created by Liverpool and produced by Micron Semiconductors Ltd to be read out with a low density channel system.

10.4.1 Geometry Description

The pixel devices produced are $1 \times 1\, cm^2$ *n-in-p*, $14\,\mathrm{k\Omega}$ bulk resistivity, sensors. Each detector features 2048 DC coupled pixels with cell dimensions of $250 \times 50\,\mu\mathrm{m}^2$ and is designed to be readout using two Beetle chips. To connect 2048 pixels to 256 readout channels each channel is connected to 8 pixels which are distributed over the sensor and inter-connected using additional metal routing lines obtained by mean of a second metal layer on top of the usual metal. This second layer is isolated from the first metal layer using SiO_2 with openings over relevant pixels for direct contact. This pixel structure is surrounded by the bias ring which connects to metal bias rails between rows of pixels perpendicular to the long pixel direction ($250\,\mu$m). The metal bias rails ground all the pixels independently using punch through bias structures in every pixel, thus retaining the segmented readout structure. Outside the bias ring and at two opposite sides there are 128 wire bonding pads connecting to the readout. Finally, the traditional RD50, 6 guard ring structure is used to surround the whole structure for high voltage breakdown prevention.

Two flavours of these special pixel detectors were produced, each with a different pixel ganging scheme and implant orientation compared to the readout pads. Devices named "APC" (ATLAS Pixel Column) have a 32×64 pixel matrix, where the pixel cell orientation relative to the readout pads is $250 \times 50\,\mu$m, which ca be seen in Figure 10.15a. Each channel is connected to eight pixels, where each subsequent pixel in a column is shifted down by 8 pixels for even columns (0, 2, 4 etc..) and up by 8 pixels for odd number columns (1, 3, 5 etc..). Readout channels adjacent to each other were also offset by 4 pixels from each other to prevent very large clusters to form because otherwise hits would be duplicated in neighbouring pixels. Secondly, devices named "APR" (ATLAS

Pixel Row) have a 128 x 16 pixel matrix where the pixel cell orientation relative to the readout pads is 50 x 250 μm^2, shown in Figure 10.15b. As with the APC device each readout channel is connected to eight pixels. However, each of the 128 readout channels is directly connected to the first pixel of the 128 column wide matrix. Each first pixel is then connected to other pixels in alternating rows. Magnified images of both design variations APC and APR are shown in Figure 10.15a and Figure 10.15b respectively.

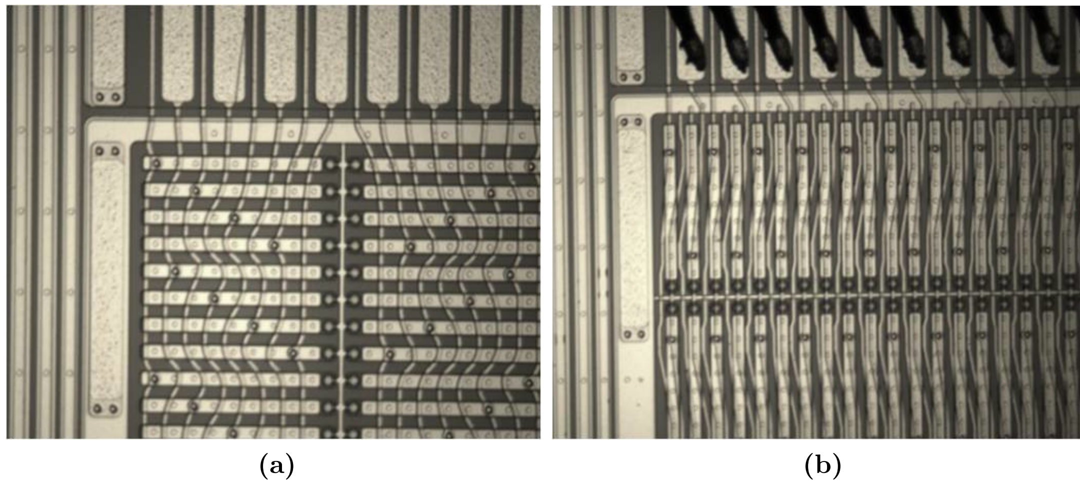

(a) (b)

Figure 10.15: Pixel sensors with 250 x 50 cell dimensions using special double metal connection for readout with analogue electronics designed for micro-strip sensors. Both design variations are shown APC and APR in (a) and (b) respectively. Both figures show the position and relative size of the wire bonding pads as well as the punch through biasing structures used to provide power.

When using radioactive sources the hit is assigned to all 8 pixels. Finally, the ganged pixels are DC coupled to the Beetle readout, resulting in a relatively elevated reverse current slightly changing its performance in term of noise and gain. In order to account for the difference in response, we performed a dedicated calibration run of the electronics chain. In both designs the readout scheme creates a position ambiguity because it is not possible to determine which pixel in the set of 8 connected to the same readout channel has been hit.

10.4.2 Charge collection as a function of bias voltage

The degradation of the charge collection as a function of the applied bias voltage (CC(V)) with fluence for both APR and APC detectors has been studied after neutron irradiation. The sensors have been irradiated with reactor neutrons at the TRIGA Mark II research

reactor (JSI, Ljubljana) to 5, 10 , 30, 50, 100 and 200 $\cdot\, 10^{14}\, \mathrm{n_{eq}/cm^2}$. The charge collection properties of the sensor were studied with the usual set-up for MIP-like particles. The irradiated sensors were cooled to - 25 °C to reduce their reverse current and prevent annealing.

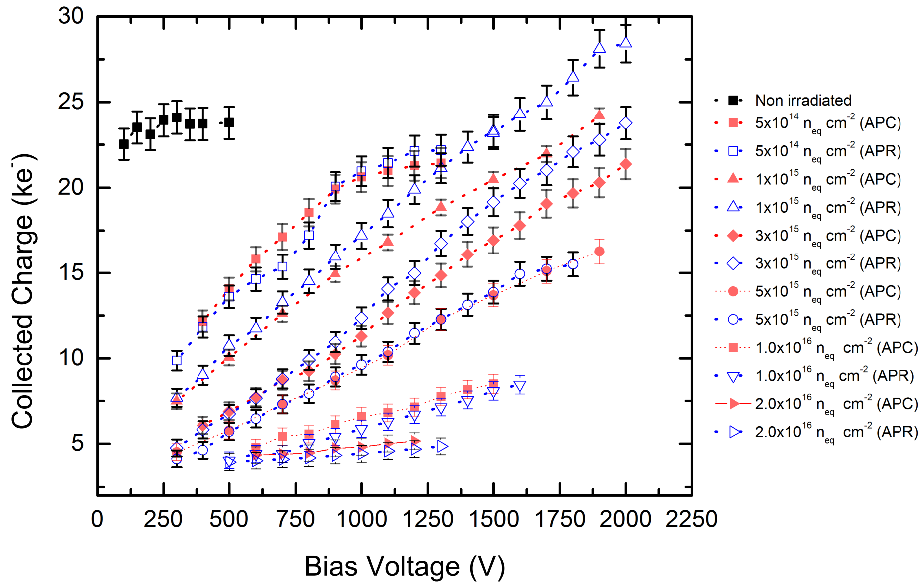

Figure 10.16: Degradation of the CC(V) with hadron fluences up to $2 \cdot 10^{16}\, \mathrm{n_{eq}/cm^2}$ measured with APC and APR sensors.

Figure 10.16 shows the degradation of the CC(V) with neutron fluence. The collected charge is progressively reduced by charge trapping caused by the radiation induced defect centres. The signal ($> 4\,$ke) is still measurable even at the higher fluence of $2 \cdot 10^{16}\, \mathrm{n_{eq}/cm^2}$, which corresponds to the maximum dose expected in ATLAS inner pixel layers after 10 years operation at HL-LHC (normalised to $3000\,\mathrm{fb^{-1}}$). This is an acceptable signal level because of the low noise electronics used for readout. The equivalent noise charge (ENC) is about 600 e and practically independent of sensor bias voltage. The collected charge recorded at bias voltage greater than 1600 V and 1900 V for the $1 \cdot 10^{15}\, \mathrm{n_{eq}/cm^2}$ and $3 \cdot 10^{15}\, \mathrm{n_{eq}/cm^2}$ fluences respectively, exceeds the saturation value shown by the unirradiated sensor. The difference is not due to measurement uncertainty but to charge multiplication in the n^+-p junction region. Evidence for charge multiplication has been reported on several occasions [191, 192] by members of the RD50 collaboration [19]. Both APC and APR devices were irradiated together in the same irradiation campaign, therefore they have received the same fluence, although with an uncertainty of about 10 % on its absolute value. Both design variations show excellent

agreement in CC(V) up to very high bias voltages despite featuring different pixel ganging schemes. The differences in CC(V) at very high voltages are most likely caused by the different ganged layouts with poor cluster separation between separate hits.

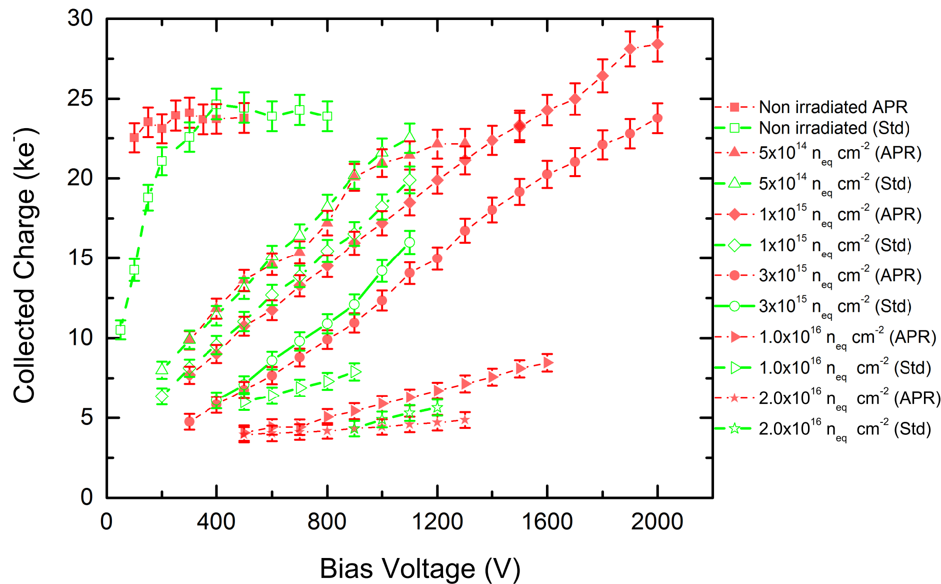

Figure 10.17: Degradation of the CC(V) with hadron fluences up to $2 \cdot 10^{16}\,\mathrm{n_{eq}/cm^2}$ measured with DC coupled APR and AC coupled standard micro-strip sensors. Each device at each fluence was tested until breakdown occurred.

The behaviour of the DC coupled APR sensors was then compared with traditional AC coupled micro-strip sensors at each hadron fluence, these devices have a lower bulk resistivity and therefore have a higher depletion point, 350 V compared to the ATLAS pixel devices which deplete at around 100 V. Figure 10.17 shows the CC(V) comparison after various fluences. The AC coupled micro-strip detectors were tested under similar conditions. However, their irradiation took place at different times compared to the pixel sensors and therefore a 10 % uncertainty in relative fluence needs to be considered. Considering errors associated with the fluence uncertainty and the unknown variation in charge multiplication, the agreement between these two types of sensors is excellent.

10.4.3 Charge sharing as a function of bias voltage

The charge sharing between adjacent electrodes has been measured with both APC and APR designs after various neutron irradiation fluences up to $2 \cdot 10^{16}\,\mathrm{n_{eq}/cm^2}$. Every device was measured under similar conditions with 100,000 events recorded at each value

of the in bias voltage for a given fluence. The amount of charge sharing is displayed by comparing the relative occupancy of one, two and three hit clusters compared to the total number of clusters. Figure 10.18 shows the fractions of pixel hit clusters for an unirradiated APC device. Two and three hit clusters have larger relative occupancies than single hit clusters. The fraction of two, three and one hit clusters is about 40 %, 30 % and 15 % respectively.

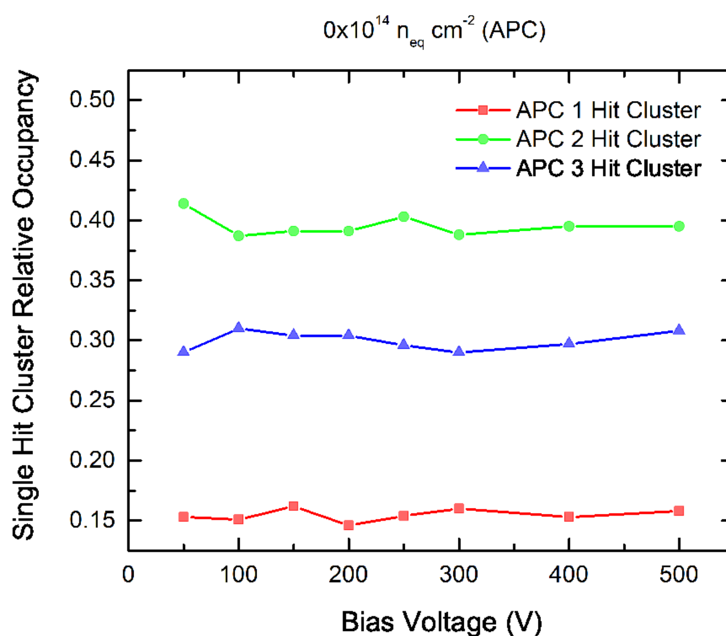

Figure 10.18: Fraction of one, two and three hit pixel clusters as a function of bias voltage for a unirradiated APC device.

The cluster size distributions change substantially with irradiation. Figure 10.19a, Figure 10.19b and Figure 10.19c show the changes in relative hit occupancy for one, two and three hit cluster, respectively, as a function of the neutron irradiation fluence and the sensor bias voltage. The changes are very similar for both configurations and therefore corresponding charge sharing plots for the APR devices are not shown. The number of single pixel clusters becomes dominant already after the lower fluence of $5 \cdot 10^{14}\,\mathrm{n_{eq}/cm^2}$. Only with very high bias voltages do the relative occupancies of two hit clusters increase with respect to the one hit clusters. The dependence of the cluster size on the bias voltage is different after the various fluences. Before irradiation the cluster size (Figure 10.18) is independent of bias voltage. The cluster size changes significantly at different bias voltages for the sensors irradiated to 5, 10, 30 and $50 \cdot 10^{14}\,\mathrm{n_{eq}/cm^2}$, with an increased charge sharing with increasing bias voltages. This is caused by the higher carrier mobility which reduces the chance of trapping and possibly due to charge multiplication near the

readout implants. At higher fluences only one and two hit clusters have significant values while larger clusters are being suppressed by the reduction in charge sharing because of radiation damage (charge trapping), even at very high bias voltages (up to 1800 V). Small changes in one and two hit clusters are seen for the $100 \cdot 10^{14}\, n_{eq}/cm^2$ irradiated device at above 1600 V shown in Figure 10.19a and Figure 10.19b. However, the device breaks-down before any significant change can be seen.

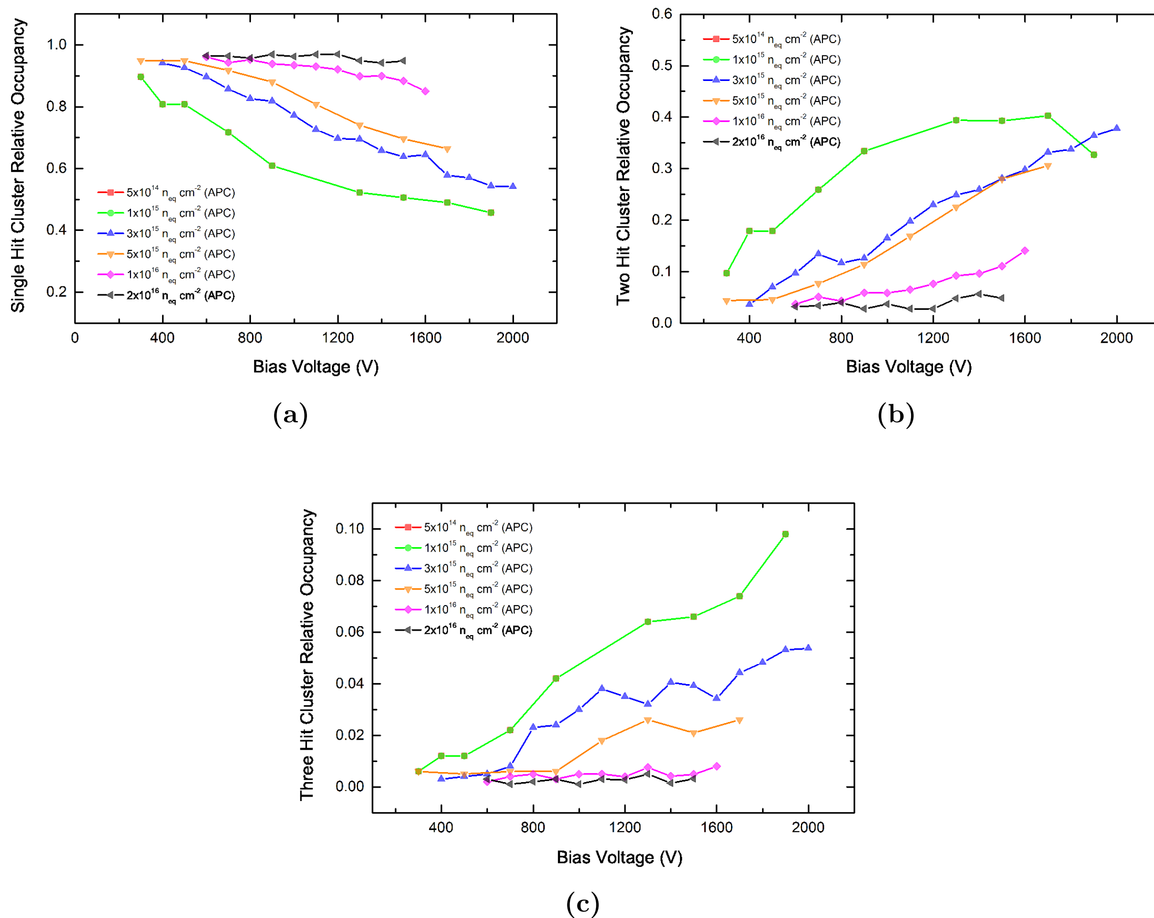

Figure 10.19: Changes in charge sharing (relative occupancy): (a) single hit clusters, (a) two hit clusters and (c) three hit clusters for APC devices as a function of neutron irradiation and bias voltage.

At doses of 100 and $200 \cdot 10^{14}\, n_{eq}/cm^2$ the charge sharing is seen to behave like a binary system (mainly single hits). It is unlikely that devices will be operated at bias voltages much more than 1000 V because of the inherent danger of sparking between modules in close proximity to each other. Furthermore, the required increase in cooling power would necessitate an increased coolant pressure in the cooling pipes. The cluster distribution

dependence on fluence is shown for 500 V, 700 V, 900 V and 1100 V in Figure 10.20a, Figure 10.20b, Figure 10.20c and Figure 10.20d respectively for both APC and APR devices. These voltages have been chosen because they represent a range of bias voltages at which various pixel barrel and disk layers may operate ATLAS during HL-LHC operation depending on the received dose.

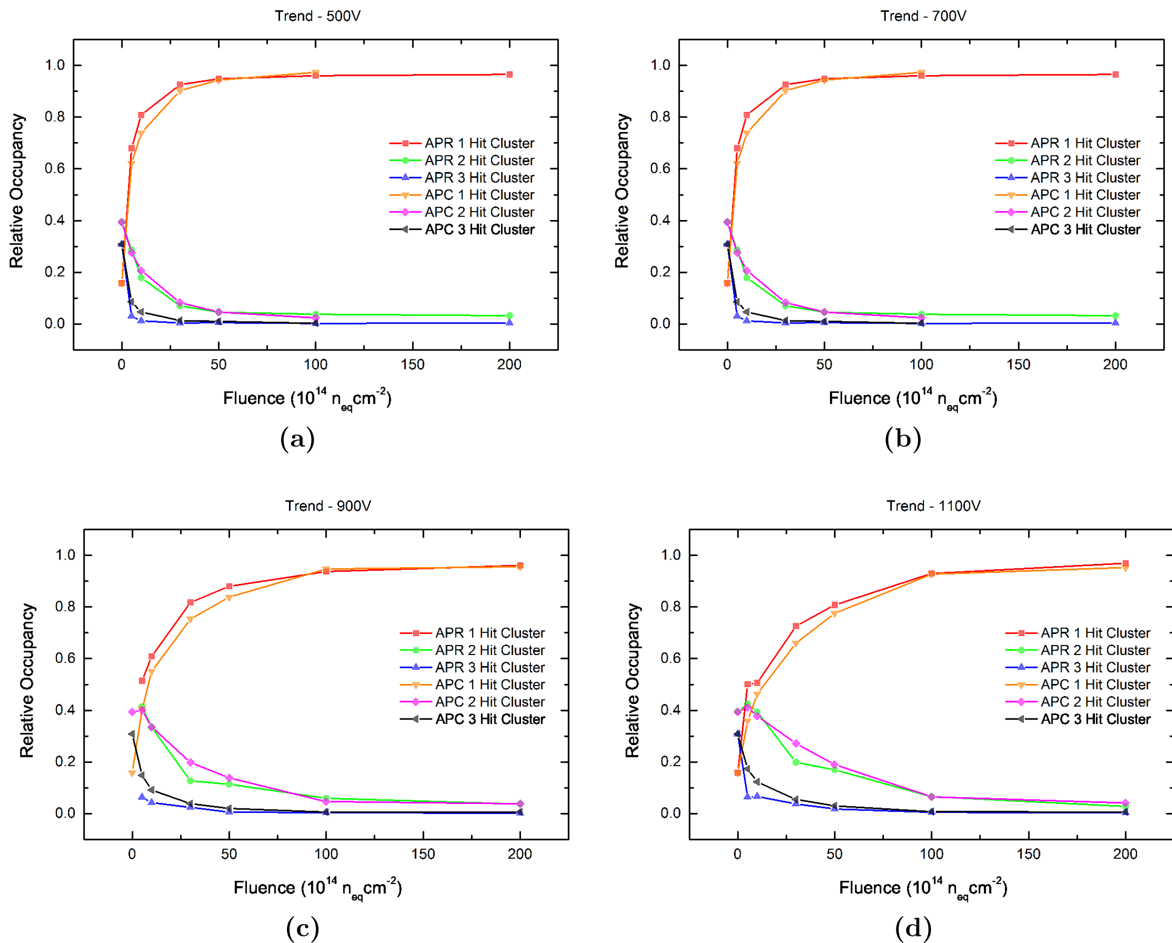

Figure 10.20: Dependence of the cluster size on the fluence at four different bias voltages: (a) 500 V, (b) 700 V, (c) 900 V and (d) 1100 V.

10.4.4 Conclusion

The special DC coupled pixel sensors (APC/APR) which features an additional top metal routing layer readout with analogue electronics designed for operation with micro-strip detectors exhibits similar CC(V) degradation compared to more traditional AC coupled micro-strip detectors. The pixel sensors show evidence of charge multiplication, where

the collected charge at high bias voltages is in some cases (10 and $30 \cdot 10^{14}\,\mathrm{n_{eq}/cm^2}$) is larger than the saturation value measured with un-irradiated APC and APR devices.

The charge sharing is shown to decrease with irradiation, with significant changes in cluster sizes seen at $5 \cdot 10^{14}\,\mathrm{n_{eq}/cm^2}$. The charge sharing results indicate that the use of charge sharing to enhance the resolution of pixels erectors is compromised by radiation damage when received dose exceeds $10 \cdot 10^{14}\,\mathrm{n_{eq}/cm^2}$. The effects mentioned have been measured with analogue electronics digitised with a 10 bit ADC, typically pixel electronics only utilise 4 to 5 bits to digitise their time over threshold information. This will provide coarser hit information and is likely to suffer reduced charge sharing as a result.

The charge sharing of heavily irradiated devices (100 to $200 \cdot 10^{14}\,\mathrm{n_{eq}/cm^2}$), such as those expected within ATLAS's inner pixel barrel layers at HL-LHC will behave like a binary system. However, because these layers will be mounted very close to the interaction point, resulting tracks from secondary vertices traverse the pixel detectors with large track inclinations with respect to the surface of the sensor. This will deposit charge across many pixels creating large hit clusters even with little or no charge sharing.

10.5 Thick vs Thin planar Sensors

It has been shown that n-type readout planar sensors are more radiation tolerant at large doses when compared to p-type readout devices [193, 194]. This is due to the shorter collection time of electrons with respect to holes, thus, reducing the total charge trapping. Charge trapping increases with fluence to the point of making the charge carrier life time shorter than the collection time and therefore, the collection distance shorter than the actual thickness of the device. After a fluence of $1 \cdot 10^{16}\,\mathrm{n_{eq}/cm^2}$, assuming a bias voltage high enough to saturate carrier mobility, the total collection distance in silicon is $\sim 24\,\mu$m using a trapping time calculated according to the parameterisation in [152]. In this situation, where the collection distance is significantly shorter than the actual device thickness, thinner detectors could have an advantage with respect to thicker devices because of higher electric fields at the same bias voltage. They would also be less susceptible to charge trapping , because of increased carrier mobility and should have an increased charge multiplication effect due to the larger electric fields. To study this, a selection of Micron produced, 1x1 cm^2 n-in-p micro-strip sensors of thicknesses, 106, 144 and 296 μm have been characterised as a function of fluence and bias voltage.

Before irradiation all devices were tested with the ALiBaVa system to measure their response with respect to a MIP to be used as reference values. Figure 10.21 shows the results for the 106, 144 and 296 μm thick devices. All devices are operated above their full depletion voltage to guarantee the maximum charge is collected, a saturation in the collected charge for each device is seen as indicated by the flat distributions.

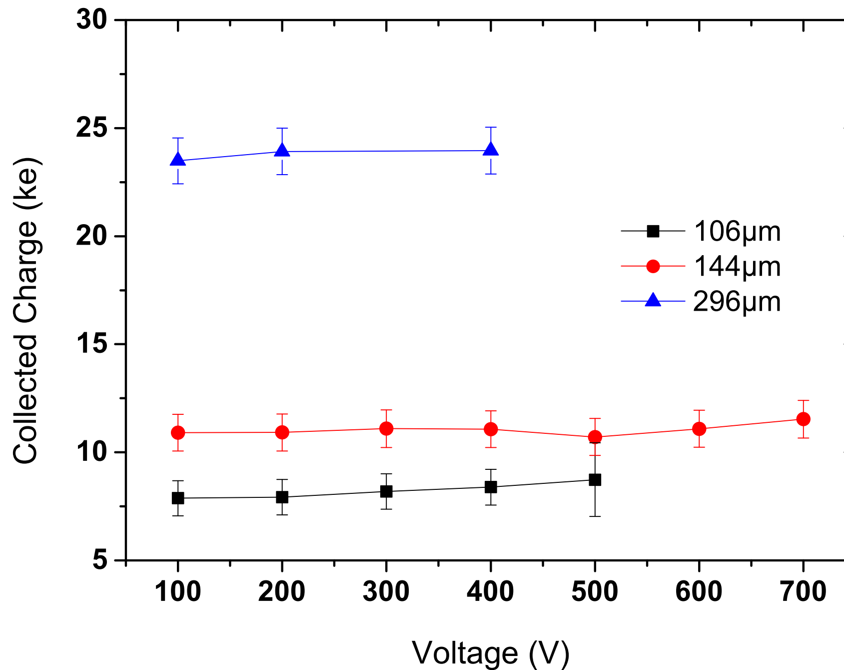

Figure 10.21: Signal as a function of bias voltage for 50, 106, 144 and 296 μm thick planar silicon sensors.

10.5.1 Irradiation and Characterisation

Devices were irradiated to 2, 5, 10 and $20 \cdot 10^{15}\,\mathrm{n_{eq}/cm^2}$ at the Birmingham irradiation facility. The ALiBaVa system was used to measure each device response in the usual way. Current-voltage (IV) measurements were performed along side the ALiBaVa measurements. Throughout storage and measurement all devices were cooled to - 25 °C. The total annealing time for each device has been estimated to be around 1 day (at 20 °C).

Figure 10.22 shows the measured IV characteristics for all devices at each fluence as a function of bias voltage. All the leakage currents have been corrected to a temperature of - 25 °C.

Figure 10.23 shows the CC(V) results for each device thickness and for fluences up to $20 \cdot 10^{15}\,\mathrm{n_{eq}/cm^2}$. At low doses the thinner sensors collect less charge than the thicker sensors, as expected. At $2 \cdot 10^{15}\,\mathrm{n_{eq}/cm^2}$ the 144 and 296 μm thick sensors behave similarly while the 106 μm sensors collected charge starts to saturate. The same trend is

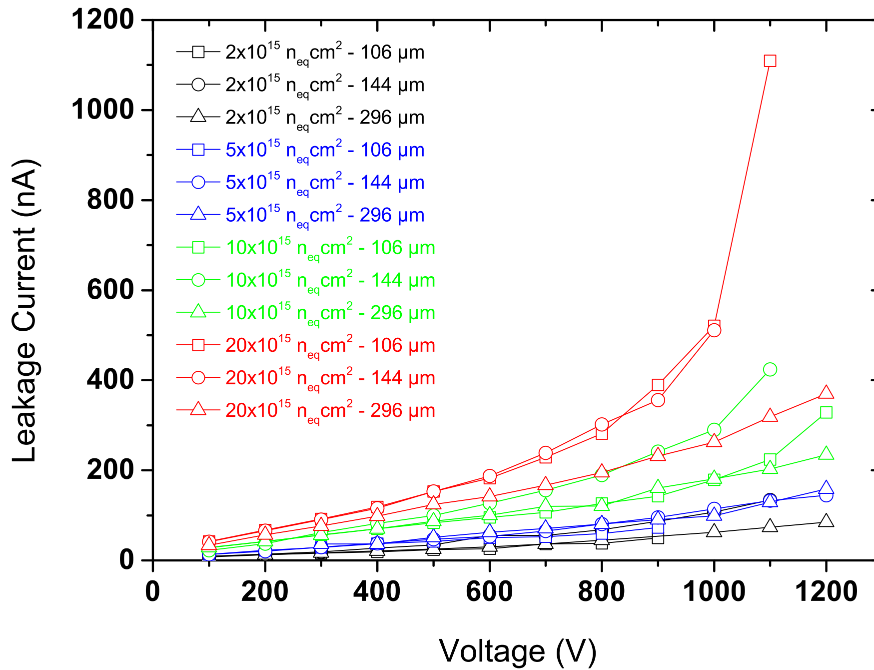

Figure 10.22: Measured current-voltage (IV) characteristics of 106, 144 and 296 μm thick devices after irradiation to 2, 5, 10 and $20 \cdot 10^{15}\,\mathrm{n_{eq}/cm^2}$ all cooled to - 25 °C.

seen at $5 \cdot 10^{15}\,\mathrm{n_{eq}/cm^2}$, the thicker sensors collect the highest charge but the difference in collected charge between the 296 and 106 μm devices is severely reduced.

After very high doses, $10 \cdot 10^{15}\,\mathrm{n_{eq}/cm^2}$ and $20 \cdot 10^{15}\,\mathrm{n_{eq}/cm^2}$, the thinner sensors perform better. At $10 \cdot 10^{15}\,\mathrm{n_{eq}/cm^2}$ the 144 μm shows the best performance relative to peak charge collected while at $20 \cdot 10^{15}\,\mathrm{n_{eq}/cm^2}$ the 106 μm sensors performs the best.

The collected charge of all devices across the full fluence range ($2 \cdot 10^{15}\,\mathrm{n_{eq}/cm^2} \rightarrow 20 \cdot 10^{15}\,\mathrm{n_{eq}/cm^2}$) at 600 V and 900 V is shown in Figure 10.24a and Figure 10.24b, respectively.

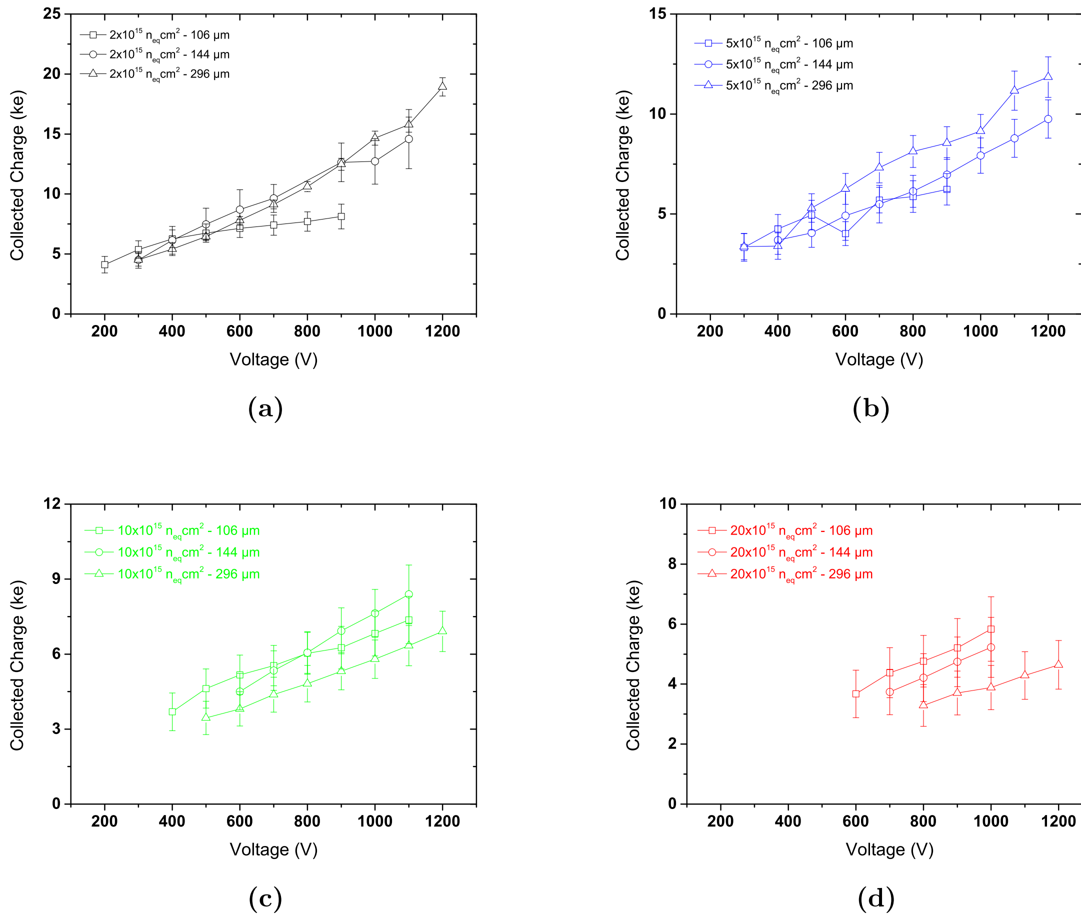

Figure 10.23: CC(V) dependance for 106, 144 and 296 μm thick *n-in-p* sensors as a function of fluence. (a) $2 \cdot 10^{15}\,\mathrm{n_{eq}/cm^2}$, (b) $5 \cdot 10^{15}\,\mathrm{n_{eq}/cm^2}$, (c) $10 \cdot 10^{15}\,\mathrm{n_{eq}/cm^2}$ and (d) $2 \cdot 10^{15}\,\mathrm{n_{eq}/cm^2}$.

10.5.2 Conclusion

In conclusion, thinner devices are found to be more radiation tolerant than thicker devices at the same operating voltage. At lower fluences the peak signal measured by thicker devices is greater than the thinner devices. However, the response of thinner devices varies significantly less with irradiation, yielding a superior signal after the highest fluences. Additionally, the use of thinner devices reduces the amount of material within the tracker, reducing the multiple scattering effect of low energy particles.

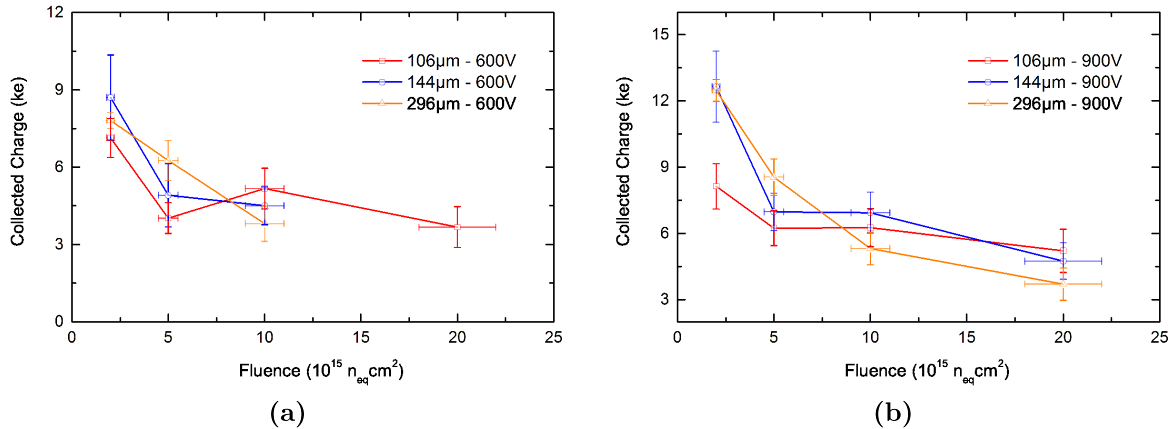

Figure 10.24: Charge collected as a function of fluence for 106, 144 and 296 μm thick sensors at (a) 600 V and (b) 900 V.

10.6 Charge Multiplication Device Characterisation

Results presented at the 14th RD50 workshop [195] have provided further evidence for enhanced charge collection (already suggested by previous measurements [196, 197]). The underlying mechanism has been labeled as "charge multiplication". Silicon sensors with various choices of strip pitch and strip width over pitch (w/p) ratios have been produced in order to determine if charge multiplication is seen and if it can be controlled using junction engineering. A study discussed in Section 10.3 explored possible exploitation of the charge multiplication effect by changing the implant structures using none standard planar processing techniques (trench etching). The interleaving of readout strips with intermediate strips designed to modify the electric field profile has also been investigated. The geometrical changes made in this study should influence the charge multiplication and charge sharing between adjacent strips using only standard planar processing techniques. The initial results are discussed but this study is still ongoing [198].

10.6.1 Geometry Description

The RD50-CM mask features 60 1x1 cm^2 micro-strip sensors with variations on strip pitch and strip width over pitch ratio. Some sensors also feature intermediate strips of different types. The purpose of the intermediate strips is to improve the resolution of AC coupled micro-strip detectors while keeping a reduced number of readout channels [199]. The sensors geometry is *n-in-p*, using a high resistivity, 14 kΩ cm, p-bulk silicon,

for increased radiation tolerance. The intermediate structures are similar to the readout implants. The implants are connected to the bias ring using 1 - 1.5 $M\Omega$ poly-silicon resistors. However, the intermediate strips do not feature an AC coupled top metal layer for readout. A significant improvement of the hit resolution is expected due to the enhanced charge sharing introduced by the intermediate strips. However, a reduction in the total cluster charge readout is expected due to losses to the biased intermediate strips. This is because these strips will "steal" charge from neighbouring readout strips. For this reason, this design is not suited for high radiation environments because of the severe reduction in signal charge that is caused by radiation damage. A variation on the intermediate strip design is to disconnect them from the bias rail, leaving the implant floating. Thus, the intermediate strip would not "steal" charge from the readout strips, but its presence would effect the electric field in the strip regions. Table 10.5 shows the sensor design variations, all featuring 128 readout strips.

The thickness of the sensor also has an effect on the charge multiplication, because stronger electric fields are expected in thinner devices biased to the same voltage [191, 192]. For this reason, 150 and 300 μm thick wafers where produced at Micron Semiconductors Ltd [20].

Name	Strip Pitch (μm)	Strip Width (μm)	Intermediate Biased Strip (μm)	Intermediate Floating Strip (μm)
P40-W6	40	6	No	No
P40-W15	40	15	No	No
P40-W27	40	27	No	No
P40-W15-I6	40	15	6	No
P40-W15-F6	40	15	No	6
P40-W15-F15	40	15	No	15
P40-W15-I15	40	15	15	No
P80-W6	80	6	No	No
P80-W60	80	60	No	No
P80-W25-F10	80	25	No	10
P80-W25-I10	80	25	10	No
P80-W25-F35	80	25	No	35
P80-W25-I35	80	25	35	No
P100-W10	100	10	No	No
P100-W33	100	33	No	No
P100-W70	100	70	No	No
P100-W33-I15	100	33	15	No
P100-W33-F15	100	33	No	15
P100-W33-F33	100	33	No	33

Table 10.5: Main geometry variations available on the RD50-CM mask. The detector names reflect the different geometries: P# is the strip pitch in μm. W# is the strip implant width in μm. I# is the width of the intermediate strip (when present) in μm. F# is the width of the intermediate floating strip (when present) in μm.

10.6.2 Irradiation and Characterisation

Sensors from 150 and 300 μm thick wafers where irradiated at the TRIGA Mark II research reactor (see Section 9.3) to a fluence of $5 \cdot 10^{15}\,\mathrm{n_{eq}/cm^2}$. The sensors have been characterised after irradiation, the total annealing time is estimated to be 12 hours at 20 °C.

10.6.3 Results after Irradiation

The results of the CC(V) measurements of all sensors irradiated to $5 \cdot 10^{15}\,\mathrm{n_{eq}/cm^2}$ are reported in Figure 10.25. The plot shows a large variation of values for the same applied bias voltage, indicating significantly different performances from sensors with different geometries. Some of the difference is due to the thickness of the sensors, thinner sensors have been found to be more radiation tolerant because they produce larger signals at the same bias voltage than thicker sensors after high irradiation doses (see Section 10.5).

Figure 10.26 shows the CC(V) for thin and standard thickness sensors of different geometries but with no intermediate strips. Despite the changes in strip pitch and strip width little variance in collected charge is seen at each thickness with the exception of P80-W6 (300 μm, green) which comes from a different 300 μm thick wafer than the blue points. The electric field gradient with thinner sensors is higher than their thick counter parts. As a result, any changes to a devices charge multiplication characteristics would be more easily seen. For the thin (150 μm) sensors the maximum collected charge is about 11 $\pm$ 0.7 ke at $5 \cdot 10^{15}\,\mathrm{n_{eq}/cm^2}$ compared to 12 $\pm$ 0.6 ke unirradiated. 296 $\pm$ 3 μm

To assess the influence of other geometrical parameters on the collected signal charge, the CC(V) of detectors of the same thickness should be compared. Figure 10.27 shows the results for 300 μm thick sensors only. Designs with no intermediate strips are illustrated in black, devices with intermediate strips in blue, and devices with floating intermediate strips in orange.

A significant separation in the collected charge is only observed at high bias voltages, (where charge multiplication is expected). With the exception of the P100-W10 (black) device, devices with floating intermediate strips (orange) consistently have the highest collected charge at a given bias voltage and all collect approximately the same charge. The distinction between the rest of the devices, biased intermediate strip (blue) and no intermediate strip (black) is unclear. However, a larger fraction of the worst performing

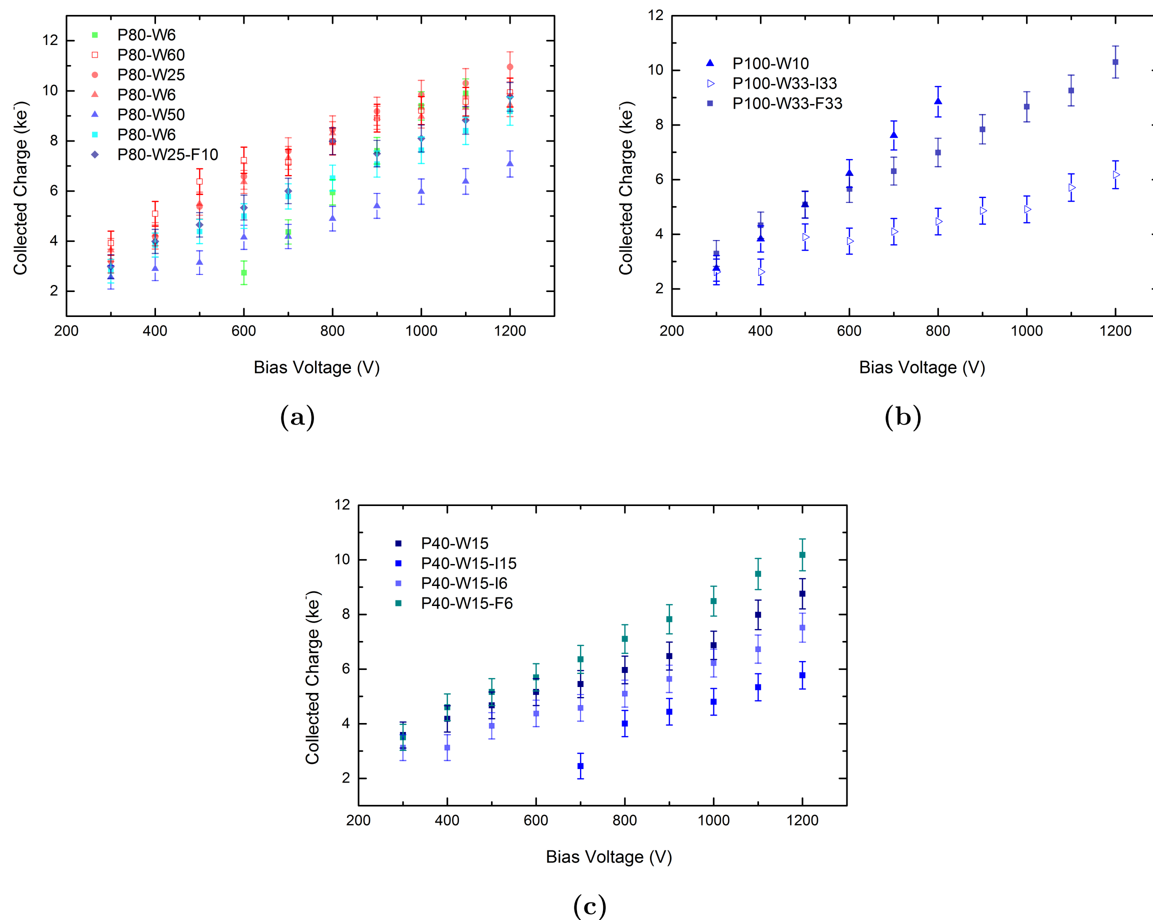

Figure 10.25: CC(V) of various geometry (see Table 10.5) sensors irradiated with neutrons to $5 \cdot 10^{15}\,\mathrm{n_{eq}/cm^2}$. Red indicates 150 μm, green and blues indicate 300 μm thick sensors. (a) 80 μm strip pitch, (b) 100 μm strip pitch and (c) 40 μm strip pitch.

devices are devices with biased intermediate strips. This is expected since the biased intermediate strip "steals" charge but is not connected to a readout channel, so some charge is lost.

There is also an indication that wider intermediate strips have a larger impact on reducing the signal charge. This is most likely due to the change in capacitance for the strips and across the sensor. The use of floating intermediate strips does not reduce the collected charge. The variations on geometry designs for floating intermediate strips sensors are shown to not significantly affect their collected charge in Figure 10.25. However, further tests with more design variations are needed to prove the existence of any possible signal enhancement.

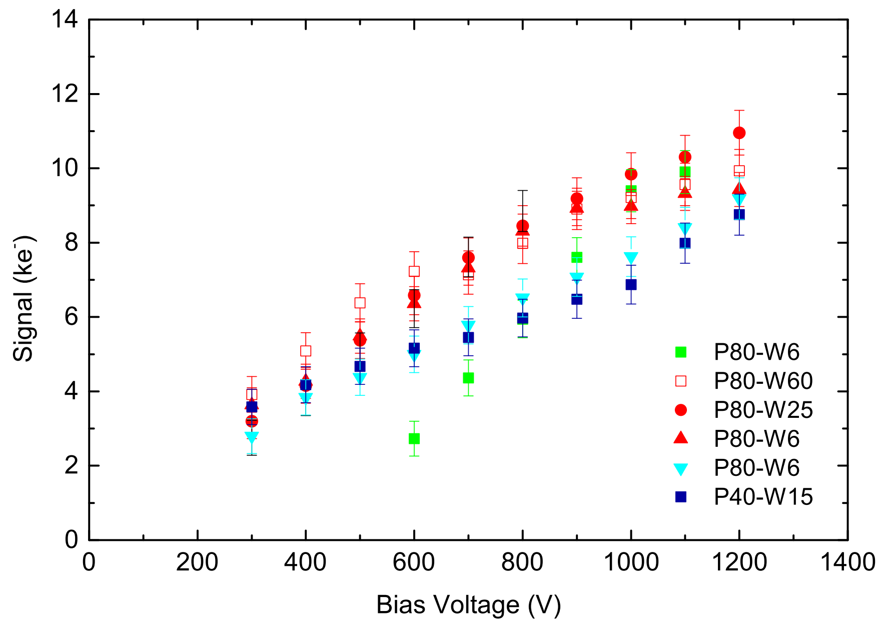

Figure 10.26: Signal (MPV) as a function of the bias voltage, with various geometries (see Table 10.5), 150 (red) and 300 μm (blue and green) thick sensors irradiated with neutrons to $5 \cdot 10^{15}\, \mathrm{n_{eq}/cm^2}$.

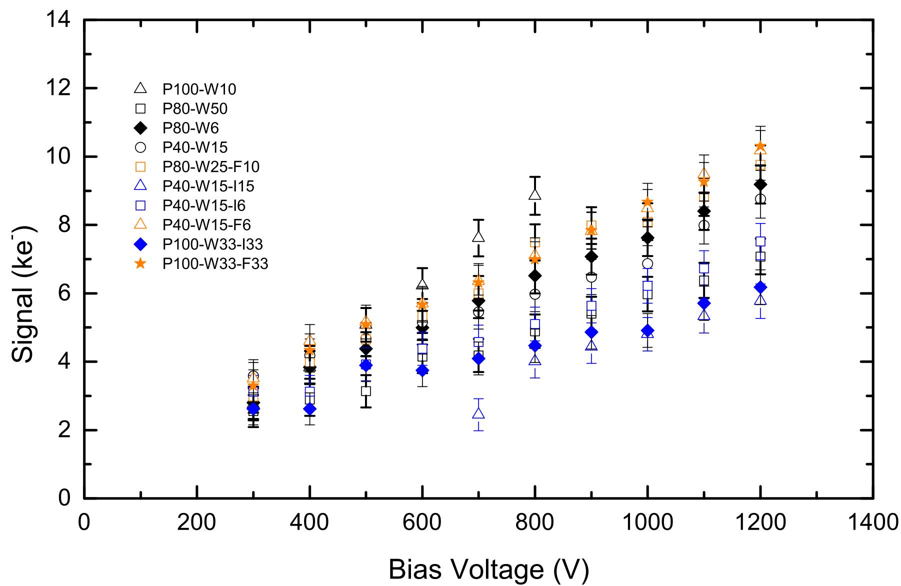

Figure 10.27: Signal (MPV) as a function of the bias voltage with various geometry (see Table 10.5) 300 μm thick sensors irradiated with neutrons to $5 \cdot 10^{15}\, \mathrm{n_{eq}/cm^2}$. Black symbols indicate designs with no intermediate strips, blue with intermediate strips and orange with floating intermediate strips.

Another important parameter for segmented silicon sensors is the resolution. This is known to degrade with irradiation, because of the decreased charge sharing with fluence. At very large fluences the charge sharing is so low that a binary resolution is expected. Designs featuring the intermediate strips are expected to affect the charge sharing and therefore the cluster sizes of a device. Figure 10.28 shows the ratios of hit cluster for 300 and 150 μm thick sensors. The thinner sensor has an increased number of two hit clusters and a decrease in single hit clusters compared to the thicker sensor.

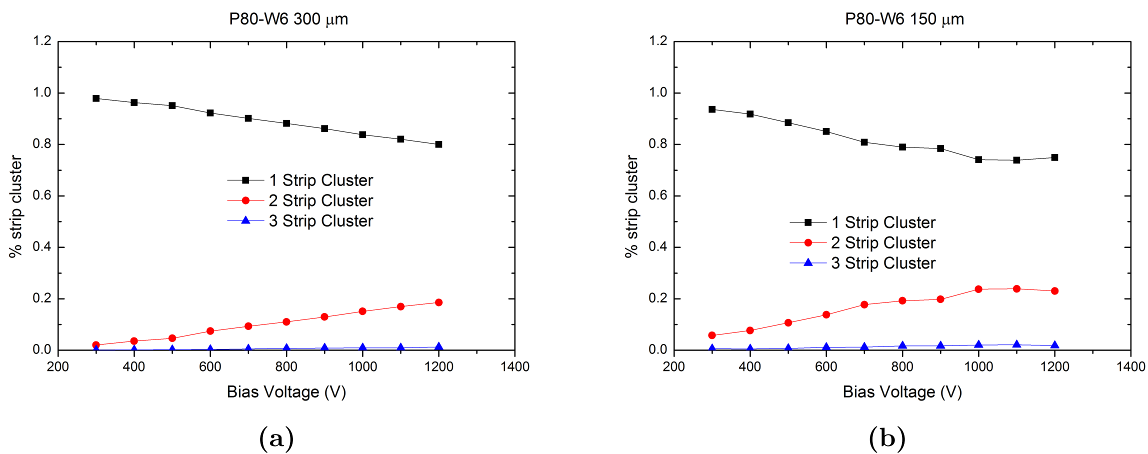

Figure 10.28: (a) Hit cluster ratio for a 300 μm thick P80-W6 sensor as a function of bias voltage. (b) Hit cluster ratio for a 150 μm thick P80-W6 sensor as a function of bias voltage.

Figure 10.29 shows the comparison of the percentage of one, two and three hit strip clusters as a function of the bias voltage for detectors with 40 μm pitch, 15 μm strip width, without and with intermediate, biased or floating strips. The effect of the biased intermediate strips on the cluster size is evident, while the intermediate floating strips only exhibit a very small enhancement of two strip clusters with respect to the standard geometry sensor [200].

10.6.4 Conclusion

Sensors irradiated with reactor neutrons to $5 \cdot 10^{15}\,\mathrm{n_{eq}/cm^2}$ have shown enhanced CC(V) values at high bias voltage, in thinner devices. They also show that the use of intermediate strips can enhance the charge sharing but has a negative effect on the total signal after irradiation if the strips are connected to the bias. Floating intermediate strips have been found not to reduce the signal charge with respect to standard devices. These

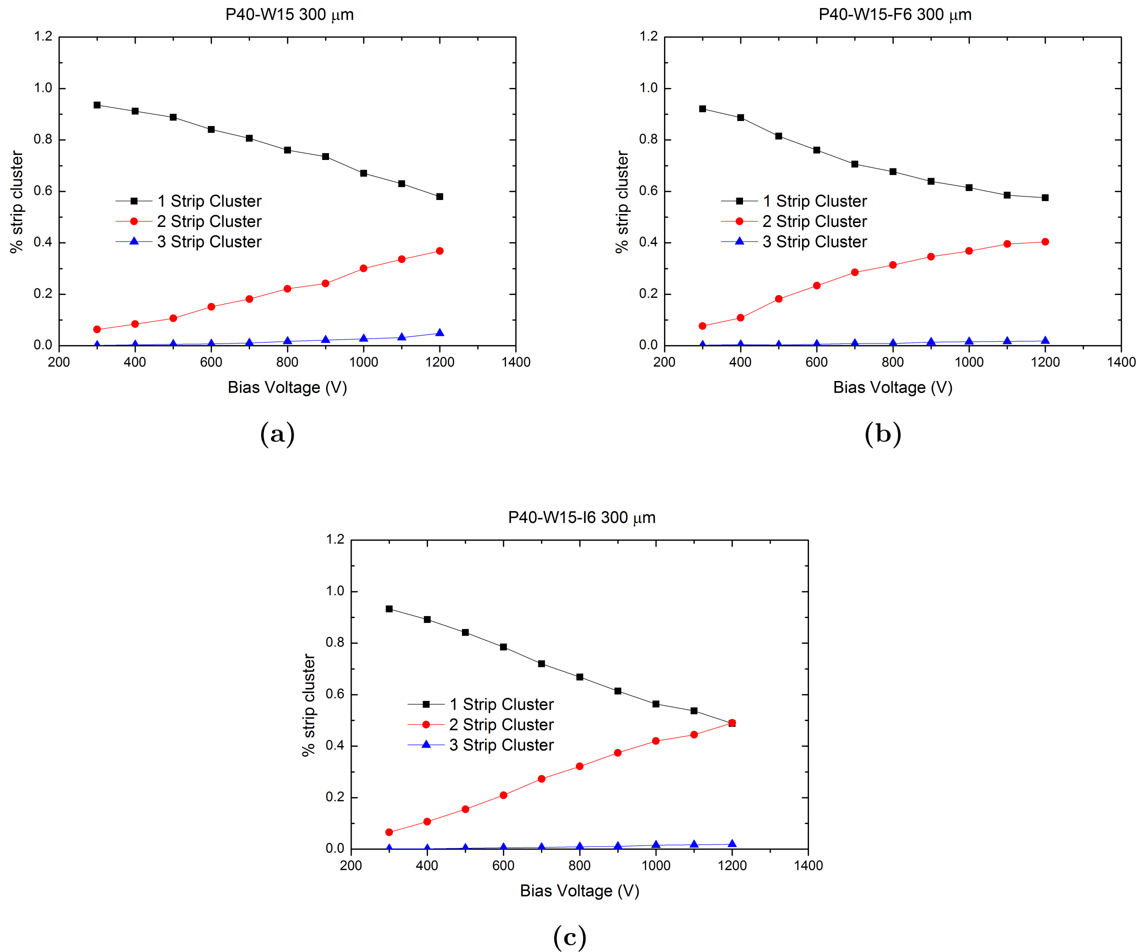

Figure 10.29: Percentage of one, two and three hit strip clusters as a function of the bias voltage for (a) 40 μm pitch, 15 μm strip width, without intermediate strips. (b) with floating intermediate strips, and (c) with biased intermediate strips irradiated to $5 \cdot 10^{15}$ n_{eq}/cm^2 with neutrons.

latter sensors exhibit a small improvement in the signal charge and a more important important in the charge sharing relative to the standard devices (with no intermediate strips). Further data is required with more detector types at a range of fluences and particle types to demonstrate the extent of the enhancement possible [198].

Chapter 11

Quad FE-I4 Modules

Large area pixel modules are envisaged in the ATLAS inner detector upgrade. Increasing the module size reduces the total number required for full coverage and helps the the ratio of inactive to active areas of silicon, since less overlap between modules is needed. The supporting mechanics and cooling system can also be simplified, lowering their material budget. The effect of the changes in the structure and sensor material in both the pixel and strip layers for the Phase-II letter of intent (LoI) [18] baseline layout has been simulated for 5 GeV particles on the tracking resolution (d_0) as a function of η, where d_0 is the difference between the recorded track vertex position and its true position. Results are shown in Figure 11.1a while the tracking resolution including the calorimeter is shown in Figure 11.1b as a function of η. A negligible effect is seen in both cases where only the material of the strip layers has been altered. However, the amount of material in the pixel layers affects the tracking resolution substantially.

It is not possible to produce a readout chip larger than the existing IBL readout chip, the FE-I4. Its size ($\sim$ 2x2 cm^2) corresponds to the full reticule size used for imaging in deep sub-micron feature size CMOS electronics and it is regarded as being the largest possible for an ASIC. Therefore, a similar module structure to the existing FE-I3 modules (see Figure 4.11) has been considered, where multiple readout chips readout chips are attached to a larger area sensor. The following sections will describe the design and measured characteristics of Quad FE-I4 modules.

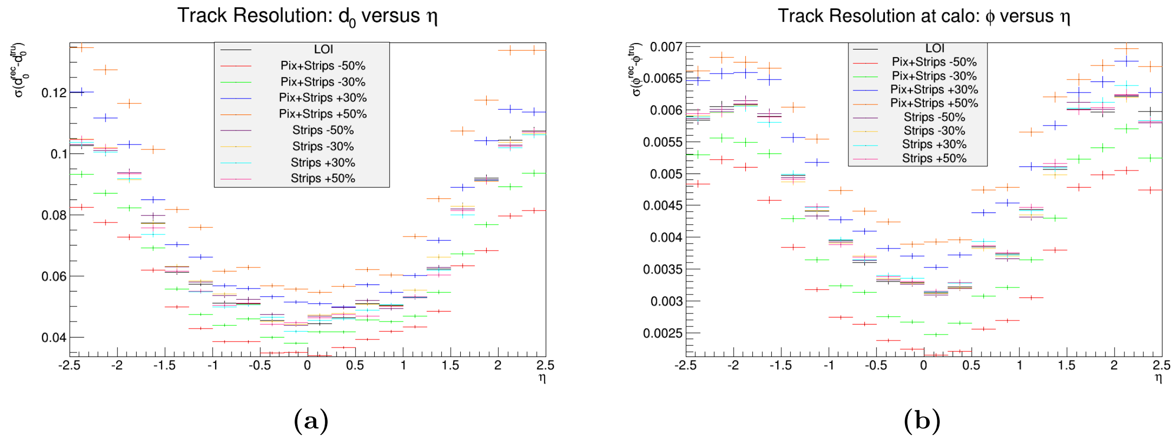

Figure 11.1: Track resolution simulations of (a) d_0 as a function of η and (b) of ϕ at the calorimeter as a function of η. In both cases 5 GeV particles and the Phase-II LOI baseline layout have been used [201].

11.1 CERN PIXEL IV Design

Quad module sensors are fabricated in the UK, using the Liverpool CERN PIXEL IV wafer design. This design features five "true" Quad FE-I4 sensors surrounded by single FE-I4 modules and diodes, only Quad sensors will be discussed. A Quad sensor has double the x and y dimensions of a single sensor FE-I4 readout chip, forming an $\sim 4\,\text{x}\,4\,cm^2$ square. Four readout chips are bump bonded to the sensor to create a Quad module. The bumping process requires a small gap (500 μm) to separate adjacent readout chips. This leaves any pixels within this area uncovered by the readout ASIC. Quads produced in the UK, use the same interconnection techniques used for current FE-I3 modules (Figure 4.12) to keep the whole detector area active. This is done using double length (500 μm) pixels in the gap between readout chip along the 250 μm direction (Xgap, see Figure 11.2b) [81]. A ganged pixel structure is used in the gap along the 50 μm pixel direction (Ygap, see Figure 11.2b). The top metal layer is used to link together multiple pixels distributed across the centre line of the sensor to a single readout channel. A close up of the CAD drawing for these pixels is shown in Figure 11.2b. Quads are referred to as being "true Quads" if they feature no inactive space within their guard ring structure. Another type of Quad named "pseudo Quads" exist which feature some in-active space within the ganged pixel structure. The wafer design with the positioning of Quads is shown in Figure 11.2. Four of five Quads feature a 400 μm cut edge and one a 300 μm slim cut edge design. Two versions of Quads labeled "Production" and "Test" are present on the wafer. The difference between the two variations is the numbers of ganged pixels

per column, eight and sixteen respectively. The FE-I4 chip features some redundant circuitry that is needed only for testing before module assembly which can be removed with dicing. This requires a dedicated dicing process that could damage the readout chip. However, removing this circuitry reduces the chips size and therefore the number of ganged pixels needed on the Quad sensor, lowering the input capacitance and therefore the noise for the connected readout channel. All Quad modules produced at the time of writing this thesis were constructed using the FE-I4A chip. Only test variation Quads have been produced.

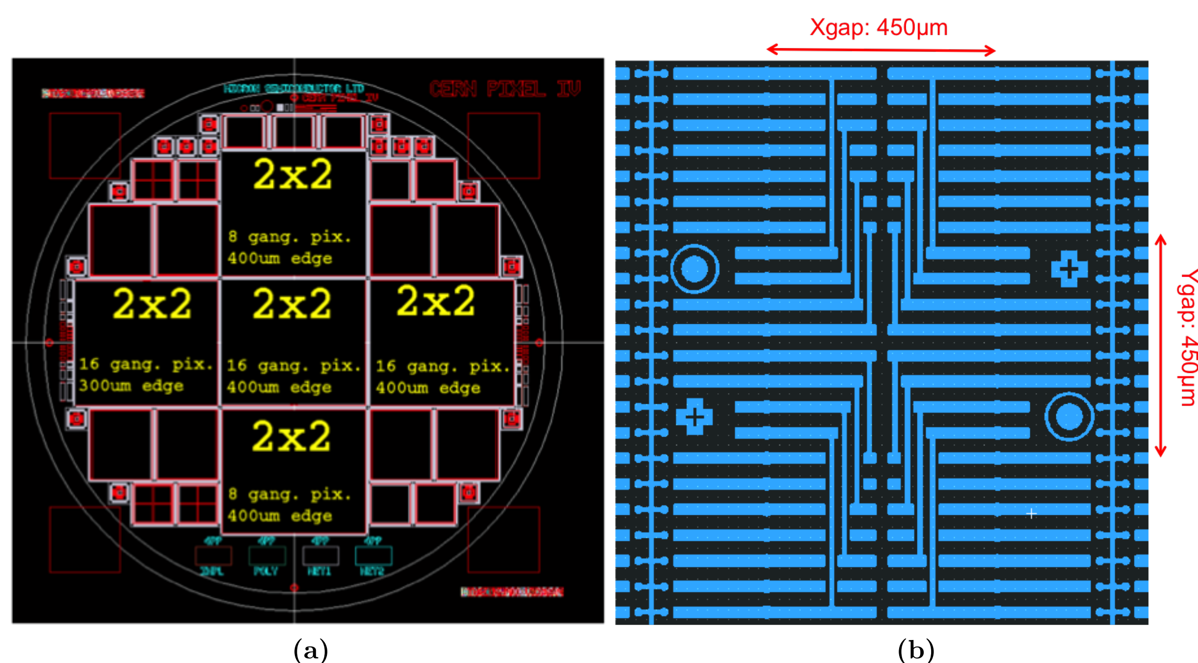

Figure 11.2: (a) Wafer diagram showing the positioning of Quad modules on a Micron 6" wafer, with key information such as number of ganged pixels per column and the cut edge distances. (b) The inner structure of a quad module showing long and ganged pixels along the Xgap and Ygap, respectively.

11.2 Wafer Characteristics

Quads were produced using 150 and 300 μm thick *n-in-p* silicon wafers. Because of the large sensor area, the electrical characteristics of Quad sensors are expected to be worse than for single FE-I4 sensors. Many wafers were produced and tested, however only characteristics for a single 300 μm thick wafer are shown in Figure 11.3. Characteristics for 150 μm wafers are not shown because only Quads from 300 μm thick wafers were

assembled into modules. Figure 11.3 shows the current voltage characteristics of Quads on a CERN PIXEL IV wafer along with the depletion point.

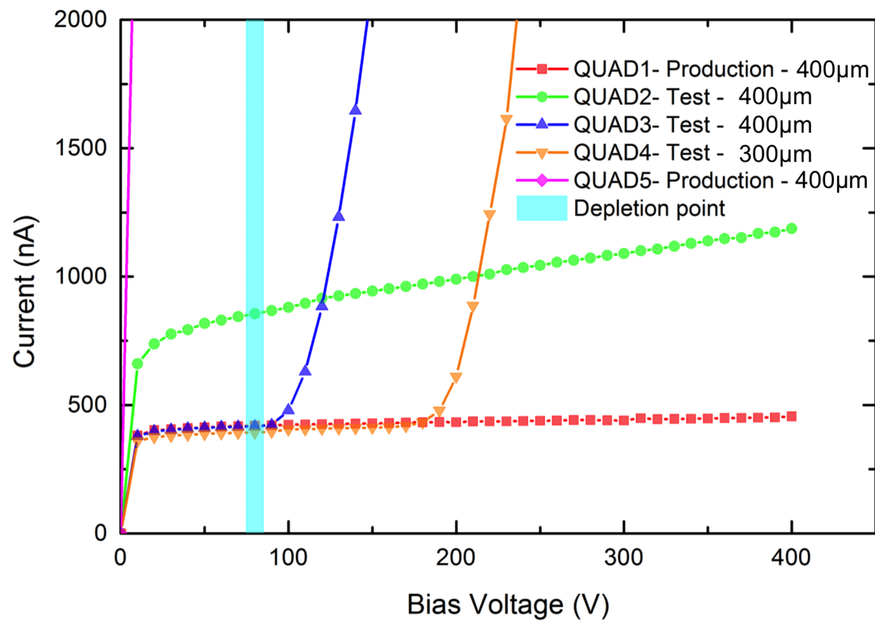

Figure 11.3: Quad FE-I4 sensor current voltage characteristics for a 300 μm thick *n-in-p* silicon wafer, where the depletion voltage is approximately 80 V.

Generally, production yields of Quad FE-I4 sensors is high (approximately 80 %) although the production yield of single FE-I4 sensors is usually above 95 %. Figure 11.3 shows that most Quads from a single wafer achieve full depletion before breakdown occurs. A large variation in Quad breakdown voltages is seen across the wafer. Comparing current voltage characteristics across many wafers does not indicate that the position of a Quad on the wafer affects its characteristics, therefore the most likely cause is a flaw in the design.

Thermal imagery of devices under stressed bias conditions was used to diagnose reasons for early breakdown and to improve the design and feedback to the processing at Micron. The main reason for high leakage currents (larger than expected) and relatively low break down voltages in Quad sensors is attributed to the pixel biasing structures used to provide power to all pixels. Punch through bias structures are important for assessing the quality of sensors before module assembly and are an ATLAS requirement for the production. This is because large area modules require multiple readout chips. Hence, if a sensor or wafer is identified as faulty before assembly significant cost savings are possible. After these measurements, the bias structures were redesigned to improve

sensor performance by lowering the leakage current and increasing the breakdown voltage. The re-design was introduced in the next UK ATLAS pixel wafer, the CERN PIXEL V which is discussed in Chapter 12. Details on the design changes and their implications are given in Section 12.3.

11.3 Module Characterisation

Quad modules are mounted on specially designed daughter boards for read out with USBpix or RCE systems. The daughter boards are then mounted in set-ups similar to those used with the ALiBaVa system for testing. Each readout chip (ROC) is operated separately (no data multiplexing) and therefore each ROC has its own data cable (Figure 11.4a). However, because the low voltage power supplied to a readout chip is very rarely changed from standard (Analogue 1.5 V and Digital 1.2 V) each Quad module is supplied with a common low voltage line to all its ROCs. The readout chip labelling convention used in this thesis is shown in Figure 11.4b with only one exception, the Quad module designated VTTQ4 was mounted on a prototype daughter board where the positions of ROC3 and ROC4 are swapped. A picture of a module mounted in the testing box with all data and power cables is shown in Figure 11.4a.

Two versions of Quad module daughter boards exist, labeled as V2.1 and V2.2. Both versions are identical except for the opening in the centre where the Quad is mounted, which is larger in V2.1. This version has extra space to allow pitch adapters to be placed between the readout chips and the surrounding daughter board (Figure 11.4b). Using pitch adapters allows a Quad to be fully tested before being sent for irradiation without having to break wire bonds to the ROC bond pads. An unfortunate feature of IBM's 130 nm processing means that the readout chips wire bond pads are composed of chromium with 1 % silicon. As a result they are very soft. This combined with their physical size means that only few attempts at bonding per pad are possible. Quad modules are attached to their daughter boards using mechanical support plates. Thermal and conductive glue is used to secure the module to a stiff conductive mechanical plate (for handling) which doubles as a central ground contact. Generally aluminium is used, however some modules have used thinner multi-layer carbon fibre plates.

Additional production complications have been encountered during the bump bonding of Quad modules. Some FE-I4 chips have been found to be un-responsive after being "bumped" to a Quad sensor. The reasons for this have not yet been investigated as this

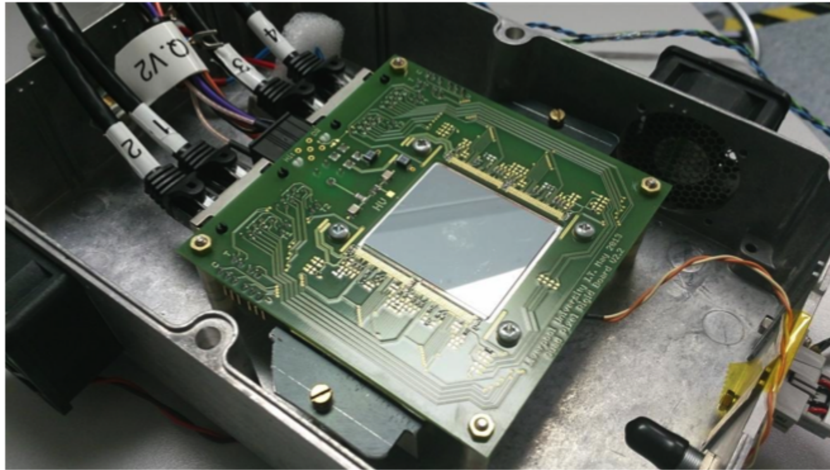

(a)

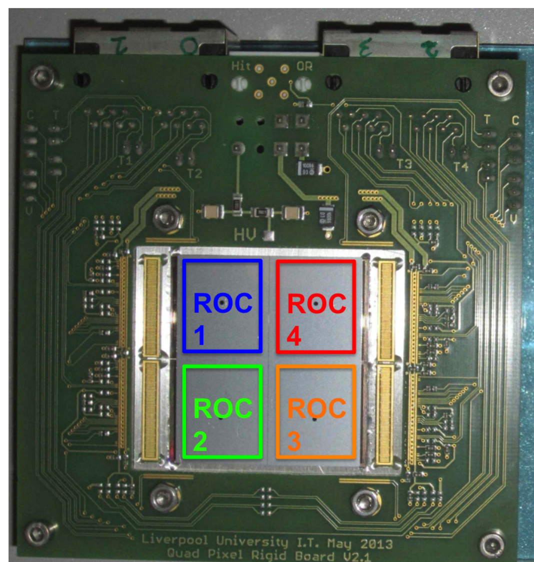

(b)

Figure 11.4: (a) Quad module mounted in a testing box which provides cooling via Peltier elements and fans. System also features plastic scintillator mounted under the module for triggering. (b) Close up of a quad module mounted on its daughter board showing relative positions of each of the four FE-I4 readout chips (ROCs).

would require removing the readout chips destroying the module. Similar difficulties have been encountered by other ATLAS pixel R&D groups producing Quad modules. The cause of this issue has been attributed to the tooling used to handle the modules after bumping and the bumping process of multiple readout chips to the same sensor. The focus of pre-irradiation tests is on VTTQ4 which is a Quad module composed of 300 μm thick *n-in-p* silicon with full thickness readout chips (750 μm). This module has three

functioning readout chips: ROC1, ROC2 and ROC4. The focus of post-irradiation tests will be on VTTQ-IRRAD01 ($5 \cdot 10^{15}\,\mathrm{n_{eq}/cm^2}$), with all four ROCs fully functional.

11.3.1 Pre-Irradiation

Module IV

The characterisation of Quad module reverse currents is important before and after irradiation to correctly estimate the cooling power for a given bias voltage and irradiation dose. The pixel biasing structures used in this design have been found to drastically increase the reverse current of sensors causing early breakdown. However, after module assembly the individual pixels on the sensor are also grounded via the ROC. The biasing structure is bypassed because of the lower resistance connection through the readout chip. As a result the module reverse current is expected to decrease. The leakage of the Quad module VTTQ4 was measured without powering any of its readout chips on, followed by subsequent measurements as each ROC was powered up. This was done to see how the leakage current changes as multiple FE-I4 readout chips dissipate power through the sensor, raising its temperature in order to estimate the required cooling power for room temperature operation. The results are shown in Figure 11.5.

As expected, an increase in leakage current is seen as consecutive ROCs are turned on. The module has a depletion voltage of $\sim 80\,\mathrm{V}$, determined by measuring the sensors bulk capacitance. The total reverse current of VTTQ4, if it had four working ROCs has been estimated based on the measured increase in current as each consecutive readout chip was turned on, which was then added to the leakage current with three ROCs turned on. Based on this estimation and before signs of early break down the module has a baseline reverse current of approximately $0.05\,\mu\mathrm{A}$. This is roughly 10 times lower than the baseline current measured before module assembly, and clearly indicates the effect PTB structures have on the leakage currents of devices. The module shows signs of current increase at around $120\,\mathrm{V}$. This is approximately 1.5 times the full depletion and the module can therefore be operated safely and efficiently at room temperature. Cooling reduces current and would allow for higher bias voltages to be applied but this was not necessary for our intended tests.

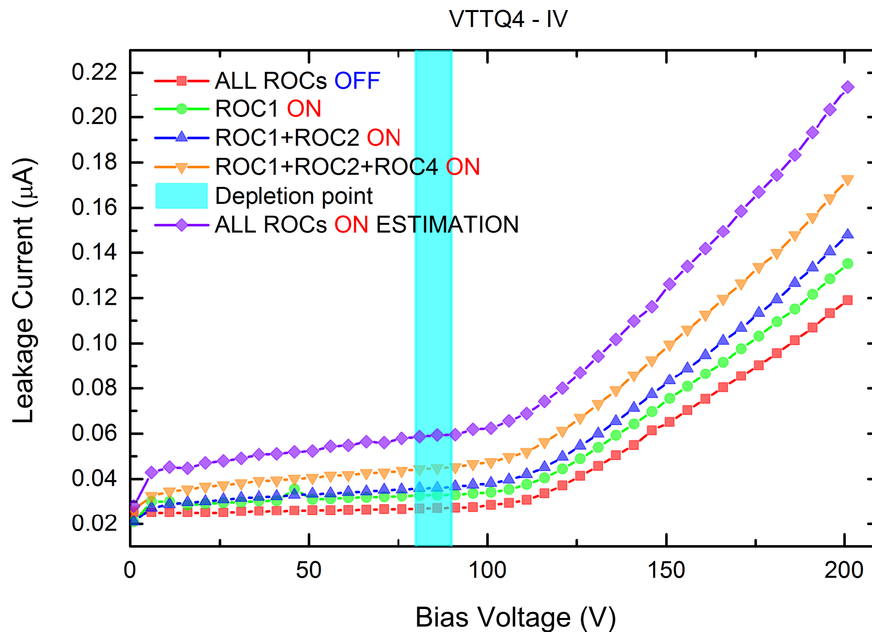

Figure 11.5: Current voltage characteristics of Quad module VTTQ4. Showing the change in reverse current as consecutive ROCs are turned on. An estimation of the reverse current has been made for all four ROCs based on the change in current measured as consecutive ROCs are turned on.

Module Tuning

The following will outline tuning results with Quad module VTTQ4 with the RCE system. The tuning procedure is similar to the testing procedure used to qualify IBL modules during stave assembly and won't be discussed, for more information refer to [202, 203]. However some basic information concerning the tuning can be found in Section 9.5.5.

The module is over-biased to 100 V ($\sim$ 80 V full depletion) and initially tuned at a high threshold followed by subsequent tunings at lower thresholds. Figure 11.6 shows the results from the highest threshold tune of 3000 e. This Quad module uses pitch adapters, which has implications on the noise. The pitch adapters increase the distance between the readout chips and the filtering capacitors on the daughter board which supply power and clock. Furthermore, the extra wire bonds and their fine spacing is expected to increase inductive pickup.

To test wether using pitch adapters has any effect of the performance of a module, the readout chips were tuned by lowering the threshold in 100 e steps. Single FE-I4 modules have been demonstrated to show no significant increase in noise or threshold down to

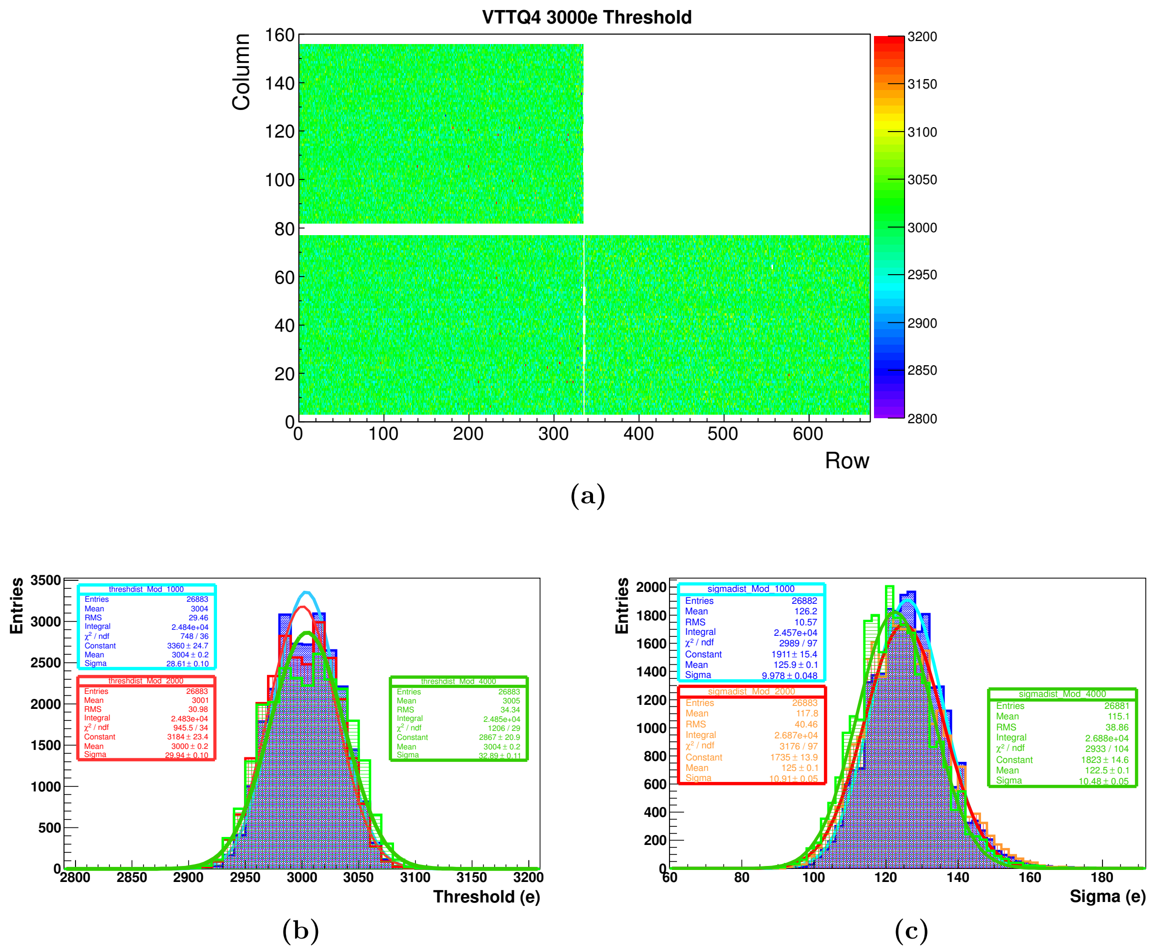

Figure 11.6: (a) 2D threshold plot showing the relative positions of each pixel across each active FE-I4. (b) 1D threshold distribution for all active ROC's as a function of threshold in electrons. (c) 1D noise distribution of all active ROC's as a function of sigma (noise) in electrons.

1500 e. The resulting tuned threshold and noise values is shown in Figure 11.7 for each readout chip, where each chip was tested simultaneously.

No significant difference was observed compared to a single module down to 2300 e. A small increase in noise is seen with the decreasing threshold. The performances of ROC1 and ROC4 are very similar but ROC2 consistently has higher noise or a wider threshold spread which only worsens with decreasing threshold. Some indication of inductive pickup can therefore be inferred.

It was not possible to tune the module below 2300 e. During the TDAC tune (threshold trimming) the analogue circuitry is affected by the inductive pickup. As a result the pixel starts to exhibit failures or they are not responsive to the tuning. Further tests revealed

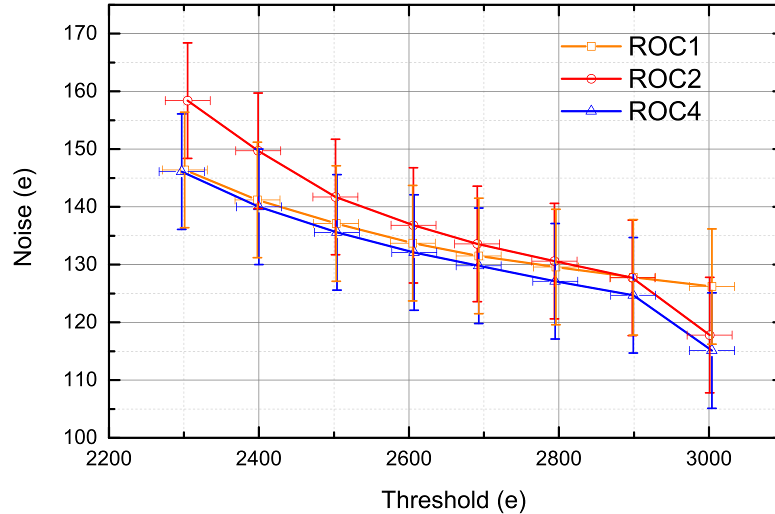

Figure 11.7: Tuned Threshold vs noise for VTTQ4 at 100 V.

that this effect is already present at higher thresholds but it gets worse as the threshold is reduced. Nonetheless this effect involves a small number of pixels. Figure 11.8 shows the response from the analogue circuitry after a successful 2300 e threshold tuning. Successful, denotes that the discriminator thresholds and ToT calibrations are good with little noise or spread across pixels. Each pixel is expected to have a value of 50, which is the number of units of charge injected into each pixel. This behaviour is most likely due to inductive pickup, since this behaviour is not seen in the digital test.

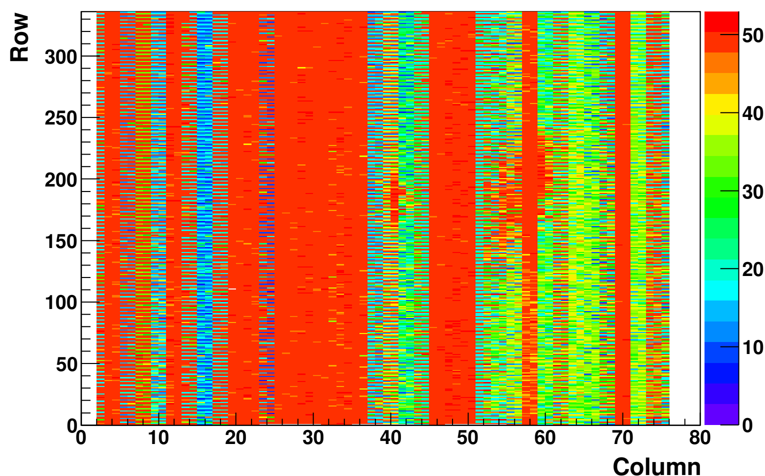

Figure 11.8: Analogue response after reading back the number of charges injected into each pixel (50 charges injected).

The percent of bad pixels in each readout chip was calculated based on the sigma of threshold, Figure 11.9a and noise Figure 11.9b distributions. Any pixel outside the range of $2 \cdot \sigma_{width}$ from the peak position of the Gaussian distribution in either direction is regarded as being bad.

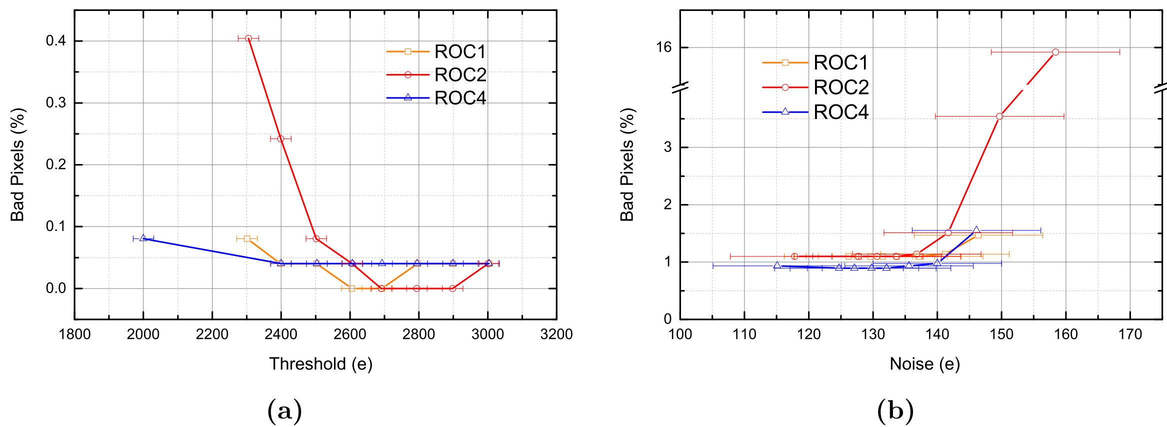

Figure 11.9: (a) Percentage of bad pixels based on the spread of threshold distributions for each ROC. (b) Percentage of bad pixels based on the spread of noise distributions for each ROC.

The number of bad pixels was calculated based on the total number of pixels after the application of the initial masking used with FE-I4A devices (see Section 9.5.2). The reference number of pixels is therefore 24,840 instead of 26,880. The bad pixel count increases with decreased tuning threshold. However, the percentage of bad pixels calculated using the spread of the threshold distributions is very low ($< 1\,\%$) even at 2300 e. This shows that the tuned threshold is not significantly affected by inductive pick-up. The number of bad pixels calculated based on the spread of the noise distributions is much larger indicating that the inductive pickup affects the noise of each pixel, especially at lower thresholds. Above 140 e the number of bad channels starts to increase significantly. The higher noise in ROC2 has lead to significant numbers of bad pixels, $\sim 16\,\%$ at 2300 e. A large fraction of these bad pixels is due to threshold tune failing to read back a noise value for many pixels, if this happens, bin zero fills with entries instead. These entries will therefore be in the bad pixel range.

The ToT needs to be tuned at each threshold, but it uses digital circuitry instead of analogue circuitry. Consequently, the ToT is only slightly affected by inductive pickup at lower thresholds, and is more likely affected by previous threshold tunes. Figure 11.10a shows the ToT tuning for each pixel after a 2300 e threshold tuning, where 8 ToT is equal

to 20 ke. The tuning is mostly uniform with small variances in the pixel columns with different responses (see Section 9.5.2). Figure 11.10b shows a 1D comparison between ToT results after 2300 e and a failed 2200 e threshold tune. At 2300 e a double peak is seen which corresponds to the different pixel types discussed in Section 9.5.2. At 2200 e (failed threshold tuned) the ToT distribution has widened slightly compared to the result at 2300 e although the spread is still small. The broader ToT distribution is attributed to the increase in noise of each pixel.

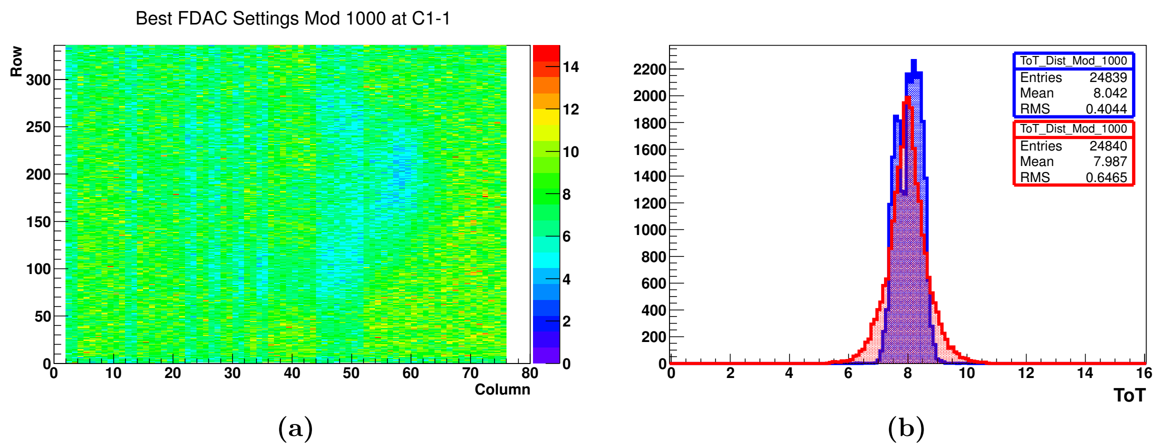

Figure 11.10: (a) Tuned ToT where the target 8 ToT represents a 20 ke signal (2300 e threshold). (b) 1D comparison between ToT values with the same target value (8 ToT) at 2300 e (blue) and 2200 e (red) threshold tune.

As a result of these tests, pitch adapters with built-in filtering capacitors and wider tracks were produced. So far initial tests with bare FE-I4 chips have been done, showing reduced effects from inductive pickup. The results of these tests are beyond the scope of this thesis and further tests are needed with a functioning Quad module. Another method being explored to reduce the noise and the effect of inductive pickup is to use the FE-I4's built in LDO regulators to provide regulated power. due to a shortage of FE-I4 chips at the time of writing this thesis, this method of powering hasn't been fully tested. Any result for Quad modules shown from here on have been obtained without using pitch adapters.

11.3.2 Post-Irradiation

The following sections focus on two modules with the same composition as VTTQ4 (*n-in-p*, full thickness). Both modules were irradiated at CERN's PS to $5 \cdot 10^{15}\,\mathrm{n_{eq}/cm^2}$.

VTTQ-IRRAD01 has a 400 μm cut edge while VTTQ-IRRAD02 has a 300 μm cut edge. both modules were mounted on V2.2 daughter boards. VTTQ-IRRAD01 is fully functional (four working readout chips) and VTTQ-IRRAD02 has three out of four readout chips functional.

Module IVs

Both devices are mounted to a support plate which also provides cooling. This is usually made of aluminium ($\sim$ 1 - 2 mm thick) and cooled using Peltier elements or via copper tape to dissipate the heat cooled by forced air circulation within a cold box/freezer. Instead, VTTQ-IRRAD01 uses a 400 μm thick carbon fibre plate. This lower mass support plate was used because the module was prepared for test beam characterisation at DESY using 4 GeV positrons. The IV characteristics of each module were measured with readout chips on or off to measure the effect of heating caused by the power dissipation in the readout electronics.

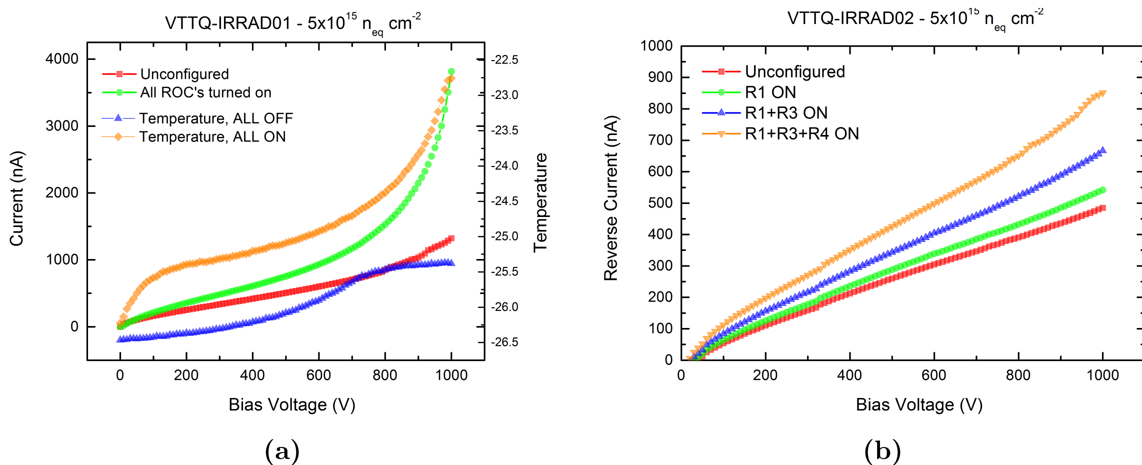

(a) (b)

Figure 11.11: (a) Current voltage measurements of VTTQ-IRRAD01, with all ROCs turned on and off (un-configured). The measured change in temperature is shown in both cases respectively. (b) Current voltage measurements of VTTQ-IRRAD02 showing the change in reverse current as subsequent ROCs are turned on.

Figure 11.11a shows the measured reverse currents for VTTQ-IRRAD01 with electronics turned on and off. With the ASICs off, the module can be biased up to 1000 V ($\sim 1\,\mu A$) without a sharp increase of the current at high voltage. During the test only a small variation in module temperature ($\sim$ 1 °C) was recorded. the reverse currents of the module drastically increase when all readout chips are turned on. In this case the modules can be biased up to 1000 V but the reverse current starts to increase rapidly

after 800 V. The change in temperature measured across the module is also substantial, $\sim 4\ ^{\circ}$C and follows the same trend as the leakage current measurement. The ability to bias the module up to 1000 V, while having lower pre-irradiation breakdown voltages was expected after $5 \cdot 10^{15}\ \mathrm{n_{eq}/cm^2}$. The insufficient removal of the heat generated by the electronics is due to the poor transfer through the thin carbon support plate. Therefore, VTTQ-IRRAD02 (300 μm cut edge) was mounted on the more traditional thicker aluminium plate. Figure 11.11b shows the IV characteristics of VTTQ-IRRAD02 measured under the same conditions as VTTQ-IRRAD01, as each readout chip is turned on. An increase in reverse current is still observed. However, this increase is substantially reduced, especially at very high bias voltages. Since this module has a slimmer cut edge it could have been expected to have worse current voltage characteristics compared to the 400 μm cut edge VTTQ-IRRAD01, but this effect is most probably compensated by the more effective heat removal. The slim edge module can be biased to 1000 V without breaking down or showing any severe increases in reverse current.

Module Tuning

This section will focus on the characterisation of VTTQ-IRRAD01 because at the time of writing this thesis VTTQ-IRRAD02 was still being characterised. As mentioned in the previous section VTTQ-IRRAD01 suffered from overheating caused by insufficient heat removal when the electronics are operated. It was possible to characterise the module up to 800 V maximum bias (measurements were taken at 500, 600, 700 and 800 V).

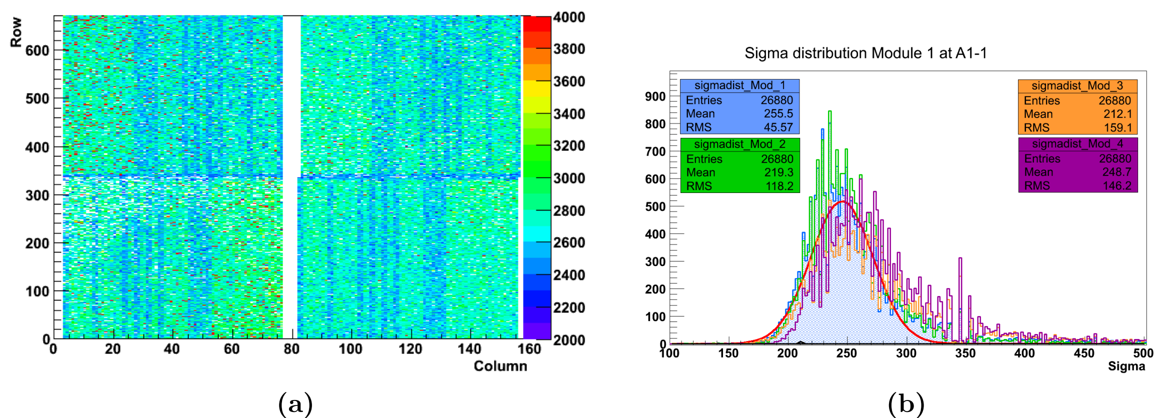

(a) (b)

Figure 11.12: (a) 3200 e threshold tune where all four ROCs are enabled. As with all FE-I4A modules the end columns have been masked out on each readout chip, any other white pixels are unresponsive pixels. (b) 1D noise distributions of each ROC overlaid.

Figure 11.12a shows a 2D hitmap of the tuned pixel threshold at 800 V. The corresponding noise distribution is shown in Figure 11.12b for each ASIC. All pixels that are white and do not belong to the standard FE-I4A mask shown in Section 9.5.2 are dead or unresponsive pixels. The module has a relatively small amount of dead/un-responsive pixels for its dose. Most of the dead pixels are in ROC3 and these might be due to local damage caused by handling or unidentified problems with this ASIC. The pixel columns with different responses are clearly distinguishable from the rest of the readout chip. Typically, these pixels tune ~ 400 electrons lower than the target threshold. However, although not shown, their ToT responses do not vary much from the target set during tuning. An increase in noise is seen compared to an unirradiated module. This is expected since the module has been irradiated to its maximum qualified operational dose. Despite this the noise for each ROC is relatively small with little variance (noisy pixels have not been masked out).

The module was tuned at 3000 e at each bias voltage and then subsequently retuned at a lower threshold in 200 e steps. The results are summarised in the threshold vs noise plots for 500, 600, 700 and 800V in Figure 11.13. In each case a small variation in the threshold is seen with respect to its target value. Only full tunings at 3000 and 2800 e were possible at any voltage. Below this point the noise per pixel becomes non-Gaussian and very large ranging from 400 to 1000 e. As a result the number of bad pixels drastically increases.

Table 11.1 shows a summary of the percentage of bad pixels for each ROC at a given sensor bias voltage and threshold tune. ROC3 has the greatest percentage of bad pixels. Given the modules irradiation dose and issues associated with self heating the number of bad pixels at 3000 and 2800 e at any voltage is acceptable. However, a major increase in noise at 2600 e results in a significant increase in the number of bad pixels. The cause of this sharp increase in noise is unknown, the effect of thermal instability on the modules performance requires tuning results using VTTQ-IRRAD02.

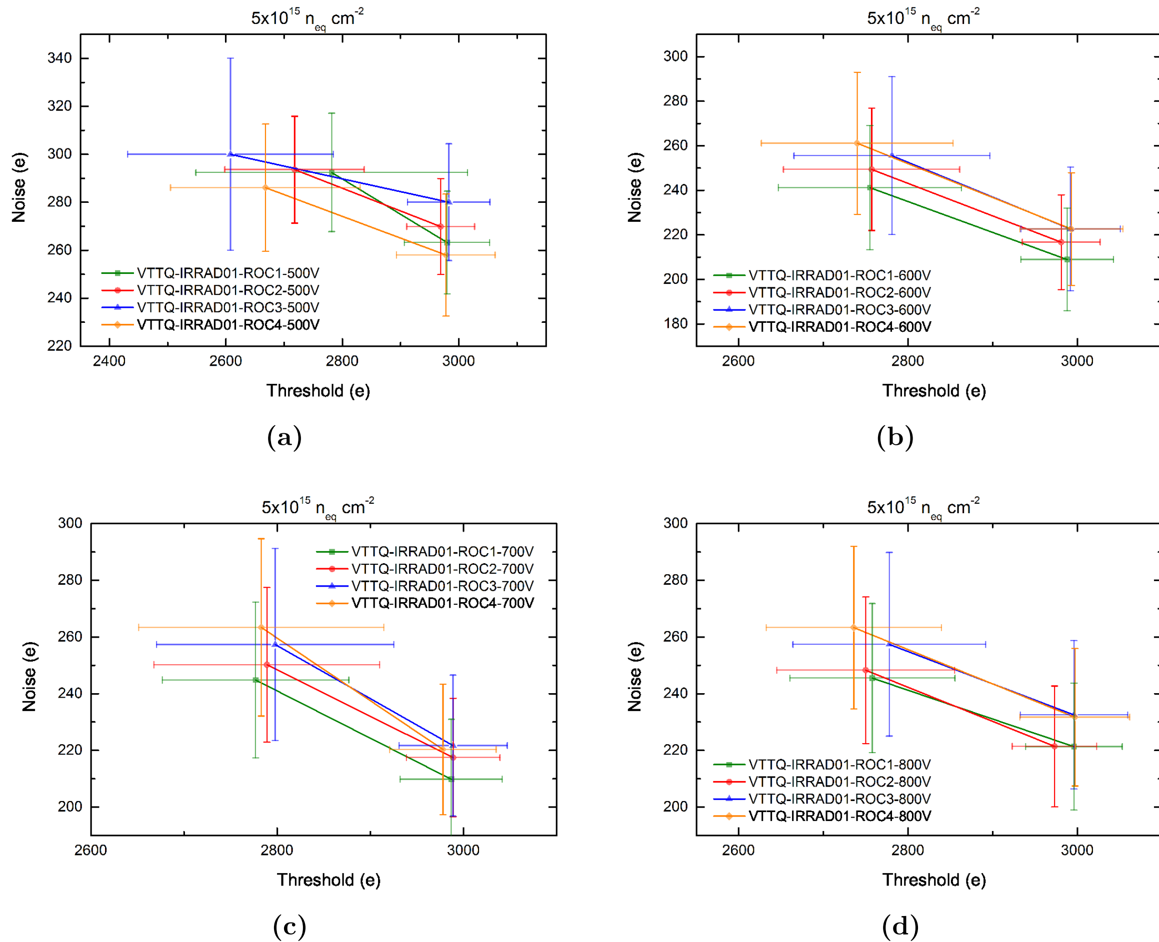

Figure 11.13: Threshold vs noise (electrons) results from lab tunings of VTTQ-IRRAD01 at (a) 500 V, (b) 600 V, (c) 700 V and (d) 800 V.

11.4 Summary

The results shown in this chapter show, significant work has been done to create Quad sized pixel modules for use at HL-LHC. Many obstacles in the design and production of modules has been overcome. However, work performed in the next chapter has shown substantial improvements with regards to leakage currents of pixel sensors with very high over depletion voltages before breaking down.

A significant amount of work still needs to be done to isolate the module and thus readout chips from external sources of noise which affect module performance. The reliability of FE-I4 chips at their maximum operation dose of $5 \cdot 10^{15}$ $\mathrm{n_{eq}/cm^2}$ is still in question. Further testing of modules composed of the FE-I4B readout chip is needed before and after irradiation.

Voltage (V)	Threshold (e)	ROC1 bad pixels (%)	ROC2 bad pixels (%)	ROC3 bad pixels (%)	ROC4 bad pixels (%)
800	3000	12.4	10.3	21.0	6.3
	2800	15.5	13.2	24.3	10.6
	2600	84.8	65.0	74.8	86.5
700	3000	13.7	11.4	22.6	6.4
	2800	16.5	15.4	26.0	8.4
	2600	90.2	72.1	81.3	91.7
600	3000	17.1	12.9	25.0	7.4
	2800	22.4	15.4	28.3	14.0
	2600	91.3	71.6	82.7	91.2
500	3000	31.5	15.9	33.2	14.9
	2800	47.1	20.4	47.5	32.2
	2600	92.4	76.4	85.6	79.5

Table 11.1: Percentage of bad pixels in each ROC after a given bias voltage and threshold tune. Each device was irradiated to $5 \cdot 10^{15}\ \mathrm{n_{eq}/cm^2}$.

Chapter 12

Alternative Geometry Single FE-I4 Modules

The Phase-II LOI states that outer pixel barrel layers and disks will use sensors with a cell size of 250x50 μm^2, and 125x25 μm^2 in the inner barrel layers. These sizes have been dictated by the need for fine granularity and tracking. The expected track density per unit of η and the required radiation tolerance, dictate the necessity for a new readout chip for the inner pixel barrel layers, called FE-I5, now being designed. This new ASIC will have a higher density of active electronics with higher requirements for cooling and powering. For this reason, it is envisaged that a variation of the IBL FE-I4 chip will be used in the outer pixel barrel and disk layers [18].

The pixel cell dimension of 250x50 μm^2 is not necessarily the best option for every layer or forward wheel of the Phase-II ATLAS tracker. It is also not possible to produce multiple versions of readout ASICs with different pixel sizes intended for different areas of the tracker. However, one possibility would be to alter the implant geometry on the sensor while retaining a pre-existing bump bonding foot print to allow the use of one type of ASIC (FE-I4 or even FE-I5). To investigate the feasibility of this solution, Liverpool has designed a new mask set (CERN PIXEL V) with altered pixel cell dimension on the sensor, while retaining the FE-I4 bump bonding foot print.

The following sections describe the reasoning for the chosen geometries. Besides, following the intensive testing and evaluation done during and after the production of the QUAD FE-I4 modules, all pixel on the CERN V wafer feature a new standard biasing structure to correct the less performant one previously implemented. This is discussed in Section 12.3.

12.1 CERN PIXEL V

The CERN PIXEL V wafer features sensors with standard, 250x50 μm^2, and alternative geometry pixel cells, whilst still being compliant with the FE-I4 bump bonding foot print. The wafer layout and labelling of all the designs is shown in Figure 12.1. Every sensor features a new biasing structure designed to test the sensors before module assembly. There are two variations on the new biasing structure that utilise different powering methods. These are denoted by AC or DC, where AC refers to surface poly silicon resistors which connect every pixel implant to the bias ring via bias rails. The DC variant uses the traditional punch through biasing structure, the biasing dot has been moved outside the pixel cell and is now shared by four neighbouring pixels (see Section 12.3).

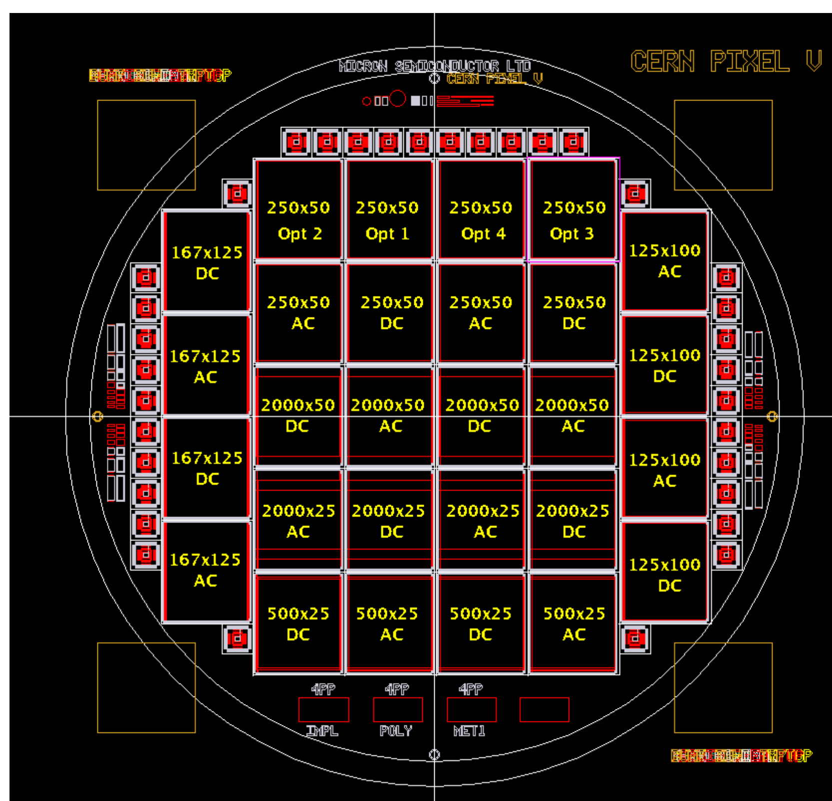

Figure 12.1: Wafer diagram of the CERN PIXEL V design, each device is a $\sim$ 2x2cm^2 FE-I4 compliant sensor with different pixel implant geometries.

There are five variants of the standard pixel cell design, listed in Table 12.1 along with their pixel cell dimensions, number and percentage of FE-I4 readout channels used. The first two designs use all the available channels, while the other three use less. The advantage of making a bigger pixel, providing there is still adequate granularity, is that unused readout channels can be turned off, reducing the overall power consumption of the

Name	X Cell Dimension (μm)	Y Cell Dimension (μm)	Number of Channels Used	Percentage of Channels Used
250x50	250	50	26880	100 %
500x25	500	25	26880	100 %
125x100	125	100	26880	100 %
167x125	167	125	16080	59.82 %
2000x50	2000	50	3660	12.5 %
2000x25	2000	25	6720	25 %

Table 12.1: Description of each design on the CERN PIXEL V wafer, giving the pixel cell dimensions and total number of channels used.

readout chip. The present version of the FE-I4 (B) doesn't have the option to completely turn off a readout channel, but this functionality could be included in a future version.

500x25 μm^2: This design, allows for increased r/ϕ resolution at the expense of z resolution in the barrel layers. This benefits the high η barrel regions, because hit cluster sizes are relatively large along this direction (due to the low angle tracks) and the expected impact on the z resolution would thus be minimal.

125x100 μm^2: This more square design could be useful in regions where the z resolution starts to become just as important as the r/ϕ resolution in the barrel or the x/y resolution in the disks i.e. the forward disks.

167x125 μm^2: The same motivation as for the 125x100 μm^2 design, although with bigger pixels. This design does not use all readout channels and could be used with in the outer disks.

2000x50 μm^2: This design is referred to as a strixel (strip-pixel). The design serves two purposes, firstly, testing the FE-I4s response to pixels with large capacitances and secondly, the possibility to have an intermediate strip pixel layer (5th pixel layer). Only 1/8 (12.5 %) of all readout channels are used, therefore, significant power savings can be achieved.

2000x25 μm^2: This design serves the same purpose as the 2000x50 μm^2 design, but with increased r/ϕ resolution at the expense of using more readout channels, 1/4 (25 %) of all readout channels.

The 500x25 μm^2 and 125x100 μm^2 designs serve to allow key parameters such as charge sharing and hit cluster sizes to be studied as a function of fluence, device thickness and track inclination. This will help inform the design of the next readout chip (FE-I5).

12.2 Simulation

Some basic simulations using the Phase-II LOI baseline layout and 1, 10, 100 and 500 GeV have been performed using the 500x25 μm^2 and 125x100 μm^2 designs. These "fast" simulations show the differences in track resolutions for σ_{p_t}/p_t (%) and z_0 (μm), by simply changing all pixel cell dimensions. The resulting σ_{p_t}/p_t and z_0 are given in Figure 12.2a and Figure 12.2c for 500x25 μm pixels and in Figure 12.2b and Figure 12.2d for 125x100 μm pixels respectively.

Improved σ_{p_t}/p_t resolution at high η is seen in the 500x25 μm^2 design and is reduced in the 125x100 μm^2 design from 10 GeV onwards. Decreased z_0 resolution is seen in the 500x25 μm^2 design and increases in the 125x100 μm^2 design but only from 100 GeV upwards, no difference is seen at lower p_t. More detailed simulations where different sections of the tracker use different pixel geometries are still needed.

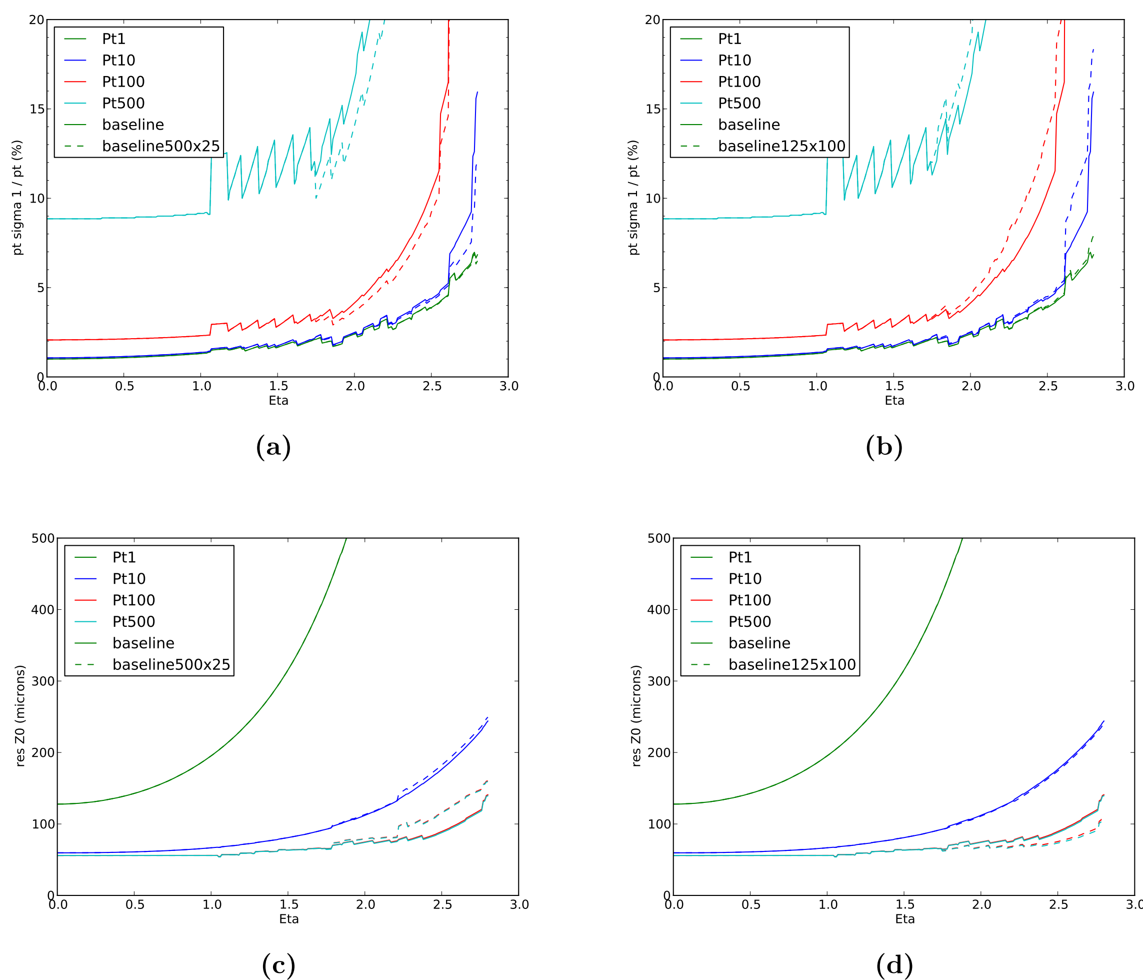

Figure 12.2: Simulation results showing the $\sigma_{p_t}/p_t\,(\%)$ distributions as a function of η for (a) 500x25 μm^2 pixels and (a) 125x100 μm^2 pixels. The expected z_0 residuals (μm) for (c) 500x25 μm^2 pixels and (d) 125x100 μm^2 pixels. All plots use 250x50 μm^2 pixels as a bench mark for comparison using 1, 10 , 100 and 500 GeV [204].

12.3 Poly silicon resistors vs Punch Through Bias structures

A comparison of the old (Figure 12.3a) and new (Figure 12.3b) punch through biasing structure is shown. The new design is simpler, only a single biasing implant is needed to power every four pixels. The isolation region present between implants is utilised to separate the biasing structure from the pixel implant structures. This has enabled the biasing structure to be reduced in size. While the size and curvature of the biasing structure have been optimised for processing at Micron Semiconductors Ltd.

The biasing dots are placed outside the pixel implant, simplifying the design and removing inefficient areas from each pixel. The new scheme reduces the total inefficient area and the number of possible high leakage current generation sites. Thermal imagery has shown that the PTB structures create high field regions which in turn can create large leakage currents which can cause device breakdown. Reducing the number of these structures reduces the leakage current. Devices featuring this punch through biasing structure are labeled as DC on the CERN PIXEL V wafer design.

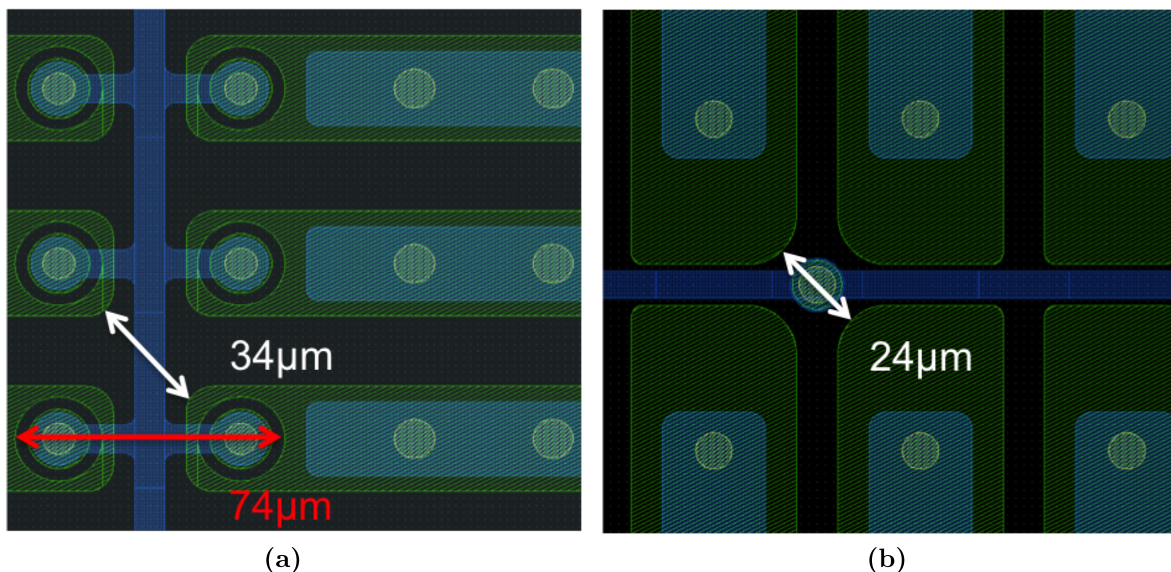

(a) (b)

Figure 12.3: CAD drawings of the (a) old and (b) new punch through bias design.

The AC biasing option uses poly silicon resistors to connect every pixel to the bias rail. The advantage of this design is that no biasing dot is implanted on the sensor and therefore there are no other implants to "steal" charge from neighbouring pixels. The size of the pixel does effect whether a poly silicon biasing structure with the required

resistance can be implemented. The CERN PIXEL V uses two variants of poly silicon resistors. The resistor (Figure 12.4a) is wrapped around the pixel or (Figure 12.4b) is placed on top of the pixel. The latter variation is only used on the strixel devices because of their size.

Both options have been produced and tested to see if there are any un-expected issues after irradiation, such as capacitive charge losses from neighbouring pixels towards the poly silicon resistors wrapped around the pixel implants. The poly silicon resistors placed on top of the strixel implants may also suffer from planarity issues, where the surface is no longer planar (flat) which could have repercussions for bump bonding.

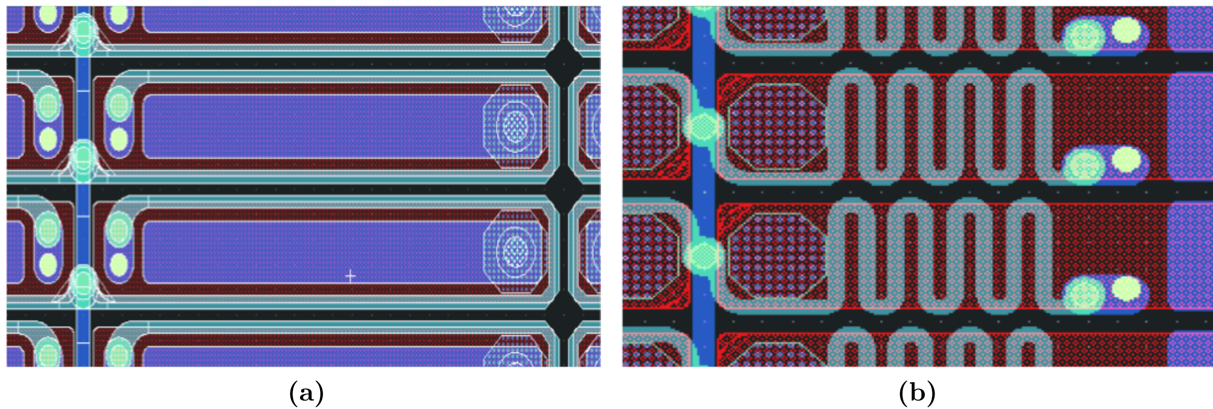

(a) (b)

Figure 12.4: CAD drawings of the two types of poly silicon resistor used in the CERN PIXEL V design. Both have lengths that are approximately the same. (a) The poly silicon resistor is wrapped around the pixel. (a) The poly silicon resistor is placed on top of the pixel, this is only implemented on strixels due to their size.

12.4 Wafer Characteristics

The production of CERN PIXEL V wafers is still on-going, Several *n-in-p* type wafers with thicknesses of 100, 150, 200 and 300 μm and bulk resistivities from 5, 10 and 14 $k\Omega/cm$ are planned or have already been produced.

Figure 12.5 shows the IV characteristics for a fully processed AC/DC wafer, 300 μm thick with a 10 $k\Omega/cm$ bulk resistivity. Each design variant is colour coded. The labelling of the key is as follows, the first two sets of numbers reference the wafer followed by the pixel design and powering structure type. The final number references the sensor position on wafer, and is also used as a unique identifier.

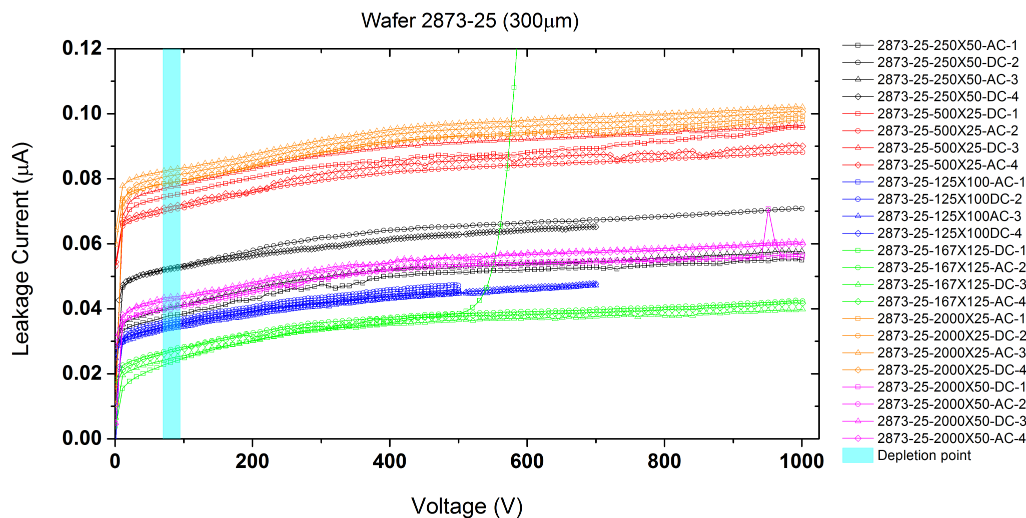

Figure 12.5: Current voltage (IV) measurements of a fully processed AC/DC wafer. Devices are capable of being biased to 1000 V before breakdown.

Figure 12.5 shows almost flat stable leakage currents up to 1000 V, with few examples of hard or soft breakdown for most devices. Some devices were not tested all the way up to 1000 V because they were not expected to reach this 1000 V. No significant difference is observed in the performances of AC vs DC devices with respect to any of the designs. However, devices can be seen to be grouped together into bands. These bands correspond to the density of biasing structures. The top band featuring the largest leakage currents composed up of 2000x25 and 500x25 μm^2 devices, both of these devices have different numbers of biasing structures but they both have the highest local density of biasing structures. Where local refers to the region between neighbouring pixels.

The middle band is composed of 2000x50 μm^2 and 250x50 μm^2 devices. The increased pixel cell size in the y direction (sensor reference frame, see Ygap in Figure 11.2b) has a

lower local density of biasing structures compared to the 25 μm designs and thus, has lower leakage currents. In both cases, no electrical difference can be seen between the pixel and strixel devices.

The lower band, has only a small separation from the middle band. It is composed of the square devices, 125x100 μm^2 and 167x125 μm^2. Their structure again lowers the local density of biasing dots, lowering the average leakage current for a device. However, in all cases the leakage currents are low and the 250x50 μm^2 devices show about half the leakage current measured with 250x50 μm^2 devices with the old punch through biasing structure.

The depletion point indicated is wider than usual. This is due to the different design variations having slightly different depletion points. It has been experimentally observed that the longer the implant (longest direction) is, the higher the depletion point is. The difference is negligible for all designs except for the strixels that consistently require $\sim$ 10 V extra to reach full depletion.

The IV characteristics of DC only devices on; 200 μm thick 5 $k\Omega/cm$, 150 μm thick 10 $k\Omega/cm$ and 100 μm thick 10 $k\Omega/cm$ *n-in-p* wafers are shown in Figure 12.6a, Figure 12.6b and Figure 12.6c respectively.

The higher resistivity of the 200 μm thick wafer leads to a similar full depletion voltage compared to the 300 μm thick devices shown in Figure 12.5. However, leakage currents are slightly higher. For the 150 μm (10 $k\Omega/cm$) thick devices, some breakdown occurs before 1000 V, but even the first device to breakdown biases over 10 times its full depletion voltage. This trend is expected as the electric field gradient is larger than in thicker devices for a given bias voltage. The 100 μm thick device again shows the same leakage current trends for all the designs and starts to breakdown at a lower bias voltages, again because of the higher electric fields. Most devices are capable of being biased up to 20 times their full depletion voltage before any signs of breakdown are seen. Electrically the thinner sensors have superior performances compared with thicker sensors because of the amount they over deplete. Currently only 300 μm sensors have been assembled into modules, because of bump bonding issues associated with lower thickness devices. Since, the devices characterised in Figure 12.6 vary in thickness and bulk resistivity which effect there depletion point. they have to be compared by looking at the amount they over deplete relative to their depletion point. The depletion points shown are given as a band because of the variations in implant capacitance. Some of the bands are wide because to the strixel devices.

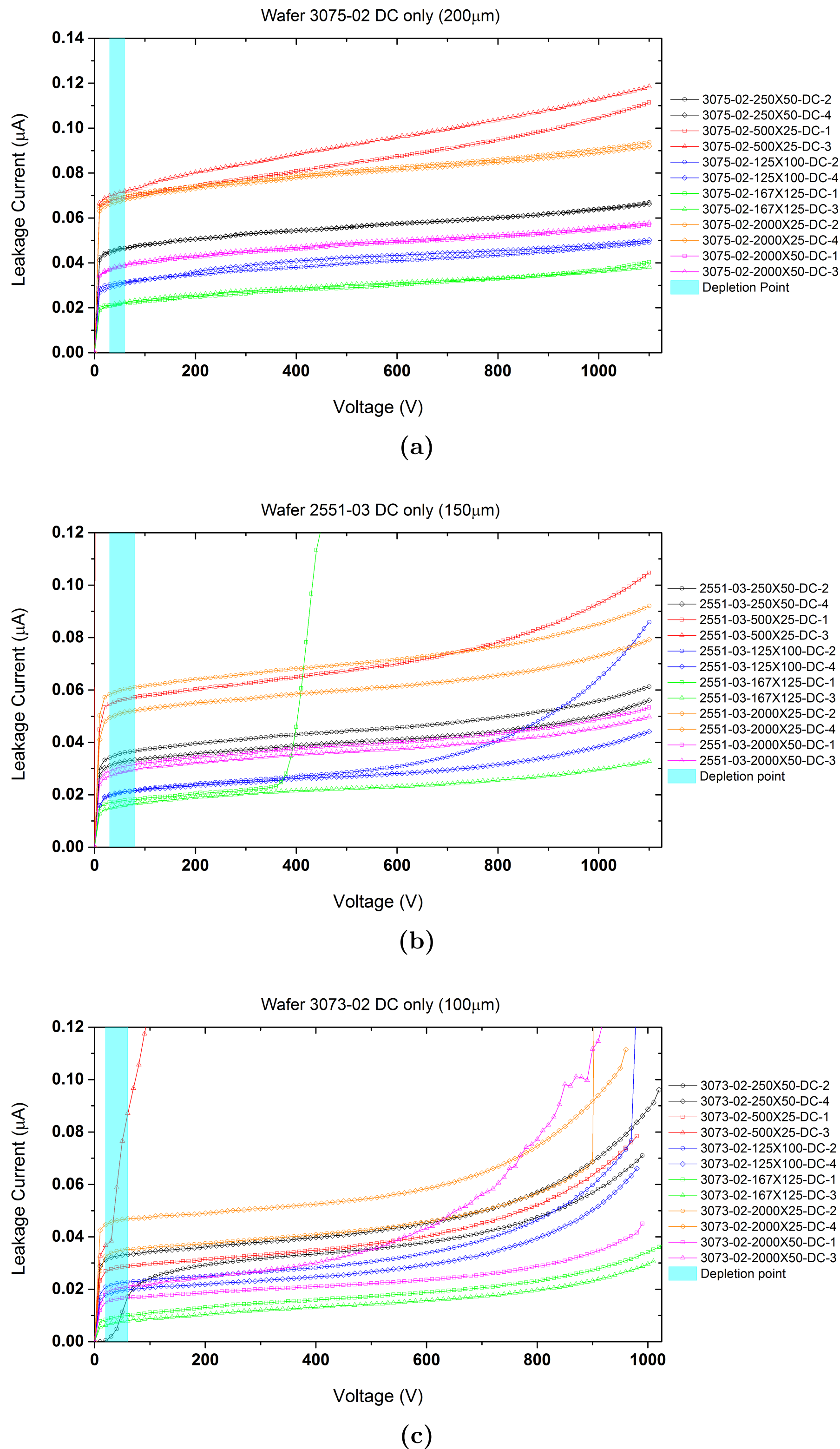

Figure 12.6: Current voltage (IV) measurements of all DC design variations on CERN PIXEL V wafer; (a) 200 μm thick and 5 $k\Omega$ bulk resistivity, (b) 150 μm thick and 10 $k\Omega$ bulk resistivity and (c) 100 μm thick and 10 $k\Omega$ bulk resistivity. The full depletion voltages for devices is $\sim$ 80 V, $\sim$ 40 V and $\sim$ 25 V on average respectively.

12.5 Single Module Characterisation

Only full thickness modules have been assembled: this refers to both the thickness of the readout chip (750 μm) and the sensor (300 μm). The readout chip thickness is foreseen to be to be thinned to 150 μm. However, because bump bonding is a high temperature process and the ASIC is a multi-metal layer built, thinner devices tend to “peel” away from each other as they cool (after bumping), especially at the edges of modules. All modules discussed in this section use the FE-I4B chip.

The modules discussed in the following sections have a different naming convention. All CERN PIXEL V modules have the following naming convention: ADVxxxx-yy-zz, where ADV refers to the company who assembled the modules (Advacam [205]), xxxx is replaced with the pixel cell size, yy is the powering option AC or DC and zz is a unique identification number for that pixel cell design.

12.5.1 Pre-Irradiation

Module IV

The IV characteristics of modules with different pixel geometries have been measured. Issues associated with wire bonding have meant that only 500x25 μm^2, 125x100 μm^2 and 2000x25 μm^2 module variants will be discussed, all devices discussed are DC powered because of the extra time needed to complete the AC processing. Figure 12.7 shows the results from modules where the readout chip is turned off and on. As with QUAD modules an increase in leakage current is observed, although the effect is reduced.

The wafer IV for the wafers used to produced these modules are not shown. They were among the first CERN PIXEL V wafers produced where the typical breakdown point was around 500 V. The modules show comparable IV characteristics compared to their on wafer results. This is good because the wafers have gone through significant handling and processing (sensor dicing, under bump metallisation, bump bonding) during assembly and shipping, which can damage and therefore affect their performance. These modules unfortunately had the added complication of damage to the sensors when being removed from the UV tape after sensor dicing. Despite this all modules apart from ADV125-DC-1 ($\sim$ 350 V, which was the most severely damaged) bias to around 500 V before breaking down.

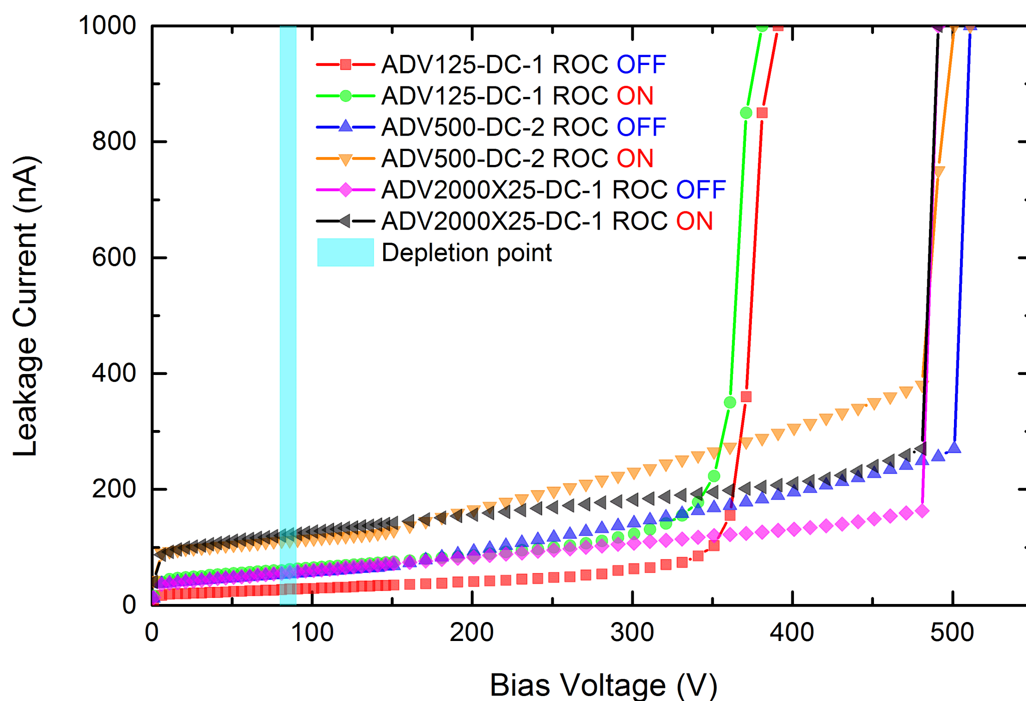

Figure 12.7: Measured current-voltage characteristics of single FE-I4B modules, 500x25 μm^2, 125x100 μm^2 and 2000x25 μm^2.

Module Tuning

During wafer testing the different pixel cell designs were found to have different total sensor capacitances. The longer the largest pixel dimension was the lower the total sensor capacitance was. Only small differences in capacitance were seen for the 125x100 μm^2, 500x25 μm^2 pixel cell variations compared with the standard 250x50 μm^2 design. The strixel devices have significantly lower total sensor capacitances despite individual strixel having a very large capacitance. As a result the response of an attached FE-I4 chip could be affected. No meaningful variation in pixel response or noise was seen in the non-strixel modules (assembled), but a significant increase in noise is seen in channels connected to strixels, which was expected.

Figure 12.8 shows the analogue pixel response measured using the USBpix system for the strixel module, ADV2000X25-DC-2. The analogue response is measured by injected and reading back a constant number of injected charges. If each pixels analogue circuitry is working correctly, then the same number of injected charges will be read back. However, the large capacitance of the strixel devices will effect performance. The analogue response of pixels connected to strixels on the sensor can clearly be seen in Figure 12.8a. However,

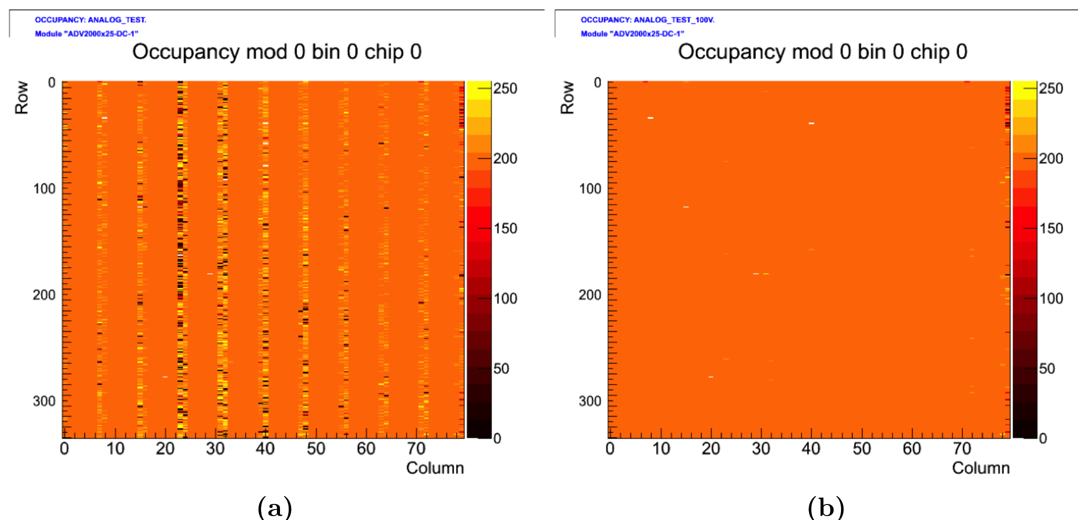

Figure 12.8: Measured analogue pixel response (USBpix) for a strixel module ADV2000X25-DC-2 (a) with no external high voltage and (b) with 100 V external bias, in both cases 200 charges were injected into each pixel.

the response returns to normal (what is expected) with application of external bias equal to or greater than the sensors depletion voltage, Figure 12.8b. As a result, the FE-I4 chip is able to handle sensor implants with large capacitances without being adversely affected as long as the sensor is full depleted or sufficiently biased.

Each module was tuned at a threshold of 3200 e down in 100 e steps until the tuning failed to reach its target value. All modules could be tuned down to a threshold of 800 e apart from ADV500-DC-2 which would only tune down to a 1200 e threshold. This is shown in Figure 12.9. The lower capacitance of the 500x25 μm^2 module with respect to the 125x100 μm^2 module leads to slightly lower average noise values at high thresholds. As the tuned threshold is lowered, the average noise across the modules increases. The noise of the strixel module is displayed for channels that are connected to strixels on the sensor and channels which are disconnected from the sensor. As expected the channels that are connected to the strixels have significantly increased noise. A 80 - 100 e increase in average noise is seen for the non strixel devices compared to disconnected channels, whereas an increase of $\sim$ 200 e is seen for channels connected to strixel sensor implants.

The characterisation results when using alternative geometry sensor pixels combined with a single readout chip are very encouraging. There were no technical difficulties encountered when assembling these modules. The change in pixel cell size and therefore capacitance per pixel/sensor has not affected FE-I4's operation, with only a modest (100 e) increase in noise seen when connected to a strixel device.

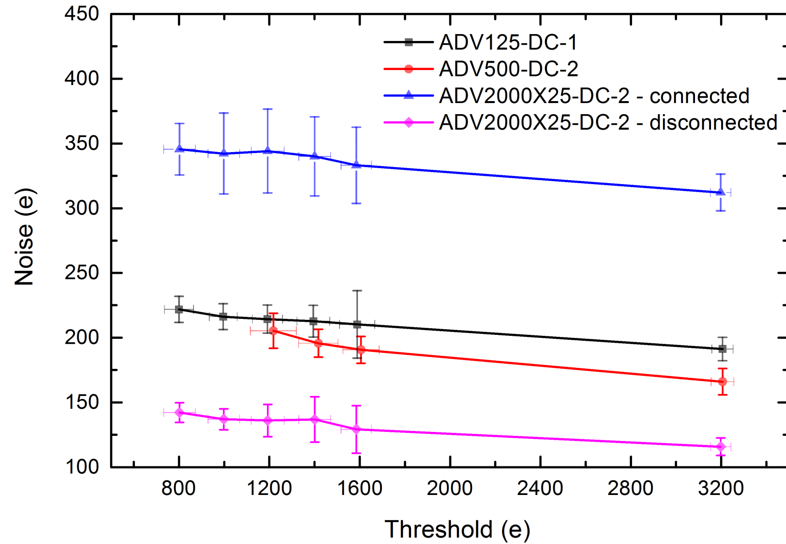

Figure 12.9: Tuned threshold vs noise (electrons) comparison for modules, ADV125-DC-1, ADV500-DC-2 and ADV2000X25-DC-2.

12.5.2 Post-Irradiation

Module IV

Only two irradiated modules were still usable at the time of IV characterisation, ADV125-DC-3 and ADV167-DC-3. The other designs either behaved erratically or failed during the first characterisation to determine if the readout chip behaved normally and to what extent it has been affected by assembly. Figure 12.10 shows the IV characteristics of full thickness devices, ADV125-DC-3 and ADV167-DC-3 after being irradiated to $1 \cdot 10^{15}\ \mathrm{n_{eq}/cm^2}$ at the Birmingham irradiation facility. As with pre-irradiation characterisation, each module's leakage current is measured while the readout chip is turned off and on. In both cases a larger increase in leakage current than expected is observed.

Module Tuning

Modules irradiated to $1 \cdot 10^{15}\ \mathrm{n_{eq}/cm^2}$ were characterised in the lab before being sent to test beam. Figure 12.11 shows the noise as a function of threshold at a single bias voltage for all irradiated devices. All irradiated modules behave similarly to each other apart from ADV250-DC-3 which has a high noise due to significantly higher leakage currents.

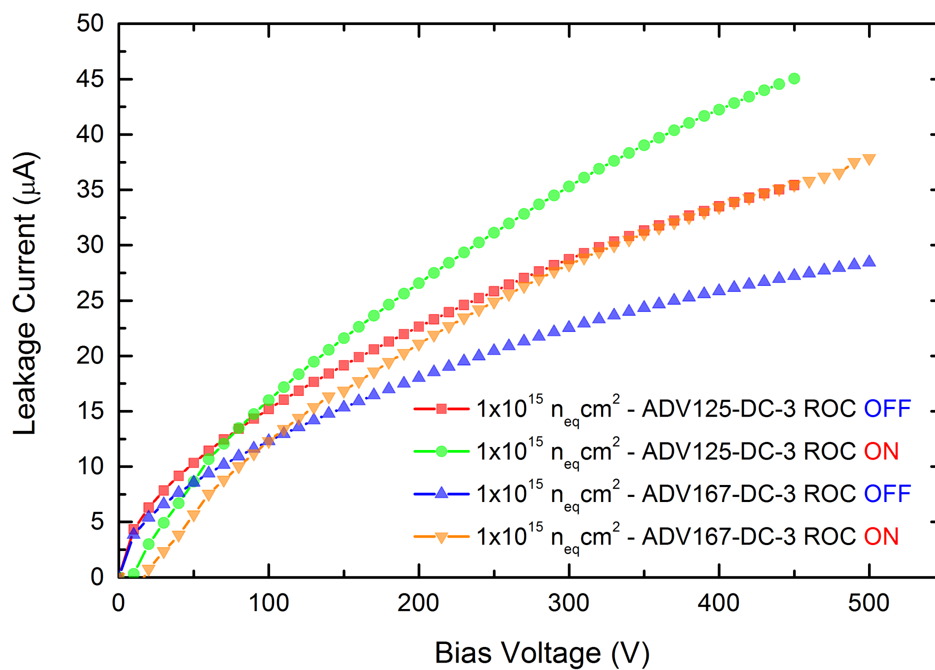

Figure 12.10: Measured current voltage (IV) characteristics of single FE-I4B modules, 125x100 and 167x125 μm^2 irradiated to $1 \cdot 10^{15}$ n_{eq}/cm^2 .

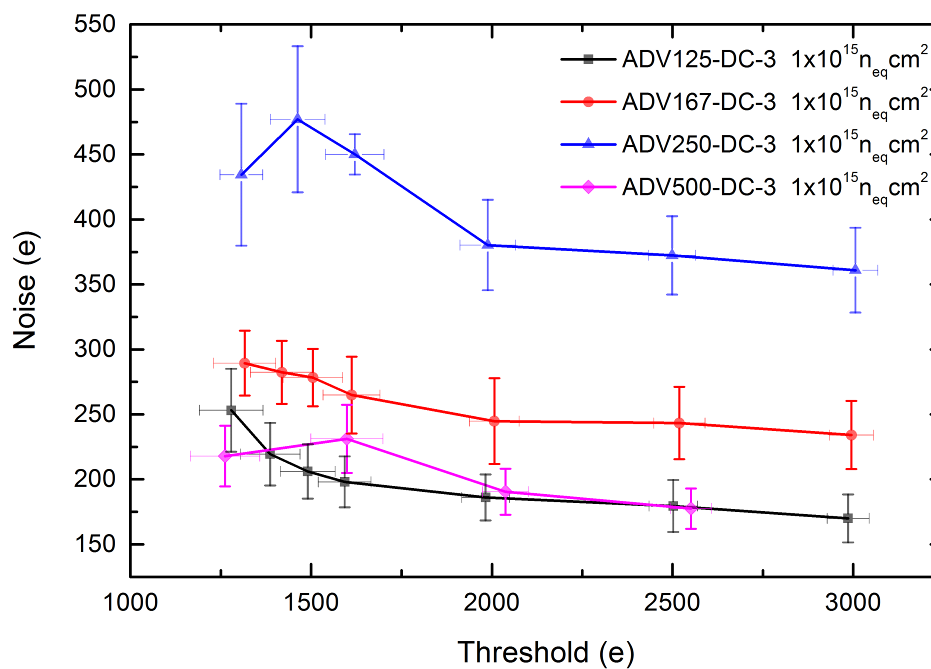

Figure 12.11: Threshold vs noise of four modules (ADV125-DC-3, ADV167-DC-3, ADV250-DC-3 AND ADV500-DC-3) irradiated to $1 \cdot 10^{15}$ n_{eq}/cm^2

All the modules, apart from ADV167-DC-3, use all readout channels. Results for ADV167-DC-3 shows double threshold and noise peaks which are expected. This is shown in Figure 12.12a and Figure 12.12b respectively. Since only channels which are connected to sensor pixels are of interest only results from these channels will be used.

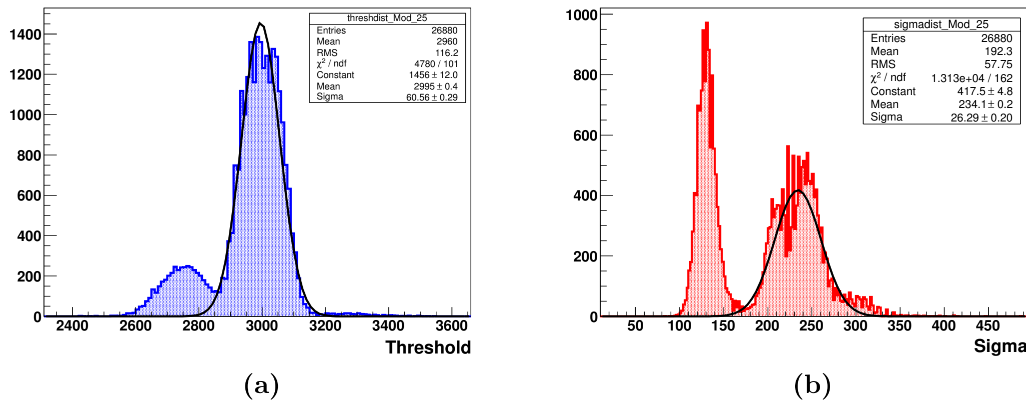

(a) (b)

Figure 12.12: (a) threshold (e) and (b) noise (e) distributions for ADV167-DC-3. In both cases two peaks are seen, this is due to some readout channels not being connected to sensor implants.

12.6 Test Beam Results

12.6.1 125x100 μm^2 ($1 \cdot 10^{15}$ n_{eq}/cm^2)

This section contains test beam results from an irradiated 125x100 μm^2 full thickness FE-I4B module (ADV125-DC-3) tested at DESY with 4 GeV positrons. A second 125x100 μm^2 module of the same construction (ADV125-DC-1) was used as a reference sensor. Both modules were mounted perpendicular to the beam ($\eta = 0$), the reference module was biased at 100 V (fully depleted) for all tests and tuned to a trigger threshold of 2500 e and 8 ToT = 20 ke. The irradiated module used a similar configuration, except the tuned charge was altered due to its irradiation dose and sensor thickness (8 ToT = 10 ke). Bias scans were performed up to 500 V in 100 V steps starting from 100 V. However, full data reconstruction wasn't possible when the irradiated module was biased at 100 V.

Module Efficiency:

The efficiency of both DUTs was measured by taking tracks that have hits in all telescope planes and comparing the DUT hit position (if there was one) to the hit position extrapolated via the telescope track. Quoted efficiencies do not take into account masked out noisy pixels and areas of the device which are outside the trigger scintillator region. Figure 12.13a and Figure 12.13b show 2D module efficiency maps of the un-irradiated module (ADV125-DC-1) at 100 V and the irradiated module (ADV125-DC-3) at 500 V respectively.

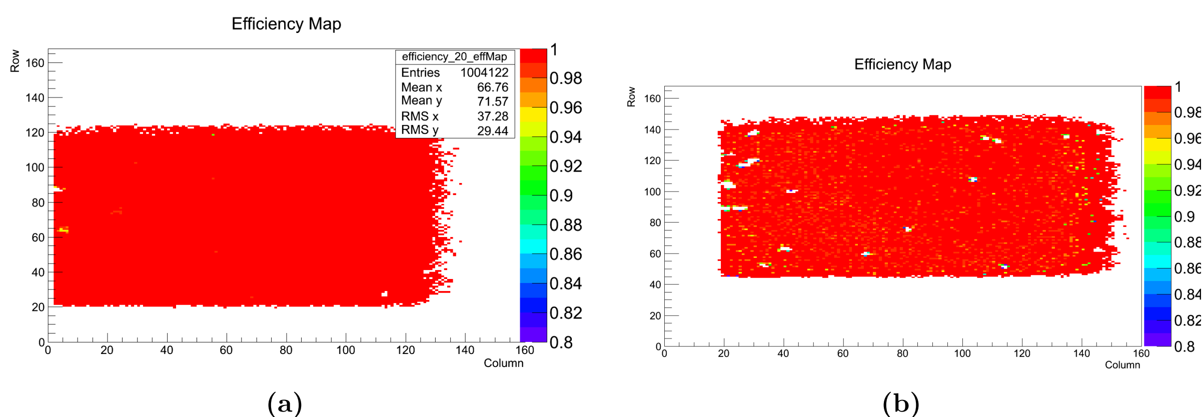

(a) (b)

Figure 12.13: Efficiency maps for (a) un-irradiated 125x100 μm^2 module biased at 100 V (fully depleted) and (b) irradiated ($1 \cdot 10^{15}$ n$_{eq}$/cm^2) 125x100 μm^2 module biased to 500 V with a 2500 e threshold.

A summary of module efficiencies with their associated errors for both modules is given in Table 12.2.

ADV125-DC-1 ($0 \cdot 10^{15}$ n$_{eq}$/cm^2)		ADV125-DC-3 ($1 \cdot 10^{15}$ n$_{eq}$/cm^2)	
Voltage (V)	Efficiency (%)	Voltage (V)	Efficiency (%)
100	99.98 ± 0.03	200	98.67 ± 0.03
100	99.97 ± 0.03	300	99.01 ± 0.03
100	99.98 ± 0.03	400	99.38 ± 0.03
100	99.95 ± 0.03	500	99.39 ± 0.03

Table 12.2: Summary of total module efficiency, excluding masked or out of scintillator area pixels for both square devices, ADV125-DC-1 and ADV125-DC-3 at 2500 e.

Inner Pixel Efficiency:

Inner pixel efficiency results rely on the DUTs being aligned properly and their residual distributions centred around zero. The efficiency of a pixel is plotted using extrapolated hit positions. All hits are plotted across the smallest repeatable regular structure which includes four pixels, this is shown for a 125x100 μm^2 module in Figure 12.14. All hits are then folded into a single pixel which is represented by the green box in Figure 12.14. The implant, which is smaller than the pixel pitch is entered with the small isolation distance between pixels sounding the implant. As a result the folding procedure the punch through bias structure is replicated, as a result it is displayed in two corners instead of one. Any inefficiency due to the punch through bias structures will be displayed in the right side corners of inner pixel efficiency plots, while any drop in efficiency in the left side corners are due to charge sharing between the corners of pixel implants.

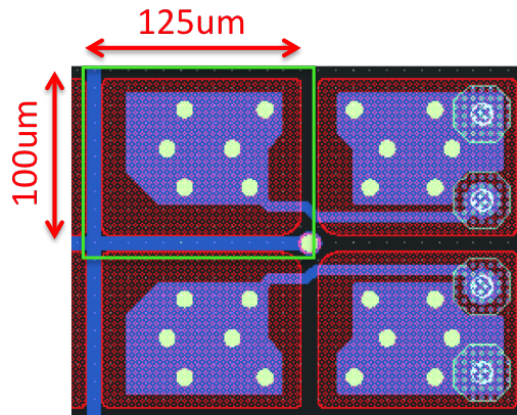

Figure 12.14: CAD drawing of a four pixel repeatable structure from the 125x100 μm^2 design indicating implant dimensions.

Inner pixel efficiency plots for the irradiated module ADV125-DC-3 at different bias voltages are shown in Figure 12.15 with their respective X and Y projections. Plots for the reference sensor are not shown because as expected no inefficient regions are present prior to irradiation because of the small size of the biasing structures and the absence of charge trapping. The size of the inefficient regions decreases as the sensor bias voltage is increased. Inefficient regions due to charge sharing between neighbouring pixels quickly disappear with increasing voltage, while the inefficient region due to the punch through biasing structures significantly decreases in size. A summary of inner pixel efficiencies is given in Table 12.3. The resolution of the telescope is 4 μm, the tracks alignment is good resulting in track

ADV125-DC-1 $0 \cdot 10^{15}\,\mathrm{n_{eq}/cm^2}$)		ADV125-DC-3,$1 \cdot 10^{15}\,\mathrm{n_{eq}/cm^2}$)	
Voltage (V)	Efficiency (%)	Voltage (V)	Efficiency (%)
100	99.92 ± 0.03	200	99.98 ± 0.03
100	99.98 ± 0.03	300	99.98 ± 0.03
100	99.97 ± 0.03	400	99.98 ± 0.03
100	99.95 ± 0.03	500	99.98 ± 0.03

Table 12.3: Summary of inner pixel efficiencies, excluding masked or out of scintillator area pixels for both square devices, ADV125-DC-1 and ADV125-DC-3.

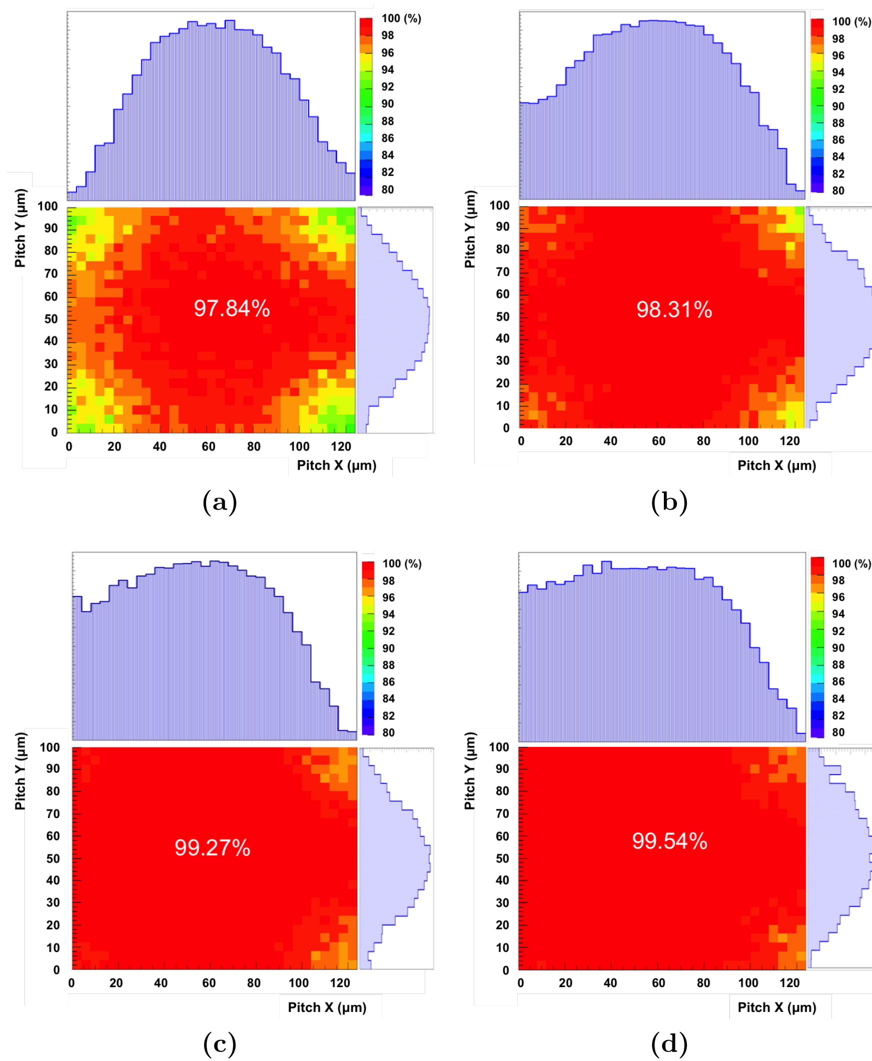

Figure 12.15: Inner pixel efficiencies for ADV125-DC-3 irradiated to $1 \cdot 10^{15}\,\mathrm{n_{eq}/cm^2}$ at (b) 200 V, (c) 300 V, (d) 400 V and (e) 500 V.

Charge Sharing:

The charge sharing between pixels is an important aspect of sensor performance, helping to achieve better spatial resolution compared with binary hit information. It also helps to highlight flaws in the pixel design and the effect punch through biasing structures have on the detector performance before and after irradiation. The fraction of charge shared surrounding a single pixel, with particular focus around the punch through bias structure is shown in Figure 12.16. Here the charge sharing fraction is defined as the number of tracks that share charge (cluster sizes larger than 1) divided by the total number of tracks. For comparison the un-irradiated module biased at 100 V is shown in Figure 12.16a. The remainder of the sub-figures are results from the irradiated module (ADV125-DC-3) biased at 200 V to 500 V respectively.

As expected the highest fraction of charge sharing is found in the centre of the pixels and reduces extending to the outer edge of the implant. The fraction of charge is lowest in-between pixels and especially in regions surrounding the punch through bias structures. This is because tracks that are close to the edge of a pixel can often be under threshold in irradiated devices. Additionally the punch through bias structures steal charge from neighbouring pixels and since they are not connected to a read out channel the charge is lost. The fraction of charge shared increases with increased external sensor bias voltage after irradiation. While substantial charge is shared around the punch through structure the fraction of charge lost does not increase substantially with respect to increased bias voltages.

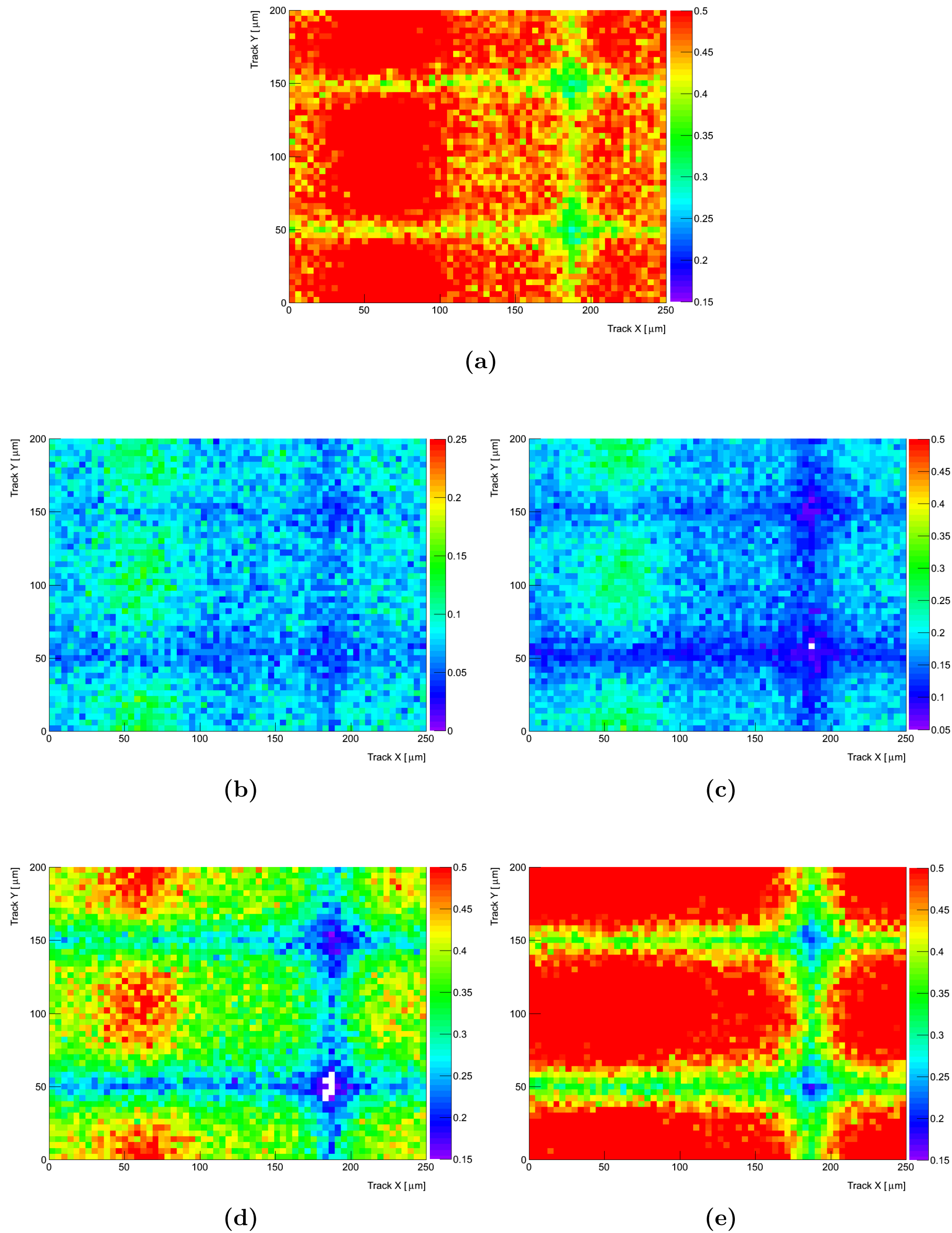

Figure 12.16: Fraction of charge sharing for a single pixel in 2D (a) ADV125-DC-1 (un-irradiated) with 100 V external bias Voltage. (b) ADV125-DC-3 ($1 \cdot 10^{15}\,\mathrm{n_{eq}/cm^2}$) at 200 V, (c) 300 V, (d) 400 V and (e) 500 V. The contour plot range is has been chosen in such a way that the pixel structure can be distinguished easily for all plots.

12.6.2 250x50 μm^2 ($1 \cdot 10^{15}\,n_{eq}/cm^2$)

This section features results from the same analysis steps detailed in Section 12.6.1 except that the DUTs used are ADV250-DC-1 (250x50 μm^2) as the reference sensor and ADV250-DC-3 (250x50 μm^2) which has also been irradiated to $1 \cdot 10^{15}\,n_{eq}/cm^2$. The DUT's were tested under the same conditions as the 125x100 μm^2 square modules.

Module Efficiency:

Module efficiency results are summarised in Table 12.4. At 100 V the irradiated module shows relatively low efficiency compared to the other bias settings. Much of this efficiency is recovered when the bias voltage is increased.

ADV250-DC-1 ($0 \cdot 10^{15}\,n_{eq}/cm^2$)		ADV250-DC-3 ($1 \cdot 10^{15}\,n_{eq}/cm^2$)	
Voltage (V)	Efficiency (%)	Voltage (V)	Efficiency (%)
100	99.81 ± 0.03	100	93.76 ± 0.03
100	99.75 ± 0.03	200	98.51 ± 0.03
100	99.74 ± 0.03	300	99.01 ± 0.03
100	99.75 ± 0.03	400	99.20 ± 0.03
100	99.72 ± 0.03	500	99.32 ± 0.03

Table 12.4: Summary of total module efficiency, excluding masked or out of scintillator area pixels for both devices, ADV250-DC-1 and ADV250-DC-3.

Inner Pixel Efficiency:

The 2D efficiency plots for the irradiated module (ADV250-DC-3) are shown in Figure 12.17. The 100 V bias plot has been left out because of the severe drop in efficiency which is caused by a combination of a relatively high threshold (2500 e) and substantial charge trapping. However, its efficiency is listed in Table 12.5 with the bias settings. As with the square module high pixel efficiencies are seen throughout for bias voltages above 200 V.

The reconstruction for this device resulted in residual distributions (Y direction, 50 μm pitch) that were twice as big as expected, assuming a resolution scaling with the pitch over $\sqrt{12}$. Even after restricting the residual cuts to not allow anything outside

of the pixel cell size (250x50 μm^2). The only way this can be the case is if two readout channels have been merged. In other words two of the closely spaced metal contacts (bump bonds) that connect readout and sensor pixels have merge together each channel would readout the same signal, reducing the granularity along the merged direction. This is not seen along the X direction, 250 μm pixel pitch direction giving further reason to suspect merged bump bonds as they are more closely spaced along the Y direction. This has not been observed in any previous modules so we can conclude that the bump bonding process is not the cause, i.e. consistent misalignment throughout the device since all the modules discussed were produced ("bumped") at the same time. The most likely cause is localised heat during irradiation or electrical discharges during operation, all devices were not passivated to prevent electrical discharges.

However, because the DUT was not tilted with respect to η larger clusters sizes and therefore smeared residuals should not effect the total module efficiency or the total inner pixel efficiency. Instead, only the region between bias structures would be affected. Since this has implications for charge sharing and cluster sizes no further analyses have been performed using this data.

ADV250-DC-1 $0 \cdot 10^{15}$ n_{eq}/cm^2)		ADV250-DC-3,$1 \cdot 10^{15}$ n_{eq}/cm^2)	
Voltage (V)	Efficiency (%)	Voltage (V)	Efficiency (%)
100	99.95 ± 0.03	100	94.10 ± 0.03
100	99.93 ± 0.03	200	99.17 ± 0.03
100	99.95 ± 0.03	300	99.68 ± 0.03
100	99.94 ± 0.03	400	99.71 ± 0.03
100	99.95 ± 0.03	500	99.81 ± 0.03

Table 12.5: Summary of inner pixel efficiencies, excluding masked or out of scintillator area pixels for both devices, ADV250-DC-1 and ADV250-DC-3.

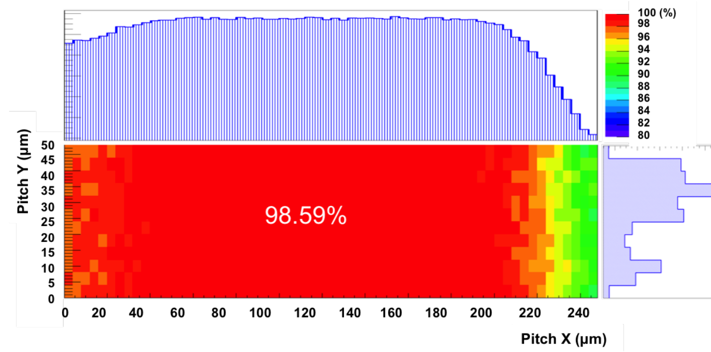

(a)

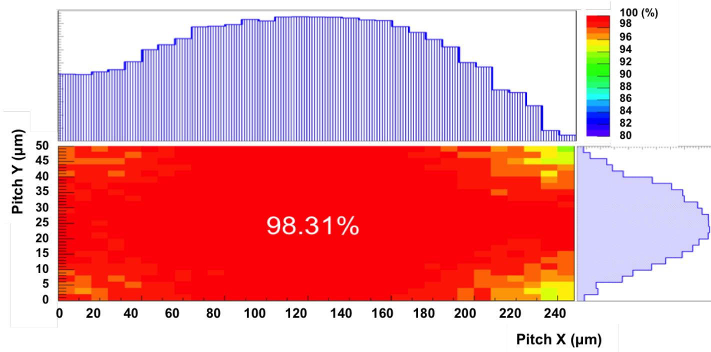

(b)

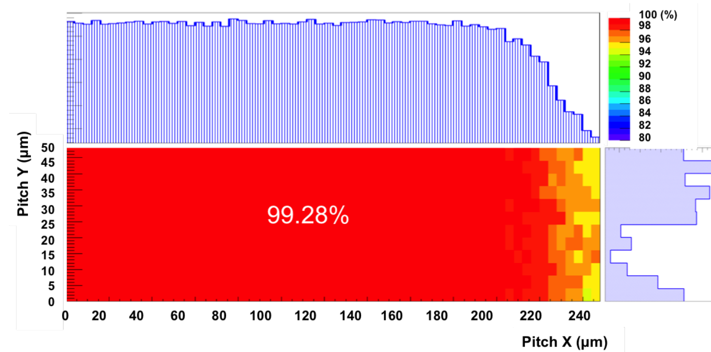

(c)

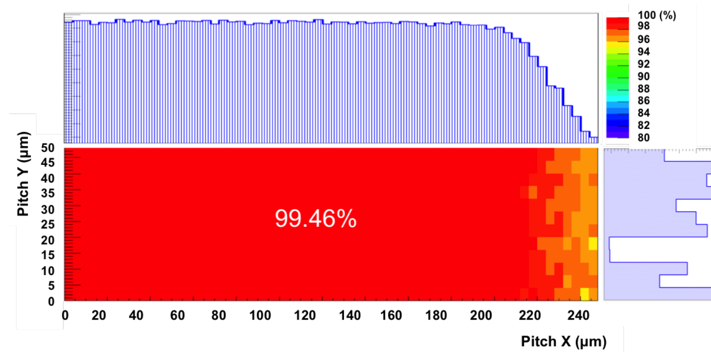

(d)

Figure 12.17: Inner pixel efficiencies for ADV250-DC-3 irradiated to $1 \cdot 10^{15}\,n_{eq}/cm^2$ at (a) 200 V, (b) 300 V, (c) 400 V and (d) 500 V.

12.6.3 500x25 μm^2- un-irradiated

The results presented in this section are for two full thickness FE-I4B 500x25 μm^2 modules. Where the first DUT has its bias voltage, angle of tilt along the telescope xz axis and tuned trigger threshold varied, while the reference is kept constant. The reference sensor named here glas500, is mounted perpendicular to the beam and biased to 100 V with a 3000 e trigger threshold (8 ToT = 20 ke). The first DUT (ADV500-DC-2) has been tested at 40 and 100 V at 3000, 2500, 2000 and 1500 e thresholds and tilted at 15 ° and 30 °. Since both DUTs are un-irradiated inner pixel efficiencies will not be shown because no significant inefficient area is expected and or seen.

Module Efficiency

The change in module efficiency as a function of trigger threshold for both DUTs as their bias voltages and mounting inclinations are changed, is shown in Figure 12.18. Reducing the bias voltage below full depletion affects its efficiency but the effect is small since the devices deplete from the readout implant side (*n-in-p*). As the module is tilted its efficiency increases because more charge is deposited. This effect also reduces the inefficient area around the punch through biasing structures.

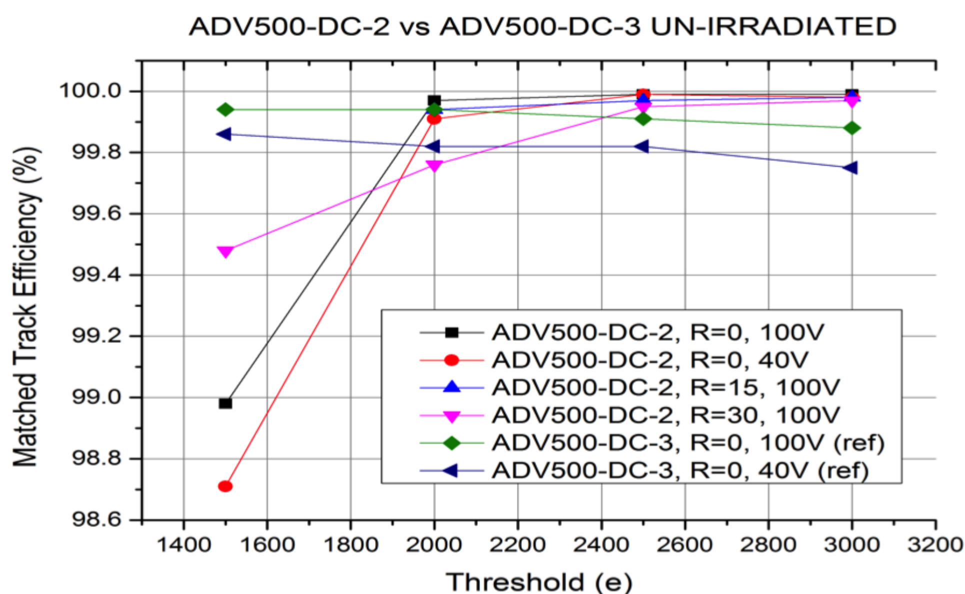

Figure 12.18: Module efficiency for ADV500-DC-2 vs the reference sensor glas500 as a function of module tilt and bias voltage.

Cluster Distributions

The cluster sizes of a 500x25 μm^2 module are important in order to determine their resolution as a function of η along barrel staves. A small loss in resolution is expected along the z-axis (x-axis of the module), because of the increase in the implant size. The amount of charge sharing along the whole module x-axis will also be reduced but this is expected to be mitigated by the increased track inclination. An increase in resolution along the r/ϕ direction (ATLAS) is expected because the pixel dimension along the module y-axis is decreased, which increases its intrinsic binary resolution but also increases the charge sharing.

Figure 12.19a and Figure 12.19b show the cluster distributions along the x- and y-axis respectively as a 500x25 μm^2 module is tilted which represents track inclinations at increasing η. In both cases the mean cluster size increases with increasing tilt. However, because this data was taken at DESY ($4\,GeV$) multiple scattering is an issue as tilting a module increases the amount of material the beam must traverse. This affects the total number of good tracks after reconstruction. At 0 ° there are 1.4 M tracks. This decreases to 800 k and 600 k as the modules tilt is increased to 15 ° and 30 ° respectively. Above 30 ° track reconstruction was not possible due to multiple scattering. Therefore future tests will be required at CERN, where a higher momentum particle beam can be used.

The mean cluster size in each direction (X and Y) is summarised in Table 12.6.

R (°)	Cluster Mean X	Cluster Mean Y
0	1.538	2.086
15	1.615	2.129
30	1.743	2.159

Table 12.6: Summary of mean cluster size along x and y directions.

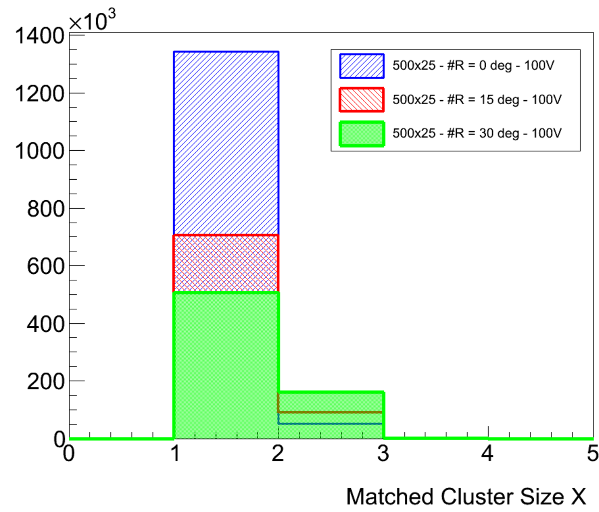

(a)

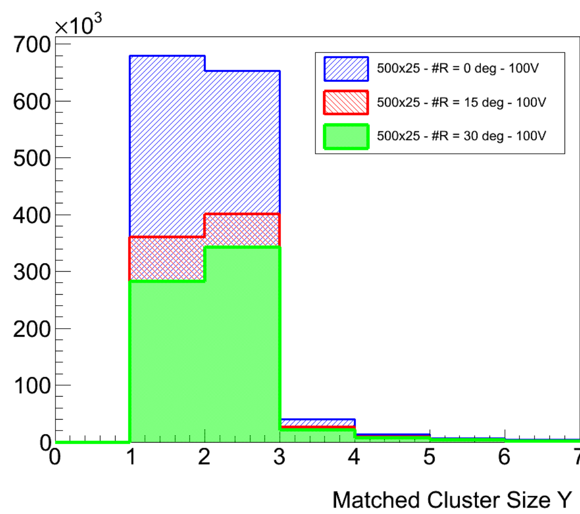

(b)

Figure 12.19: Cluster distributions for a 500x25 μm^2 module as a function of tilt in (a) x direction (500 μm) and (b) y direction (25 μm).

Chapter 13

Conclusion

The work presented within this thesis has shown that silicon detectors intended for the ATLAS tracker at the future HL-LHC can be produced with the required radiation tolerance to $2 \cdot 10^{16}\,\mathrm{n_{eq}/cm^2}$. Furthermore, detector solutions that use the more cost effective *n-in-p* geometry compared to the conventional radiation hard *n-in-n* geometry have been demonstrated.

Work undertaken within the CERN-RD50 framework has shown that thin sensors outperform their thicker counter parts after high fluences. Further evidence for charge multiplication using pseudo ATLAS IBL pixels designed to be read out via an analogue micro-strip readout system (ALiBaVa) has been shown. The ability to create and control the charge multiplication after irradiation has been demonstrated using planar junction engineering, varying implant pitch and width and with trenched junction engineering (trenches) etched in planar readout implants.

The feasibility of large area pixel modules (Quads) for the ATLAS Phase-II have been shown. Extensive stress testing has resulted in flaws in the sensor design being fixed, improving the device's leakage current. Traditional and slim edge modules irradiated to the maximum expected dose at the relevant radius ($5 \cdot 10^{15}\,\mathrm{n_{eq}/cm^2}$) have been shown to function up to 1000 V with minimal noise effects. The test modules were found to be highly susceptible to external signal pickup and self heating which affected there ability to function normally, significant numbers of dead pixels were also observed. Further development is needed to develop Quad modules that are suitable for operation at HL-LHC. The next step of the R&D should to be to produce modules that feature the FE-I4B readout chips and make use of their built in low voltage LDO circuitry in an effort to reduce external noise pickup.

Modules produced with pixel implant dimensions that are drastically different from those of the FE-I4 readout chip have been shown to have excellent current voltage characteristics (biasing $\gg$ 1000 V un-irradiated). Where each devices maximum pre-breakdown bias exceeds their depletion voltage by a factor of ten times. The use of top metal routing to enable bump bonding of sensors with differing geometries to FE-I4 chips has not encountered any production, module assembly or testing issues. Irradiated alternative geometry modules have been shown to work as well as standard IBL (250x50 μm^2) pixel geometries and offer the possibility to optimise inner tracker parameters such as, granularity and track occupancy at the HL-LHC.

Looking to the future, work still has to be undertaken as part of the CERN-RD50 and ATLAS upgrade collaborations, to continue qualifying and developing more radiation hard silicon sensors. The exploitation of the charge multiplication effect still needs to be investigated via detailed simulations and sensor productions. Additionally, cheaper more cost effect sensor solutions should also be investigated. Further R&D in the production of pixel modules intended for use within ATLAS still needs to be done. This will involve detailed physics simulations to help refine the ITk design and extensive sensor developments/productions using many different vendors. Much of there work presented in this thesis will also have to be repeated with the FE-I4B readout chip and the new FE-I5 readout chip when it is available.

Bibliography

[1] An introduction to the Standard Model of particle physics, W. N. Cottingham, D. A. Greenwood ISBN-0-521-58191-5, 1998.

[2] Particle-symmetries of weak interactions, S. L. Glashow, Nucl. Phys. 22 no. 4, (1961) 579.

[3] A model of leptons, S. Weinberg, Phys. Rev. Lett. 19 (1967) 1264.

[4] Weak and electromagnetic interactions, A. Salam, Elementary particle theory: relativistic groups and analyticity, N. Svartholm, ed.,p. 367. Almqvist and Wiksell, 1968, proceeding of the eigth Nobel symposium.

[5] Regularization and renormalization of gauge fields, G. 't. Hooft and M. Veltman, Nucl. Phys. B44 (1972) 189.

[6] Lecture notes for the 2011 RAL school for experimental high energy physics students, M. Thomson, Technical Report, RAL-TR-2011-014, August 2011.

[7] Broken symmetries, massless particles and gauge fields, P. W. Higgs, Phys. Lett. 12 (1964) 132.

[8] Broken symmetries and the masses of gauge bosons, P. W. Higgs, Phys. Rev. Lett. 13 (1964) 508.

[9] Spontaneous symmetry breakdown without massless bosons, P. W. Higgs, Phys. Rev. 145 (1966) 1156.

[10] Observation of a new particle in the search for the Standard Model Higgs boson with the ATLAS detector at the LHC, The ATLAS Collaboration, CERN-PH-EP-2012-218, Phys.Lett. B716 (2012) 1-29. `http://arxiv.org/abs/1207.7214`

[11] LHC machine, L. Evans and P. Bryant, ATLAS Collaboration, JINST 3 no. 08, (2008) S08001.

[12] Perspectives on LHC physics, The ATLAS Collaboration, arXiv:1004.5293v2, (2008).

[13] The ATLAS experiment at the CERN large hadron collider, ATLAS Collaboration, JINST 3 no. 08, (2008) S08003.

[14] ATLAS website, accessed febuary 2013, `http://atlas.ch/`

[15] ATLAS detector and physics performance, Atlas Collaboration, ATLAS TDR 14, CERN/LHCC 99-14, May 1999. `http://cds.cern.ch/record/391176?ln=en`

[16] Post-installation status of the ATLAS pixel detector, M. Garcia-Scivere, 2009 JINST 4 P03021 `doi:10.1088/1748-0221/4/03/P03021`.

[17] HL-LHC status and detector upgrades, P. Allport, Royal Society Chicheley Higgs meeting, Chicheley Hall, 22-23th january 2014.

[18] Letter of intent for the phase-II upgrade of the ATLAS experiment, ATLAS Collaboration, CERN, (2013), ATL-COM-UPGRADE-2012-04.

[19] Radiation hard semiconductor Devices for very high luminousity colliders, RD50, `http://rd50.web.cern.ch/rd50/`

[20] Micron semiconductor ltd, UK `http://www.micronsemiconductor.co.uk/index.asp`

[21] LHC design report, O. S. Bruning *et al.*, CERN, Geneva, (2004).

[22] There is no explosion risk associated with superfluid helium in the LHC cooling system, M. Fairbairn, B. McElrath, arXiv:0809.4004 [physics.pop-ph], 2008.

[23] The injector chain for the LHC, K. Schindl, CERN, (1999), CERN-PS-99-018-DI.

[24] Image taken from `http://maalpu.org/lhc/LHC.main.htm`, accessed 07/03/14.

[25] Expected pile-up values at the HL-LHC, The ATLAS and CMS collaborations, ATL-UPGRADE-PUB-2013-014, September 2013.

[26] plots taken from `https://twiki.cern.ch/twiki/bin/view/AtlasPublic/LuminosityPublicResults#Annual_plots`

[27] First measurments of the total proton-proton cross section at the LHC energy of $\sqrt{s} = 7$ TeV, TOTEM Collaboration, Europhys. Lett. 96 (2011) 21002.

[28] Characterisation and beam test data analysis of 3D silicon pixel detectors for the ATLAS upgrade, C. Nellist, PhD Thesis, University of Manchester, 2013.

[29] The HL-LHC project, L. Rossi, HL-LHC kick-off meeting Daresbury 11 November 2013 http://indico.cern.ch/event/257368/session/0/contribution/3

[30] Consolidation of the LHC superconducting magnets and circuits during LS1, J. Ph. Tock proceedings of the Chamonix 2012 workshop on LHC performance, CERN, Geneva https://espace.cern.ch/acc-tec-sector/Chamonix/Chamx2012/papers/JPT_5_03.pdf

[31] The large hadron collider, O. Brüning, H. Burkhardt and S. Myers, Prog. in Part. Nucl. Phys. 67 (2012) 705.

[32] Image illustrating the consolidation of the LHC during LS1 http://cds.cern.ch/record/1516031?ln=en# accessed 07/03/14.

[33] Linac4 technical design report, L. Arnaud CERNAB2006084 ABP/RF, December 2006, CERN, Geneva, Switzerland.

[34] LINAC4 and the upgrade of the LHC injector complex, R. Garoby, PIMS production meeting, 27 February 2013, CERN, Geneva, Switzerland.

[35] Investigation of properties of novel silicon pixel assemblies employing thin n-in-p sensors and 3D-integration, P. Weigell, PhD Thesis, Max-Plank-Institut fur Physik, Munich, January 2013.

[36] LHC upgrade options, L. Rossi, Grenoble, July 2011, HEP-EPS.

[37] ECFA high luminosity LHC experiments workshop: physics and technology challenges, Prepared from inputs provided by the ALICE, ATLAS, CMS and LHCb Collaborations, 21st November 2013.

[38] private communication with Prof. P. Allport, febuary 2013.

[39] Accelerator-experiment interface & LS constraints, summary and next steps, B, di Girolamo, ECFA workshop - Aix-les-Bains, 3 October 2013.

[40] Strongly interacting Higgs bosons, T, Appelquist and C. W. Bernard, Phys. Rev., D22:200, 1980.

[41] Resonances and unitarity in weak boson scattering at the LHC, A. Alboteanu, W. Kilian, and J. Reuter, arXiv:0806.4145, 2008.

[42] WHIZARD: simulating multi-particle processes at LHC and ILC, W. Kilian, T. Ohl, and J. Reuter, Eur.Phys.J., C71:1742, 2011.

[43] LHC beam-beam compensation using wires and electron lenses, U. Dorda *et al.*, 22nd Particle Accelerator Conference PAC07, Alburquerque, USA, 25-29 June 2007.

[44] Electron lens as beam-beam compensation wire compensator in HL-LHC, A. Valishei *et al.*, arXiv:1312.1660, 21 November 2013.

[45] The high luminosity LHC programme science case, challenges and R&D, N. Konstantinidis, HEP Seminar, RHUL, 20/11/2013.

[46] Higgs discovery press release 2013,`http://press.web.cern.ch/press-releases/2013/03/new-results-indicate-particle-discovered-cern-higgs-boson`

[47] Search for higgs boson in the $H \rightarrow ZZ$ and $ZH \rightarrow ll + invisible$ channels with the ATLAS detector, J. Price, PhD Thesis, University of Liverpool, UK, April 2013.

[48] Introduction to elementary particles, D. J. Griffiths, TextBook Physics. Wiley, New York, NY, 1987

[49] Image taken from, `http://www.controlyourcash.com/wp-content/uploads/2013/07/1000px-Standard_Model_of_Elementary_Particles.svg_.png`, accessed December 2013.

[50] The discovery of quarks, M Riordan, SLAC-PUB-5724, April 1992, `http://www.slac.stanford.edu/cgi-wrap/getdoc/slac-pub-5724.pdf`

[51] The LEP electroweak working group, `http://lepewwg.web.cern.ch/LEPEWWG/stanmod/`.

[52] The Standard Model Higgs boson, I. van Vulpen, Part of the Lecture Particle Physics II, UvA Particle Physics Master 2013-2014

[53] An introduction to Quantum field Theory, M. E. Peskin and D. V. Schroeder, ISBN-0201503972, 1995.

[54] Quantum field theory II, N. Beisert, ETH Zurich, FS13, lecture notes. `http://www.itp.phys.ethz.ch/research/qftstrings/archive/13FSQFT2/Chapter04.pdf`

[55] TASI 2004 lecture notes on Higgs boson physics, L, Reina, `http://arxiv.org/abs/hep-ph/0512377v1`

[56] Quarks & leptons: an introductory course in modern particle physics, F. Halzen, A. D . Martin, 1984, by John Wiley & Sons, Inc.

[57] Structure of the Standard Model, P. Langacker, arXiv:hep-ph/0304186, 19 Apr 2003.

[58] The hierarchy problem of the electroweak Standard Model revisited, F. Jegerlehner, arXiv:1305.6652 [hep-ph] 28 Sep 2013

[59] Advanced particle physics Volume 2: the standard model and beyond, O. Boyarkin, Advanced Particle Physics (2010).

[60] The temperature of the cosmic microwave background, D. J. Fixsen, The Astrophysical Journal **V**ol 707, page 906, (2009).

[61] Standard Model at the LHC (lecture 4: precision measurements), M. Schott, CERN, `http://mschott.web.cern.ch/mschott/ShareDocus/LectureVietnam/`.

[62] Search for the Standard Model Higgs boson in the H to $\tau^+\tau^-$ decay mode in $\sqrt{s}=$ 7 TeV pp collisions with ATLAS, The ATLAS Collaboration, JHEP, 1209:070, 2012.

[63] LHC Higgs cross section working group, S. Dittmaier, C. Passarino, and R. Tanaka (Eds), Handbook of LHC Higgs Cross Sections: 2. Differential Distributions. CERN-2012-002, arXiv:1201.3084 [hep-ph], 2012

[64] MadGraph/MadEvent v4: The web generation, J. Alwell *et al.*, JHEP, 09:028, 2007.

[65] Upper Bounds on Supersymmetric Particle Masses, R. Barbieri and G. Giudice, Nucl.Phys. B306 (1988) 63.

[66] Natural SUSY Endures, M. Papucci, J. T. Ruderman, and A. Weiler, JHEP 1209 (2012) 035, arXiv:1110.6926 [hep-ph].

[67] Sensitivity study for ECFA: heavy vector-like charge 2/3 quarks, CMS Collaboration, CMS-PAS-FTR-13-026 (2013).

[68] A search for flavour changing neutral currents in top-quark decays in pp collision data collected with the ATLAS detector at $\sqrt{s}=7TeV$, ATLAS Collaboration, G. Aad *et al.*, JHEP 09 (2012) 139, arXiv:1206.0257 [hep-ex].

[69] Search for flavour changing neutral currents in top-quark decays in pp collsions at 7 TeV, CMS Collaboration, S. Chatrchyan *et al.*, Phys. Lett. B718 (2013) 1252-1272, arXiv:1208.0957 [hep-ex].

[70] Search for flavour changing neutral currents in top quark decays in pp collsions at 8 TeV, CMS Collaboration, CMS-PAS-TOP-12-037, 2012.

[71] The ATLAS trigger system, The ATLAS Collaboration, C. Padilla *et al.*, IEEE Trans. Nucl. Sci. 57 (April 2010), 650-657.

[72] ATLAS technical design report, The ATLAS Collaboration, CERN/LHCC/94-43, December 1994

[73] Track and vertex reconstruction in the ATLAS inner detector, M. Limper, PhD thesis, Universiteit van Amsterdam, 2009.

[74] ATLAS DAQ, EF, LVL2 and DCS technical design progress report, ATLAS Collaboration, CERN/LHCC/98-16, June 1998.

[75] ATLAS trigger performance status report, ATLAS Collaboration, CERN/LHCC/98-15, June 1998.

[76] The ATLAS muon spectrometer: commissioning and tracking, J, Snuverink, PhD Thesis, Universiteit Twente, Enschede, Netherlands, Submitted October 2009.

[77] Technical design report for the phase-I upgrade of the ATLAS TDAQ system, The ATLAS Collaboration, CERN-LHCC-2013-018, ATLAS-TDR-023, 2013.

[78] ATLAS liquid argon calorimeter technical design report: trigger electronics for the LHC phase-I upgrade,ATLAS Liquid Argon Calorimeter Group, CERN-LHCC-2013-006, ATLAS-TDR-020, CERN, Geneva, `https://twiki.cern.ch/twiki/bin/view/LAr/LArPhaseITDR`

[79] New small wheel technical design report, The ATLAS Collaboration, CERN-LHCC-2013-006, ATLAS-TDR-20, CERN, Geneva, June 2013. `https://cds.cern.ch/record/1552953`

[80] Fast tracKer (FTK) technical design report, The ATLAS Collaboration, CERN-LHCC-2013-007, ATLAS-TDR-021, CERN, Geneva, June 2013, `https://cds.cern.ch/record/1552953`

[81] ATLAS insertable b-layer technical design report, The ATLAS Collaboration, CERN-LHCC-2010-013 ; ATLAS-TDR-19, `https://cds.cern.ch/record/1291633/` (2010).

[82] ATLAS muon spectrometer technical design report, The ATLAS Collaboration, CERN/LHCC/97-22, May 1997.

[83] Image of muon system, The ATLAS Collaboration, `http://www.atlas.ch/photos/muons-combined.html` accessed, 15/02/2014.

[84] Letter of intent for the phase-I upgrade of the ATLAS experiment, The ATLAS Collaboration, CERN, (2011), CERN-LHCC-2011-012.

[85] Image of calorimeter, The ATLAS Collaboration, `http://www.atlas.ch/photos/calorimeters-combined-barrel.html` accessed, 15/02/2014.

[86] ATLAS liquid argon calorimeter technical design report: trigger electronics for the LHC phase-I upgrade, The ATLAS Collaboration, ATL-COM-GEN-2013-007

[87] ATLAS liquid argon calorimeter technical design report, The ATLAS Collaboration, CERN/LHCC/96-41, December 1996.

[88] Image of inner detector, The ATLAS Collaboration, `http://www.atlas.ch/photos/inner-detector-combined.html` accessed, 15/02/2014.

[89] Inner detector technical design report, The ATLAS Collaboration, Volume 1, ATLAS TDR 4, CERN/LHCC 97-16, April 1997. `http://cds.cern.ch/record/331063/files/ATLAS-TDR-4-Volume-I.pdf`

[90] Inner detector technical design report, The ATLAS Collaboration, Volume 2, ATLAS TDR 4, CERN/LHCC 97-17, April 1997. `http://cds.cern.ch/record/331063/files/ATLAS-TDR-4-Volume-II.pdf`

[91] Operation of the atlas transition radiation tracker under very high irradiation at the cern LHC, ATLAS TRT Collaboration, T. Akesson *et al.*, Nucl. Instrum. Meth. A 522 (2004) 25

[92] Study of straw proportional tubes for a transition radiation detector / tracker at LHC, T. Akesson *et al.*, CERN-PPE/94-224, Nucl. Instrum. Meth. A 361 (1995) 440.

[93] ATLAS inner detector technical design report Vol. 2, ATLAS Collaboration, ATLAS TDR 5, CERN-LHCC-97-17, CERN (1997).

[94] The ATLAS transition radiation tracker (TRT) proportional drift tube: design and performance, ATLAS TRT Collaboration, 2008 JINST 3 P02013 doi:10.1088/1748-0221/3/02/P02013

[95] ATLAS silicon microstrip detector system (SCT), Y. Unno *et al.*, Nucl. Instrum. Meth. A 511 (2003) 58-63.

[96] ATLAS silicon microstrip Semiconductor Tracker (SCT), Y. Unno *et al.*, Nucl. Instrum. Meth. A 453 (2000) 109-120.

[97] The ATLAS semiconductor tracker (SCT), J. N. Jackson, The ATLAS SCT Collaboration, Nucl. Instrum. Meth. A 541 (2005) 89-95.

[98] Status of the ATLAS SCT, A. Clark, U. Parzefall, M. Tyndel, For the ATLAS SCT Collaboration, Nucl. Instr. and Meth. A, 579 (1997), p. 580-591.

[99] Image of pixel detector, The ATLAS Collaboration, `http://www.atlas.ch/photos/inner-detector-pixel.html` accessed, 15/02/2014.

[100] ATLAS pixel detector: technical design report, The ATLAS Collaboration, CERN/LHCC/98-13, 31 May 1998

[101] Dynamic efficiency measurments for irradiated ATLAS pixel single chip modules, M. Pfaff, PhD Thesis, Georg-August-Universität, Göttingen, Germany, 2011.

[102] Summary of bump bonding techniques for pixel systems, M. Lozano *et al.*, `http://www.physics.purdue.edu/vertex/talks/lozano/` accessed, 15/02/2014.

[103] Development of an FPGA-based FE-I3 pixel readout system and characterization of novel 3D and planar pixel detectors, J. Janssen Diploma Thesis, Universität Bonn, 2010.

[104] Characterisation and testbeam analysis of irradiated silicon n-in-p pixel detectors for the ATLAS upgrades, P. Weigell *et al.*, 18th RD50 Workshop, Liverpool, May, 2011.

[105] The FEI3 readout chip for the ATLAS pixel detector, I. Peric *et al.*, Nucl. Instr. Meth. A 565 (2006) 178.

[106] Commissioning perspectives for the ATLAS pixel detector, D. Dobos, PhD Thesis, University of Dortmund, 2007.

[107] Particle data group, J.Beringer *et al.*, Phys. Rev. D **8**6, 010001 (2012).

[108] Digital architechture and interface of the new ATLAS pixel front-end IC for upgraded LHC luminousity, D. Arutino *et al.*, IEEE Nuclear Science Conf. Rec., Dresden, Germany (2008).

[109] Submission of the first full scale prototype chip for upgraded ATLAS pixel detector at LHC, FEI4A, M. Barbero *et al.*, Nucl. Instr. and Meth. A 650, 111 (2011).

[110] FE-I4 ATLAS pixel chip design, M. Barbero *et al.*, in proceedings of 'VERTEX 2009 Workshop', PoS (VERTEX2009) 027.

[111] The FE-I4 pixel readout integrated circuit, M. Garcia-Sciveres *et al.*, in proceedings of the Seventh International Hiroshima Symposium on the development and Application of Semiconductor Tracking Detectors, 29 th August - 1st September 2009, Hiroshima, Japan.

[112] FE-I4 summary, M. Backhaus, Desy Workshop, Hamburg, 05/04/2011.

[113] Prototype ATLAS IBL modules using the FE-I4A front-end readout chip, The ATLAS IBL Collaboration, JINST 7 P11010, (2012), DOI:10.1088/1748-0221/7/11/P11010.

[114] Characterisation of the FE-I4B pixel readout chip production run for the ATLAS insertable b-layer upgrade, M. Backhaus, JINST 8 C03013, (2013) arXiv:1304.4424 [physics.ins-det].

[115] Pixel detector readout limitations, B. di Girolamo `https://edms.cern.ch/file/1161191/1/PixelReadoutLimitations-v2-120228.pdf`

[116] The ATLAS pixel nSQP readout chain, S. Welch, J. Dopke. `https://cds.cern.ch/record/1478166?ln=en`

[117] ATLAS insertable b-layer technical design report, G. Aad *et al.* , 2008 JINST 3 P07007 doi:10.1088/1748-0221/3/07/P07007

[118] Operational experience with the ATLAS pixel detector at the LHC, M. Keil, Vertex 2012, to be published in Proceedings of science.

[119] Operational experience with the ATLAS strip detector at the LHC, S, Yacoob, Vertex 2012, to be published in Proceedings of science.

[120] Radiation background simulation and verification at the LHC, I. Dawson, Vertex 2012, to be published in Proceedings of science.

[121] Radiation damage to currently running LHC detectors, S, Gibson, Vertex 2012, to be published in Proceedings of science.

[122] Charged-particle multiplicities in pp interactions measured with the ATLAS detector at the LHC, The ATLAS Collaboration, New J.Phys., 13:053033, 2011.

[123] Final report: ATLAS phase-II Tracker upgrade layout task force, A. Clark, M. Elsing, N. Hessey, P. Mättig, N. Styles, P. Wells, S. Burdin, T. Cornelissen, T. Todorovo, P. Vankov, I. Watson, and S. Wenig, ATL-UPGRADE-PUB-2012-004, 2012.

[124] Neutron moderator studies for the ATLAS inner tracker upgrade, I. Dawson, P. Majewski and L. Nicolas, 2009, ATU-TC-ER-0002.

[125] Plans for the phase-II upgrade to the ATLAS detector, B. T. Huffman, 2014, JINST 9 C02033.

[126] Performance specifications of the tracker phase-II upgrade, A. Clark, M. Elsing, and P. Wells, ATL-UPGRADE-PUB-2012-003, 2012

[127] Radiation damage in silicon particle detectors, M. Moll, PhD Thesis, Universität Hamburg, Nov, 1999

[128] Irradiated silicon detectors for HL-LHC: characterization and simulations, M, Moya, PhD Thesis, Universitat de Valéncia, 2012.

[129] Image taken from `http://www.iue.tuwien.ac.at/phd/wittmann/node7.html`, accessed March 2014.

[130] Image taken from `http://www.electrical4u.com/energy-brands-in-silicon`, accessed March 2014.

[131] The development of p-type silicon detectors for the high radiation regions of the LHC, M. D. Hanlon, PhD Thesis, Liverpool University, 1998.

[132] Improving the radiation hardness properties of silicon detectors using oxygenated n-type and p-type silicon, G. Casse, P.P. Allport, M. Hanlon, IEEE Trans. Nucl. Sci., NS-47 (3) (2000), p. 527 June.

[133] Physics of semiconductor devices, S. M. Sze, 2nd ed, ISBN-471-84290-7.

[134] Semiconductor physics and devices: basic principles, D. A. Neamen, 3rd ed, ISBN-0-07-232107-5

[135] Techniques for nuclear and particle physics experiments: a how-to approach, W. Leo, Springer, 1994.

[136] Review of particle physics, K. Nakamura *et al.* J. Phys. G 37 (2010) 075021, Particle Data Group.

[137] Passage of particles through matter, H. Bichsel, D. E. Groom and S. R. Klein, J. Phys. G37 (2010) 285.

[138] Silicon solid state devices and radiation detection, C. Leroy and P.-G. Rancoita, World Scientific Publishing Co. Pte. Ltd., Singapore, (2012), ISBN 978-981-4390-04-0.

[139] Performance of *n-in-p* pixel detector irradiated at fluences up to 5 x 10^{15} n_{eq}/cm^2 for the future ATLAS upgrades, A. Macchiolo *et al.*, 2011, arXiv:1110.4468.

[140] Sensor concepts for pixel detectors in high energy physics, T. Rohe, Proceedings of the International Workshop on Semiconductor Pixel Detectors for Particles and X-Rays (PIXEL2002), 2012.

[141] Private communication with Ilya Tsurin, University of Liverpool, April 2014.

[142] Strip detector design for ATLAS and HERA-B using two-dimentional device simulation, R. H. Richter *et al.*, Nucl. Instrum. methods phys. Res., Sect. A 377, 412 - 421.

[143] Development of thin sensors and a novel interconnection technology for the upgrade of the ATLAS pixel system, M. Beimforde, PhD thesis, TU Munchen, 2010.

[144] Silicon and silicon dioxide neutron damage functions, M. S. Lazo *et al.*, Sandia National Laboratories, SAND87-0098 Vol.1, p85-103, 1987.

[145] Hole transport and trapping in field oxides, H. E. Boesch *et al.*, Trans, Nucl, Sci, Vol NS-32 No.6(1985)3940.

[146] Kinetics of H_2 passivation of Pb centers at the (111) Si-SiO$_2$ interface, K. L. Brower, Phys. Rev. B 38, 9657 9666 (1988).

[147] Widening the range in measuring neutron fluences with PIN silicon diodes, J. Morin *et al.*, Radiation and its Effects on Components and Systems 95, 476-480, 1995

[148] The NIEL scaling hypothesis as applied to neutron spectra of irradiation of ATLAS and CMS SCT, A. Vasilescu, RD48 Technical Note, 1997, ROSE/TN/92-2

[149] Mechanisms of radiation eects in electronic materials, V. van Lint *et al.*, John Wiley & Sons, 1980

[150] Radiation damage in proton - irradiated epitaxial silicon detectors, J. Lange, Diploma Thesis, Universität Hamburg, 2008.

[151] Review of displacement damage effects in silicon devices, J. Srour, C. Marshall, P. Marshall, IEEE Trans. Nucl. Sci., 50, 653-670, 2003

[152] Effective trapping time of electrons and holes in different silicon materials irradiated with neutrons, protons and pions, G. Kramberger *et al.*, Nucl. Instrum. Methods Phys. Res., Sect. A 481, 297-305 (2002).

[153] On pre-breakdown phenomena in insulators and electronic semiconductors, J. Frenkel Phys. Rev. 54, 647-648, 1993

[154] Radiation tolerant sensors for the ATLAS pixel detector, R. Wunstorf *et al.*, Nucl. Instrum. Methods Phys. Res., Sect. A 466, 327-334 (2001)

[155] Study of silicon detectors irradiated with 24 GeV protons between -20°C and +20°C, F. Lemeileur Nucl. Instrum. Methods. Phys., Res., Sect. A 360(1995)438

[156] Flir, website, `http://www.flir.com/GB/`

[157] Computational analysis of irradiation facilities at the JSI TRIGA reactor, L. Snoj, G. Ẑerovnik and A. Trkov, Appl. Rad. iSO. 70 (2012) 483.

[158] `https://irradiation.web.cern.ch/irradiation/`

[159] Radiation hard silicon detectors - developments by the RD48 (ROSE) Collaboration, G. Lindström *et al.*, Nucl. Instr. Meth. A466 (2001) 308.

[160] Untersuchungen zur strahlenhärte von siliziumsensoren, A. Dierlamm, PhD Thesis, Universität Karlsruhe, (2003), IEKP-KA/2003-23.

[161] The birmingham irradiation facility, P. Dervan, R. French, P. Hodgson, H. Marin-Reyes, J. Wilson, Nucl. Instr. Meth. A730 (2013) 101-104.

[162] The beetle reference manual - chip version 1.3, 1.4 and 1.5, S. Löchner and M. Schmelling CERN, (2006), LHCb-2005-105.

[163] The LHCb detector at the LHC, The LHCb Collaboration, JINST 3 (2008) S08005.

[164] Photosensor modules H5773/H5783/H6779/H6780 series, Hamamatsu, 2e edition, 2007

[165] ATLAS FE-I4 ASIC, L. Caminada *et al.*, PoS (Vertex 2012) 023.

[166] Development of a versatile and modular test system for ATLAS hybrid pixel detectors, M. Backhaus *et al.*, Nucl. Instr. Meth. A 650 no. 1, (2011) 37-40.

[167] USBpix - USB based readout system for ATLAS FE-I3 and FE-I4, University of Bonn, `http://icwiki.physik.uni-bonn.de/twiki/bin/view/Systems/UsbPix`

[168] TurboDAQ, B. LBNL ATLAS Group, `http://pixdata.lbl.gov/html/TurboDAQ.html`

[169] PixLib scans, `http://icwiki.physik.uni-bonn.de/twiki/bin/view/Systems/PixLibScans` visited on January 2014.

[170] Comparison of thin n- and p-type bulk silicon pixel sensors, J. Rieger Masters Thesis, Georg-August-Universitat, Gottingen, 2012

[171] Characterisation of the T24 electron beam line available at DESY, D. Autiero, Y. Caffari, L. S. Esposito, A. Marteau, and P. Migliozzi, OPERA Note, 2004.

[172] First test results of MIMOSA-26, a fast CMOS sensor with integrated zero suppression And digitized output, J. Baudot *et al.*, 2009 IEEE NSS Conference Record (2009) 1169.

[173] Planar pixel sensors for the ATLAS upgrade: beam tests results, J. Weingarten *et al.*, arXiv:1204.1266 [physics.ins-det], 2012.

[174] EUTelescope framework home page, `http://eutelescope.web.cern.ch/`

[175] Description of the JRA1 trigger logic unit (TLU), D. Cussans, v0.2c, EUDET-Memo-2009-4, September 2009.

[176] Linear least squares fits with a large number of paramters, V. Blobel, http://www.desy.de/~blobel, accessed April 2014.

[177] Millipede II, Online https://www.wiki.terascale.de/index.php/millepede_ii

[178] The deterministic annealing filter, S. Fleischmann, CERN-THESIS-2007-011, pp.19 - 23.

[179] A concurrent track evolution algorithm for pattern recognition in the HERA-B main tracking system, R. Mankel, Nucl. Instrum. Meth. A 395 no. 2, (1997) 169 184. http://www.sciencedirect.com/science/article/pii/S0168900297007055

[180] EUTelescope: tracking software, A. Bulgheroni, T. Klimkovich, P. Roloff, and A. Zarnecki, EUDET-Memo-2007-20 144 (2007).

[181] Full simulation of a testbeam experiment including modeling of the Bonn ATLAS telescope and ATLAS 3D pixel silicon sensors, K. N. Sjoebaek, Masters Thesis, Department of Physics, University of Oslo, Oslo, Norway.

[182] Spatial resolution of silicon microstrip detectors, R. Turchetta, Nucl. Instrum. Meth. A, 658 (2011), p. 20.

[183] Straggling in thin detectors, H. Bichsel, Rev. Mod. Phys. 60 (1988) 663

[184] Private communication with A. Greenall.

[185] Limits on upgrade tracker layout from particle uxes, signal-to-noise, and occupancy, H.F.W. Sadrozinski, A. Bogert, J. Nielsen, A. Affolder, I. Dawson, L. Nicolas, Nucl. Instrum. and Meth. A, 658 (2011), p. 20.

[186] I. Dawson, ATLAS TWiki: Radiation Background Simulations (2011). https://twiki.cern.ch/twiki/bin/view/AtlasPublic/SimulationPublicResults

[187] Private communication with G. Casse

[188] Signal and charge collection efficiency of n-in-p strip detectors after mixed irradiation to HL-LHC fluences, S. Kuehna, T. Barber, G. Casse, P. Dervan, A. Driewer, D. Forshaw, T. Huse, K. Jakobs, U. Parzefall, Nucl. Instrum. and Meth. A, 730 (2013), p. 58-61.

[189] Simulation of new p-type strip detectors with trench to enhance the charge multiplication effect in the n-type electrodes, P. Fernández-Martnez, G. Pellegrini, J.P. Balbuena, D. Quirion, S. Hidalgo, D. Flores, M. Lozano, G. Casse, Nucl. Instrum. and Meth. A, 658/1 (2011), p. 98-102.

[190] Characterisation of micro-strip and pixel silicon detectors before and after hadron irradiation, P.P. Allport, K. Ball, G. Casse, V. Chmill, D. Forshaw, K. Hadfield, A. Pritchard, P. Pool and I. Tsurin 2012, JINST 7, C01105, `doi:10.1088/1748-0221/7/01/C01105`

[191] Enhanced efciency of segmented silicon detectors of different thicknesses after proton irradiations up to $1 \cdot 10^{16}\,\mathrm{n_{eq}/cm^2}$, G. Casse, A. Affolder, P.P. Allport, H. Brown, M. Wormald, Nucl. Instr. and Meth. A, 624/2 (2010), p. 401.

[192] Evaluation of floating zone and epitaxial planar silicon detectors with different substrate thickness after irradiation up to $2 \cdot 10^{16}\,\mathrm{n_{eq}/cm^2}$, G. Casse, A. Affolder, P.P. Allport, IEEE Transactions on Nuclear Science, 56 (6) (2009), p. 3752.

[193] Efficiency and noise measurements of non-uniformly irradiated double-sided silicon strip detectors, T. Dubbs *et al.*, Nucl. Instr. and Meth. A, 383 (1996), p. 174.

[194] Improving the radiation hardness properties of silicon detectors using oxygenated n-type and p-type silicon, G. Casse, P.P. Allport, M. Hanlon, IEEE Trans. Nucl. Sci., NS-47 (3) (2000), p. 527 June.

[195] 14th RD50 workshop on radiation hard semiconductor devices for very high luminousity colliders, Freiburg, 3-5 June, 2009, `http://rd50.web.cern.ch/rd50/14th-workshop/default.htm`.

[196] First results on charge collection efciency of heavily irradiated microstrip sensors fabricated on oxygenated p-type silicon, G. Casse, P.P. Allport, S. Martí i Garcia, M. Lozano, P.R. Turner, Nucl. Instru. and Meth. A, A 518 (2004), p. 340.

[197] Studies of charge collection efciencies of planar silicon detectors after doses up to $10^{15}\,\mathrm{n_{eq}/cm^2}$ and the effect of varying diode congurations and substrate types, A. Affolder, P.P. Allport, G. Casse, Nucl. Instru. and Meth. A, 604 (2009), p. 250.

[198] A charge collection study with dedicated RD50 charge multiplication sensors, C. Betancourt *et al.* Nucl. Instru. and Meth. A, A730 (2013), p. 62-65.

[199] One micron spatial resolution with silicon strip detectors, J. Straver *et al.*. Nucl. Instru. and Meth. A, A348 (1994), p. 485.

[200] Degradation of charge sharing after neutron irradiation in strip silicon detectors with different geometries, G. Casse, D. Forshaw *et al.*. Nucl. Instru. and Meth. A, A730 (2013), p. 54-57.

[201] ATLAS ID upgrade; material studies, N. Readioff, S. Burdin, H. Hayward, ATLAS Phase II Strip Tracker, IFIC-Valencia, Spain, 3-7 Febuary 2014.

[202] Quality assurance and functionality tests on electrical components during the ATLAS IBL production, J. Jentzsch, Topical Workshop on Electronics for Particle Physics 2012, Oxford, UK. http://dx.doi.org/10.1088/1748-0221/8/02/C02048

[203] Quality assurance and functionality tests on electrical components during the ATLAS IBL production, A, Bassalat, Topical Workshop on Electronics for Particle Physics 2013, Perugia, Italy. http://dx.doi.org/10.1088/1748-0221/9/01/C01046

[204] Pixel Sensors with different pitch layouts for ATLAS Phase II upgrade, P. Dervan *et al.*, TIPP 2014, 2-6 June, Beurs van Berlage.

[205] Advacam, http://www.advacam.com/en/